# IDENTIFICATION AND MATURATION OF NEW POTENTIAL HELIUM DEPOSITS ON THE NAVAJO NATION LANDS

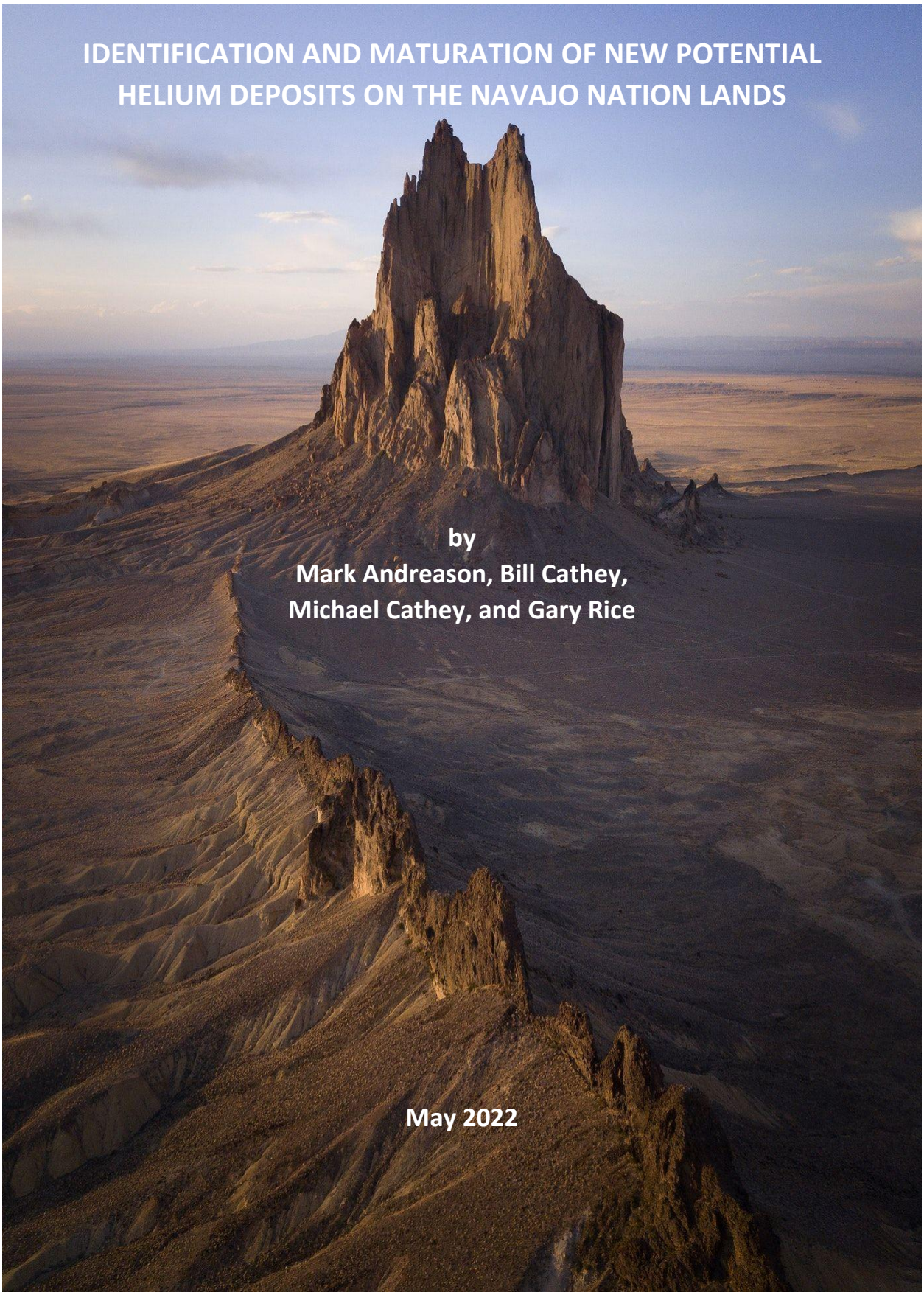

by
Mark Andreason, Bill Cathey,
Michael Cathey, and Gary Rice

May 2022

# IDENTIFICATION AND MATURATION OF NEW POTENTIAL HELIUM DEPOSITS ON THE NAVAJO NATION LANDS

**by**
**Mark Andreason, Bill Cathey, Michael Cathey, and Gary Rice**

**FINAL REPORT**
**EMDP GRANT #A21AP10056**

Submitted to the

**U.S. DEPARTMENT OF INTERIOR DEPARTMENT OF INDIAN AFFAIRS, DIVISION OF ENERGY AND MINERALS DEVELOPMENT**

by

**NAVAJO NATION OIL & GAS COMPANY**
Program Director/Principal Investigator:
Mark Andreason
VP Geosciences
24285 Katy Fwy., Suite 300
Katy, Texas 77494
281-798-5606
mandreason@nnogc.com

**May 2022**

## Table of Contents

# List of Figures and Tables

**FIGURES**

**TABLES**

## Acknowledgements

The authors would like to thank the Navajo soil gas sampling team who spent three months and collected over 2,000 sample gas samples. Members of the team were Derek Begay, Wyatt Gipson, Marty Goldtooth, Lance Johnson, Kendale Lewis, Shounova Lewis, Xavier Smiley and Tritt Smith. We also extend a special thanks to Racheal Dahozy of NNOGC who aided and supported the soil gas team and kept the local Navajo communities informed of our activities. We also want to thank Anna Khadeeva, NNOGC geotechnician, who spent days of data entry, digitizing, and assisting in log correlations. We want to extend our thanks and appreciation to the U.S. Department of the Interior, Division of Energy and Minerals Development for their support, encouragement, and funding. Lastly, we want to thank the Navajo Minerals Department, the Navajo Nation, and the Navajo people, whose support made this work possible.

## Abstract

Very high concentrations of helium (5-9%) occur within the Four Corners region within the Navajo Nation. Numerous helium accumulations were discovered in the 1940's – 1960's as a byproduct of oil and gas exploration. The purpose of this study is to understand the mechanisms that result in the accumulation of high helium deposits and to identify new potential helium resources within the Navajo Lands. In order to accomplish this objective, the study was divided into three parts: 1) the acquisition of high-resolution aeromagnetic data over an area that contains the highest concentration of known helium deposits to better understand the source and migration aspects, 2) conduct a thermal study over the entire Navajo Nation to generate current heat flow conditions to determine if there is a relationship between helium and heat flow, and 3) conduct high-density soil gas sampling over several known and prospective helium deposits to see if there is a relationship between subsurface helium deposits and helium soil gas concentrations.

The helium system consists of four major components, like a petroleum system, but very different in its details: 1) source and generation, 2) migration (both primary and secondary), 3) trap charging, and 4) retention and preservation in a trap. The radioactive decay of uranium and thorium within the crust serves as the source and generation mechanism for helium. Release of helium from the source can occur because of orogenic and/or magmatic events. In the Four Corners study area, data suggests that magmatic events, particularly those related to the Oligocene to Miocene (28-19 Ma) Navajo Volcanic field, were the primary release mechanism for helium from the crustal source rocks. Data also suggests that helium migration from a rising intrusive body is very short before encountering a trap. All the helium-rich fields that have been discovered to date in the Four Corners region are sealed by shales, silty shales,

or tight, micritic limestones. These rocks have much poorer sealing qualities than evaporites and would have a greater risk of diffusional losses of helium, certainly for older accumulations. Data from this study suggests that the helium fields surrounding the Defiance uplift would have begun charging because of the Navajo Volcanic field magmatic activity (28-19 Ma) or later.

The most helium prospective areas, as determined by this study, are regions where lineament intersections correspond to the location of subsurface intrusive bodies. Two-hundred and fifty-three (253) untested potential helium deposits are identified within the study area because of this correspondence. Thirty-five (35) of these lineament intersection-intrusive body overlap areas had been previously tested resulting in a 45% success rate for finding significant high helium-rich deposits. Helium soil gas sampling was also found to be indicative of identifying subsurface helium deposits and would be a useful and cost-effective method to reduce the exploratory risks. Heat flow as determined by the thermal study portion of this report, although not that useful in determining high helium deposits, was found to be very helpful in determining areas of high carbon dioxide occurrence.

## Introduction

Helium was first discovered serendipitously on Navajo Lands in the early 1940's as a byproduct of oil and gas exploration drilling. Helium, sometimes in very high concentrations of 5-9%, were discovered in closures around the Defiance Uplift/ Four Corners Platform area of northeastern Arizona and northwestern New Mexico (Figure 1). Many of the helium deposits discovered in the 1940's on Navajo Lands such as Rattlesnake, Hogback, and Table Mesa fields were developed and produced by the U.S. Government. Other helium fields such as Beautiful Mountain, Dineh-bi-Keyah, Pinta Dome, Navajo Springs, and Tocito Dome were developed and produced by private companies. Exploratory drilling for oil & gas in the Defiance Uplift area had mostly ceased by the end of the 1960s. Since then, there have been no new helium deposits discovered on Navajo Lands although development of some of the early discoveries has continued to present day.

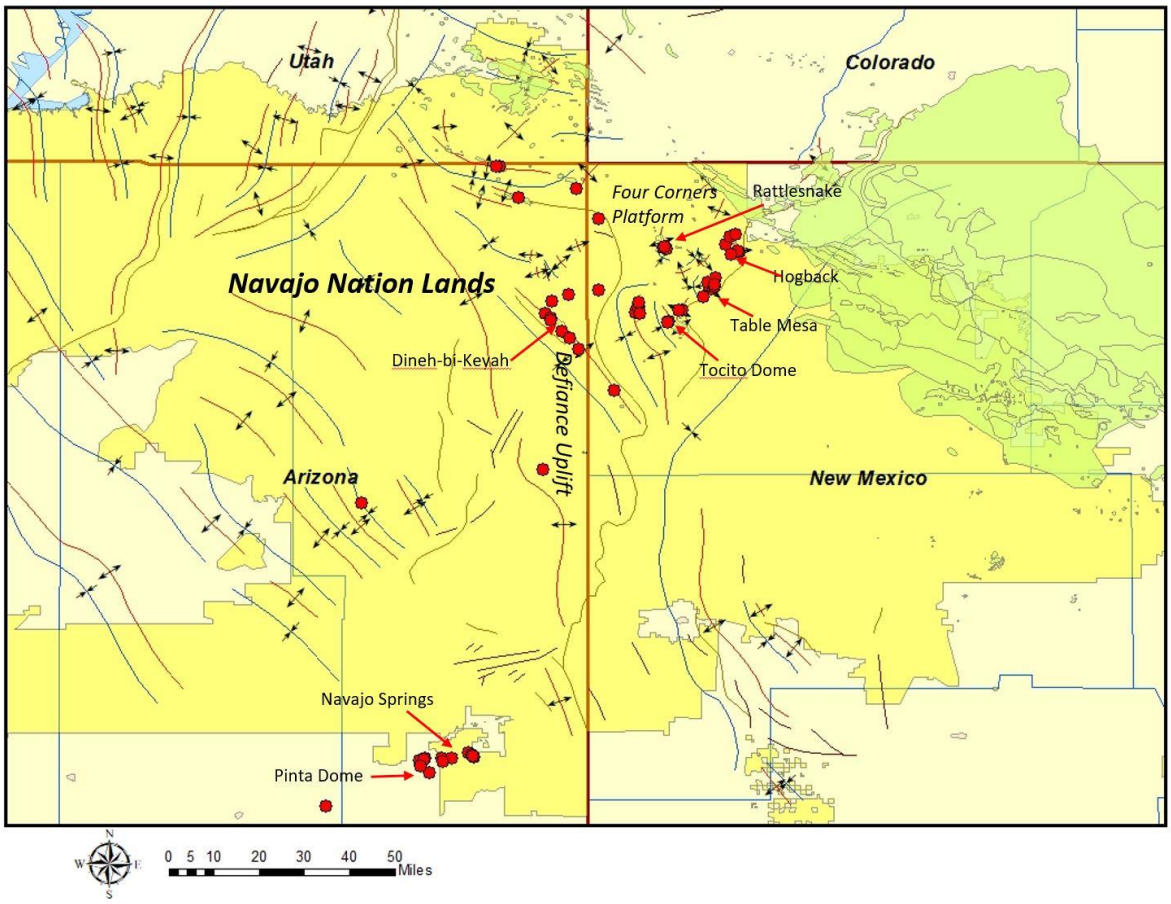


Figure 1. Location of high helium concentration wells (>4% Helium, red dots) and key helium producing fields on Navajo Lands.

The U.S. Government was the primary consumer of helium for much of the last century and effectively regulated its price by the creation of the United States National Helium Reserve. More recently, commercial demand for helium has risen as industrial applications for this gas have increased. Since 1996, the Government has acted to privatize the production and sale of helium, and prices on the open market have risen dramatically despite competition from foreign sources. Helium prices have reached record levels in recent years and helium reserves are now much more valuable than hydrocarbons. The Navajo Nation has gas deposits with some of the highest percentages of helium in the world. The potential high commercial value of this underdeveloped and underexplored resource provides a great incentive for the Navajo Nation to develop its helium reserves within their Reservation.

The Division of Energy and Mineral Development, Department of the Interior, Indian Affairs ("DEMD") and the Navajo Nation Oil and Gas Company ("NNOGC"), a wholly owned arm and instrumentality of the Navajo Nation formed under Section 17 of the Indian Reorganization Act, 25 U.S.C. § 5124 (formerly § 477), jointly funded a regional assessment of the hydrocarbon and helium resources on and around the Navajo Lands. Global Ventures/Consultants Inc.

completed this initial project in 2012 (reports are available in the tribal and DEMD libraries). This study was a high-level regional investigation of historical helium discoveries on Navajo Lands and documented several potential helium leads. No new technical data such as seismic, aeromagnetic, or helium soil gas surveys were acquired in this study and therefore none of the helium leads could be de-risked and matured to the point that drilling could proceed, or partners attracted.

In 2015, the DEMD provided funds for NNOGC to re-enter and test the Navajo Z-well in Apache Co., Arizona, a well that formerly produced gas with over 6% helium. The test was very successful and significant helium reserves were documented.

In 2019, NNOGC undertook new work to study the previously discovered helium deposits and to identify new prospective helium deposits on the Navajo Lands. The objectives of the work were 1) to understand and identify the source and migration pathways of the helium bearing gases and 2) to identify which traps contained high helium concentration gases and their approximate size. NNOGC paid Earthfield Technology LLC to process and interpret all the public aeromagnetic data (9-mile X 3-mile grid) and gravity data covering the entire Navajo Reservation. Since aeromagnetic data responds to local magnetic variations in the underlying rocks, it is extremely useful in mapping the basement structure and basement lineaments, particularly when Werner deconvolution methods are applied. Aeromagnetic data can also image ancient magma chambers at the mantle-crust boundary, intrusive plutons within the crust, and volcanic dikes, sills, and feeders. All these components (basement structure, lineaments, magma chambers, plutons, volcanic dikes, sills, and feeders) define the source and migration pathways for potential helium-rich gases being released from the crust during magmatic episodes in the past.

NNOGC, also in 2019-2020, conducted three rounds of helium soil gas surveys over the Texaco Z-well structure in NE Arizona and over the Rattlesnake field in NW New Mexico. Both areas contain known high helium concentration (>6% Helium) producing wells from the Mississippian Leadville limestone at depths of 6300 – 7000 ft. The surveys established that anomalous helium soil gas readings occur over the non-depleted Texaco Z-well structure but only background readings over the depleted Rattlesnake Field. In 2021, Navajo Nation and NNOGC, acting as the principal investigator to design and execute the study, were awarded an EMDP Federal Grant to further identify and mature new prospective helium deposits within the Navajo Nation. This report is the culmination of a 10-month study.

## Purpose of this Study

The primary goals of this helium project are 1) to provide the necessary in-depth technical analysis to support and encourage the exploration, development and marketing of the helium reserves on Navajo Lands, 2) to increase seismic, drilling and other exploration and production activity on Navajo Lands that will lead to increased employment for the Navajo people in both exploration/production activity and in industries supporting those activities, and 3) to increase revenue to the Navajo Nation through increased lease income, increased royalties, and profits from helium production. Ultimately, with the full development of the Nation's helium resources, hundreds of jobs will be created for the Navajo people. To achieve these goals, this study will conduct a very detailed study using an acquired high-resolution aeromagnetic survey and high-density helium soil gas sampling over the most helium prospective portion of the Navajo Nation over the northern portion of the Defiance uplift and the Four Corners platform. A regional thermal susceptibility study and structure and isopach mapping of the key helium bearing strata covering the entire Navajo Nation will also be included. The study area of this report is shown in Figure 2. The study products are summarized below:

- Acquire a high-resolution aeromagnetic (0.25 x 1 mile grid) survey covering 1.66 million acres to identify intrusive bodies (opens migration pathways), define basement (helium source) structure, identify potential migration pathways of the helium bearing gases through basement lineaments, potential fracture zones, fracture intersections, and intrusive dikes/sills.
- Acquire surface helium soil gas surveys over seven prospective areas to potentially determine the presence, size, and extent of the helium accumulations.
- Conduct a thermal susceptibility study using public aeromagnetic data (3 x 9 mile grid) and gravity data covering over 68 million acres. The thermal study will determine the background heat flow, heat flow from the basement or magnetic layer (top of basement to Curie point depth), and heat flow from the sedimentary section. The various basement terranes will also be mapped along with heat production from the different terranes. All these components will be used to determine a final calculated heat flow and to determine whether heat flow can be used as a predictor of helium and/or carbon dioxide occurrence.
- Create regional structure and isopach maps of the main helium-bearing intervals in the Devonian, Mississippian, Pennsylvanian, and Permian.
- Integrate the data from the above products with surface and subsurface geologic data and all previous work to identify high-potential, low-risk helium prospect and leads within the area covered by the high-resolution aeromagnetic survey.
- Final report.

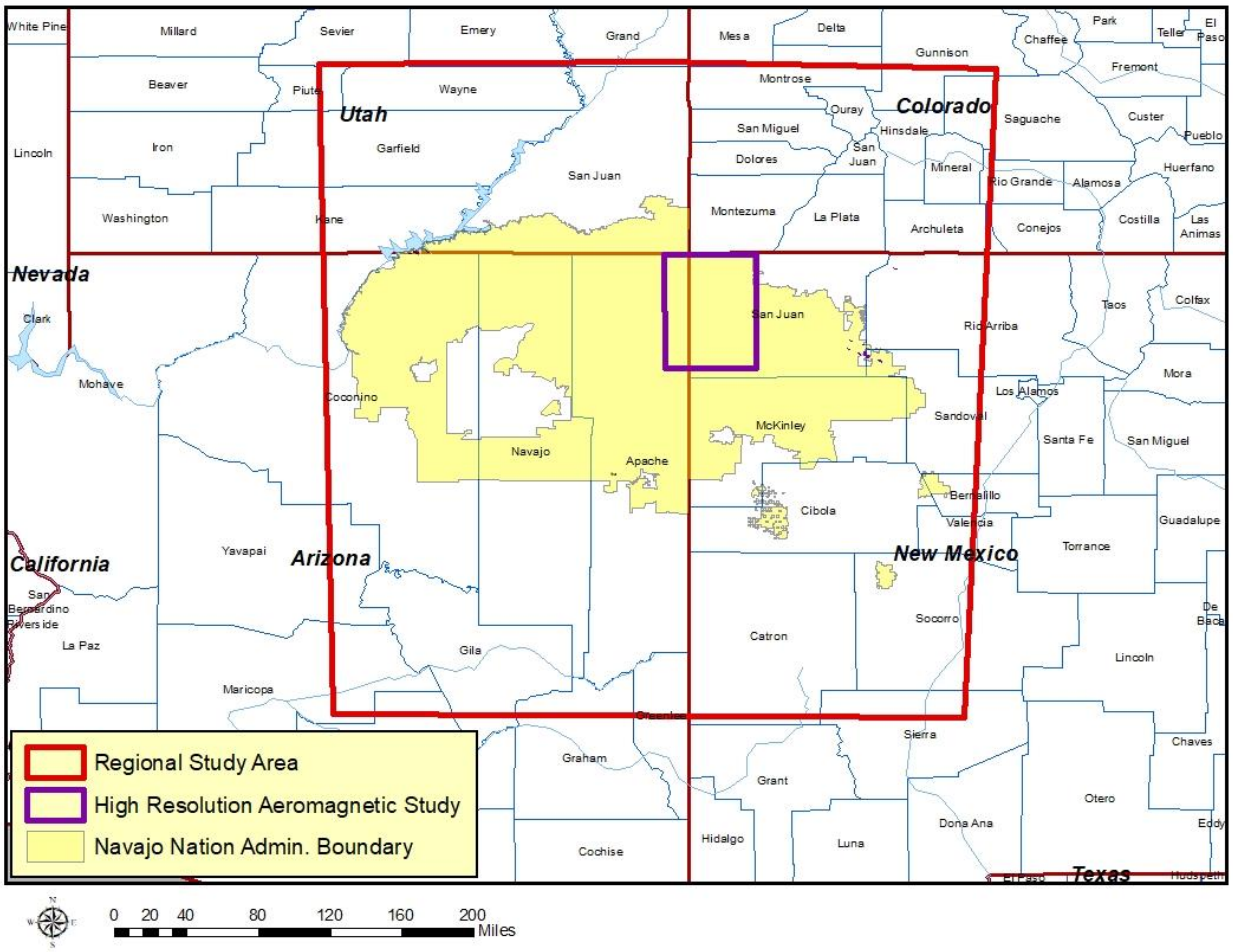


Figure 2. Location of the regional and detailed study areas covered by this report.

## The Helium System

### Helium source rocks and generation

Helium occurs as two stable isotopes, helium-3 and helium-4. Helium-3 is very rare and is referred to as "primordial helium" since the bulk of it was trapped in the Earth's mantle during the planet's formation. Helium-4, which constitutes 99.999% of helium gas, is mainly produced by the alpha decay of uranium-235, uranium-238, and thorium-232 which has led to it being called "radiogenic helium". Eight helium atoms are produced by the complete decay of uranium-238 to lead-206. Radioactive decay is a time dependent process that is unaffected by pressure and temperature. It is measured in terms of radioactive parent half-life, or, in other words, the time taken for half of the parent element to "decay" to the daughter element. Since this process is only time-dependent, the older the rock, the more decay has occurred and thus the more helium-4 that has been produced.

Typical uranium and thorium-bearing rocks such as apatite, zircon, uraninite, and monazite can retain and accumulate helium if the rock is below their closure temperature. During the alpha decay process, the released helium only travels within 10-20 µm of the parent radioelement (Martel et al, 1990). The closure temperature is the temperature at which a system (mineral or rock) has cooled so that there is no longer any significant diffusion of the parent or daughter isotopes out of the system and into the external environment (Dodson, 1973). If the source rock is below the closure temperature, the helium is trapped both within the mineral matrix and on mineral grain boundaries. If the source rock is above the closure temperature, the helium atom can diffuse out of the mineral and into fluid inclusions or fractures. Helium closure temperatures for typical helium retentive minerals are shown in Table 1.

| Mineral | Closure temperature range (degC) | References |
|---|---|---|
| Apatite | 55-100 | Lippolt et al. (1994), Wolf et al. (1996), Farley (2000), Shuster et al. (2006) |
| Hematite | 90-250 | Bahr et al. (1994), Farley (2002) |
| Zircon | 180-200 | Farley (2002), Reiners (2005), Reich et al. (2007), Cherniak et al. (2009) |
| Garnet | 590-630 | Dunai and Roselieb (1996), Farley (2002) |
| Monazite | 182-299 | Boyce et al. (2005) |
| Titanite | 150-200 | Reiners and Farley (1999), Farley (2002) |
| Uraninite | 200 | Martel et al (1990), Stuart et al. (1994) |

Table 1. Helium closure temperatures for helium-retentive minerals (Danabalan et al., 2022).

Given an average helium closure temperature of 180 °C (356 °F) of the helium retentive minerals, helium will retain and accumulate in the crystalline basement to a depth of 6 km (approx. 20,000 ft) given the average temperature gradient in the Four Corners area. Some of the highest accumulations of helium are therefore found in large, stable, shallow, granitic continental blocks known as cratons that formed in the Archean (4.0 – 2.5 billion years ago) and Proterozoic or Precambrian (2.5 billion to 543 million years ago). From a simplistic sourcing perspective, older rocks will generally have had time to produce and accumulate helium than younger ones. Archean or Precambrian-aged crystalline terranes in areas that remained tectonically stable for long periods of time should be the richest helium source rocks. All the high helium concentrations found in the Four Corners area are located around the Defiance uplift which formed 1.7 billion years ago and had remained a shallow, positive feature since then.

**Primary and Secondary Migration of Helium**

The initial stage of helium migration begins when uranium and thorium undergo radioactive decay, releasing alpha particles (helium-4 nuclei). The energy associated with this process produces “fission tracks” through the uranium and thorium-bearing mineral and the helium atoms can diffuse along these tracks.

For helium to migrate out of the low-permeability crystalline source rocks and accumulate into overlying sedimentary traps, another input of energy is necessary typically in the form of orogenic or magmatic activity. These orogenic and magmatic events open and dilate existing zones of weakness in the crystalline basement along with creating new fracture swarms as the zones of weakness are mobilized. Concentric ring and radial fractures also are created as rising magmatic plumes ascend through the basement (Koide and Bhattacharji, 1975) (Figure 3). Tertiary magmatism appears to be the driving force behind helium release and migration from the crust in the Four Corners regions which will be discussed more thoroughly later in this report.

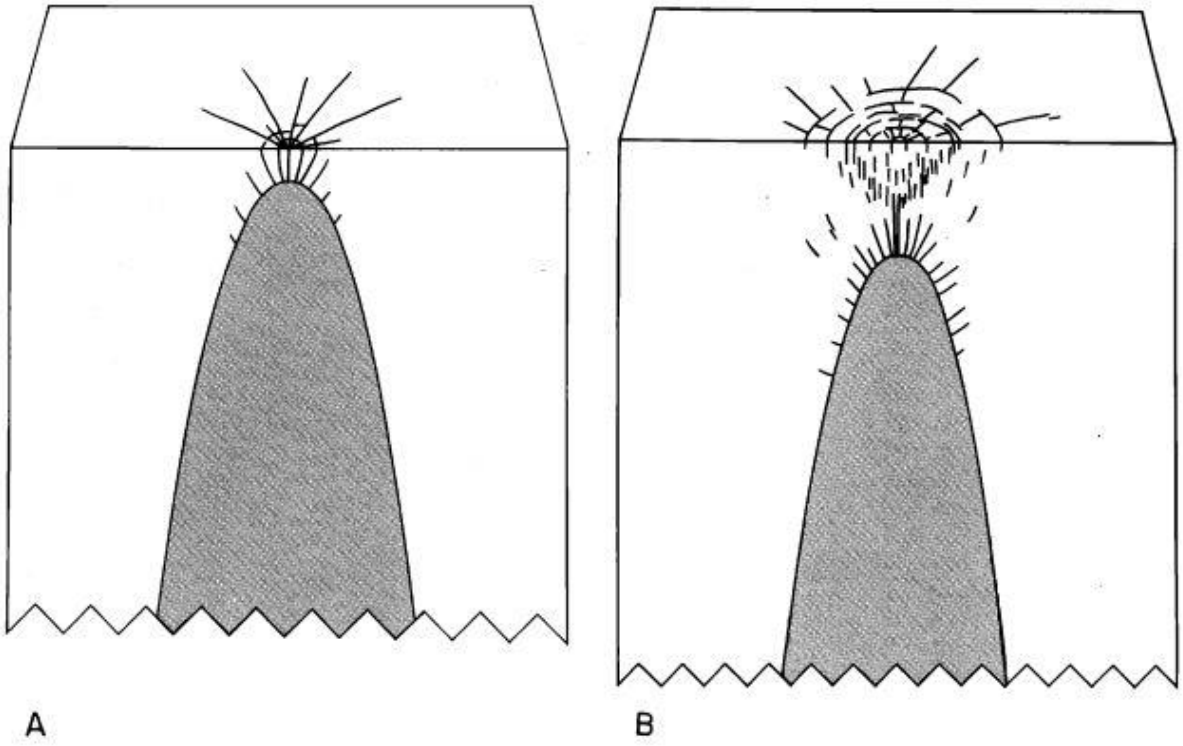


Figure 3. Possible development of fracture patterns around a vertically elongated prolate magma reservoir due to progressive increase of magma and hydrothermal fluid pressures. A. Formation of predominant radial fractures at the initial phase of intrusion when magma and hydrothermal fluid pressures are relatively low, but higher than lithostatic stress. B. Predominant concentric and peripheral radial fracture patterns due to the increase of magma and hydrothermal fluid pressures. Note the formation of funnel-shaped normal faults and en echelon concentric tension fractures (Koide and Bhattacharji, 1975).

The bulk migration of helium, although not fully understood, is theorized by Danabalan (2017) to be accomplished by the process of advection which, simply is the transfer of matter by the flow of a fluid. Danabalan (2017) states that for helium advection to occur, two events are required: 1) temperatures exceeding the closure temperature of helium retentive minerals and

2) fluids (i.e., $N_2$ or $CO_2$) are needed to enable bulk movement away from the source rock. Changes in thermal gradient, like those observed during magmatic, orogenic, and rifting events, are a prerequisite to facilitate the two conditions of advection according to Danabalan (2017). High helium concentrations are always associated with high nitrogen concentrations, yet the converse is not necessarily true. There are multiple potential sources of nitrogen in the crust, but analysis has shown that the nitrogen associated with radiogenic helium accumulations has an isotope signature characteristic of a crystalline basement source indicating that the helium and nitrogen travelled together out of the source rock. In many areas, such in the Kansas-Texas Hugoton-Panhandle gas field, radiogenically produced helium is associated with non-radiogenic nitrogen suggesting their source rocks could be different but the nitrogen, plus other gases, form a gas phase that acts as the advecting fluid (Danabalan et al., 2022). The isotopic composition of the nitrogen within the Hugoton-Panhandle area falls in a range seen both by low-temperature metamorphism of the crust or from the release of ammonia from clays (Danabalan, 2017).

Secondary migration is the lateral and vertical movement of helium and other associated gases after primary migration as either free-gas or as dissolved gases within groundwater. Vertical migration with direct input of helium-rich as a free-gas phase into a nearby trap appears to be dominant mechanism for the helium deposits in the Four Corners area, but it cannot explain large-volume helium-rich gas deposits that have not experienced any recent magmatic or tectonic activity, such as in the Texas Panhandle, Kansas, or in the Williston basin of US and Canada (Danabalan et al., 2022). These cases may require a longer distance, lateral secondary migration of helium.

Studies of air-saturated-water derived noble gas isotopes of neon, argon, helium and nitrogen in helium fields in Kansas, Oklahoma, Texas, and Arizona (southwest of the Defiance uplift) show strong evidence of groundwater involvement (Ballentine and Lollar, 2002, Gilfillan et al., 2008, Danabalan, 2017). Regional uplift, such as what impacted the above areas during the Laramide orogeny, results in a pressure drop and formation of subnormal pressures that cause gases, particularly helium and nitrogen, to exsolve from solution to generate a free-gas phase (Sorenson, 2005).

**Trap charging by helium and associated gases**

There are three mechanisms by which helium and associated gases charge a trap: 1) by direct movement of a buoyant free-gas phase, 2) degassing of oversaturated groundwater, or 3) gas stripping by hydrocarbon ($CH_4$) or magmatic ($CO_2$) gas phase (Danabalan et al., 2022). The first mechanism has been discussed in the previous section where helium and associated gases are released from the crust during via fractures created by either magma ascent or by orogenic-driven movements. In this mechanism, the helium-rich gases are directly released from the crust and from exsolved gases in mafic magmas, through the opening fractures, and into the nearest trap that the gases encounter. As mentioned previously, this mechanism appears to be

the primary charging mechanism for the helium and nitrogen-rich traps in the Four Corners region, particularly on the north and northeastern flank of the Defiance uplift.

Groundwater depressurization of oversaturated waters with respect to helium and nitrogen due to uplift and the formation of subnormal pressures may be a possible factor in some of the Four Corners helium deposits particularly in the Pinta Dome and Navajo Springs fields on the southwest flank of the Defiance uplift where both fields exhibit tilted water-gas contacts due to water flow (Figure 4). This mechanism is also suggested for the helium and nitrogen-rich fields in Kansas, on the Central Kansas Uplift, Harley Dome, Utah, and in the Williston basin (Danabalan et al., 2022).

The gas stripping mechanism occurs when groundwater containing dissolved helium and nitrogen equilibrates with a methane or carbon dioxide gas phase, insoluble helium and nitrogen will preferentially exsolve from the groundwater and partition into a free-gas phase. In this mechanism, methane or carbon dioxide migrating through groundwater dissolved helium and nitrogen will result in a helium-rich hydrocarbon or carbon dioxide phase. Since both the migrating hydrocarbons or carbon dioxide are volumetrically much larger than the volume of dissolved helium or nitrogen, the resultant accumulation contains anomalous concentration of helium but much lower than what occur in the other two mechanisms (generally less than 2% helium). This mechanism may explain the high $CO_2$ fields in southeast Utah, southwest Colorado, and the St. Johns $CO_2$ field to the south of the Defiance uplift.

Recent work conducted by the USGS, Virginia Tech, and the Aarhus University in Denmark have created stunning images of Yellowstone's subsurface hydrothermal plumbing system (Figure 5). The team acquired over 2,500-line miles of electrical and magnetic data from an instrument known as "SkyTEM" to map areas of high electrical conductivity and low magnetization indicative of hydrothermal alteration. Data showed that hot hydrothermal fluids ascend nearly vertically from depths of more than 1 km and along the way mix with shallower groundwater flowing within and beneath volcanic lava flows. Faults and fractures guide the ascent of hydrothermal fluids, while the lava flow boundaries control the groundwater aquifer boundaries. The SkyTEM data shows where helium-rich gases, which are travelling with the hot hydrothermal fluids, would either be vented at the surface or be potentially trapped beneath the volcanic lava flows.

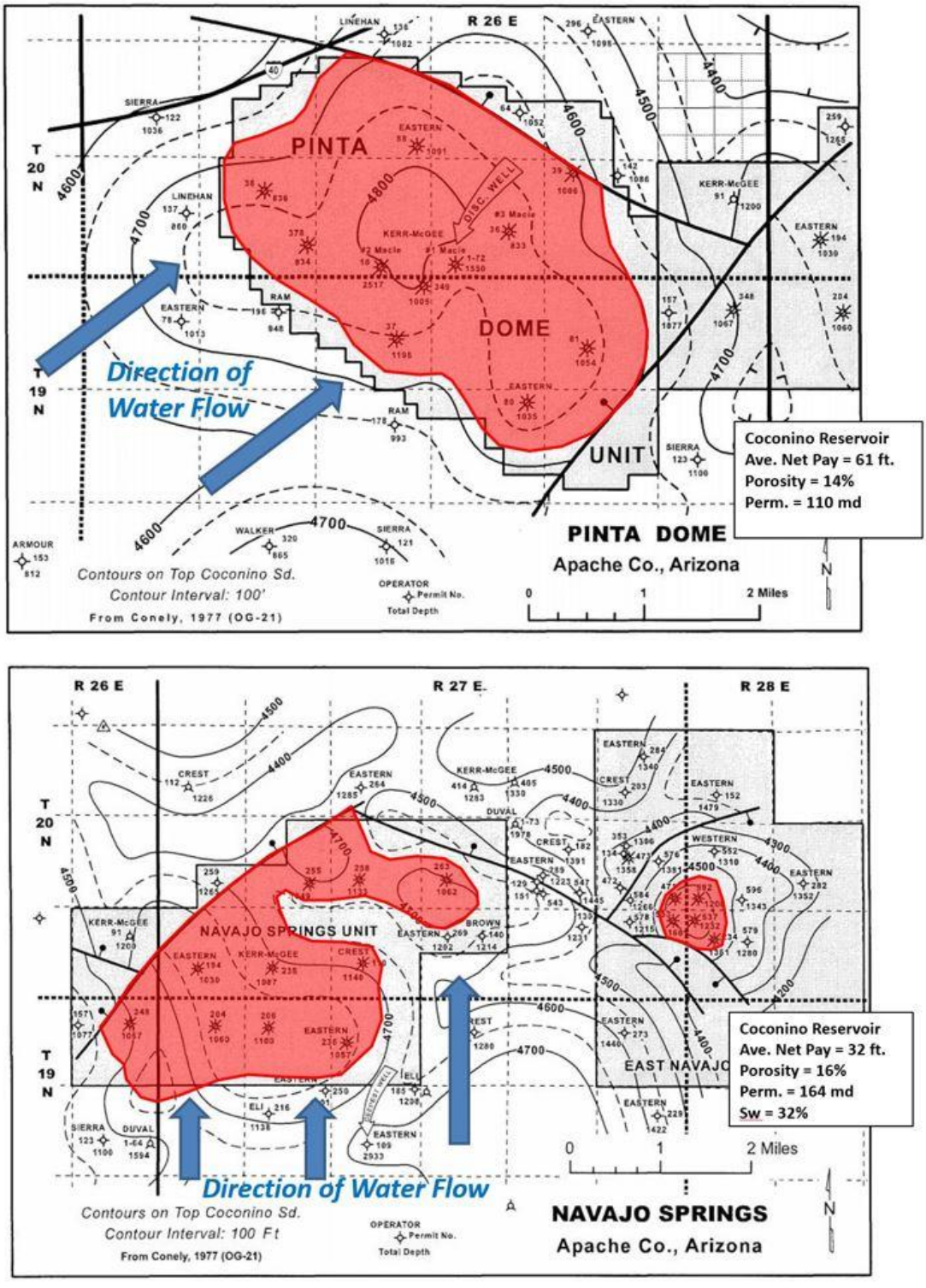


Figure 4. Tilted gas/water contacts at Pinta Dome and Navajo Springs fields in Apache Co., Arizona on the southwest flank of the Defiance uplift. Helium-nitrogen charging in these fields is possibly the result of gas depressurization due to the formation of subnormal pressures post-Laramide tilting and uplift to the south (modified from Rauzi, 2003).

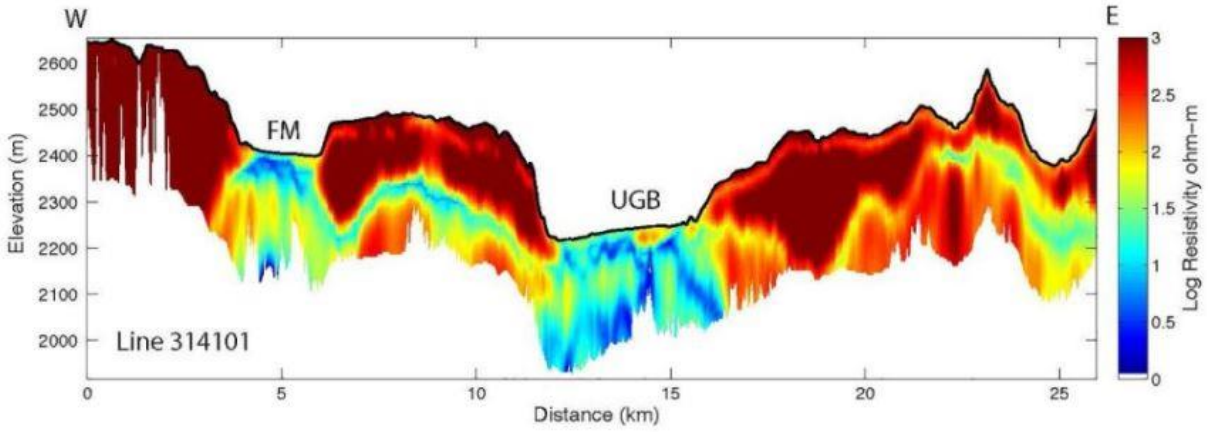


Figure 5. An example of a subsurface image of Yellowstone hydrothermal features produced from the recent (2022) SkyTEM data collected by Virginia Tech, USGS, and Aarhus University in Denmark. Blue colors are electrically conductive hydrothermal pathways and red features are electrically resistive lava flows. This example line crosses two hydrothermal areas, UGB is near "Old Faithful", and FM which represents "Firehole Meadows" within Yellowstone Park. Note hydrothermal pathways under resistive lava flows that may be traps for helium-rich gases while UGB and FM represent areas where helium-rich gases are released to the atmosphere.

**Helium retention and preservation in a trap**

The preservation and retention of helium in a trap is a function of the rate that helium continues to enter the trap minus the rate that helium is leaking out. The capillary entry pressure required to force helium through a seal is like that of carbon dioxide (Wollenweber et al, 2009) therefore seals that trap carbon dioxide or hydrocarbons would similarly trap helium. Helium does have a high diffusion coefficient, but diffusive losses would be very slow. Very low permeability seals such as evaporites (salts, anhydrites) have the highest sealing capacity and would allow helium to be stored for long periods (>100 Myr) since salts and anhydrites lack interconnected pore waters that can facilitate diffusive leakage (Downey, 1984, Broadhead, 2005). All the helium-rich fields that have been discovered to date in the Four Corners region are sealed by shales, silty shales, or tight, micritic limestones. These rocks have much poorer sealing qualities than evaporites and would have a greater risk of diffusional losses of helium, certainly for older accumulations. Data from this study suggests that the helium fields surrounding the Defiance uplift would have begun charging because of the Navajo Volcanic field magmatic activity (28-19 Ma) or later.

A summary of the components necessary for a working helium system are shown in Table 2 and Figure 6.

| Stage | Helium system |
|---|---|
| Source | U-238, U-235 and Th-232 decay in the crust, producing alpha particles that acquire electrons and become helium |
| Maturation | Time to accumulate (stability of crust) vs. volume of crust |
| Primary migration | Heat to above the closure temperatures of minerals with respect to helium retention vs. diffusion. Release of nitrogen from associated minerals and clays. Tectonism, magmatism and rock fracturing to release fluids. |
| Secondary migration | Gas buoyancy and/or solution in water and hydrostatic drive. |
| Accumulation in reservoir | Direct input into trap of a buoyant free-gas phase; or degassing of oversaturated groundwater; or gas stripping via hydrocarbon (CH4) or magmatic (CO2) gas phase. |
| Trap integrity and longevity | Risk of:microseepage; capillary failure; fracture failure; tectonic destruction of trap |

Table 2. Components of a viable helium province (Danabalan et al. 2022)

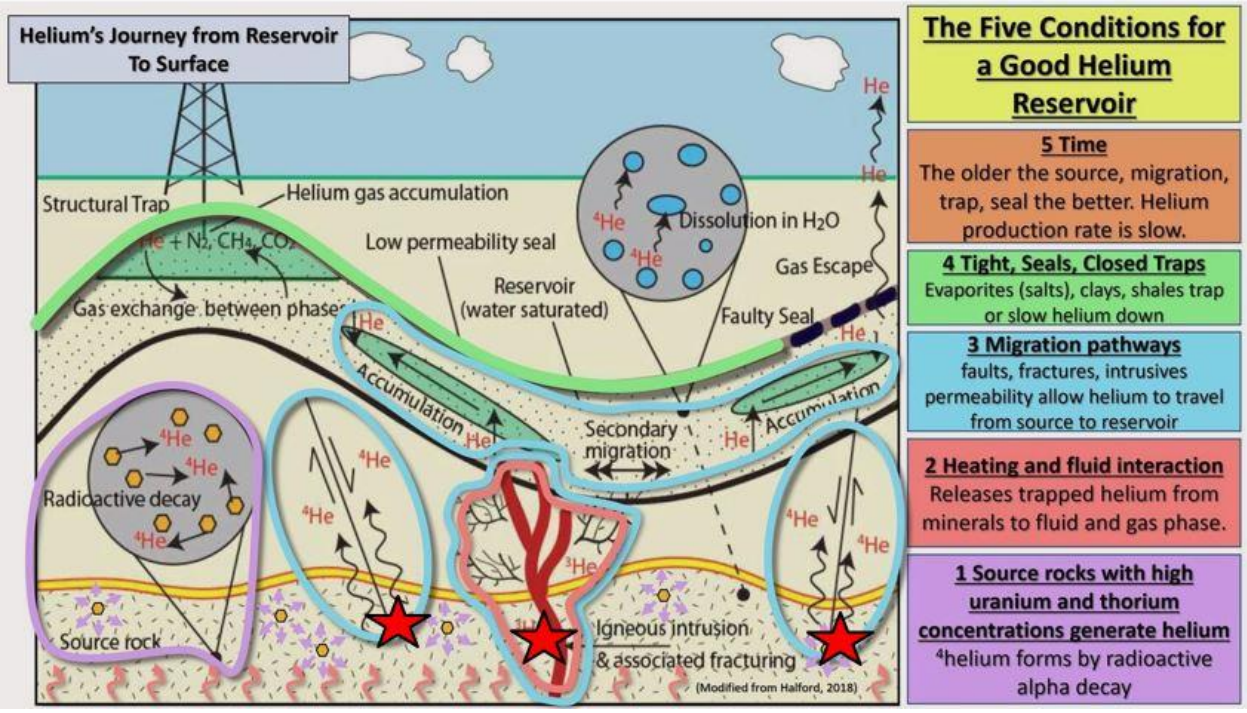


Figure 6. The Helium System summary (modified from Byrne, 2017 and Halford, 2018).

## Tectonic, Magmatic, and Depositional Evolution of the Four Corners Region

The Southern rocky Mountains region, which includes the Four Corners and our study area, experienced a complex geologic history recording lithospheric assembly during the Paleo-Proterozoic time (1.8-1.6 Ga), intracratonic magmatism during the Meso-Proterozoic (1.44-1.35

Ga), incipient rifting (1.1-0.5 Ga), development of the ancestral Rockies during the Paleozoic (350-290 Ma), Laramide tectonism during the Cretaceous-Paleogene (75-45 Ma) and Tertiary extension, magmatism and uplift (Karlstrom and Humpherys, 1998). The Four Corners region of the southwestern United States is the geographic area where the four states of Arizona, Colorado, New Mexico, and Utah converge. The Navajo Nation also lies within the Four Corners region. The regional physiologic features of the Four Corners region referred to in this report are shown in Figure 7. The Yavapai-Mazatzal crustal boundary in the Southern Rocky Mountains is a 300 km wide region with tectonically intermixed rocks of the two provinces (Figure 8). The northern edge of the transition zone is defined by the northern limit of the Mazatzal-age (1.7-1.65 Ga) deformation in southern Colorado (Shaw and Karlstrom, 1991). The southern margin of the transition zone coincides approximately with the Jemez Lineament in northern New Mexico. High helium deposits (>4% helium concentrations) in the United States occur within the Yavapai and Mazatzal provinces (particularly within the Y-M transition zone) in the Four Corners region, southeast Colorado, Texas Panhandle, and Central Kansas uplift (Figure 9).

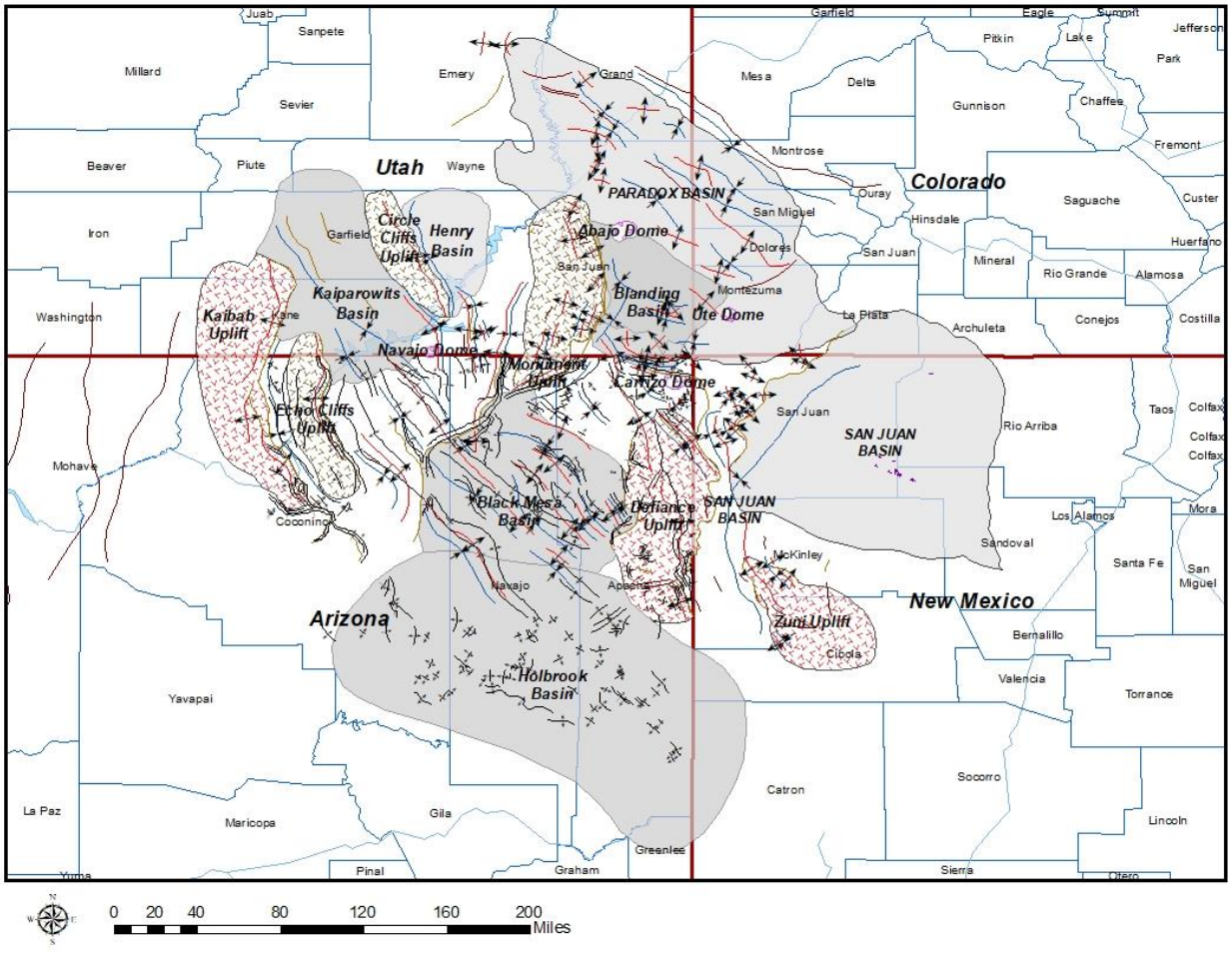


Figure 7. Physiologic features of the Four Corners region referenced in this report.

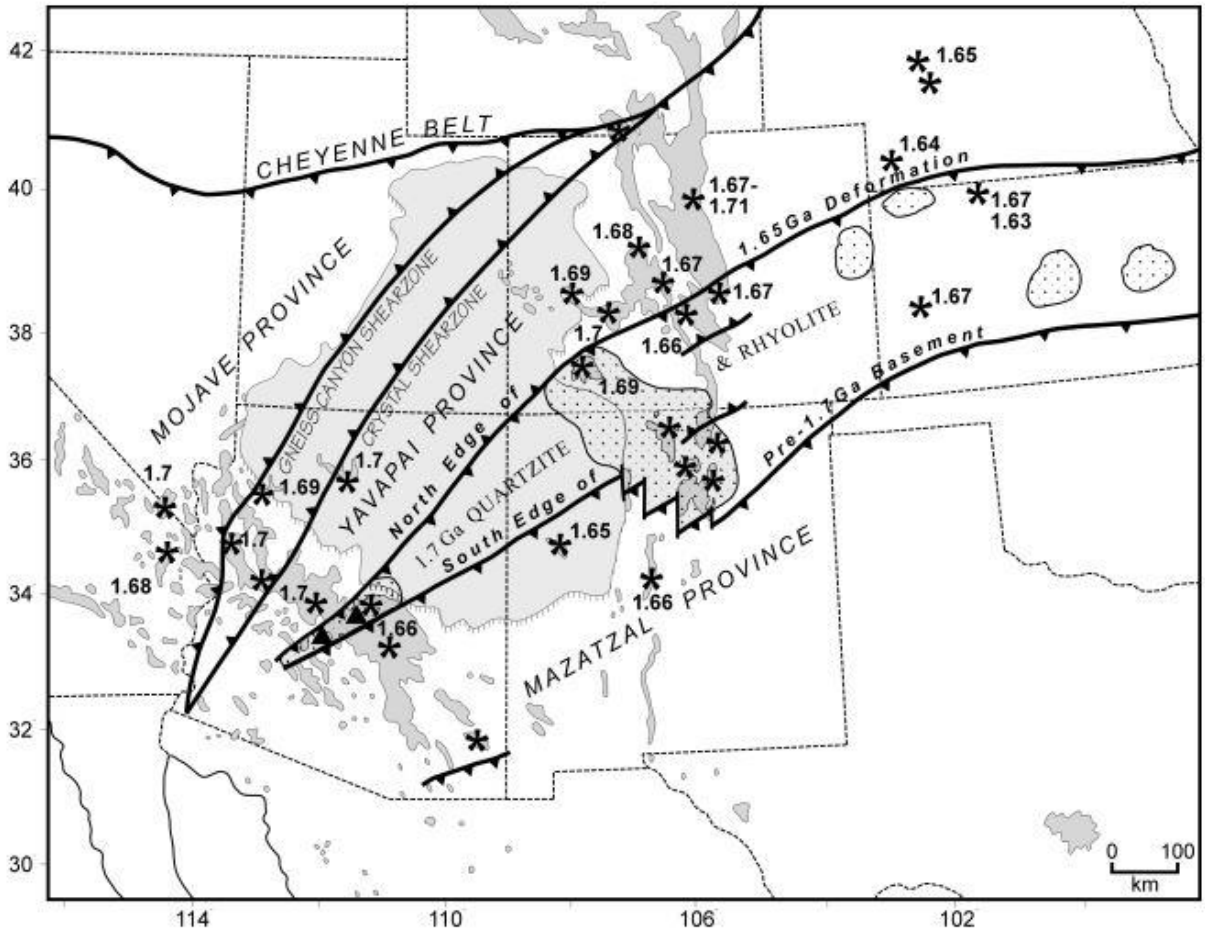


Figure 8. 1.8 – 1.65 Ga contractional amalgamation of lithosphere in the southwestern United States produced major northeast-striking tectonic boundaries. Cheyenne belt = Archean-Proterozoic suture; Gneiss Canyon to Crystal shear zones = distributed boundary between Mojave and Yavapai provinces; Yavapai-Mazatzal transition is marked at its northern edge by a northern limit of 1.65 Ga deformation; at its southern edge by the south limit of pre-1.7 Ga Yavapai province crust. Dot pattern shows areas of 1.7 Ga mature quartzite deposition; triangles are areas of 1.7 Ga rhyolitic calderas; stars show locations and dates of late synorogenic granitoids. Teeth indicate vergence(s) of contractional deformation. Precambrian rock outcrops are delineated in dark gray, and the Colorado Plateau is shown in light gray (Karlstrom and Humphreys, 1998).

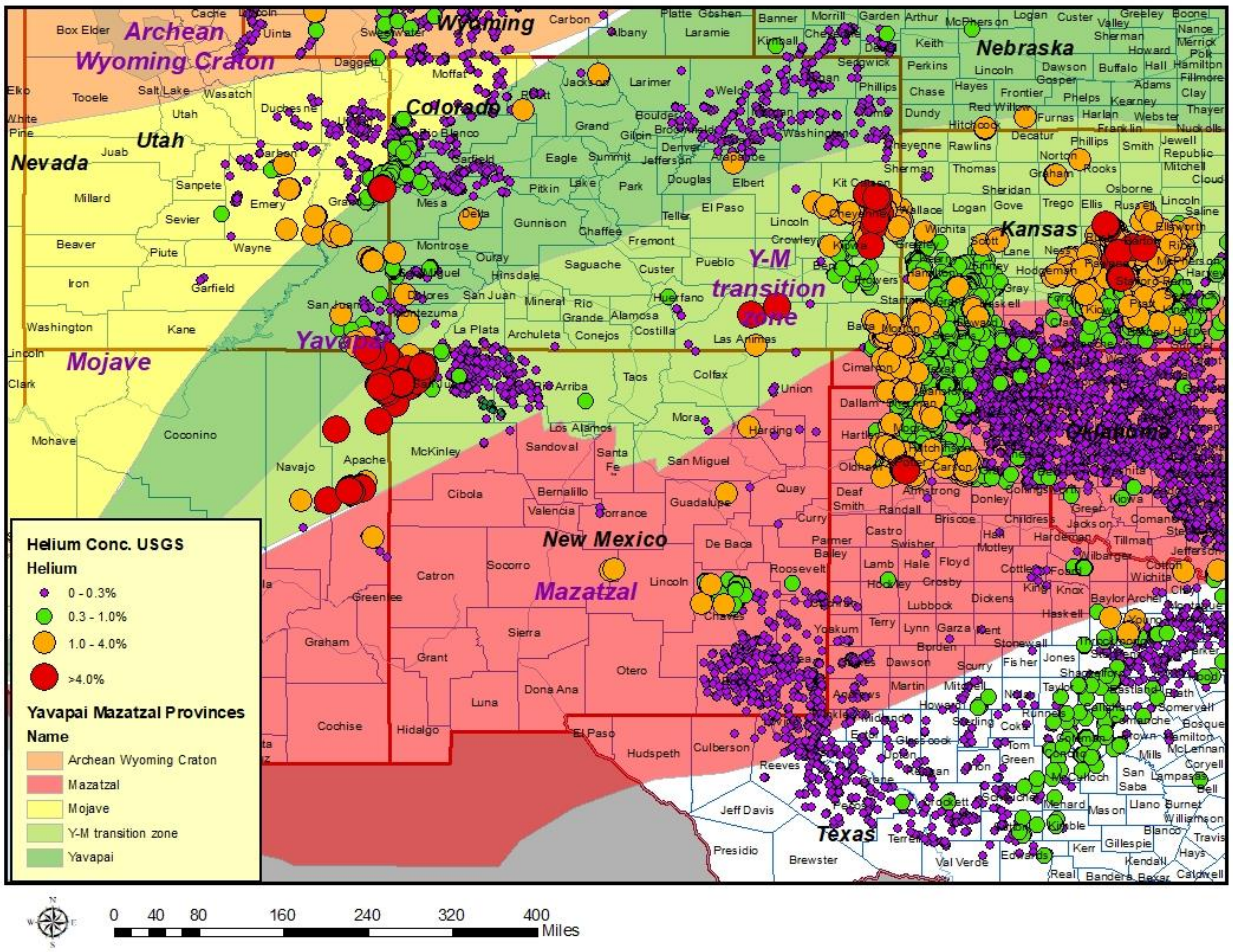


Figure 9. Distribution of helium concentrations within the Proterozoic Yavapai and Mazatzal crustal provinces.

The Phanerozoic history of the Four Corners region is also complex and reflects the very active tectonic history of the region (Figure 10). Cambrian deposition is for the most part absent within the study area since the study area was largely a persistent highland known as the "Transcontinental arch" that paralleled the northern part of the Yavapai-Mazatzal boundary zone. The area remained high throughout the Ordovician, Silurian, and early Devonian. Shallow marine sedimentation covered most of the study area during the Late Devonian resulting in the deposition of marine glauconitic sandstones and sandy dolomite in the lower part (Aneth and McCracken formations) and marine dolomite or limestone in the upper part (Elbert formation) (Figures 11-12). The Devonian is absent over the Zuni uplift and the southern portion of the Defiance uplift probably because of compression during the Antler orogeny (Mississippian-Early Pennsylvanian). Thickness of the Devonian – Cambrian sediments ranges from 0 to over 900 feet in the northwest of the study area. Helium occurs in the upper Devonian formations on the northern flanks of the Defiance uplift.

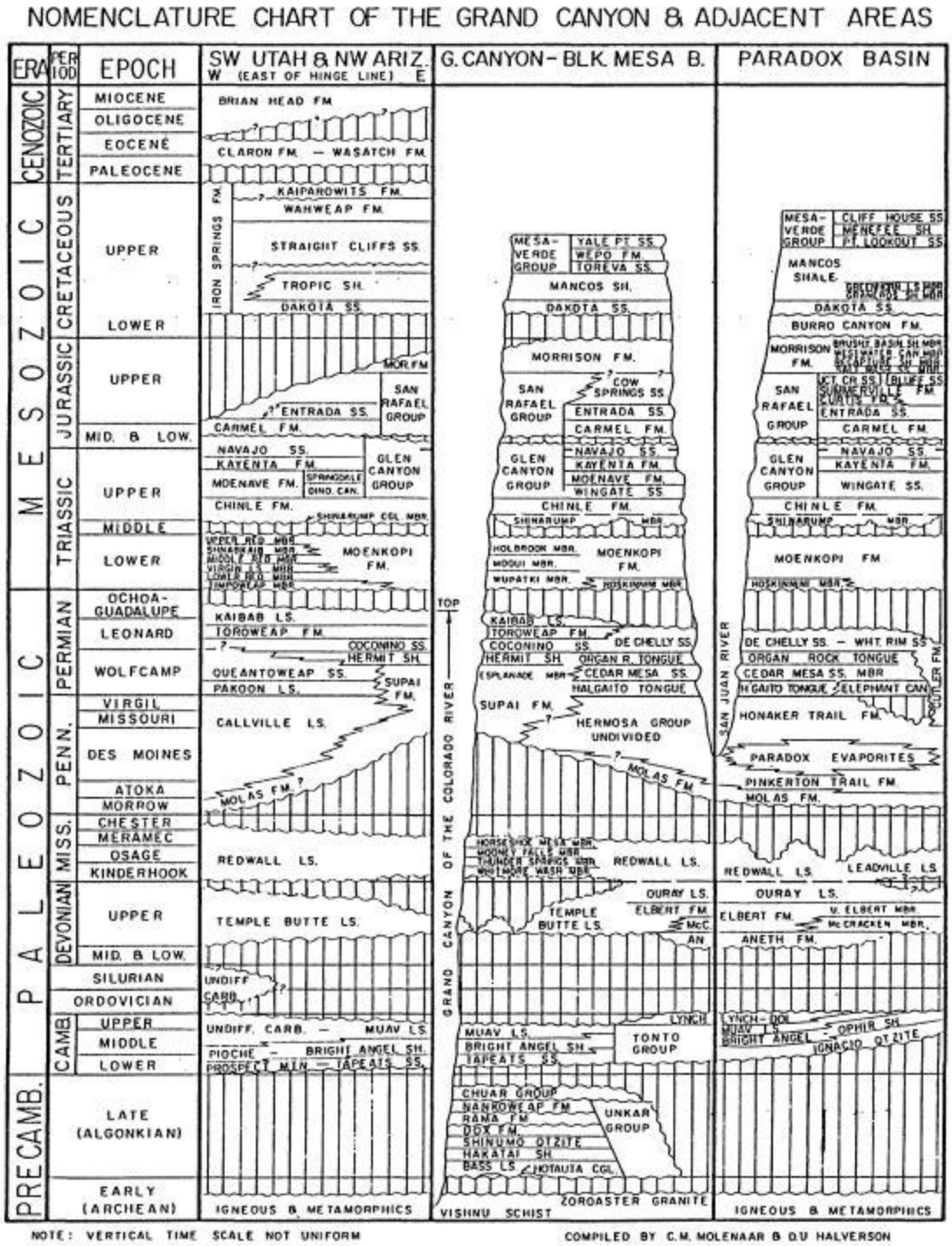


Figure 10. Generalized stratigraphic column of the Four Corners area. From Molenaar and Halvorsen, 1969.

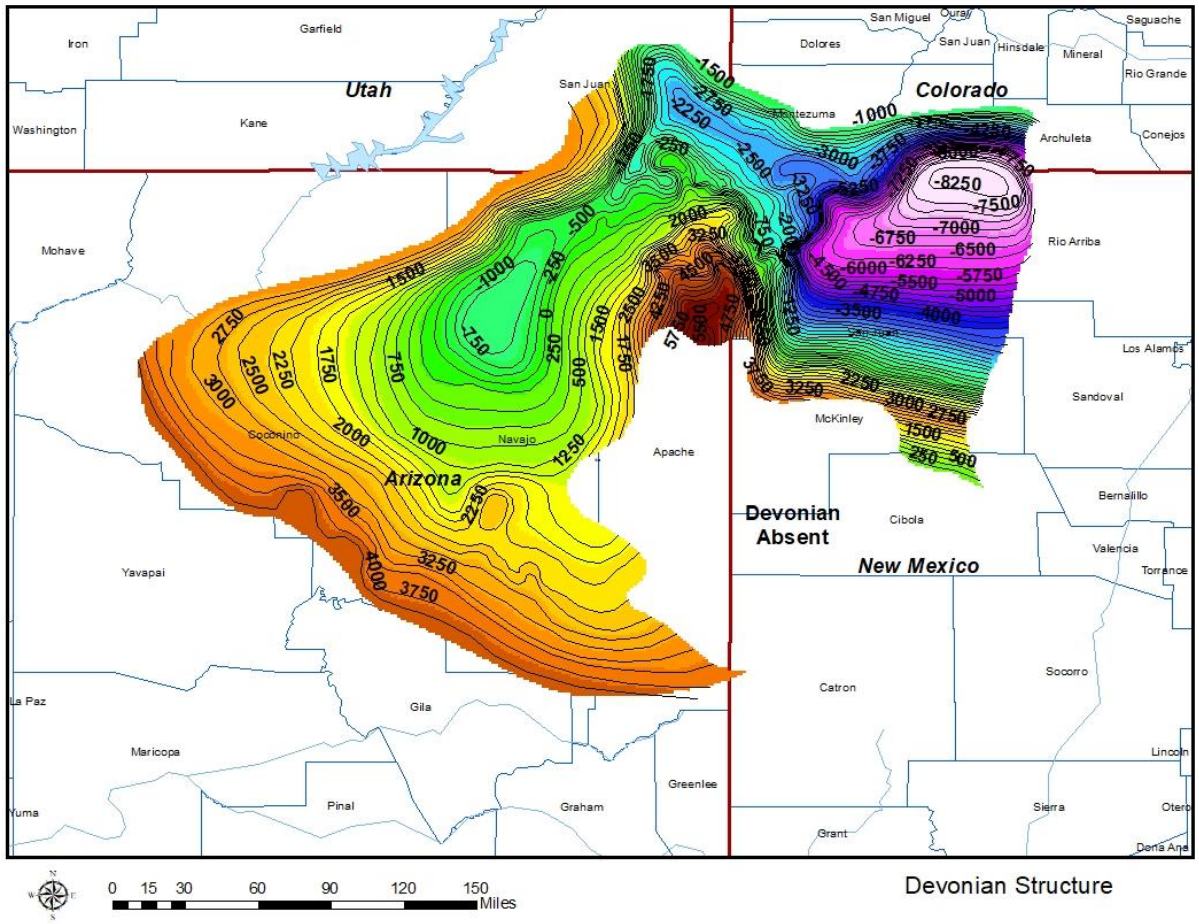


Figure 11. Structure map on top of Devonian period. Contour interval = 250 feet. The top of the Devonian is represented by either the Elbert formation or Devonian undifferentiated. The uppermost Devonian-aged Ouray dolomites, when present, are included in the Mississippian carbonate maps.

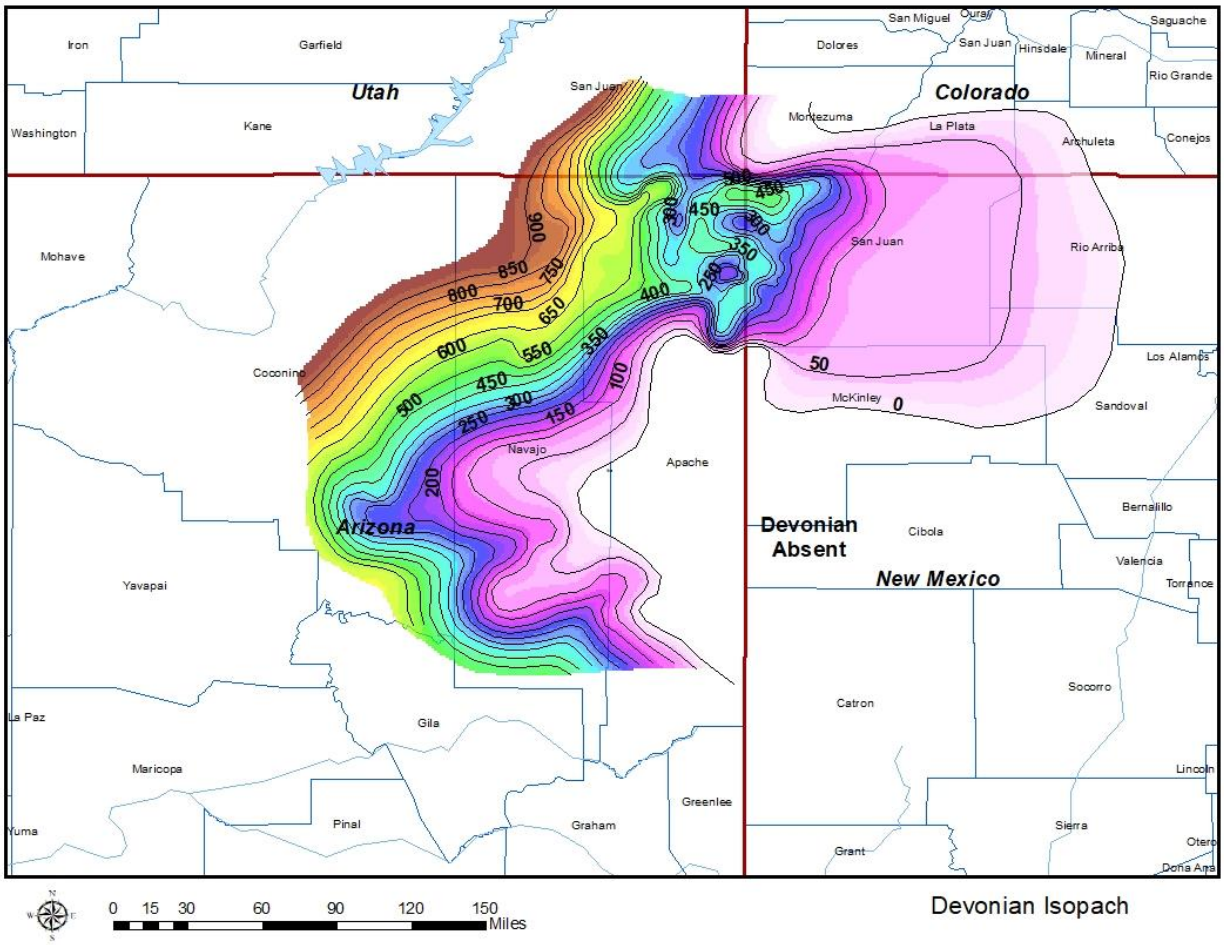


Figure 12. Isopach map of the Devonian – Cambrian periods. Contour interval = 50 feet. Thinning and removal of the Devonian in the southern Defiance and Zuni uplift areas probably resulting from Antler orogeny compression which initiated in the Mississippian.

During Mississippian time, shallow water marine carbonates deposits blanketed the entire study area Leadville or Redwall formations) (Figures 13-14). Mississippian sediments range in thickness from 0 – 500 feet in the study area. The Leadville is composed mainly of massive marine oolitic and crinoidal limestone and crystalline dolomite with variable amounts of chert. The Leadville is also a significant reservoir of oil, gas, helium, and carbon dioxide. Mississippian-Pennsylvanian sedimentation was controlled by a series of north to northwest trending uplifts of the Ancestral Rocky Mountains formed during the Antler orogeny. As seen in the Devonian isopach, Mississippian deposits were also removed during the Antler orogeny due to uplift of the southern Defiance and Zuni uplifts. Prolonged emergence in the study area during the Late Mississippian and Early Pennsylvanian resulted in the regional development of a karst topography with associated red regolith, weathered carbonate rubble, and extensive solution features at the top of the Leadville/ Redwall carbonates and including the early Pennsylvanian Molas formation.

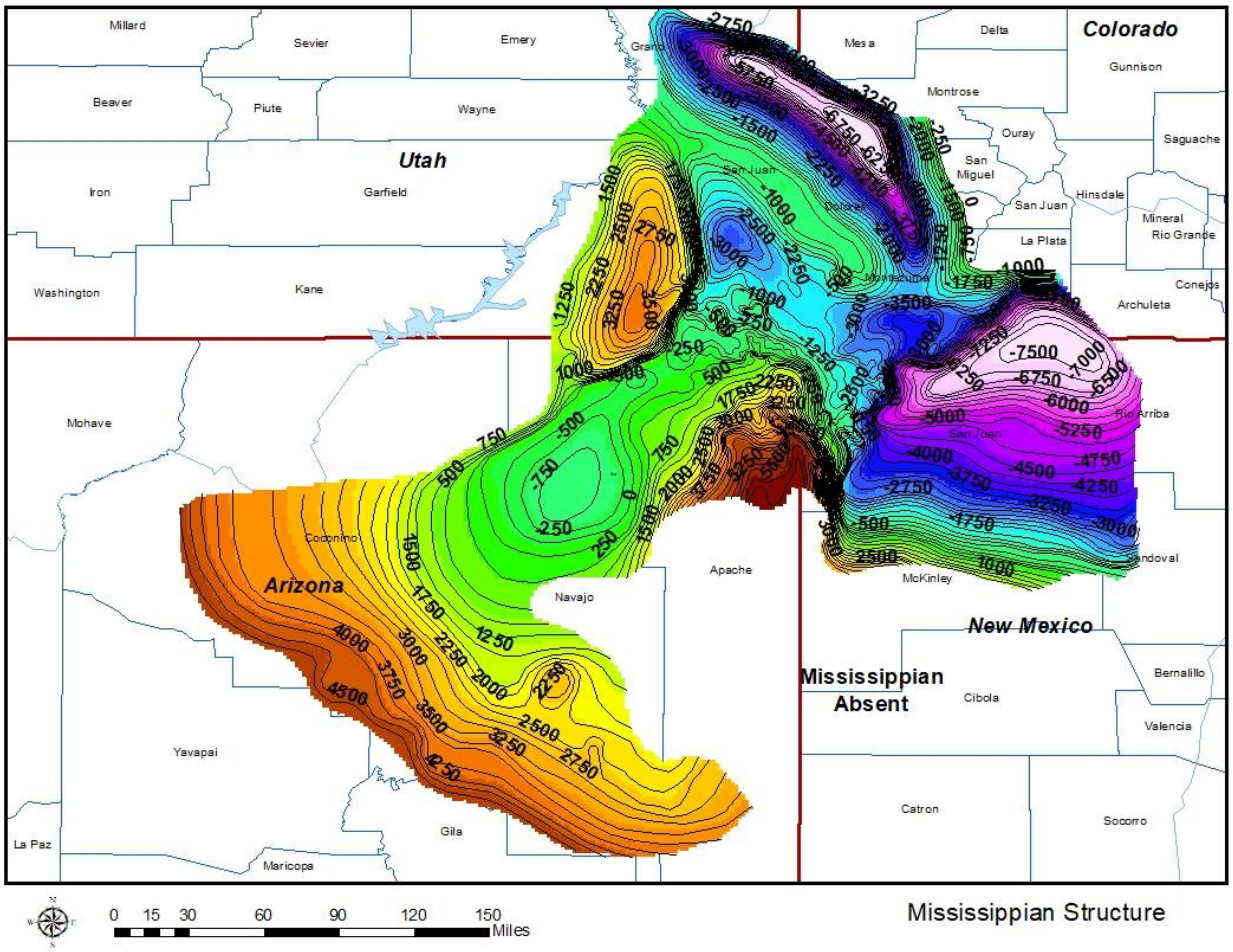


Figure 13. Structure map on top of the Mississippian period. Contour interval = 250 feet.

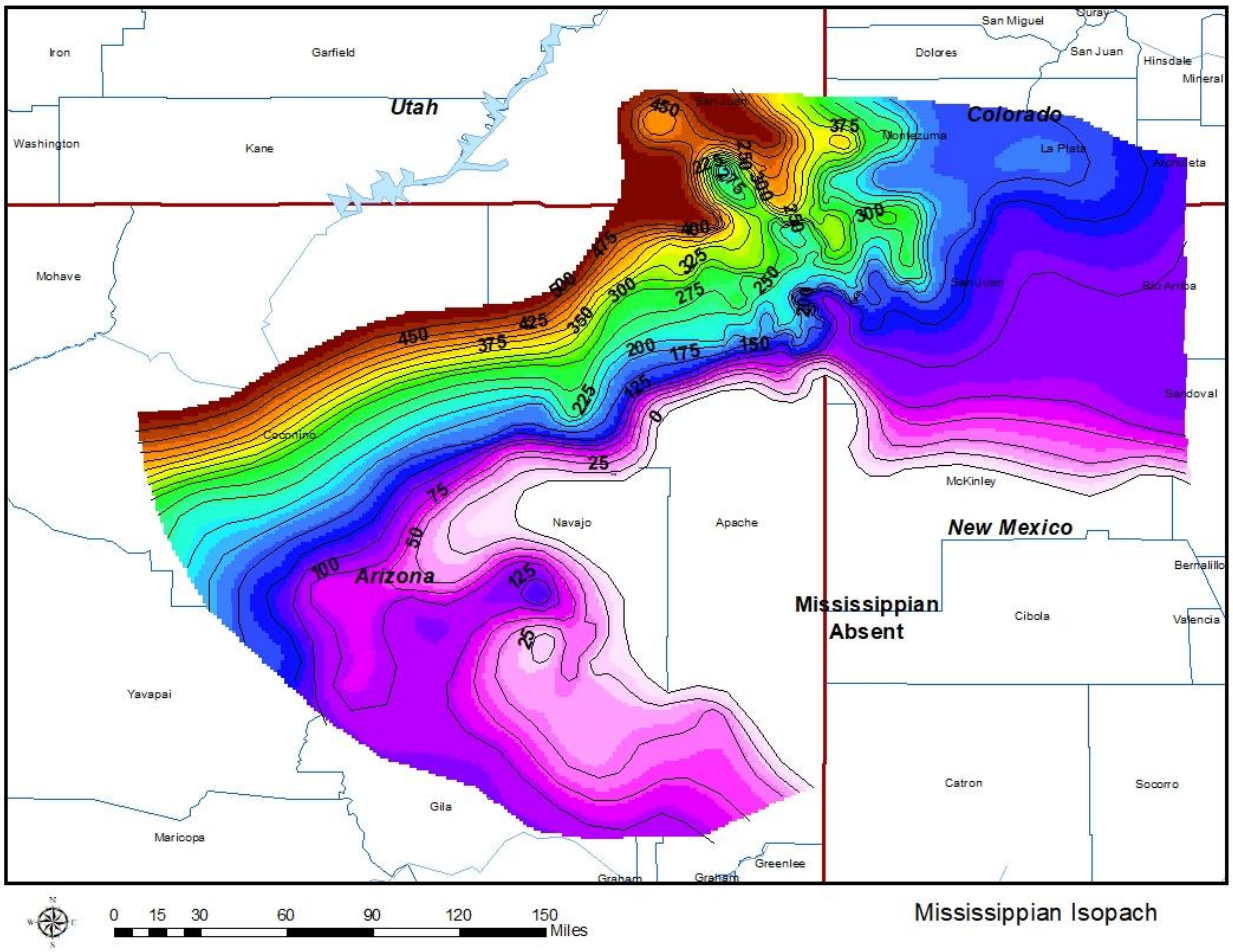


Figure 14. Isopach map of the Mississippian period (Leadville Limestone). Contour interval = 25 feet. Thinning and removal of the Mississippian in the southern Defiance and Zuni uplift areas probably resulted from Antler orogeny compression which initiated in the Mississippian.

Compression during the Antler orogeny also caused severe down warping and accelerated subsidence in the Paradox basin beginning in the early Desmoinesian and continuing through the middle Permian as evident by the northward thickening of the Pennsylvanian deposits (Figure 15-16). The thickness of the Pennsylvanian sediments range from absent on the southern Defiance and Zuni uplifts to greater than 2,700 feet in the study area to more than 5,000 feet in the Paradox basin to the north. The Desmoinesian sediments in the study area consist of strongly cyclic limestones, dolomites, black organic-rich shales, and evaporites (Paradox Group). Increased clastic debris was delivered from the peripheral uplifts by the end of the Desmoinesian and through the end of the Pennsylvanian resulting in a predominance of clastic deposition in the upper Pennsylvanian (Hermosa Group/ Honaker Trail formation). Most anomalous helium deposits have been found in the Pennsylvanian formations.

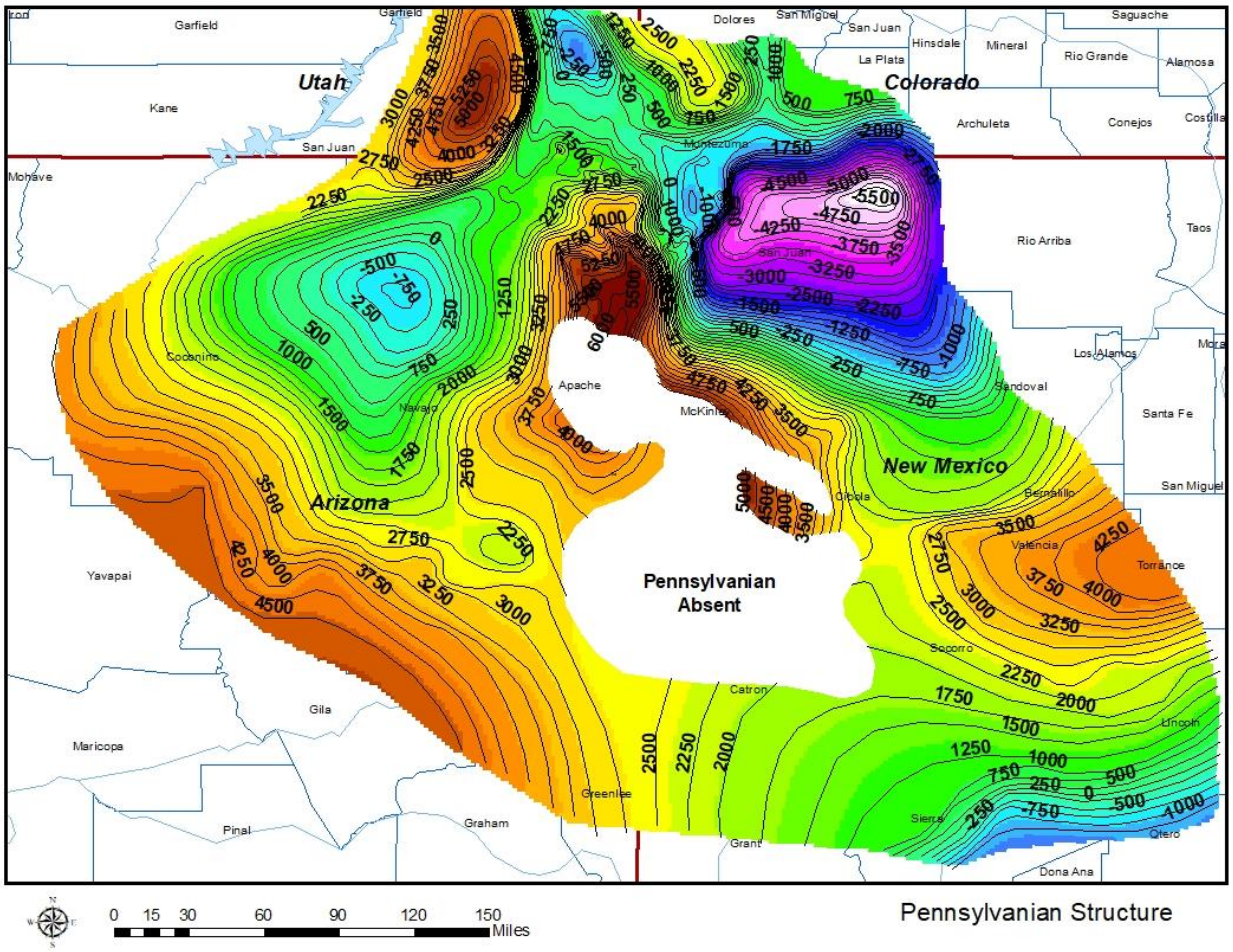


Figure 15. Structure map on top of the Pennsylvanian period (Hermosa Group). Contour Interval = 250 feet.

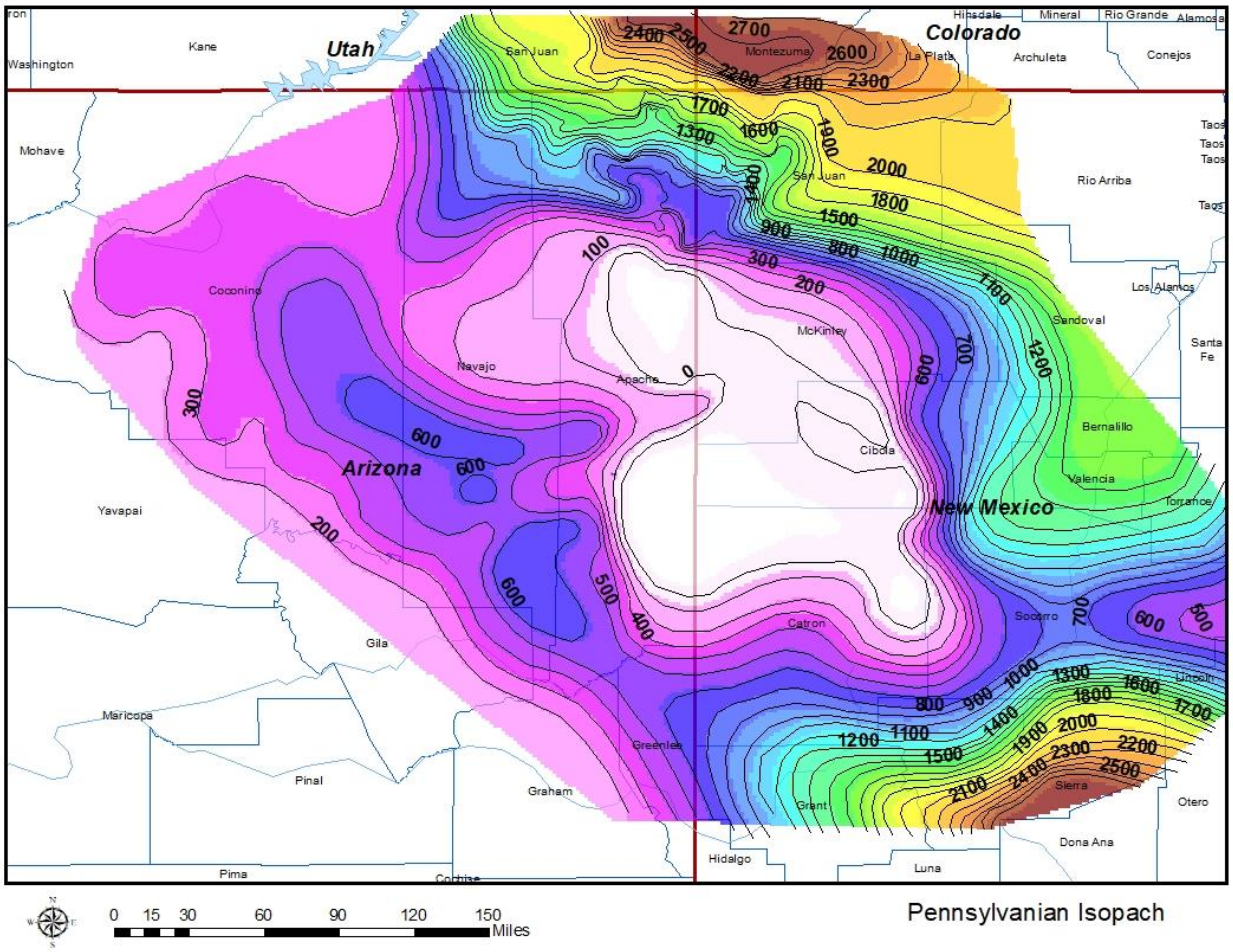


Figure 16. Isopach map of the Pennsylvanian period. Contour interval = 100 feet. Thickening to the north of the Defiance uplift is caused by major Pennsylvanian deposition in the Paradox/Blanding basins in Utah and in the Permian basin to the southeast. The Defiance and Zuni uplift areas were mostly positive features during the Pennsylvanian period.

The Permian period is dominated by increased clastic influx into the study area from the surrounding peripheral uplifts including the Defiance/ Zuni uplifts. Most of the clastic material was supplied from the Uncompahgre-San Luis uplift in southwest Colorado. The Permian sandstones are important reservoirs for helium on the southwest flank of the Defiance uplift and northeastern edge of the Holbrook basin. The Leonardian-aged sandstones (Coconino/ DeChelley/ Glorieta formations) range in thickness from 0 feet in very small pockets on the Defiance and Zuni uplifts to greater than 900 feet to the northwest portions of the study area (Figures 17-18).

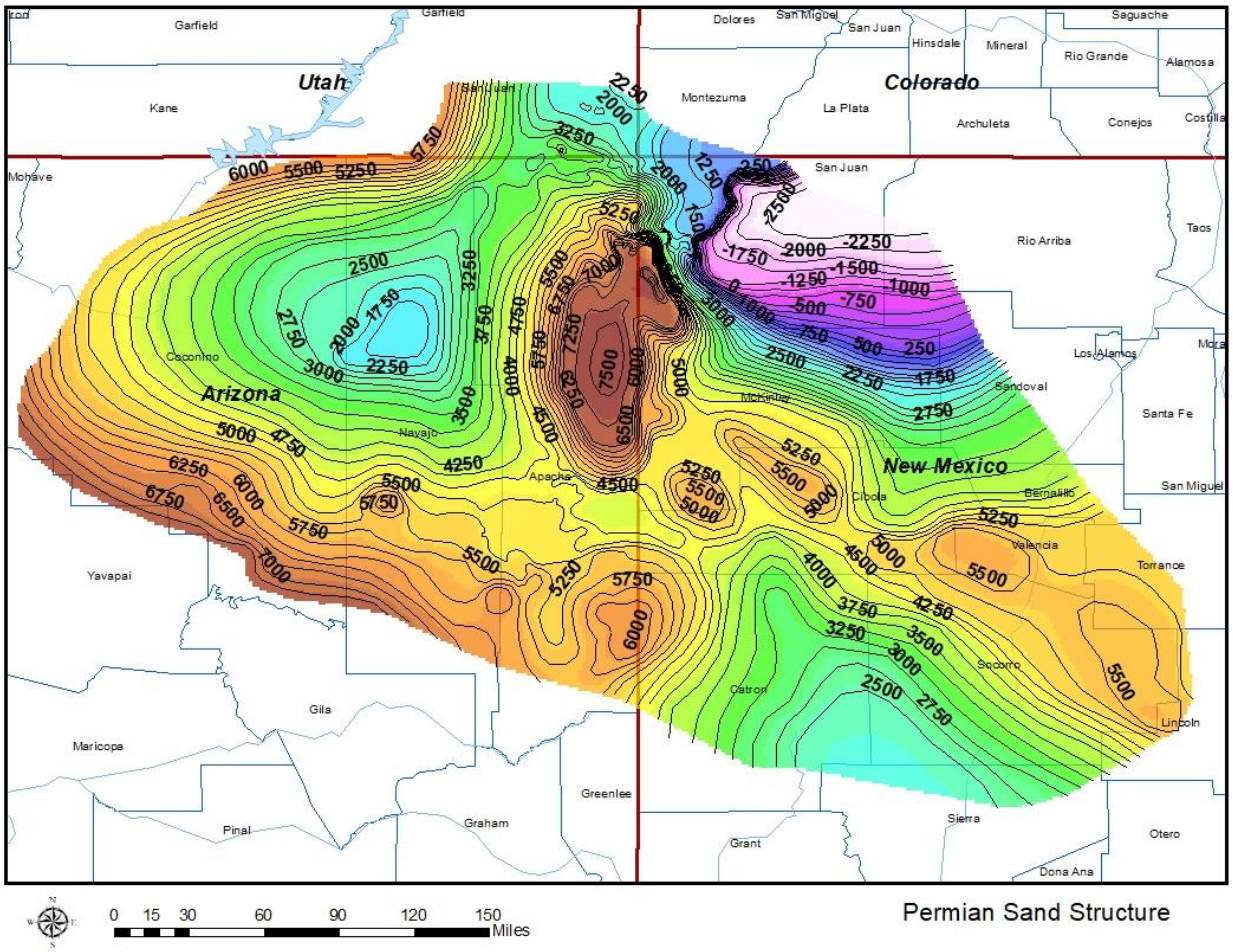


Figure 17. Structure map on the top of the Permian sandstones (Coconino-DeChelly-Glorieta). Contour interval = 250 feet.

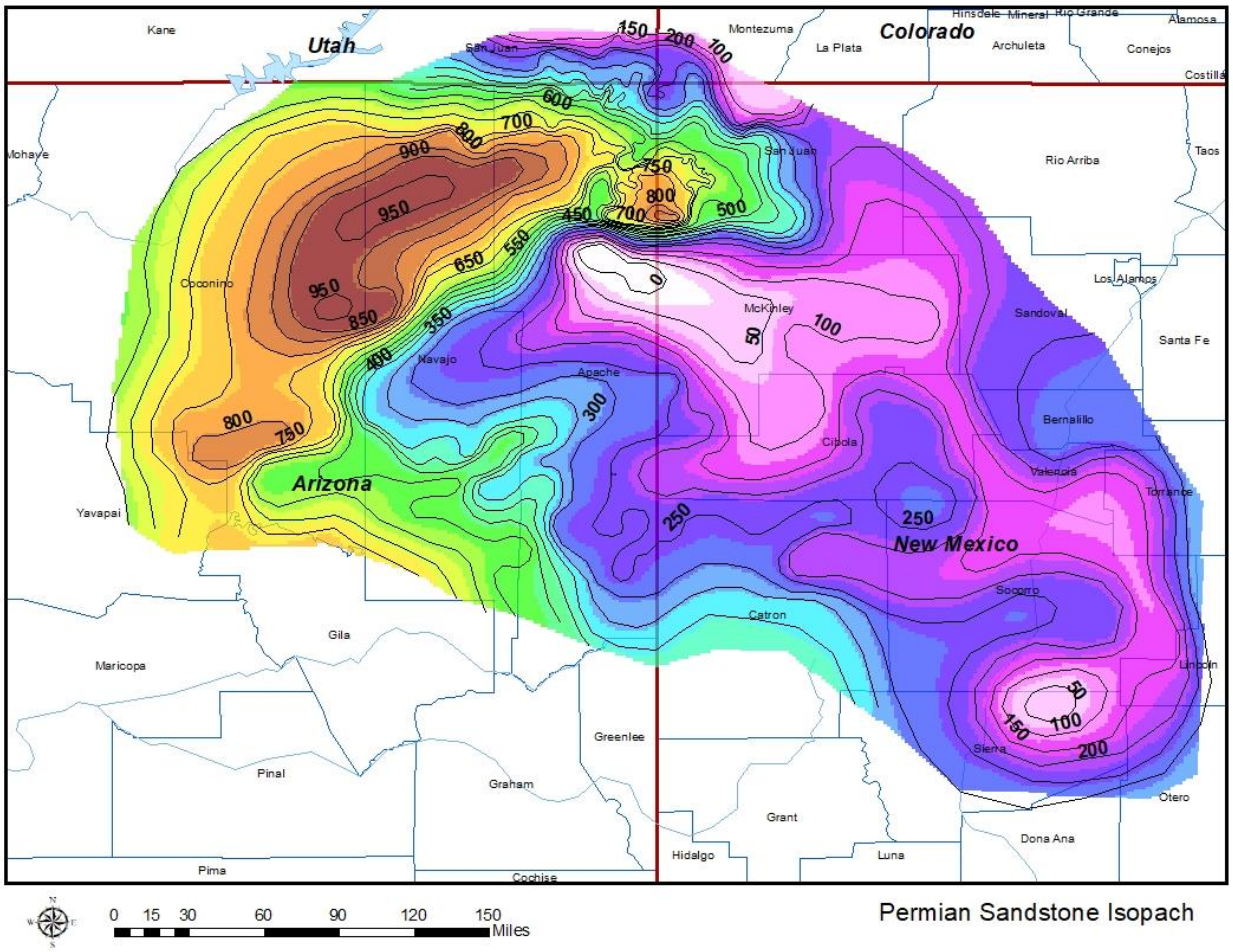


Figure 18. Isopach map of the Permian sandstones (Coconino-DeChelly-Glorieta). Thickening to the west and northwest of the Defiance uplift probably in response to continued compression and westward tilting during the Sonoma orogeny.

Through most of the early and middle Mesozoic, the study area was either emergent and/or stable. Lower through middle Triassic deposition was dominated by continental redbeds (shales, siltstones, and sandstones) in the east with intertonguing marine deposits to the west. The uppermost helium deposits that are found within the study area occur in the lower-middle Triassic Moenkopi, Shinarump, and Chinle formations. The upper Triassic and upper Jurassic are characterized by massive eolian sandstones (Navajo – Morrison formations).

In the Late Cretaceous because of Laramide orogeny (75-45 Ma) and Sevier orogeny (90-60 Ma), shallow marine deposition occurred in the rapidly subsiding San Juan and Black Mesa basins while erosion occurred in the rising Defiance, Zuni, and Monument uplifts and the northward tilting along the Mogollon slope. Laramide tectonism created cratonic shortening within the study area, resulting in crustal thickening from 40 to 45 km (Karlstrom and Humphreys, 1998). Magmatism in the late Cretaceous also occurred because of Laramide movements that followed along the Yavapai-Mazatzal northern boundary (Figure 19). This zone

of magmatic activity resulted in the emplacement of numerous Laramide plutons and Au/Ag ore deposits known as the Colorado Mineral Belt. The influence of the Laramide-aged magmatic activity and tectonism on the release of helium from the upper crust is unclear.

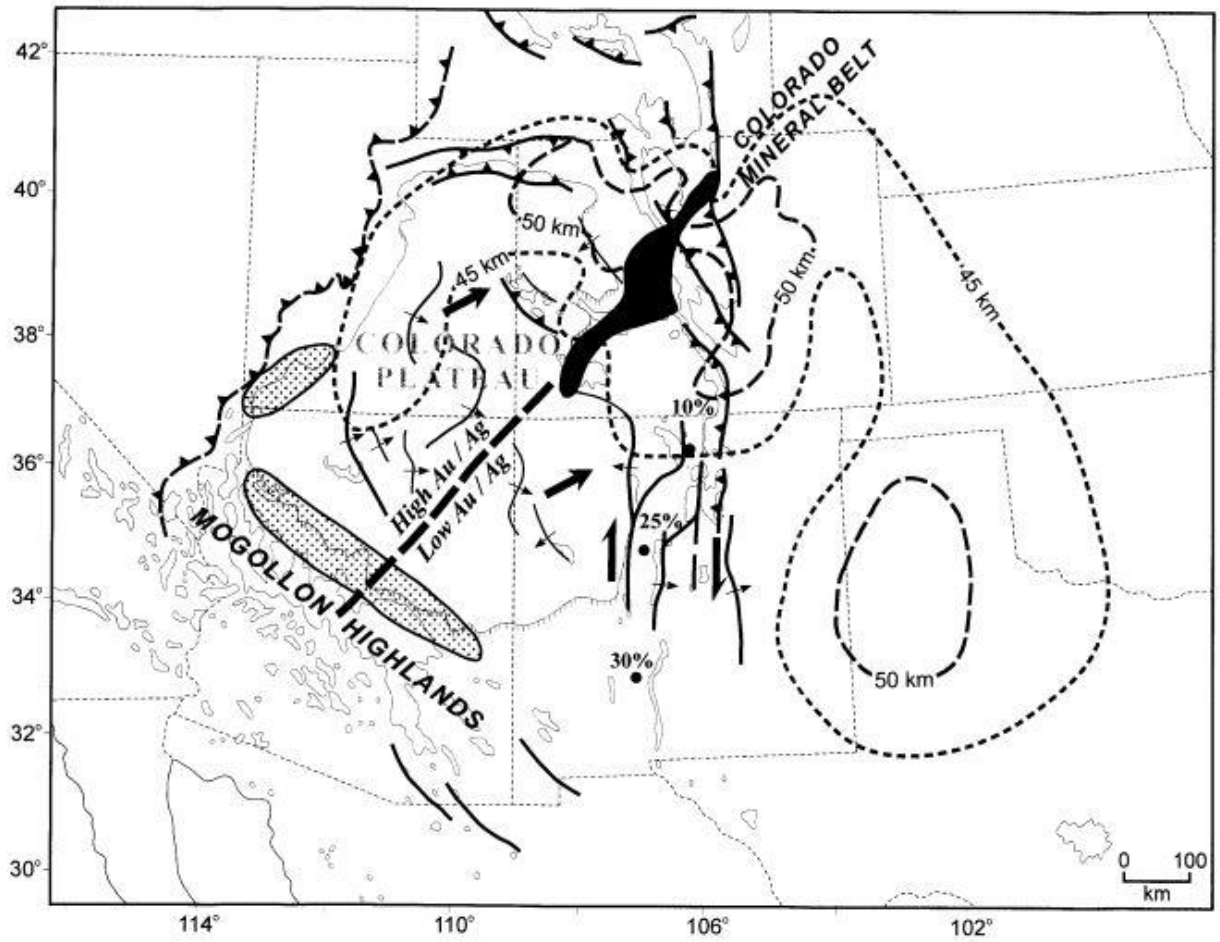


Figure 19. Laramide shortening of the craton may have produced the present-day 45-50 km thick crust along the eastern border of the study area (dotted lines). Mantle modification is expressed as different metallogenic provinces in Arizona which follow the Yavapai-Mazatzal boundary, and the Colorado mineral belt which follows northeast-striking shear zones (Karlstrom and Humphreys, 1998).

Stability, uplift, and erosion marks the entire Tertiary sedimentary history across the entire study area. The Tertiary was anything but quiet in terms of magmatic activity and is marked by almost continuous volcanism in some part of the study area (Figure 20). There were two major magmatic periods that occurred in the Tertiary and appeared to have had a profound effect on the release and distribution of helium and carbon dioxide in the study area. This topic will be covered more thoroughly later in the report. Both Tertiary magmatic events appear to be derived from Precambrian North American lithosphere at relatively great depth (Karlstrom and Humphreys, 1998). The occurrence of alkali basalts from melts typically derived from depths

where garnet is stable. The magmatism also appears to involve widespread partial melting of both the lithosphere and asthenosphere mantles (Karlstrom and Humphreys, 1998).

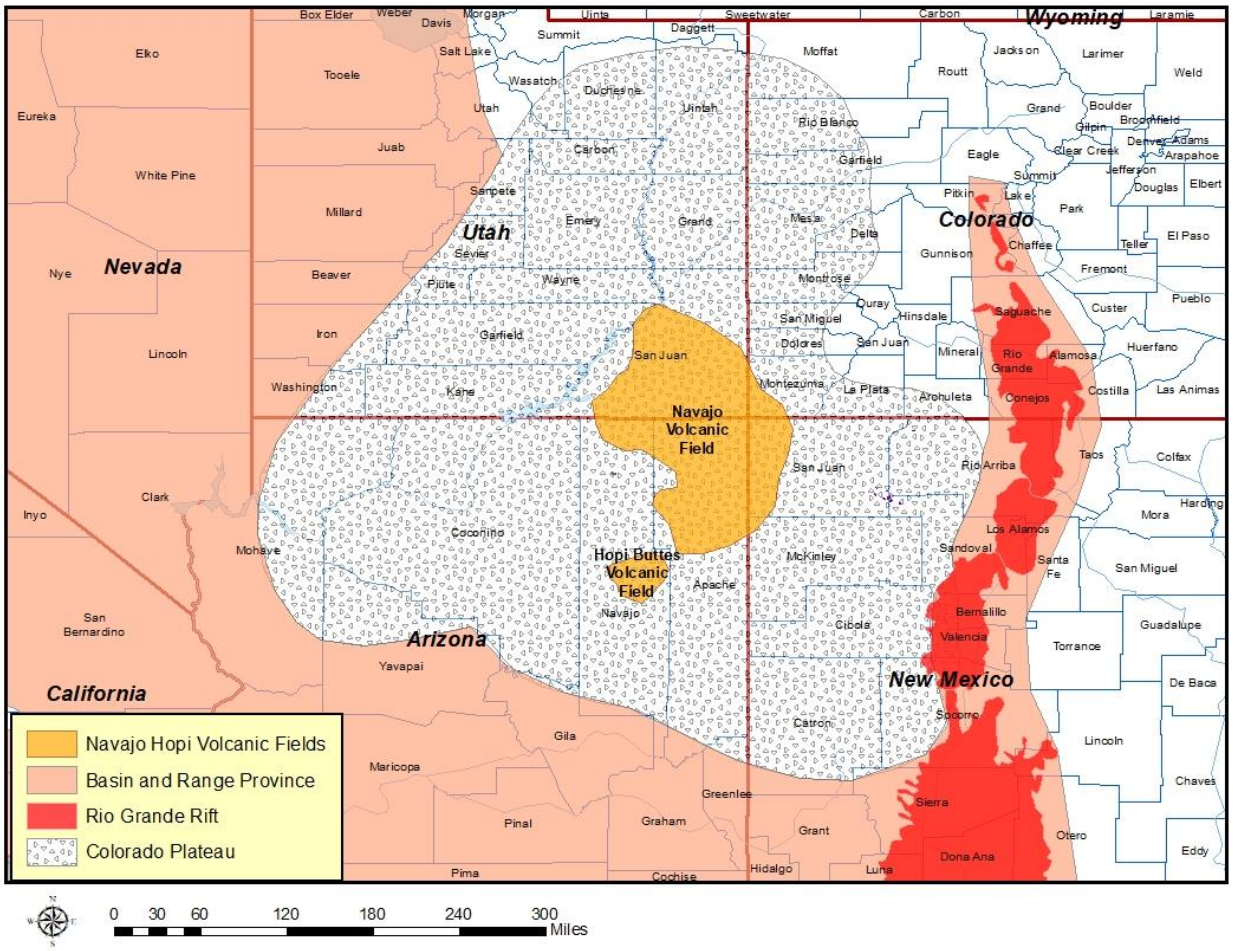


Figure 20. Distribution of Tertiary Magmatic activity around and within the study area.

The first magmatic event occurred from 40-25 Ma known as the "Mid-Tertiary ignimbrite flare-up". The Navajo Volcanic field, which consists of more than eighty Oligocene to Miocene (28-19 Ma) mafic and ultra-mafic diatremes and hundreds of intrusive plutons which penetrated various depths in the crust and sedimentary section but did not erupt at the surface, occur within the study area (Semken, 2003). Numerous dikes and sills related to these diatremes and intrusive bodies intersect and crosscut the sedimentary section. The primary tectonic driving force behind this explosive volcanic activity is slab rollback of the Farallon plate. During the Laramide orogeny, the subducting Farallon plate subducted at a very shallow angle. As the angle of subduction steepened, a mantle wedge opened causing melting in the mantle wedge and lower crust and resulting in the ignimbrite flare-up. Mafic and ultra-mafic diatremes and lamprophyres were emplaced along basement zones of weaknesses in northeastern Arizona and northwestern New Mexico in an area known as the Navajo volcanic field and had a major influence on the release and distribution of helium in the study area. Voluminous volcanic

eruptions also occurred during this 40-25 Ma period in the San Juan caldera system of southwest Colorado.

The second major magmatic event occurred from 17 Ma (early Miocene) until the end of the Pliocene (2 Ma) which was a result of Basin and Range extension and spreading along the Rio Grande rift. This magmatic activity surrounds the Colorado Plateau to the west, south, and east. Little volcanic activity occurred within the Colorado Plateau during this period except for the Hopi Buttes volcanic field with over 300 maars and diatremes erupting from 8.5 – 4.2 Ma to the southwest of the Defiance uplift. The Rio Grande rifting initiated 35 Ma and continued to present. Basin and Range extension began in the early Miocene (17 Ma) and resulted from as much of the Farallon plate had been consumed and the seafloor spreading ridge that separated the Farallon and Pacific plates approached North America. Degree of extension varied from 60 to 300 km across the Basin and Range province. Current heat flow within the study area is largely reflective of the Basin and Range volcanism and appears to have resulted in massive volumes of carbon dioxide to be released (this will be discussed further in this report).

## The Four Corners Helium System and the occurrence of Helium and CO2

**The Helium System in the Four Corners Region**

In the Four Corners study area, evidence will be presented in this report that suggests that magmatic events, particularly those related to the Oligocene to Miocene (28-19 Ma) Navajo Volcanic field, were the primary release mechanism for helium and nitrogen from the crust. The extrusive and intrusive bodies that were emplaced in the Navajo Volcanic field are either mafic or ultra-mafic in composition (Semken, 2003). This is important in the sense that mafic and ultra-mafic magmas are of low viscosity as they ascend upward to decreasing pressures, dissolved gases within the magmas exsolve and form a gas cap. Helium, nitrogen, carbon dioxide, and water vapor would compose this gas cap leading the ascending magma at shallow depths. Helium and nitrogen, which are lighter and relatively insoluble in water would tend to segregate and potentially follow different migration paths from the denser and highly soluble carbon dioxide. As the ascending magma opens fractures in the crust and sedimentary section, the gases can then migrate into these fractures and potentially be trapped in any adjacent structures formed by the rising magma body. This mechanism envisions direct input into the trap of a buoyant free-gas phase with a very short migration pathway from a rising intrusive body (Table 3). This is exactly what is observed from the high-resolution aeromagnetic data collected in this study discussed later in this report. This mechanism is different than what is observed in the Midcontinent helium deposits of the Midcontinent of the United States in places such as the Texas Panhandle and central Kansas where tectonism is driving force behind the rock fracturing (Laramide orogeny) and serves as the primary migration agent and secondary migration via gas buoyancy and water solution is very important (Danabalan, 2017).

| Helium Field | Reservoir | Ave. He Conc. | Midpoint distance to nearest crustal pluton, miles | Nearest Surface Diatreme Distance, miles |
|---|---|---|---|---|
| Rattlesnake | Leadville | 7.5 | 0.5 | 3.2 |
| Table Mesa | Leadville | 5.5 | 0 | 2.5 |
| Tocito North | Leadville | 7.25 | 0 | 5.3 |
| Tocito Dome | Leadville | 7.25 | 0 | 4.8 |
| Hogback | Leadville | 6.2 | 0 | 10.8 |
| Beautiful Mountain | Leadville | 7.1 | 0 | 3.1 |
| Beautiful Mountain | Organ Rock | 5.5 | 0 | 3.1 |
| Dineh bi Keyah | McCraken | 6 | 0 | 0.5 |
| Tohache Wash | Leadville | 6.03 | 0 | 4.7 |
| East Boundary Butte | Leadville | 4.4 | 0 | 3.7 |
| Black Rock | Leadville | 8.1 | 0.3 | 1.5 |
| Dry Mesa | Leadville | 5.1 | 2.5 | 2.6 |
| Pinta Dome | Coconino | 7 | 1.3 | 11.3 |
| Navajo Springs | Coconino | 8.25 | 0.9 | 16.6 |
| East Navajo Springs | Coconino | 9.2 | 1.8 | 21.1 |
| | | **Median** | **0** | **3.7** |
| | | **Average** | **0.5** | **6.3** |

Table 3. Distance of helium fields in the Four Corners study area from either crustal plutons or surface diatremes.

Another possible mechanism to explain the direct input of helium and nitrogen with short migration pathway from an intrusive body and may be a factor in some of the Four Corners helium deposits is the diatreme model. Within the Navajo Volcanic Field, there are over eighty diatremes observed on the surface. A diatreme, sometimes referred to as a maar-diatreme volcano, is a volcanic pipe formed by a gaseous explosion. When magma rises through a crack in the crust and contacts a shallow groundwater body, rapid expansion of heated water vapor and volcanic gases can cause a series of explosions. Diatremes breach the surface and produce a steep, inverted cone shape (Figure 21). Diatremes can extend hundreds of meters to as much as 2 km below the surface and are typically mafic to ultra-mafic in composition (Valentine et al., 2014, 2017). Diatremes are also typically initiated and rooted from dikes and sills (Valentine et al., 2017). Numerous dikes and sills have been encountered by wells in the Navajo Volcanic field and they tend to occur within preferred stratigraphic intervals. Reservoirs with high helium concentrations are typically found either in the same stratigraphic intervals that the sills and dikes occur or immediately adjacent to them (Figure 22).

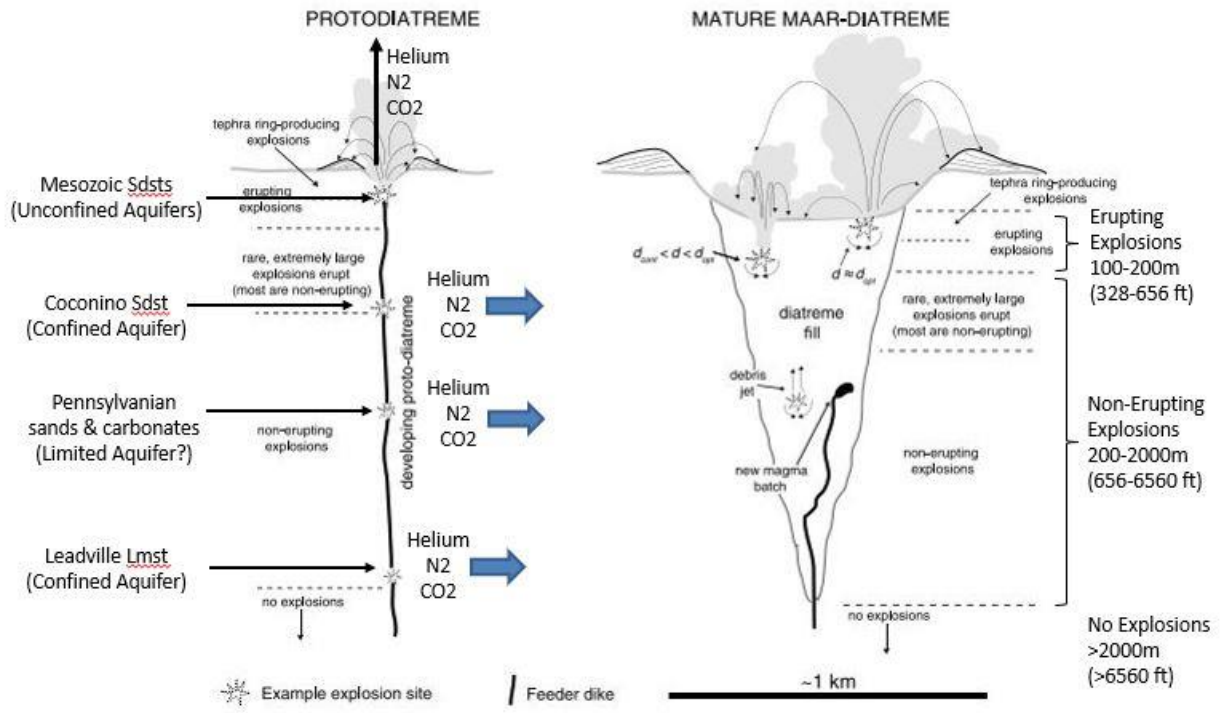


Figure 21. Diagram of explosive diatremes and the possible mechanism of crustal helium and nitrogen gases to enter the primary helium-bearing reservoirs. (modified after Valentine et al., 2014).

The diatreme model envisions that as the super-heated and high-pressure magmatic gases encountered aquifers with 2 km of the surface 28-19 Ma, groundwater is vaporized, pressurized, and potentially fracturing the water-bearing formation. The magmatic gases, including helium and nitrogen then are injected into the fractured reservoir and migrate to the nearest trap. The majority of the high helium reservoirs occur at less than 2 km (6,560 ft.) and within formations that range from significant to limited aquifers (Permian Coconino sandstone, Mississippian Leadville limestone). Although many of the known helium fields occur very close to diatremes, this model cannot adequately explain all the accumulations and is better explained by the concentric and radial fracturing related to rising magma bodies. The diatreme model is presented here as a possible emplacement mechanism for some of the helium fields.

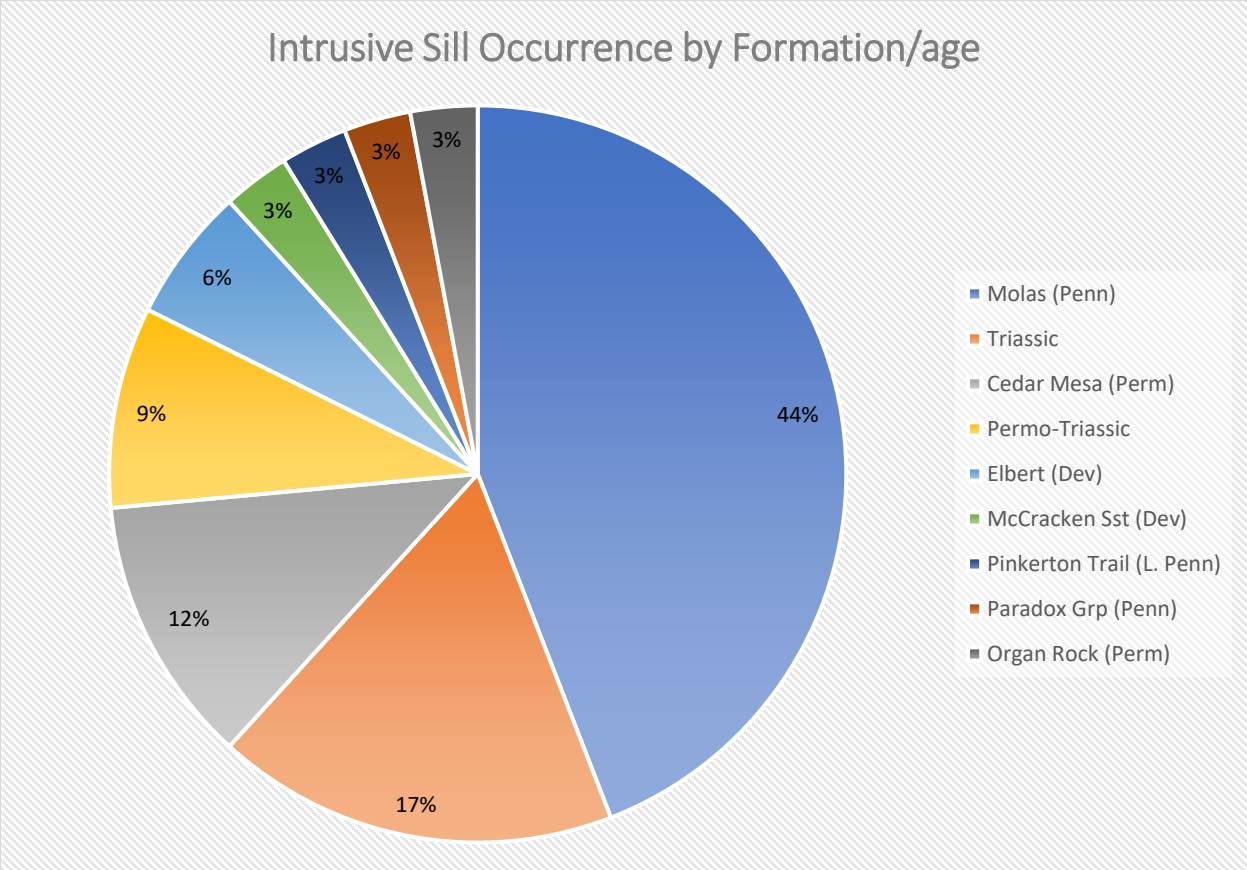


Figure 22. Distribution of sills and dikes of the Navajo Volcanic field by intruded strata age/formation as encountered by wells within the study area. The graph is based on 34 sills/dikes reported in 20 wells. Most of the sills (44%) were found in the basal Pennsylvanian Molas formation. The Molas lies directly on top of a major unconformity on the Mississippian Leadville limestone which is a common reservoir for both helium and carbon dioxide. 76% of the wells with high helium concentrations occur in either the Middle Pennsylvanian (above the Molas) or in the Mississippian below the Molas.

**Distribution of Helium and $CO_2$ by Reservoir Age**

High helium deposits found to date occur on the northern and southwest flanks of the Defiance uplift (Figure 23). Carbon dioxide is concentrated in the Paradox, San Juan, and Holbrook basins. Figures 24-31 compare helium and carbon dioxide occurrence by reservoir age to structure and isopach maps of the reservoir.

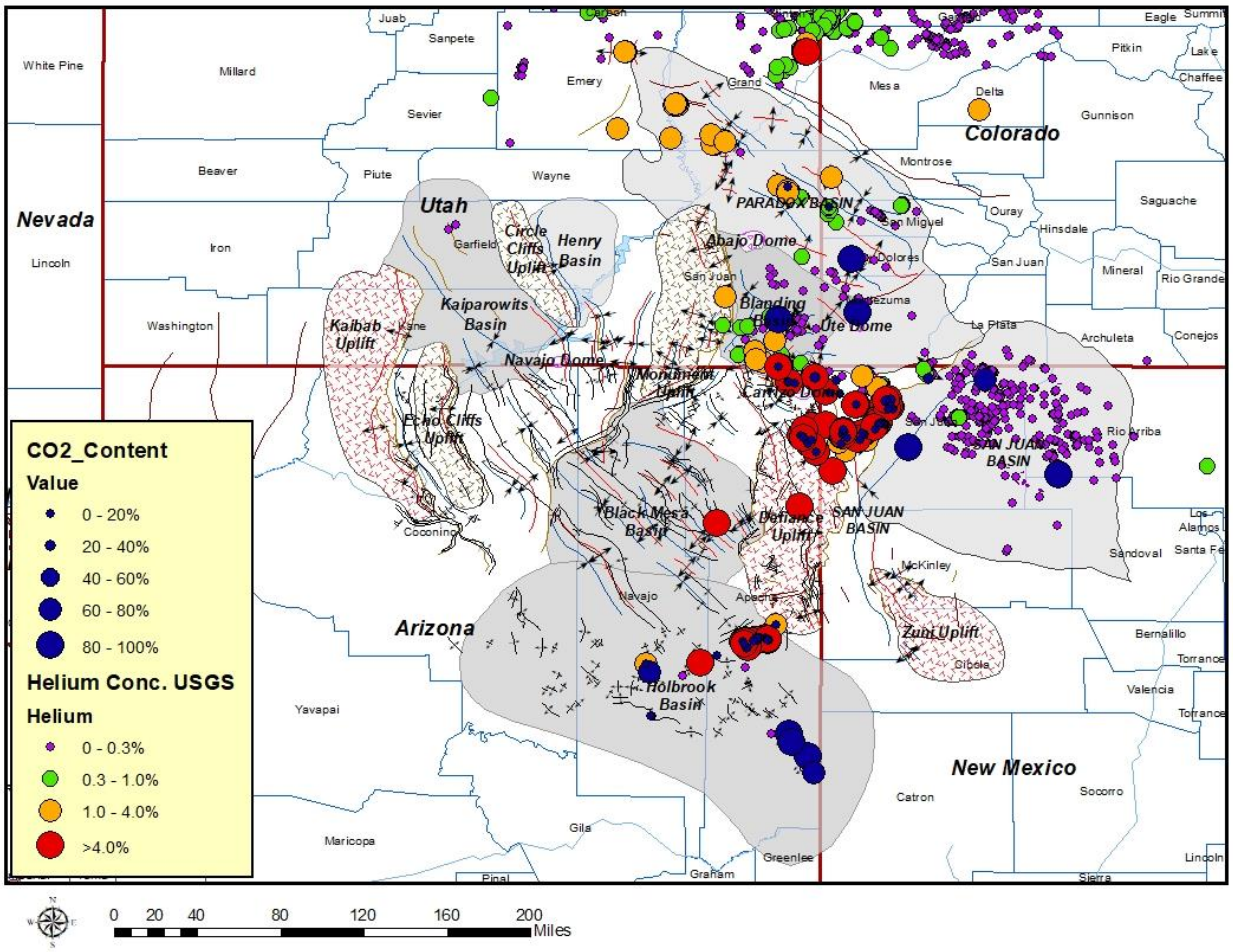


Figure 23. Regional distribution of helium and carbon dioxide in the Four Corners region.

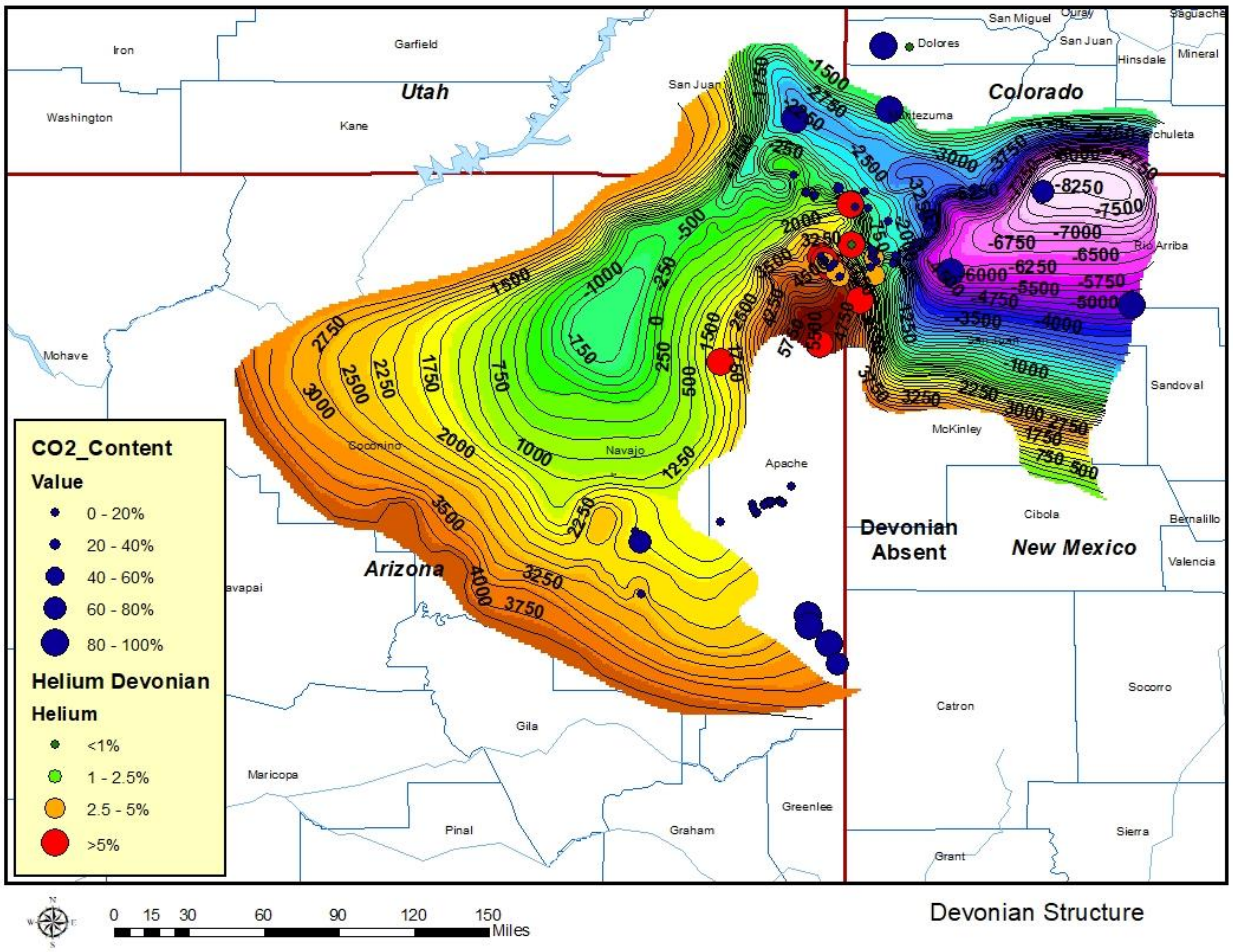


Figure 24. The occurrence of helium within the upper Devonian as related to the Devonian structure. Although carbon dioxide occurrence is shown, none of the high $CO_2$ deposits occur in the Devonian.

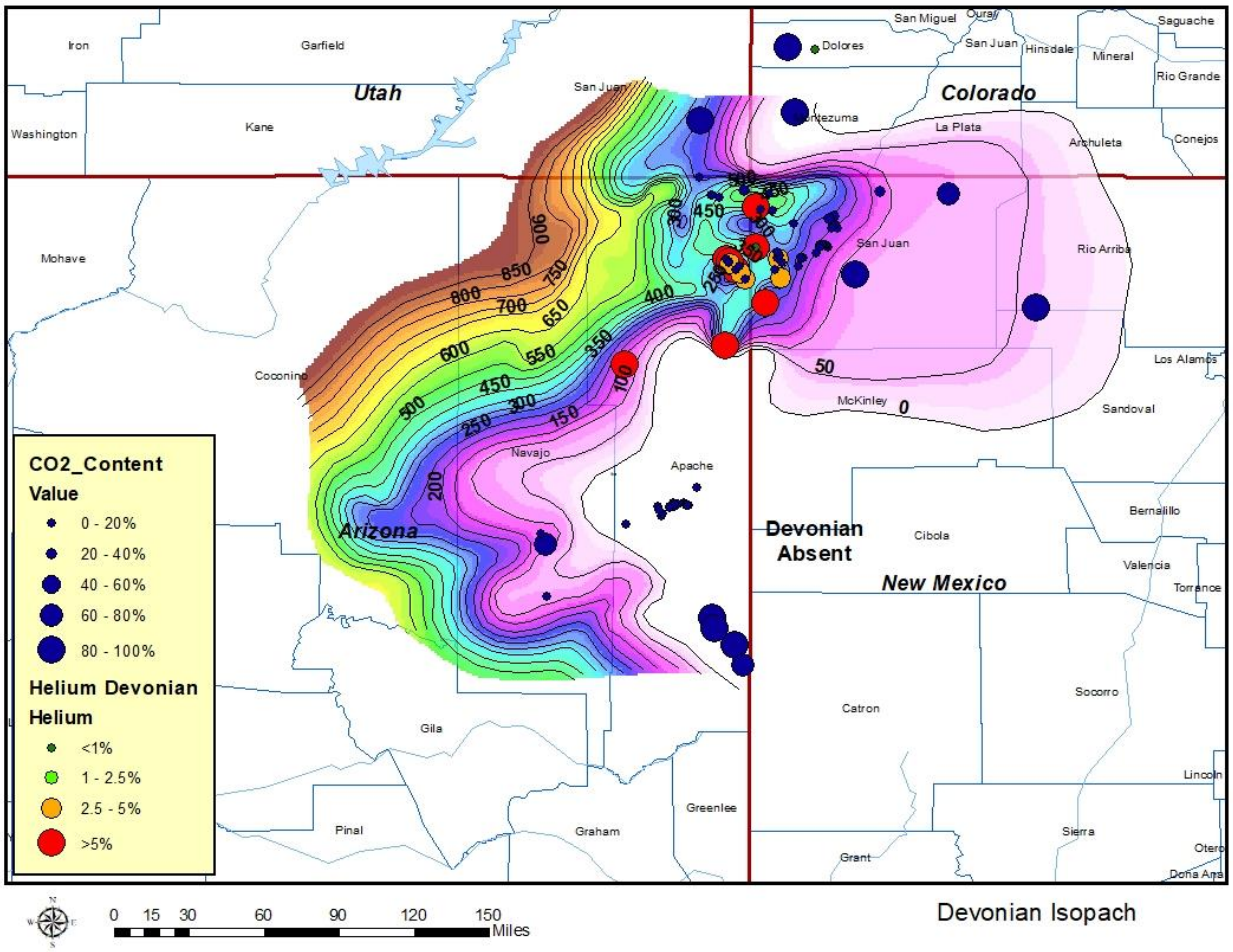


Figure 25. The occurrence of helium within the upper Devonian as related to the Devonian – Cambrian isopach. Although carbon dioxide occurrence is shown, none of the high $CO_2$ deposits occur in the Devonian.

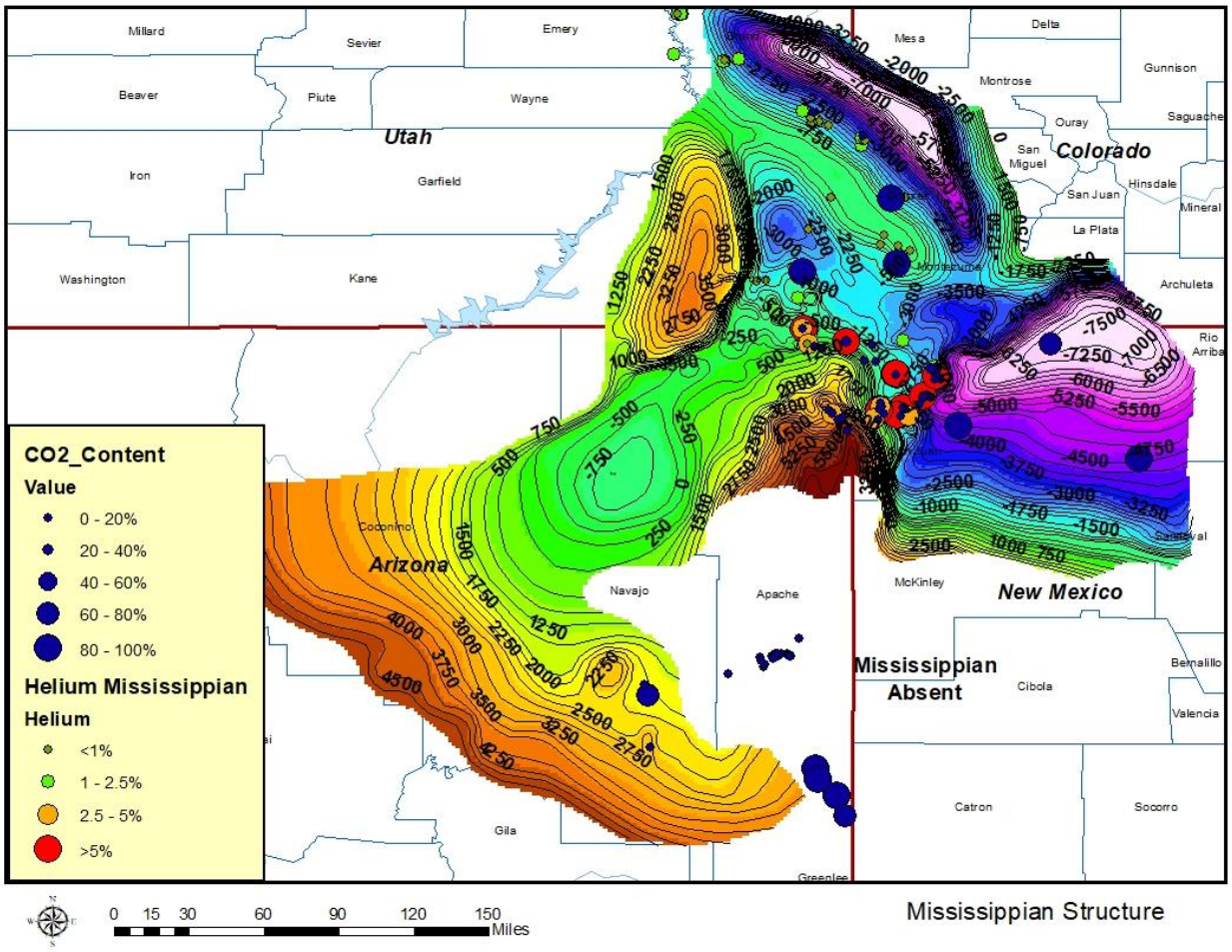


Figure 26. The occurrence of helium within the Mississippian (Leadville/Redwall Limestone) as related to the Mississippian structure. Massive carbon dioxide deposits occur in the Mississippian with the Paradox and San Juan basins. Although helium concentrations of 1-1.5% occur in the Mississippian in the Paradox basin, carbon dioxide represents >95% of the accumulations and possibly diluted previously high helium deposits in this area.

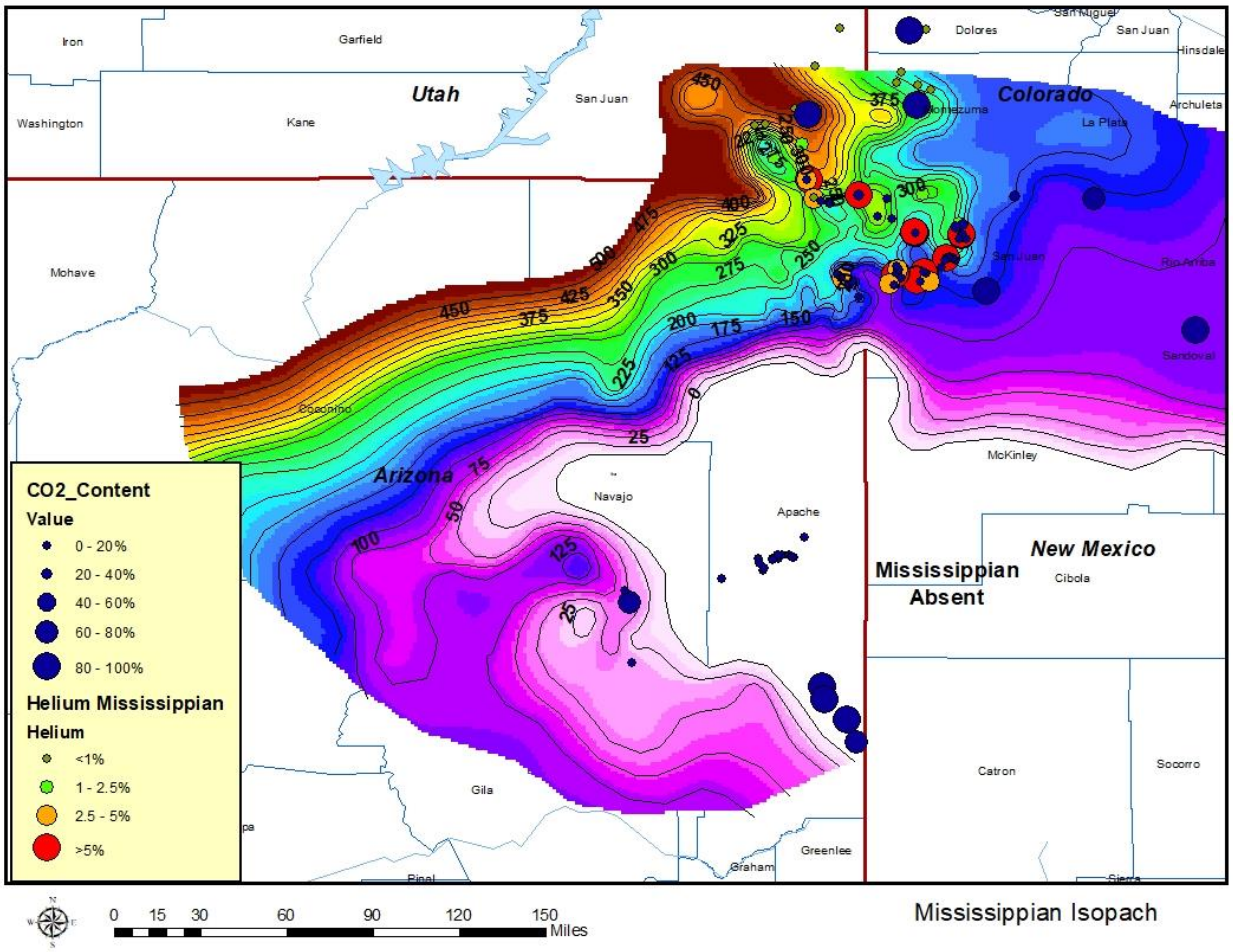


Figure 27. The occurrence of helium within the Mississippian (Leadville/Redwall Limestone) as related to the Mississippian isopach. Massive carbon dioxide deposits occur in the Mississippian with the Paradox and San Juan basins. Although helium concentrations of 1-1.5% occur in the Mississippian in the Paradox basin, carbon dioxide represents >95% of the accumulations and possibly diluted previously high helium deposits in this area.

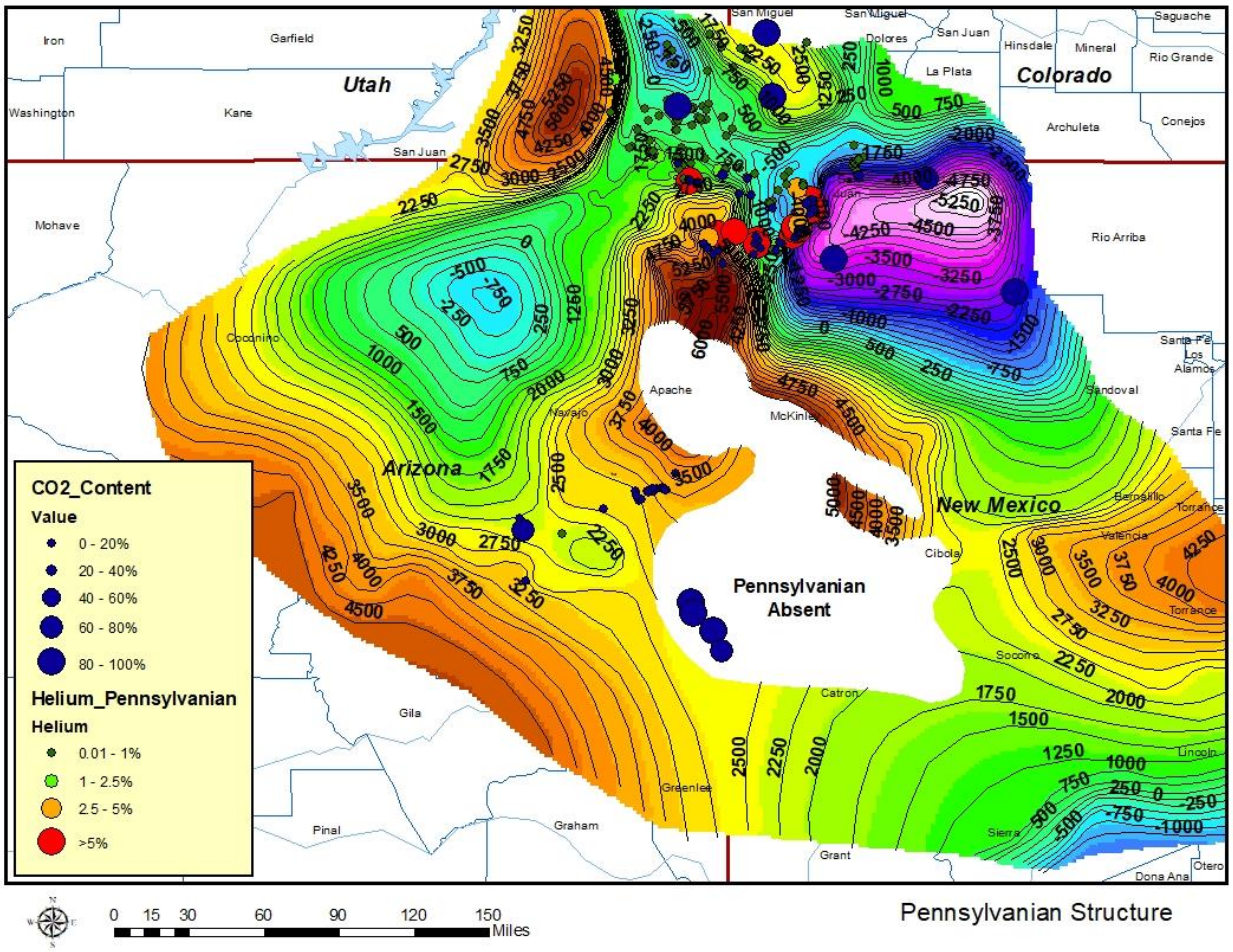


Figure 28. The occurrence of helium within the Pennsylvanian as related to the top of the Pennsylvanian structure. Although carbon dioxide occurrence is shown, none of the high $CO_2$ deposits occur in the Pennsylvanian.

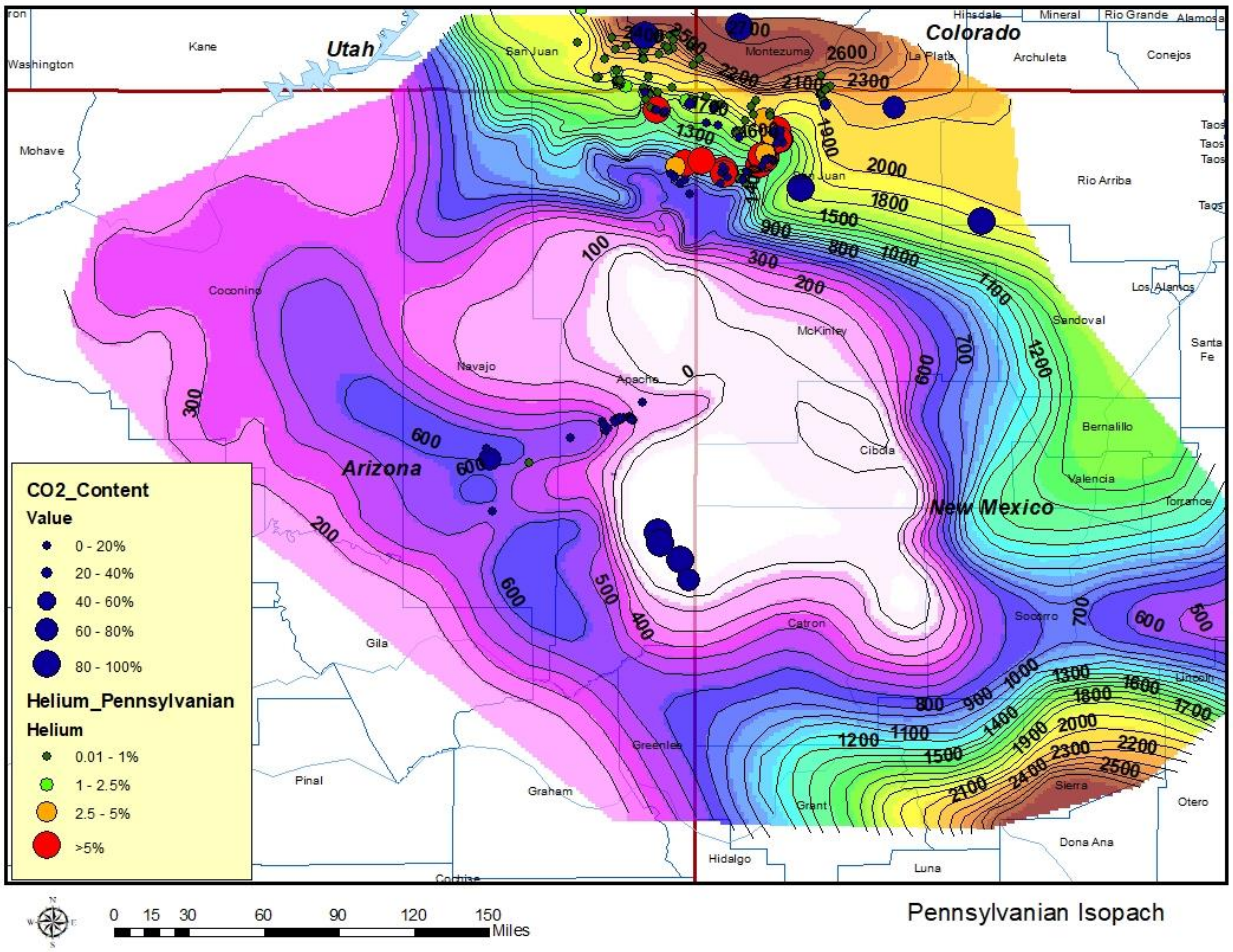


Figure 29. Occurrence of helium within the Pennsylvanian as related to Pennsylvanian isopach. Although carbon dioxide occurrence is shown, none of the high $CO_2$ deposits occur in the Pennsylvanian.

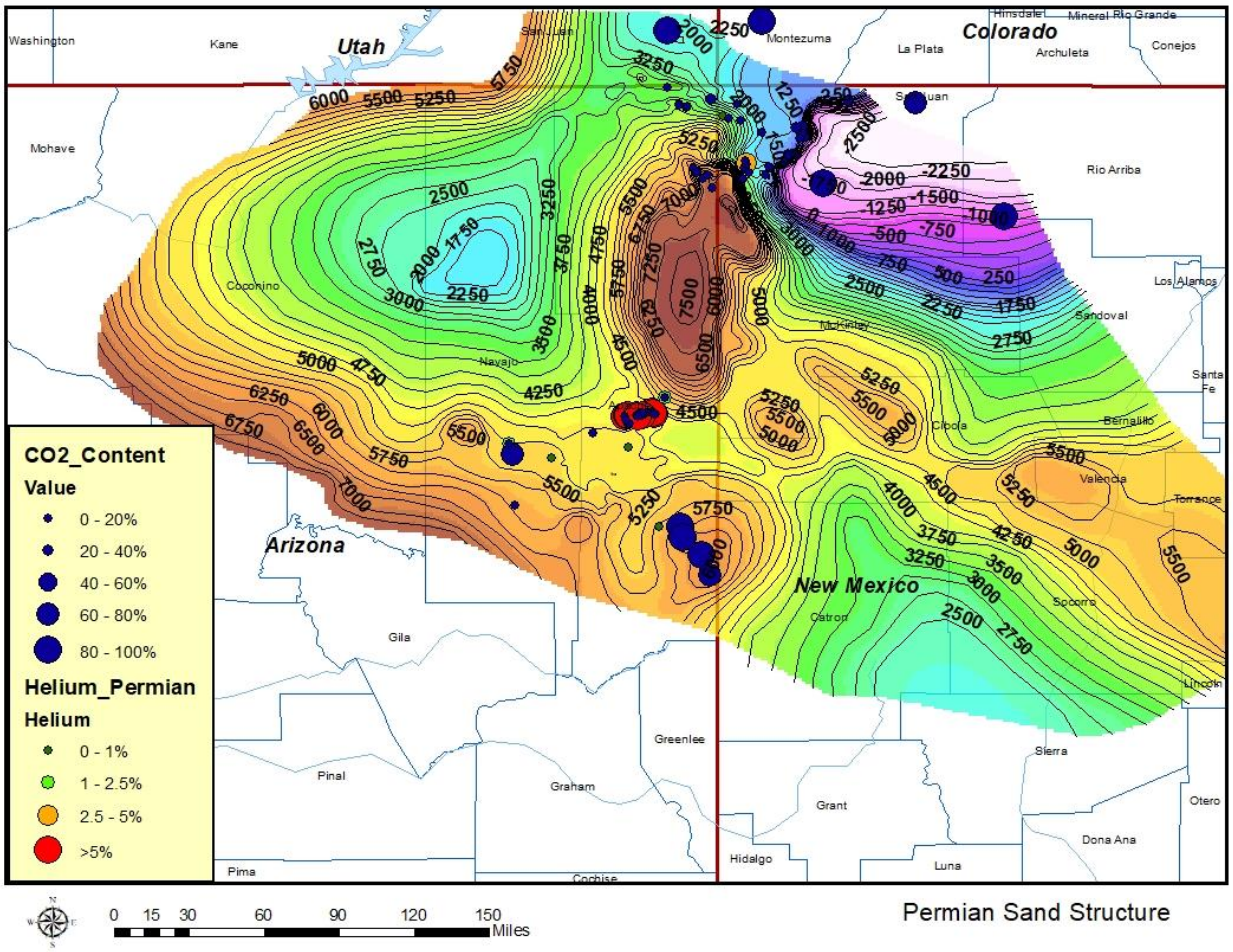


Figure 30. Occurrence of helium within the Permian as related to the Permian sandstone structure. A massive carbon dioxide field occurs in the Permian Supai Group (underlying the Permian sandstones) to the south of the Defiance uplift in the eastern part of the Holbrook basin. This carbon dioxide deposit was released during volcanism related to the Basin and Range extension in the late Tertiary.

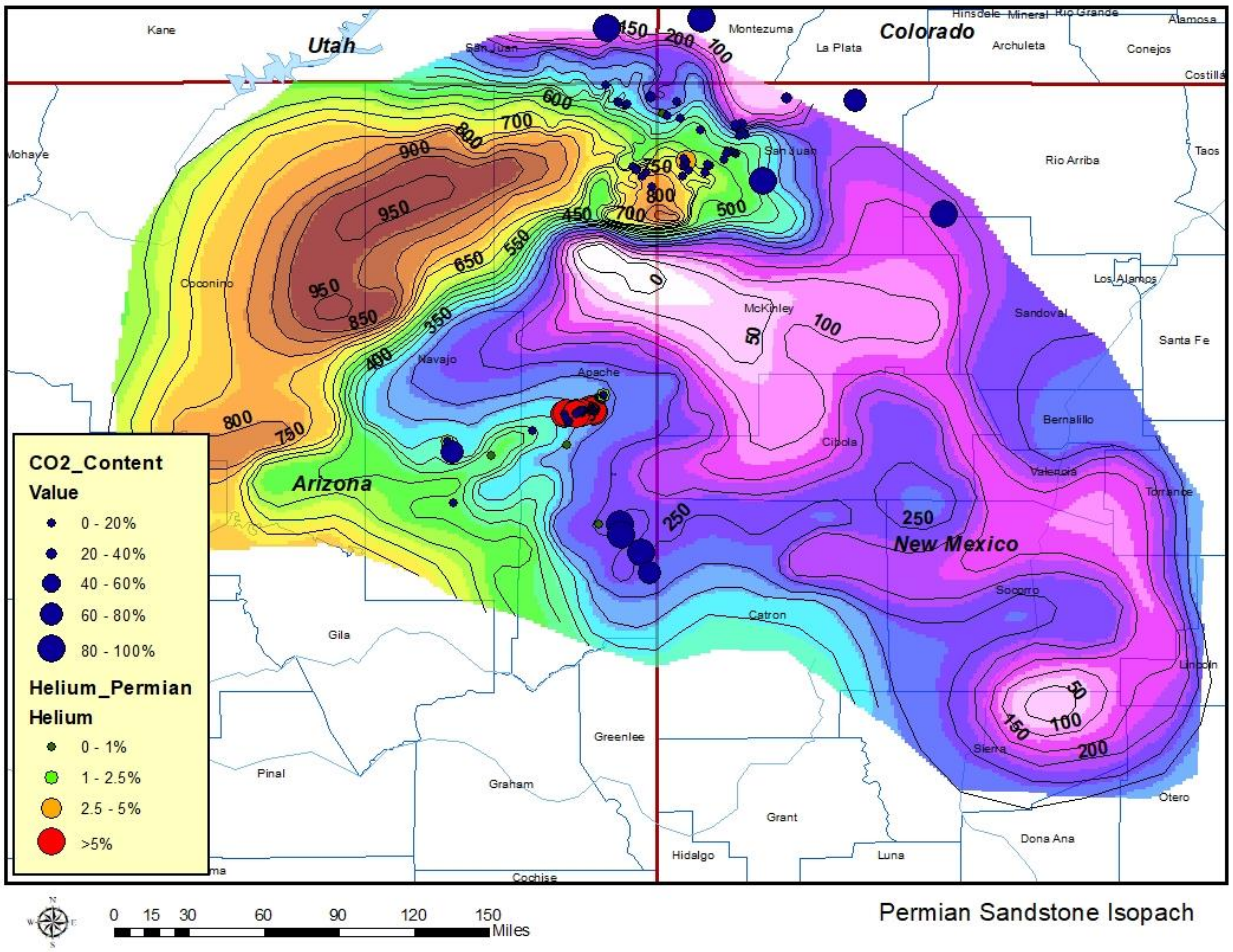


Figure 31. Occurrence of helium within the Permian as related to the Permian sandstone structure. A massive carbon dioxide field occurs in the Permian Supai Group (underlying the Permian sandstones) to the south of the Defiance uplift in the eastern part of the Holbrook basin. This carbon dioxide deposit was released during volcanism related to the Basin and Range extension in the late Tertiary.

## Analytical methods and data gathered and used in this study

### High-resolution aeromagnetic survey

#### Summary

Analysis of the regional (3 x 9-mile grid) aeromagnetic data interpreted by Earthfield Technology, LLC in 2019 showed that helium discoveries made on Navajo Lands lie either on or near basement lineaments and intrusive bodies. The high-resolution aeromagnetic survey (0.25 x 1-mile grid) acquired in this study was done to accurately position and define basement lineaments, igneous intrusions, dikes, sills, and basement structure to a degree not possible with the regional aeromagnetic data. Additionally, the high-resolution aeromagnetic data

would also identify numerous features that were unresolvable with the regional aeromagnetic data. New helium migration and accumulation sites can then be identified using the higher resolution data.

The airborne magnetometer measures and records the total intensity of the magnetic field, which is a combination of the magnetic field generated in the Earth as well as tiny variations due to the temporal effects of solar wind variations and magnetic field of the aircraft. By subtracting the solar, regional, and aircraft effects, the resulting aeromagnetic map shows the spatial distribution and relative abundance of magnetic minerals in the upper levels of the Earth's crust. Igneous rocks contain the highest magnetic mineral content (Table 4). Sedimentary and metamorphic rocks are generally non-magnetic.

TABLE OF MAGNETIC SUSCEPTABILITIES OF ROCKS
(Magnetic Mineral Content)

| Type | Susceptibility Range x $10^6$ emu | Average | Type | Susceptibility Range x $10^6$ emu | Average |
|---|---|---|---|---|---|
| **Sedimentary** | | | **Igneous** | | |
| Dolomite | 0-75 | 10 | Granite | 0-4000 | **1000** |
| Limestones | 2-280 | 25 | Rhyolite | 20-3000 | |
| Sandstones | 0-1660 | **100** | Dolerite | 100-3000 | 1400 |
| Shales | 5-1480 | 50 | Augite-Syenite | 2700-3600 | |
| Av. Var. Sed. - (48) | 0-4000 | 75 | Olivine-Diabase | | 2000 |
| **Metamorphic** | | | Diabase | 80-13000 | 4500 |
| Amphibolite | | 60 | Porphyry | 20-16700 | 5000 |
| Schist | 25-240 | 120 | Gabbro | 80-7200 | 6000 |
| Phyllite | | 130 | Basalts | 20-14500 | 6000 |
| Gneiss | 10-2000 | | Diorite | 50-10000 | 7000 |
| Quartzite | | 350 | Pyroxenite | | 10500 |
| Serpentine | 250-1400 | | Peridotite | 7600-15600 | 13000 |
| Slate | 0-3000 | 500 | Andesite | | 13500 |
| Av. Var. Met. **(61)** | 0-5800 | 350 | Av acid Ign. | 3-6530 | 650 |
| | | | Av. basic Ign. | 44-9710 | 2600 |

**IGNEOUS ROCKS MUCH HIGHER SUSCEPTIBILITY (MAGNETITE CONTENT) THAN METAMORPHIC & SEDIMENTARY ROCKS**

**DETAILED BASEMENT SUSCEPTIBILITY MAPPING CAN DETERMINE BASEMENT/INTRUSIVE/EXTRUSIVE TYPE & LITHOLOGY**

Table 4. Table of measured magnetic susceptibilities of various rock types taken from samples collected around the world.

The wavelength and amplitude of a magnetic anomaly is a function of the magnetic body's depth and composition, respectively (Figures 32 and 33). Shallow igneous bodies produce short wavelength magnetic anomalies and deep igneous bodies produce long wavelength magnetic anomalies.

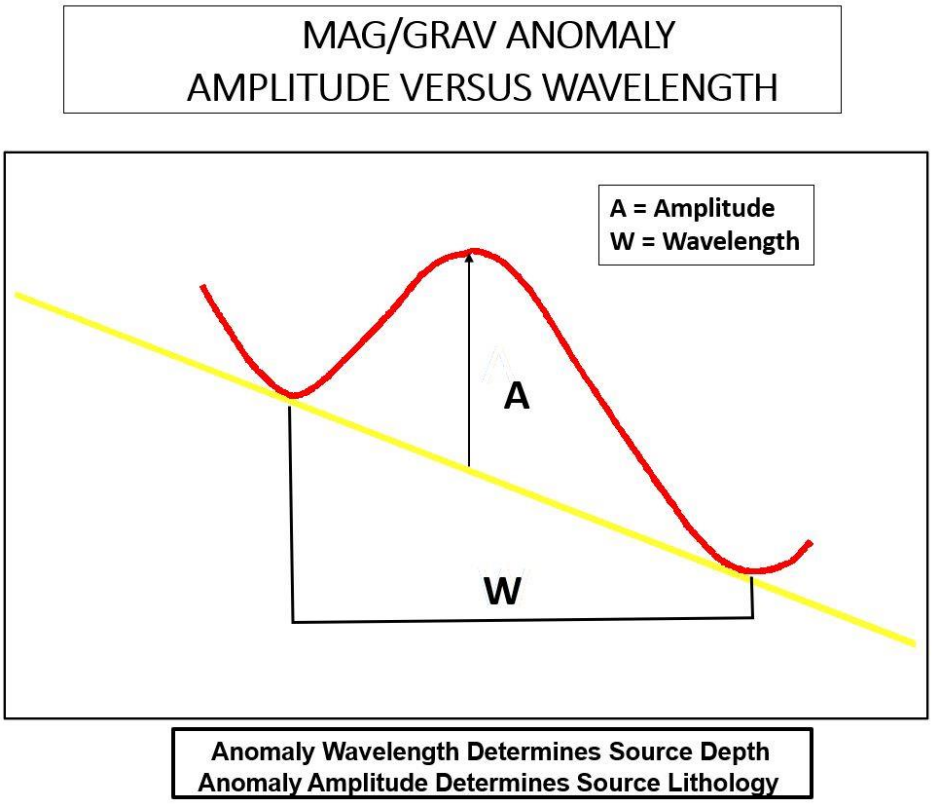


Figure 32. Relationship between magnetic anomaly amplitudes & wavelengths versus source body depth and lithology.

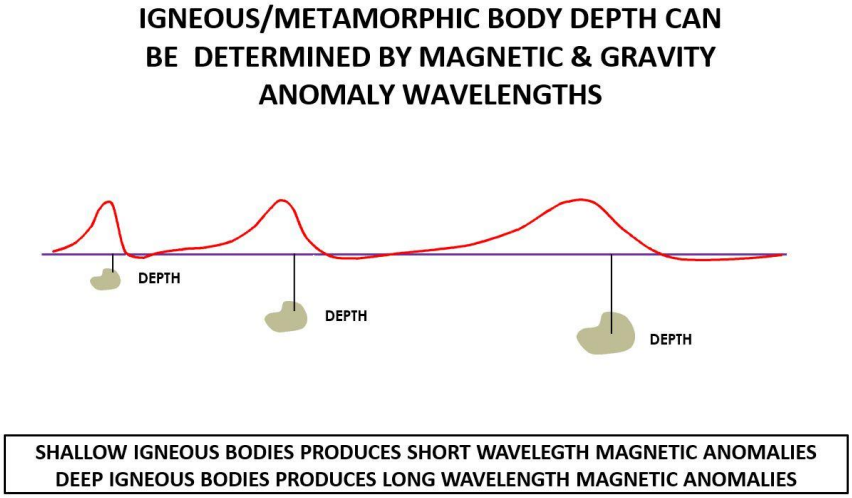


Figure 33. Graphical depiction of magnetic anomaly source body depth versus anomaly wavelength.

## Survey Design and Equipment

The project involved the acquisition of approximately 12,900-line miles of high-resolution magnetic data (Figure 34). Under the direction of Earthfield Technology, LLC, EDCON-PRJ, Inc. conducted the acquisition of the survey using a Cessna 180 fixed-wing aircraft specially fitted with a tail-stinger housing a Geometrics Cesium-vapor Magnetometer System.

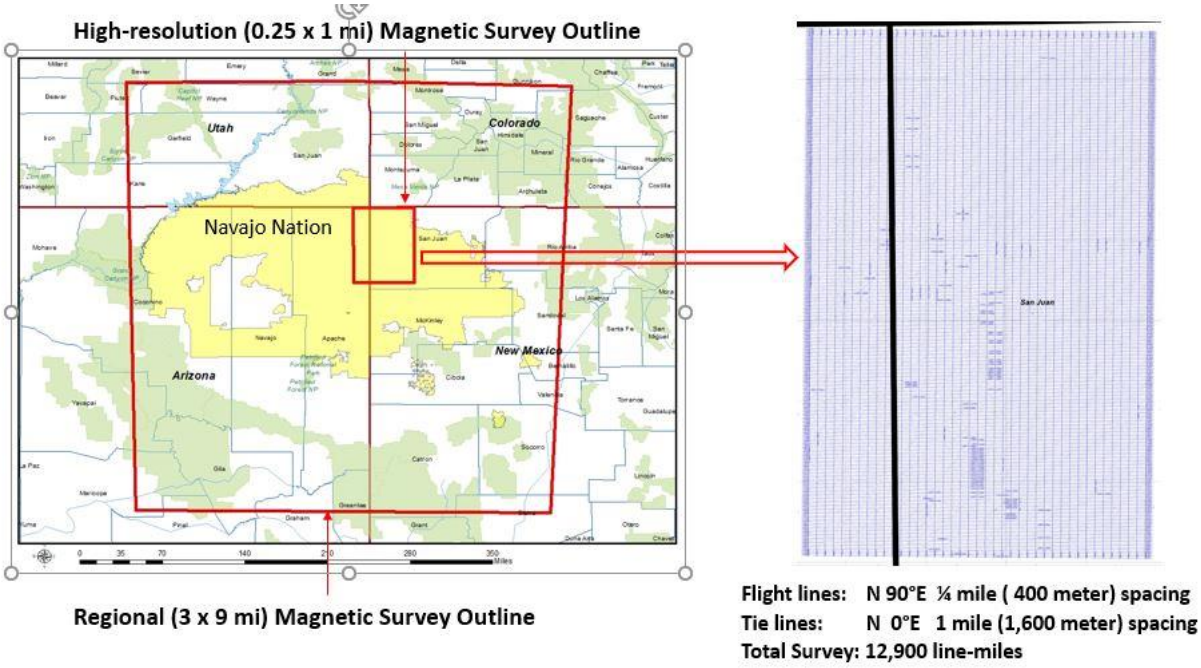


Figure 34. High-resolution magnetic survey location map, and magnetic survey flight line locations.

The survey was flown on a pre-planned drape surface nominally 500 ft. above the terrain. Earthfield generated pre-planned drape surfaces using proprietary software that incorporates a digital terrain model, the required drape height, and the flight characteristics of the survey aircraft (survey speed, vertical acceleration, and rate of climb) to produce a hyperbolically-smoothed digital surface that allowed close terrain following within a safe-flight envelope for the survey aircraft.

Equipment used for the acquisition of the magnetic data consisted of 1) an aircraft, 2) an airborne magnetometer, and ancillary 3) airborne and 4) ground-based equipment (Figure 35).

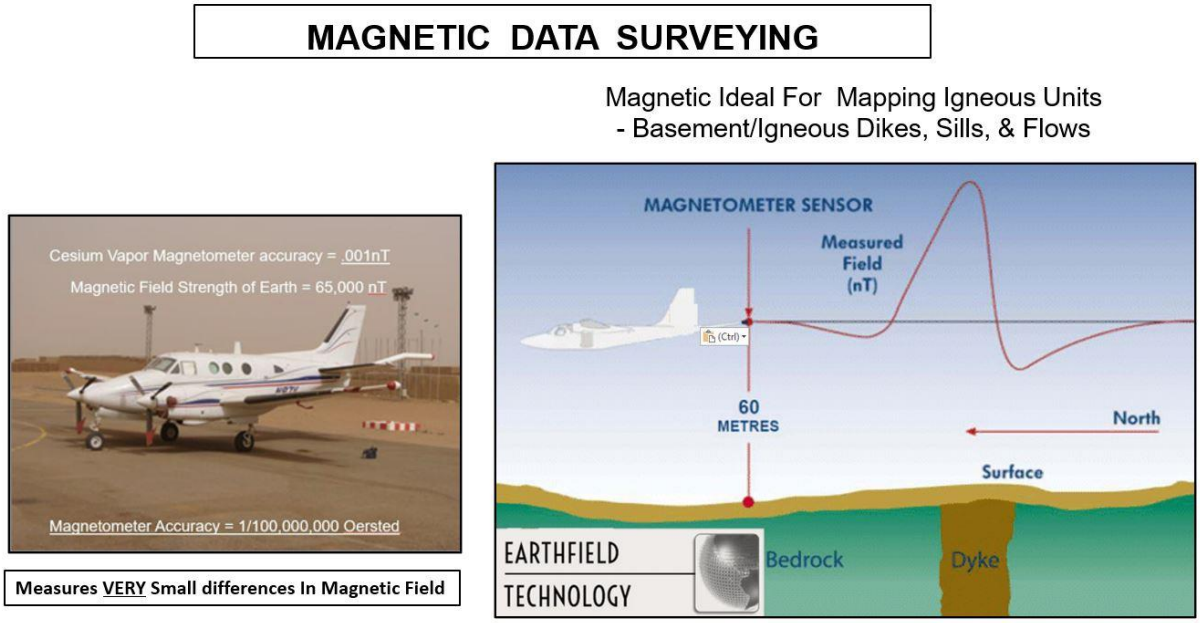


Figure 35. Illustration of magnetometer sensitivity, and measurement of lateral magnetic susceptibility variations.

Aircraft

A Cessna C-180 was used for this project. The aircraft has been extensively modified to increase its performance on draped aeromagnetic surveys. The engine is a high-performance Continental O-520 creating 308 horsepower. This engine is the typical engine used in the much bigger and heavier Cessna 206. The increased power to weight ratio of the aircraft results in a sustained climb rate of 1,600 feet per minute at 80 mph airspeed. The flight characteristics of the aircraft allows precise adherence to pre-programmed drape surfaces. The aircraft also has a STOL modification kit, which gives it better stability, climb and dive, and control characteristics while on survey operations. The carbon-fiber tail-stinger, which measures 3.0 meters from aircraft tail to magnetometer sensor pod, isolates the sensor from vibration and noise sources.

Airborne Magnetometer

A GeoMetrics G823A cesium-vapor magnetometer is housed in the sensor pod of the carbon-fiber tail-stinger. This magnetometer has a sensitivity of 0.015 nT over a range of over 20,000 nT, with a sensor noise level of less than 0.02 nT. The airborne magnetic field will be recorded at 10 Hz to a resolution of 0.001 nT.

Magnetic data points will be collected along flight lines at no more than 6.0 meters. Maneuver noise after compensation will not exceed 3 nT for pitches and rolls of +/- 20° and heading changes will not cause variations of more than 1 nT in the magnetic reading.

Ancillary Airborne Equipment

- Freeflight Systems TRI-40 Radar Altimeter
- Novatel ProPak-6 Dual Band WAAS-enabled Differential GPS Positioning
- Applied Physics Tri-axial Fluxgate Compensation Magnetometer
- AgNav Survey Planning and Three Axis Guidance System
- Geometrics MagLog Data Integration and Logging System

Ground Based Instrumentation

- Geometric G-858 Magnetometer base station

The time-synchronized ground magnetic field data will be digitally recorded at a 1.0 sec interval and to a resolution of 0.01 nT. No data acquisition shall be undertaken during magnetic storms or short-term disturbances of magnetic activity at the ground station that exceeds the following:

Monotonic changes in excess of 5 nT in any 5-minute period
A non-linear disturbance in excess of 3 nT in three minutes

## A) Survey Methodology:

Magnetic Compensation

A compensation flight will be conducted prior to survey operations to determine heading and maneuver error and to calculate compensation coefficients used during processing of the survey data. The pilot will fly a square pattern in the four survey directions at a high altitude to suppress geologic effects on the readings. The pattern will be flown twice, once "flat" as if conducting survey operations and once while performing moderate roll, pitch and yaw maneuvers. The data from the flux-gate magnetometer will be processed to generate x, y and z axis coefficients used to compensate for heading and maneuver error during survey operations.

## B) Radar Altimeter Calibration

Radar altimeter data will be acquired during a series of traverses over flat terrain in the vicinity of the survey. These traverses will be flown at increasing altitudes, from 200 ft. to 1,500 ft. This data will then be processed to generate coefficients used to convert analog radar altimeter data from millivolts to feet.

In addition to the analog radar altimeter data, we will be generating "calculated radar" values at a rate of 5 Hz. This data is generated by taking the GPS elevation of the aircraft and then subtracting the ground elevation value from the digital elevation model of the survey area. We have found the calculated radar data to be more accurate than analog radar altimeter data.

## C) Quality Control Measures

The Quality Assurance Program incorporates personnel training, equipment selection, instrumentation checks and calibrations, data acquisition methodology and procedures, field data analysis and processing, and final data analysis, processing, and mapping using a rigorous, time-proven approach that guarantees results of the highest quality.

The data from each flight are reviewed nightly by multiple individuals. The data are first reviewed by the pilot and crew immediately after each flight. Then the data are downloaded from the onboard computer and uploaded via ftp site to EDCON-PRJ's offices in Denver, Colorado, and finally, by the Earthfield Technology, LLC staff in Houston, Texas, for formal quality review.

The data are reviewed for flight line accuracy, GPS resolution, radar altimeter positioning, and magnetometer signal-to-noise values, and these reviews will be repeated by the Earthfield Technology, LLC staff to confirm that only the highest quality data are delivered.

Finally, each flight's data are then compensated and corrected for diurnal activity using data collected at the base station. This compensated and diurnally-corrected data is uploaded to our ftp site for review by the client or their consultant. Daily acquisition status reports are forwarded via e-mail to the client and consultants involved in the project.

## D) Data Processing and Mapping:

a) Pre-processing Procedures

Prior to the profile data processing and leveling procedures, a system of pre-processing procedures, incorporating a series of quality control checks, is completed. These procedures include the following:

b) Data Merging

Digital magnetic and ancillary data traces are recovered and merged with the final positioning data based on GPS time and associated fiducial time marks at 0.1 second intervals. Merged data are converted to a line location file and system lag or lead time applied, if applicable.

c) Data Editing

Merged data traces, including the base magnetometer trace, are edited for completeness and data spikes. Profile-oriented data corrections are applied to the edited and merged data traces.

d) IGRF Correction

The International Geomagnetic Reference Field (IGRF) is applied to the magnetic data trace.

e) Diurnal Correction

The IGRF-corrected diurnal data are applied to the IGRF-corrected magnetic profile data as a correction.

f) Profile Leveling

The first stage of leveling is an analysis of the network of line crossings. Each line in the survey network is shifted up or down systematically such that the sum of the square of the mis-tie errors in the network is minimized. The systematic corrections are further constrained such that the sum of the systematic corrections is zero, effectively eliminating DC shifts to the network. The micro-leveling process using Virtual Network Analysis (VNA), is a recursive process where a grid based on the edited, adjusted data forms a starting point. In the procedure, unedited and unadjusted data are reconsidered and readjusted. VNA enables recovery of map-coherent, short-wavelength components in the data, which might otherwise be lost.

## E) Magnetic Data Analysis

The objectives of the aeromagnetic analysis were to establish the depth and structural configuration of the basement surface beneath the survey area, and to identify the depth of location of possible igneous bodies within the survey area, as these bodies have been determined to be the likely sources of commercial helium accumulation within the study area.

To this end, Earthfield Technology, LLC processed and analyzed the magnetic data through a qualitative review of color shaded relief contour maps of the total magnetic intensity anomalies, reduced to the pole (RTP) transform maps, filtered residual maps, and a quantitative analysis of these data by means of an interactive generation and review of Werner deconvolution depth to source estimates along each line of magnetic data. Please see Figure 36 for an example off Earthfield's Werner deconvolution profiles.

A discussion of Werner deconvolution theory follows in the paragraphs below to aid in the understanding of how the basement map was developed.

Magnetic anomalies can be produced by a number of causative features such as lithology changes, variations in the thickness of magnetic/dense units, faulting, folding, and topographic relief. A significant amount of information can, at times, be obtained from a qualitative review of the magnetic anomaly maps. Magnetic anomaly wave numbers can often be related to the depth of anomalous sources from the magnetic/gravity sensor. Given the same rock type (equivalent susceptibilities), shallow sources produce higher wave number anomalies while

deeper sources yield broader anomalies. At the same time, variations in the relative magnetic/density base level can be indicative of regional or sub-regional variations in basement lithology. Also, the analysis of properly designed residual/ transform maps in areas of known or suspected structural tendencies, can be of great value in recognizing and mapping more subtle targeted structures.

Magnetic data can be analyzed in a number of ways by computer to yield source body parameters quickly and accurately. The primary method used in this interpretation utilized Werner deconvolution-based algorithms (Werner, 1953) as a basis for the interactive analyses of the depth to and horizontal position of source bodies and the related parameters of dip and susceptibility. The method forms a rigorous, iterative, two-dimensional inversion technique which eliminates interference from adjoining, often overprinted, anomalies. The PC-based program MAGDEPTH ©, was utilized in this study for Werner deconvolution. MAGDEPTH is Earthfield Technology's proprietary Werner deconvolution software package, and is considered the best in the industry for its effectiveness in determining anomaly source depth.

Analysis of the total magnetic intensity data yields parameters for thin, sheet-like bodies such as dikes, sills, intruded fault zones, and basement plates of minor relief compared to the source-sensor separation distance. Analysis of the horizontal gradient data (computed each pass from the filtered total intensity) yields similar parameters for geologic interface type features such as dipping contacts, edges of prismatic bodies, major faults, and slope changes of the basement surface. All thin sheets are bounded by two interfaces but these are too close together for their individual anomalies to be distinguishable from one another as the combination of the two results in a single thin sheet anomaly. It has often been shown that the magnetic/gravity anomaly for a thin sheet is precisely the same as the horizontal derivative of the magnetic/gravity anomaly for a similarly positioned interface. Thus, if interface-type anomalies are present in total field data, they can be transformed to thin sheet-type anomalies simply by calculating the derivative of the total field data. Combining analyses of both the total field and gradient data, it becomes possible to identify and calculate the geologic parameters of thin sheet-type bodies as well as interfaces.

The power of the equations employed for direct analysis of magnetic anomalies permits a unique solution even when only parts of the anomaly are undisturbed by adjacent anomalies. Such interference effects are very often the rule rather than the exception. Solutions are found from any set of equally spaced data points and these points are not confined to critical points along the profile such as minima, maxima or changes in slopes.

Sample spacings between adjacent data points forming the deconvolution operator, the order and terms of the filter to be used as well as the order of the interference operator to be applied to the data are all selected by the interpreter for each of the six operator passes in order to extract the maximum amount of information possible for any given geologic province and

structural environment. The horizontal distance subtended by the observational array (the operator length) is critical to the detection of an anomalous source. This distance must be increased to ensure that progressively deeper geologic sources having broader magnetic anomalies may be recognized. As such, the computation sequence described above can be performed for up to six passes allowing for increasing operator sizes each time. The operator length for each pass is established through the setting of the spacing parameter for each pass which specifies data decimation. There often can be sufficient overlap between the depth range covered by each pass such that an anomaly is "recognized" on multiple passes.

The spacing parameters for each operator pass used in this interpretation were based on a 1000-meter sample spacing. The actual operator length is a function of the data spacing, as acquired, the sub-sample interval used and the order of interference chosen for each pass (first, second or third corresponding to a 6, 7, or 8-point operator). During the deconvolution, the six, seven, or eight equally spaced points along the profile are used to solve the set of simultaneous equations yielding, if an anomaly has been recognized, depth and along line position of the related source body. The entire sequence of points (the operator) is then advanced by one point (regardless of the actual operator spacing and length) and another calculation is made. In this way, as many X and Z pairs are obtained as there are data points along an anomaly. The calculated positional coordinates are then examined statistically for consistency and inconsistent depth calculations are rejected. If the operator is passing over an anomaly, there will be a closely grouped set of depth points indicating a source for the anomaly and a central solution position can be determined. Susceptibility and dip values are then computed.

When applied to adequately sensitive data, this technique can identify and resolve very subtle anomalies and yield a significant amount of information. In areas where the Werner deconvolution analysis failed to yield depth solutions, manual techniques, such as half maximum slope, were attempted to established source depths. It is then for the interpreter to analyze the total set of source depths, accept or reject solutions based on their consistency, and apply any known geologic constraints to the interpretation. Please see Figure 37 for an illustration of Earthfield's methodology for conducting detailed depth to basement mapping.

The final portion of the analysis was the lineament analysis of the magnetic/gravity/topography data, along with basement faults identified from the Werner deconvolution interpretation. Lineaments have been interpreted from each data type via Earthfield's proprietary lineament analysis software. These lineaments have then been combined to produce lineament and intersection density maps. These maps are very useful in identifying subtle fractures and identifying areas most likely to contain natural fracturing. Earthfield Technology has used this approach successfully in numerous shale plays around the world, including the Barnett (originally for Mitchell Energy in the 1990's), Austin Chalk, Haynesville, Bakken, Eagle Ford, and Marcellus shale, over the past 20 years. Please see Figure 38 for an Illustration of Earthfield's methodology for generating complete lineament analysis for possible fracture identification.

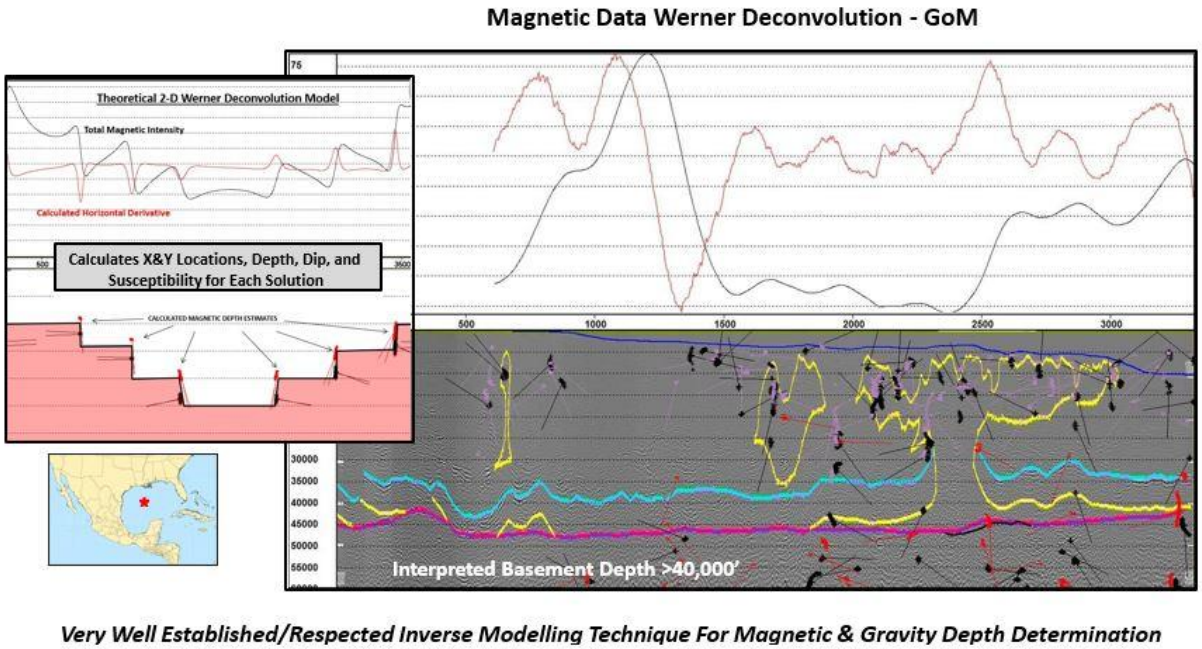


Figure 36. Example of Earthfield's Werner deconvolution depth estimation profiles.

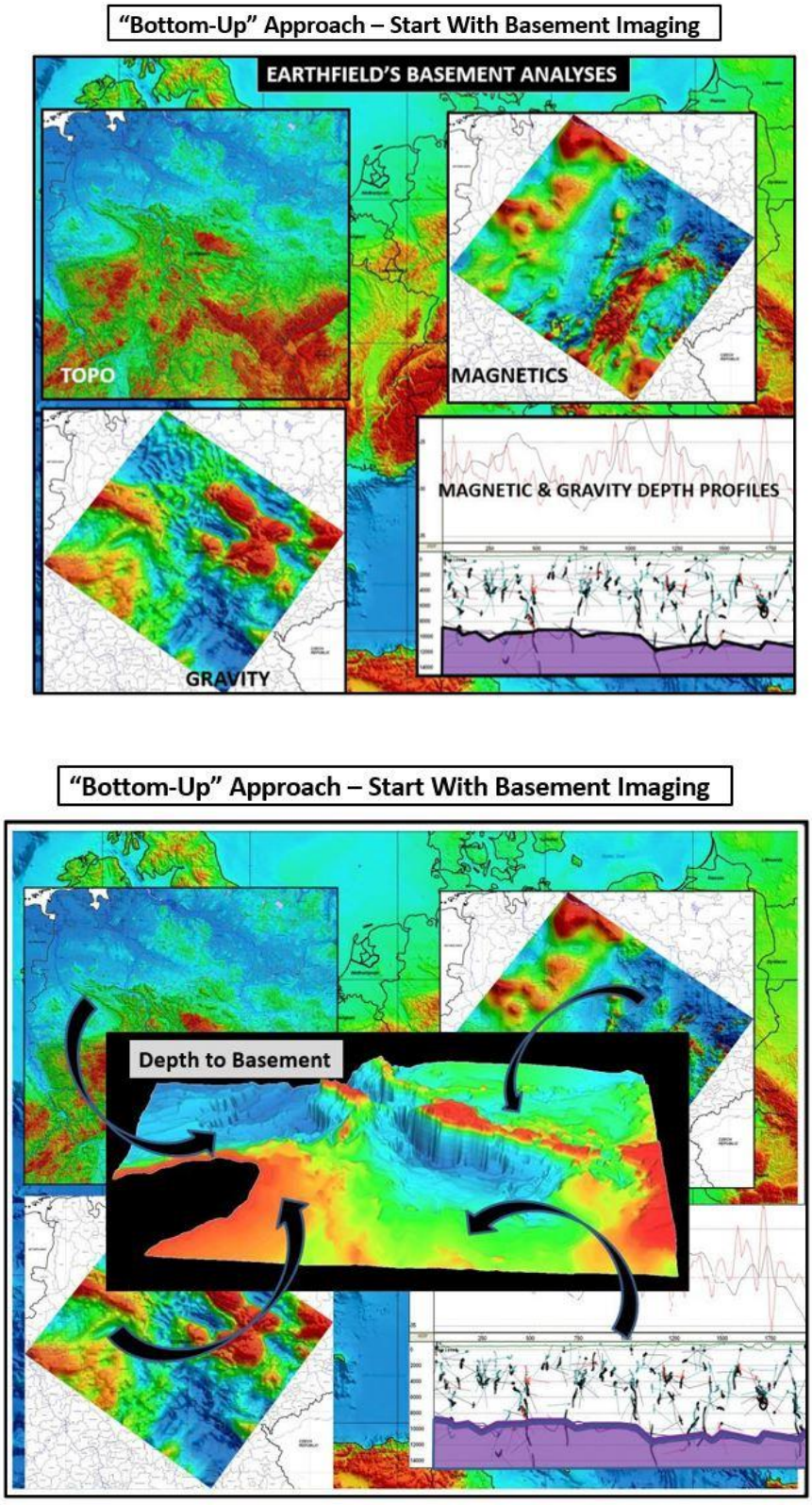


Figure 37. Illustration of Earthfield's methodology for conducting detailed depth to basement mapping.

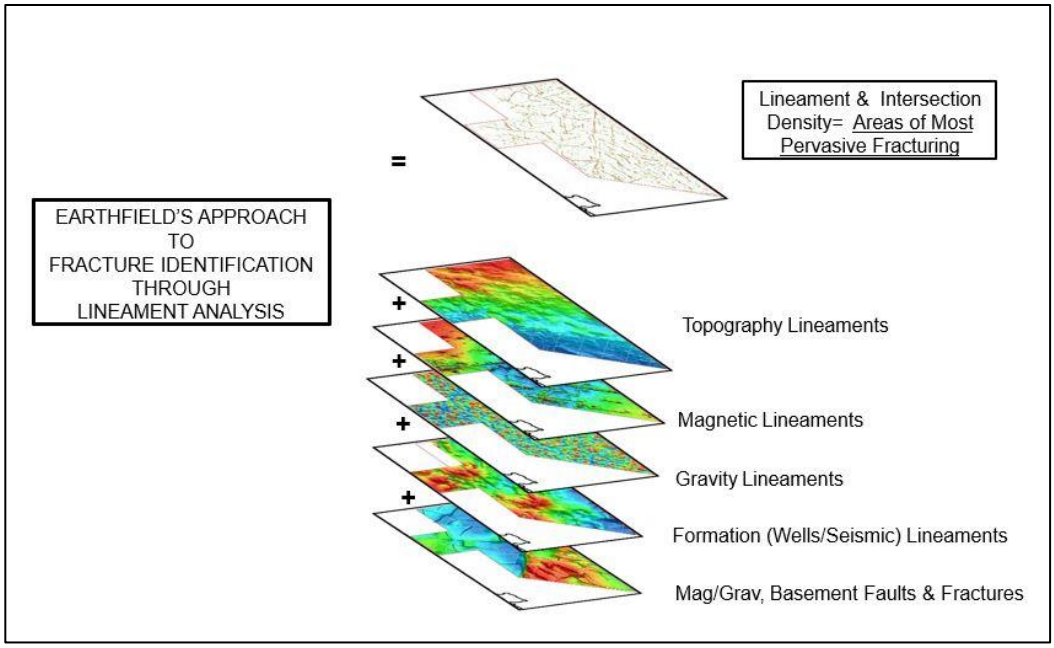


Figure 38. Illustration of Earthfield's methodology for generating complete lineament analysis for possible fracture identification.

## F). PRODUCT DESCRIPTIONS

The following figures (Figures 39-79) represent the various products generated during this project, with a brief description of how the products were generated, and the how the products are considered useful to helium exploration.

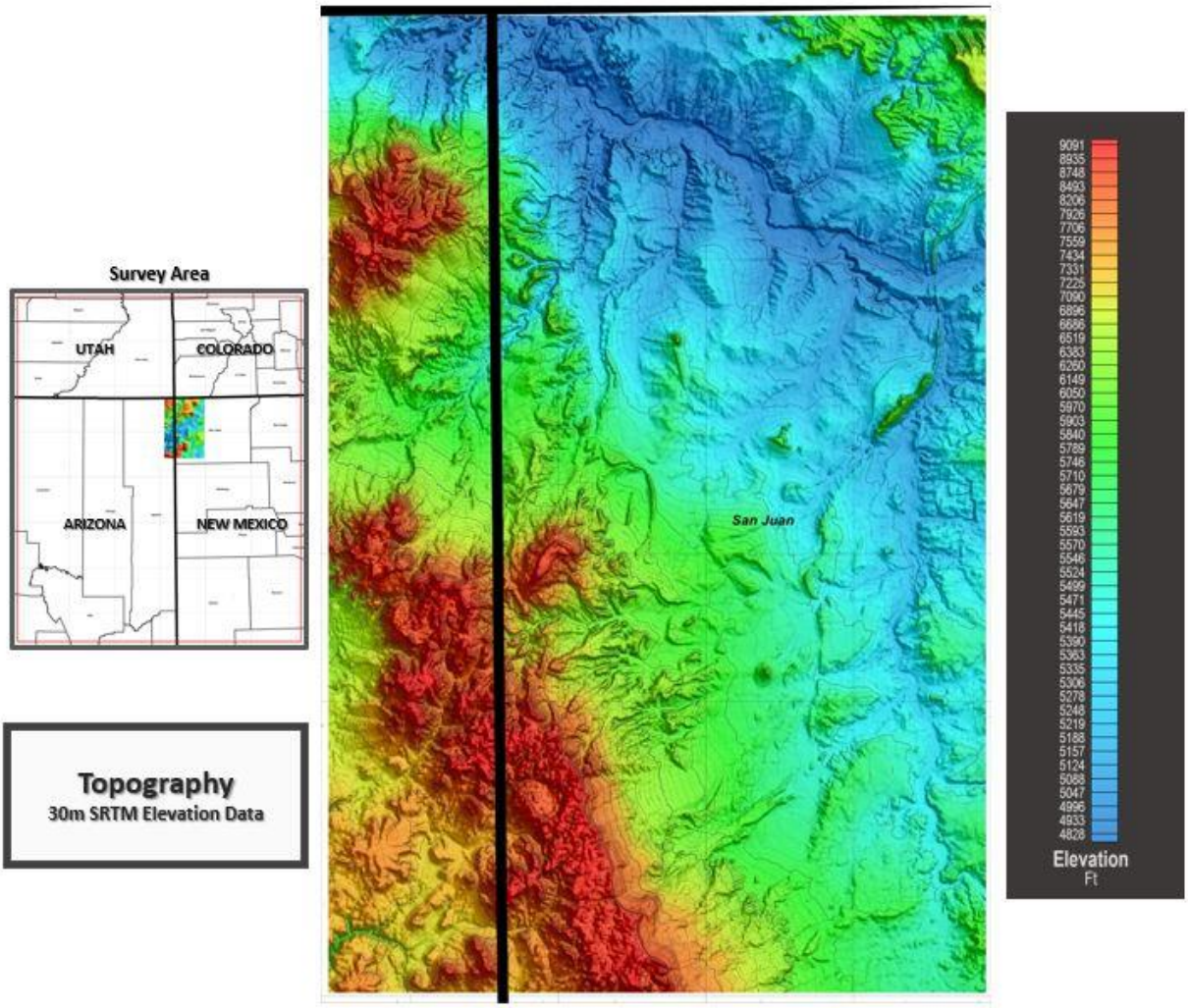


Figure 39. SRTM 30 meter digital topography used in the project. These data were used in our lineament analysis, and can define potential shallow fracture zones in the survey area.

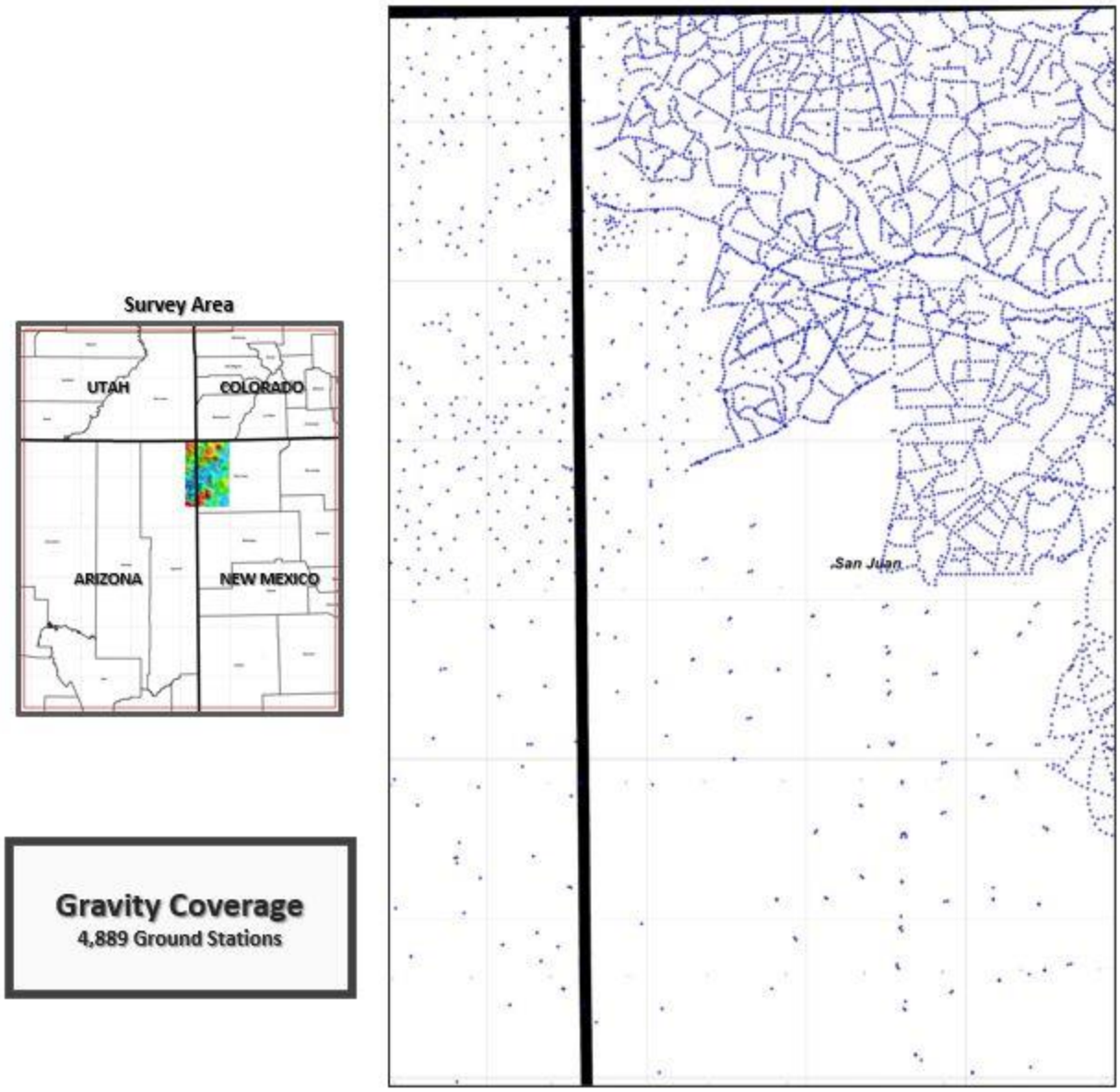


Figure 40. Station location map of Bouguer gravity stations utilized in the project. These data are from Earthfield's proprietary North American Gravity Compilation. Gravity data have been used to define density boundaries that can define fault/fracture zone at the basement surface, in addition to sedimentary structures.

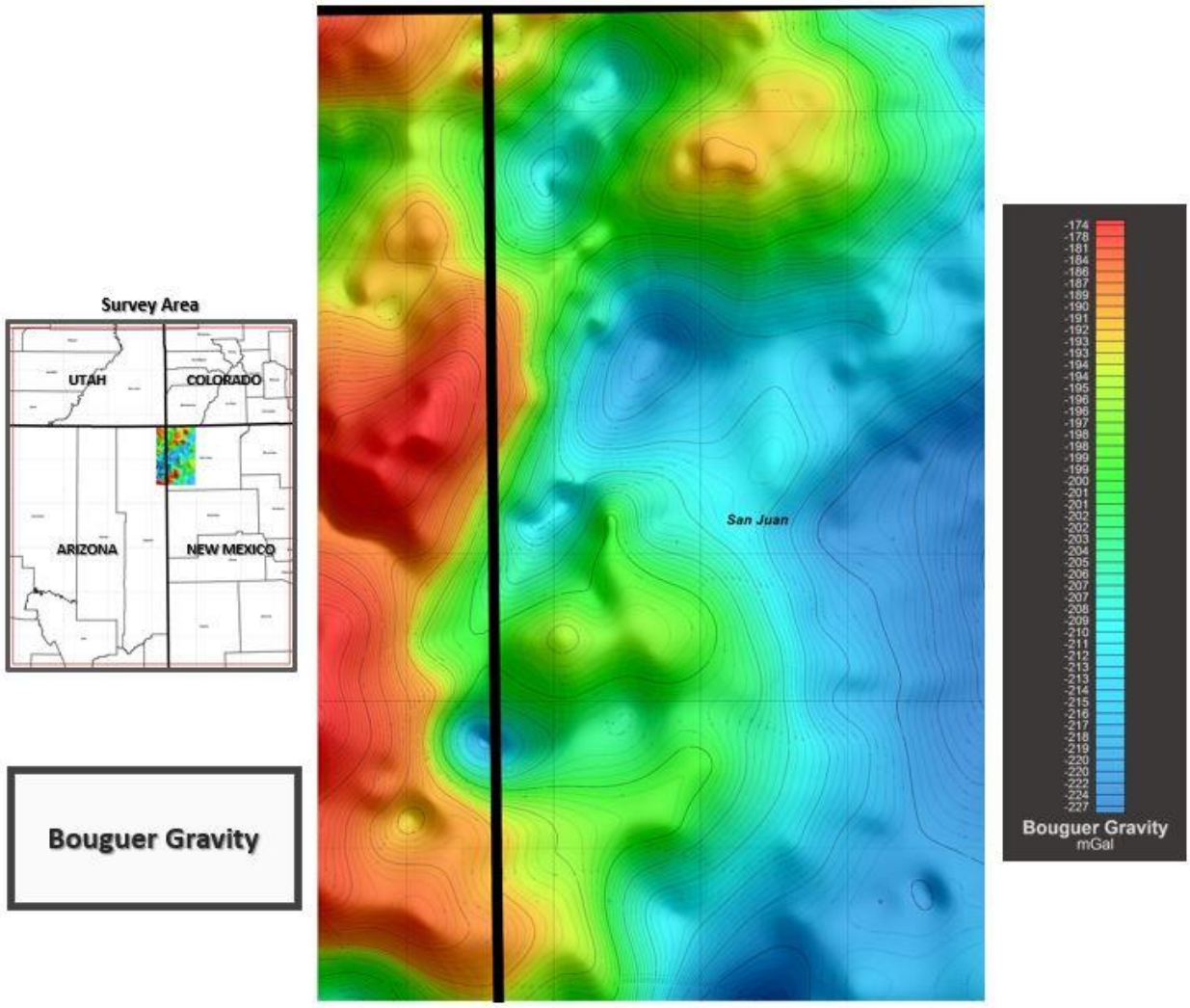


Figure 41. Bouguer gravity map made from Earthfield's proprietary North American Gravity Compilation.

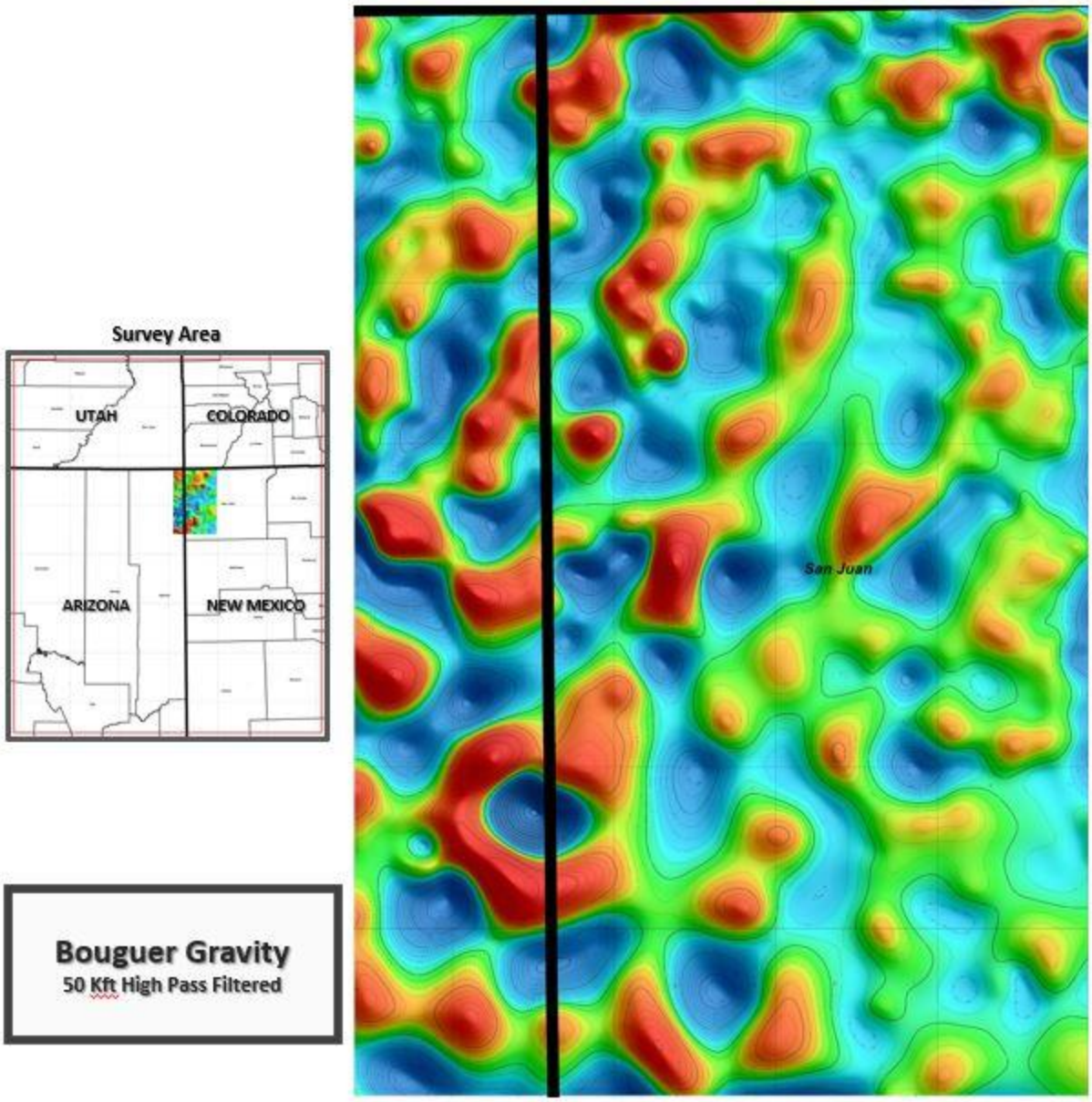


Figure 42. 50 kilo-feet (Kft) wavelength high pass filter of the Bouguer gravity data made from Earthfield's proprietary North American Gravity Compilation. High pass filtering is useful in removing long wavelength anomalies from deep sources to enhance more subtle anomalies arising from shallower sources. The high-pass filtered Bouguer gravity data is used qualitatively to help define basement faults and trends calculated using Werner deconvolution.

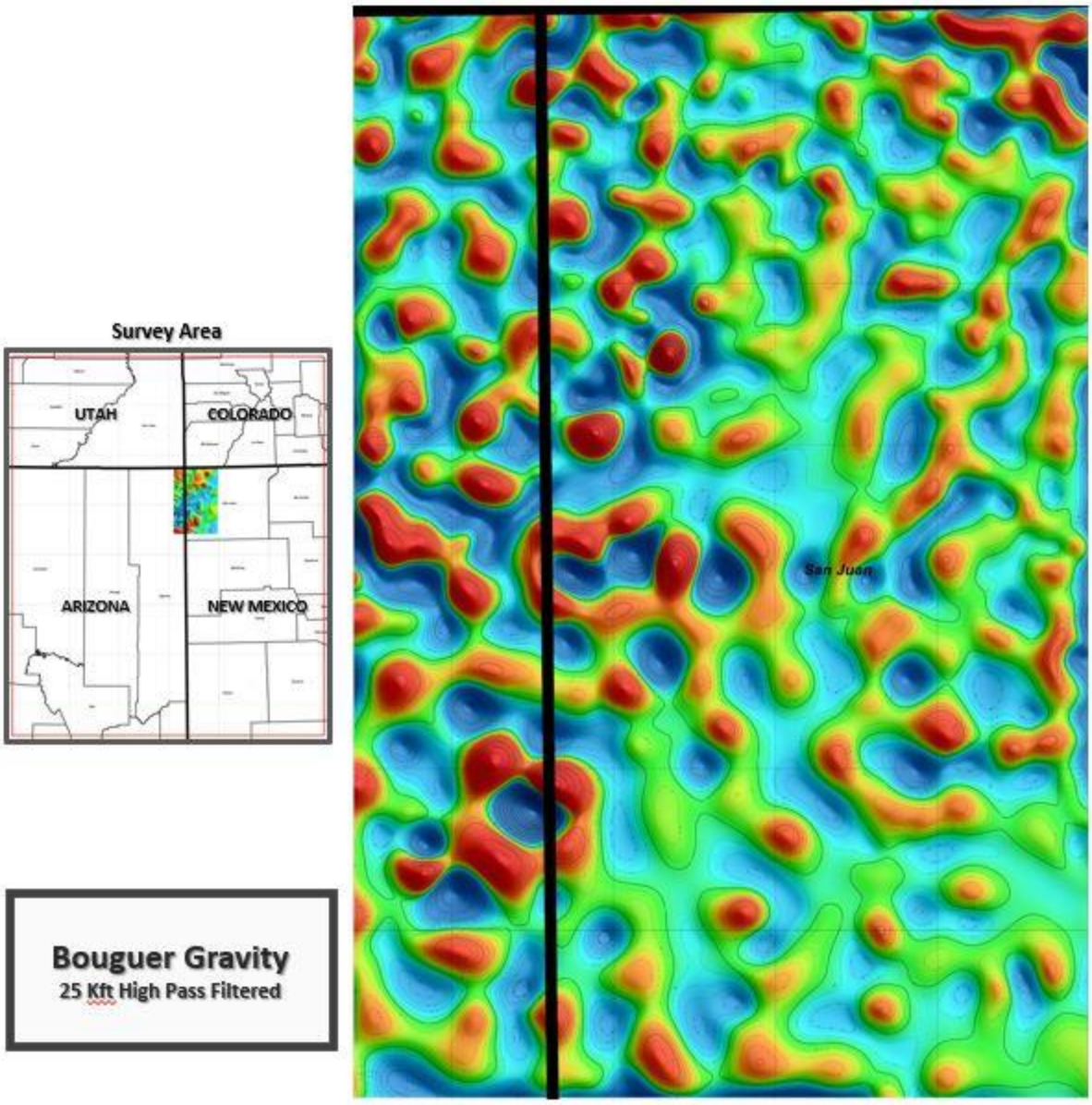


Figure 43. 25 kilo-feet (Kft) wavelength high pass filter of the Bouguer gravity data made from Earthfield's proprietary North American Gravity Compilation. High pass filtering is useful in removing long wavelength anomalies from deep sources to enhance more subtle anomalies arising from shallower sources. The high-pass filtered Bouguer gravity data is used qualitatively to help define basement faults and trends calculated using Werner deconvolution.

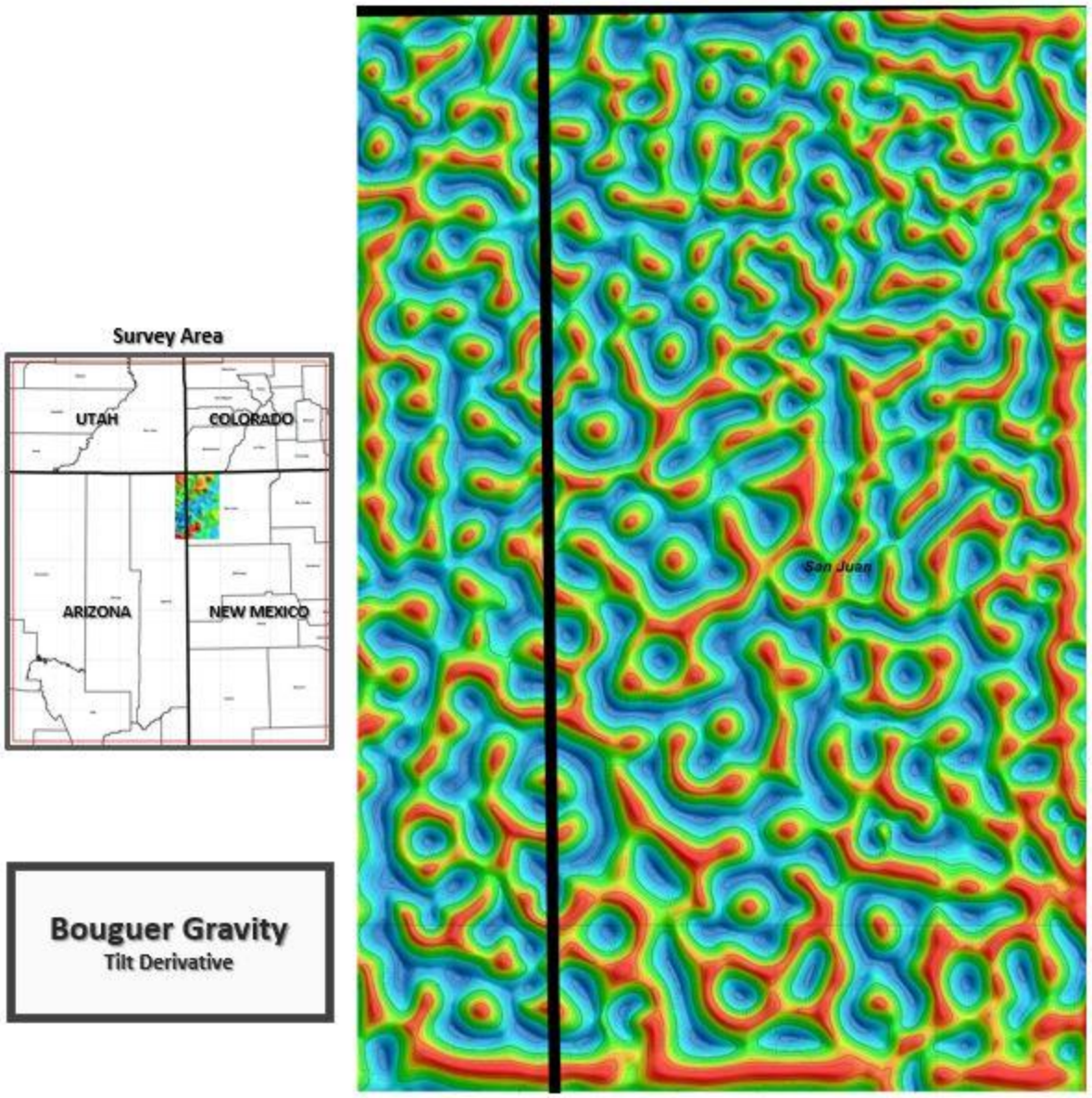


Figure 44. Tilt Derivative of the Bouguer gravity data made from Earthfield's proprietary North American Gravity Compilation. Tilt derivative enhances anomalies associated with lateral boundaries, i.e. lithologic changes and/or fractures & fault zones. The tilt derivative and high-pass filtered Bouguer gravity data are used qualitatively to help define basement faults and trends calculated using Werner deconvolution.

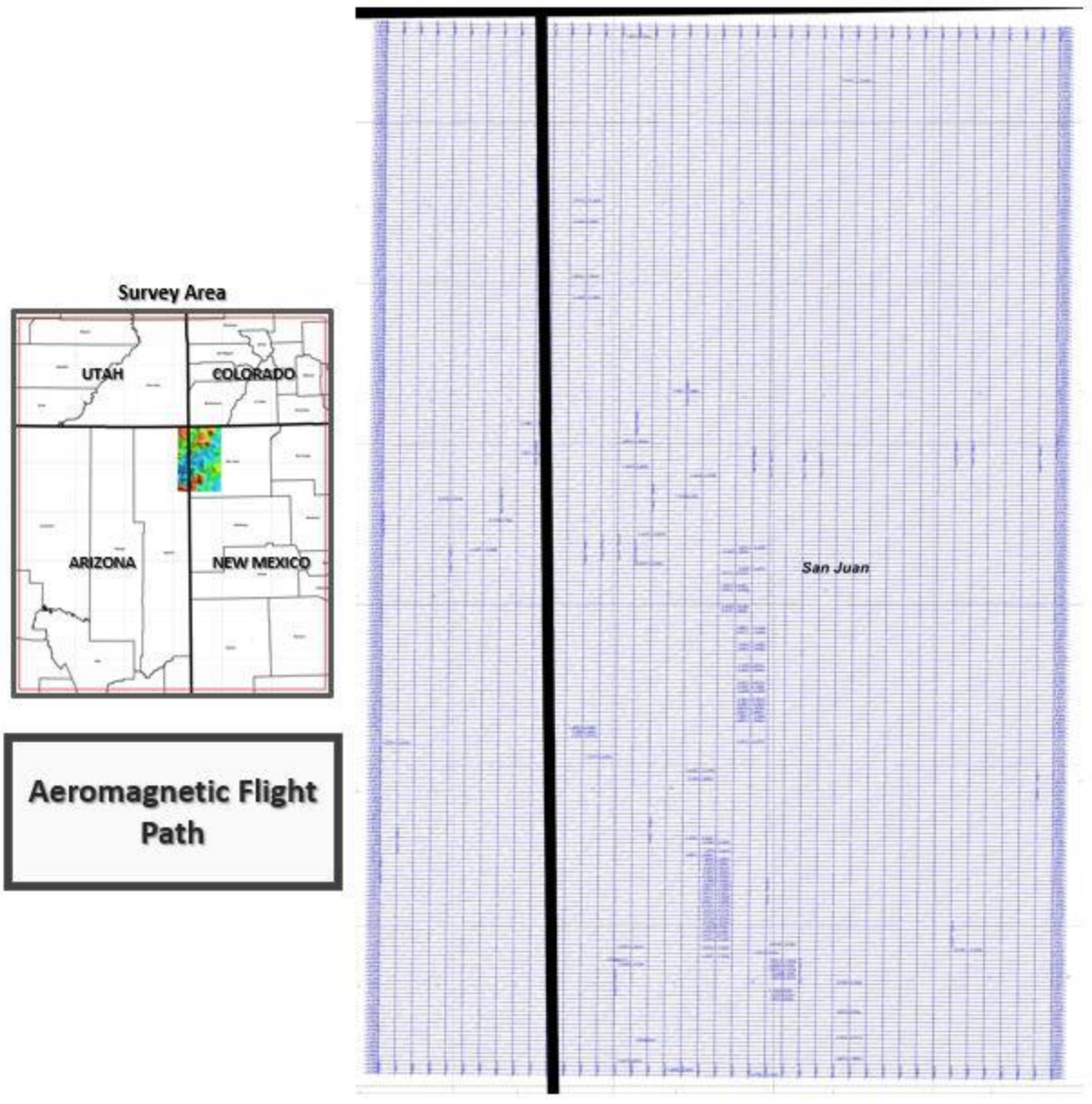


Figure 45. High-Resolution magnetic survey flight path map.

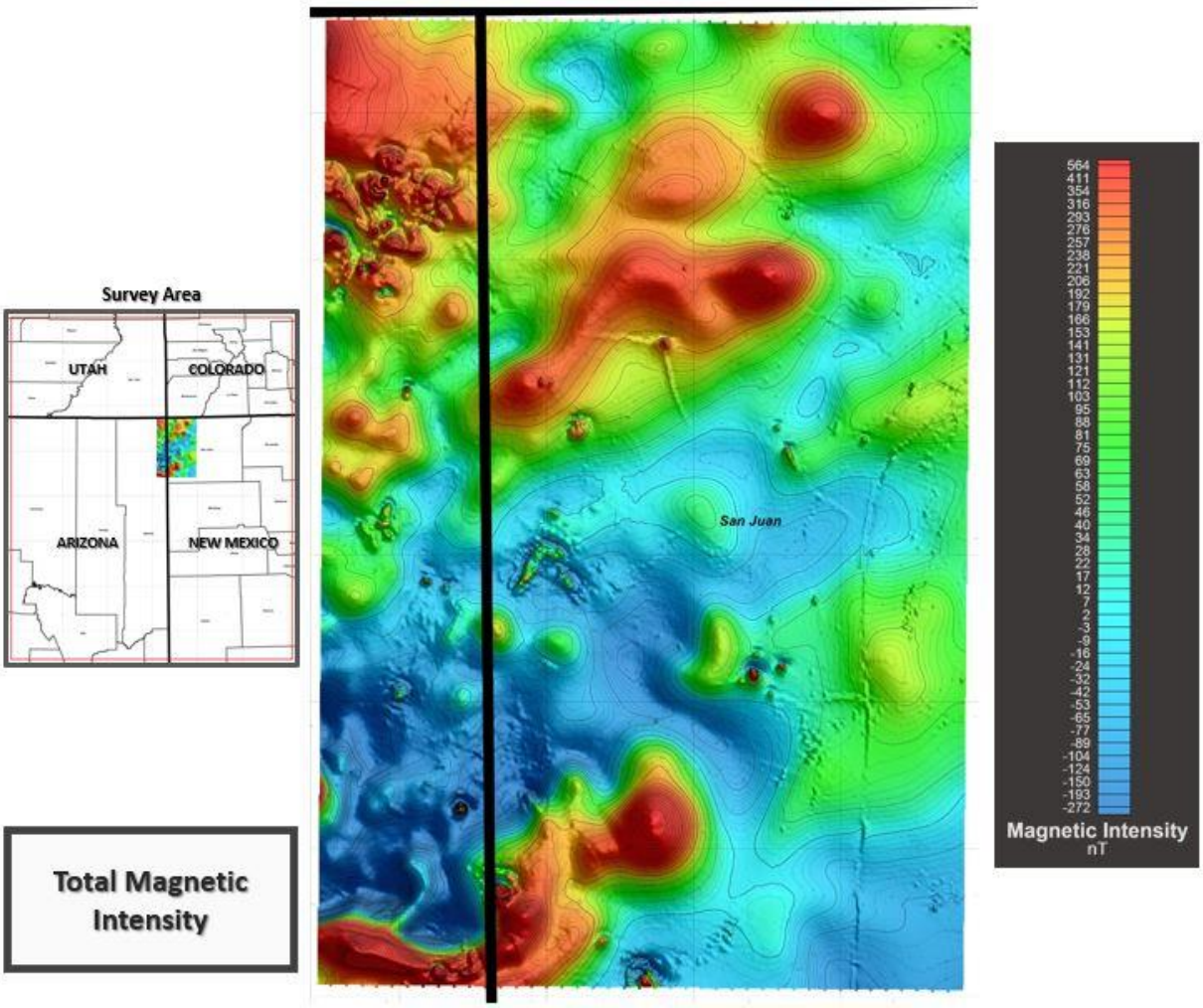


Figure 46. Total Magnetic Intensity map made from the High-Resolution magnetic survey data.

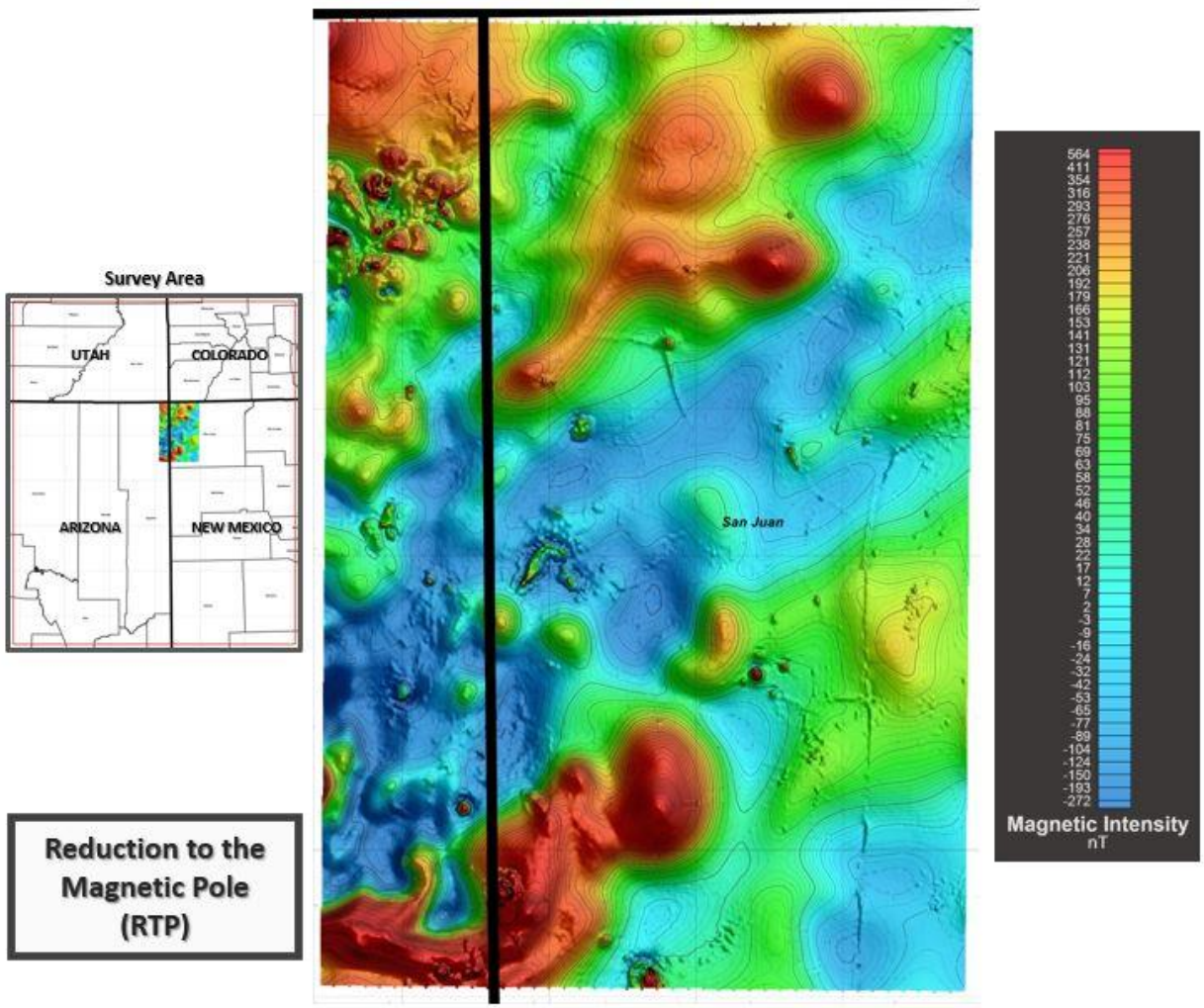


Figure 47. Reduction-to-the-Pole (RTP) map of the Total Magnetic Intensity data from the High-Resolution magnetic survey data. The Reduction-to-the-Pole technique removes the Earth's magnetic inclination/declination effects from the data, and shifts the magnetic anomalies directly over causative bodies.

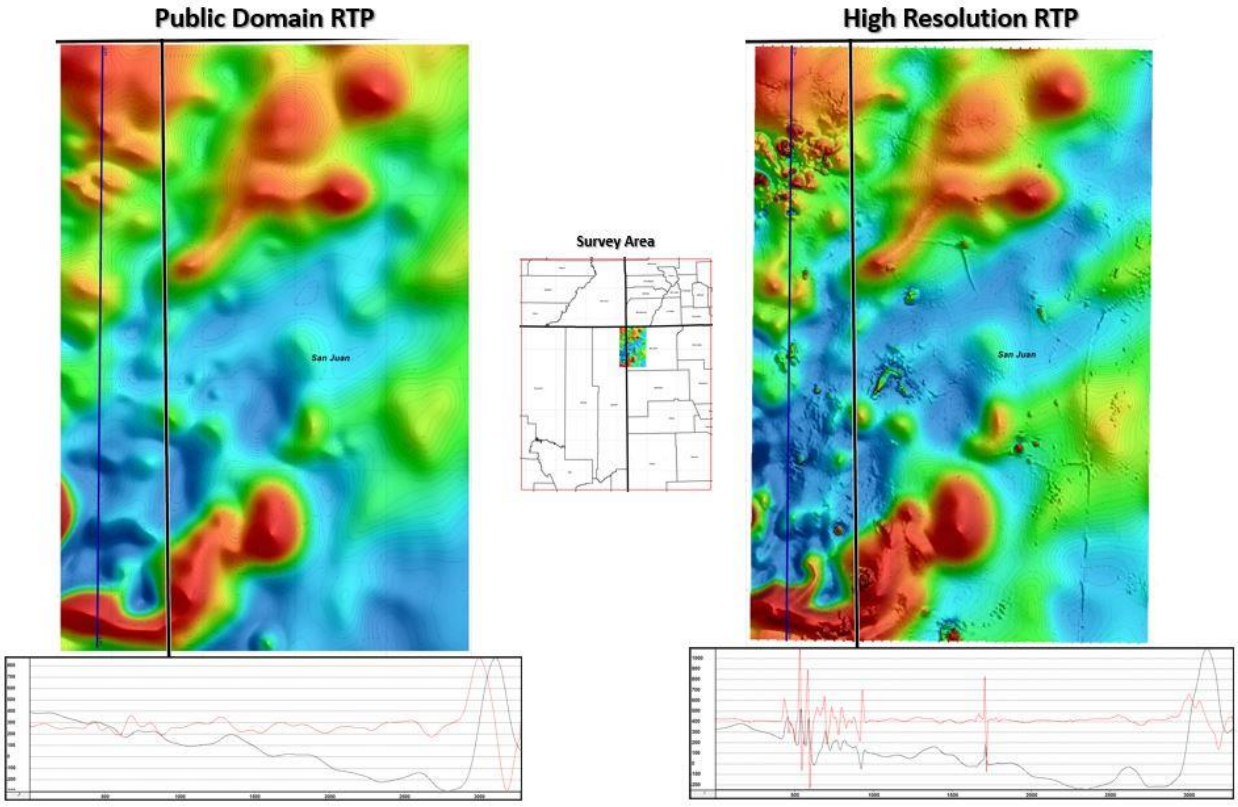


Figure 48. Comparison of the magnetic RTP data from a regional 3mi x 9mi grid of magnetic grid (left image), versus the RTP from the High-Resolution magnetic survey (right image). The level of resolution is dramatically higher for the new survey data, allows for the detailed mapping of basement and small igneous intrusions.

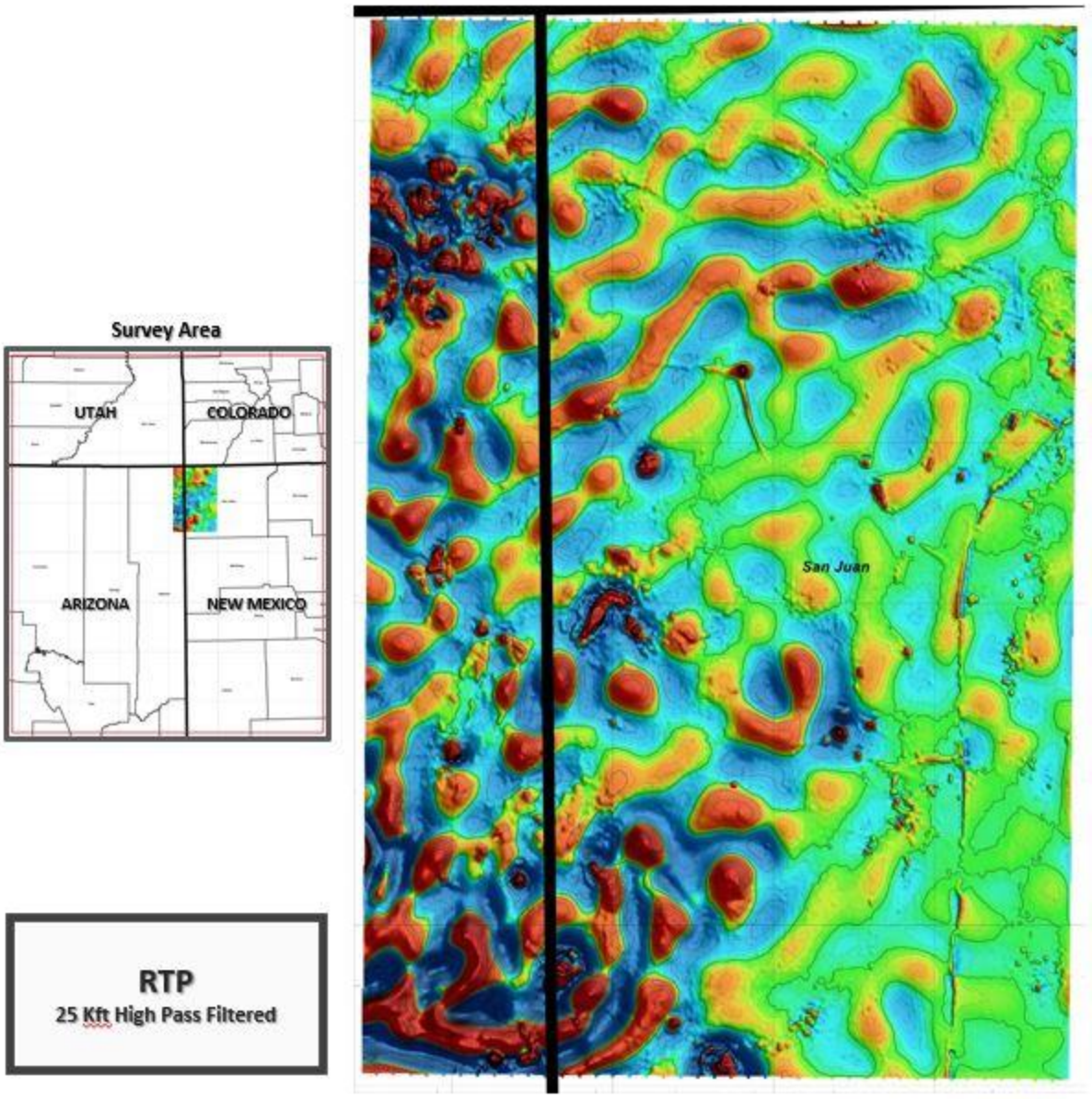


Figure 49. 25 kilo-feet (Kft) wavelength high pass filter of the High-Resolution magnetic RTP survey data. High pass filtering is useful in removing long wavelength anomalies from deep sources to enhance more subtle anomalies arising from shallower sources. The high-pass filtered RTP magnetic data is used qualitatively to help define basement faults and trends calculated using Werner deconvolution.

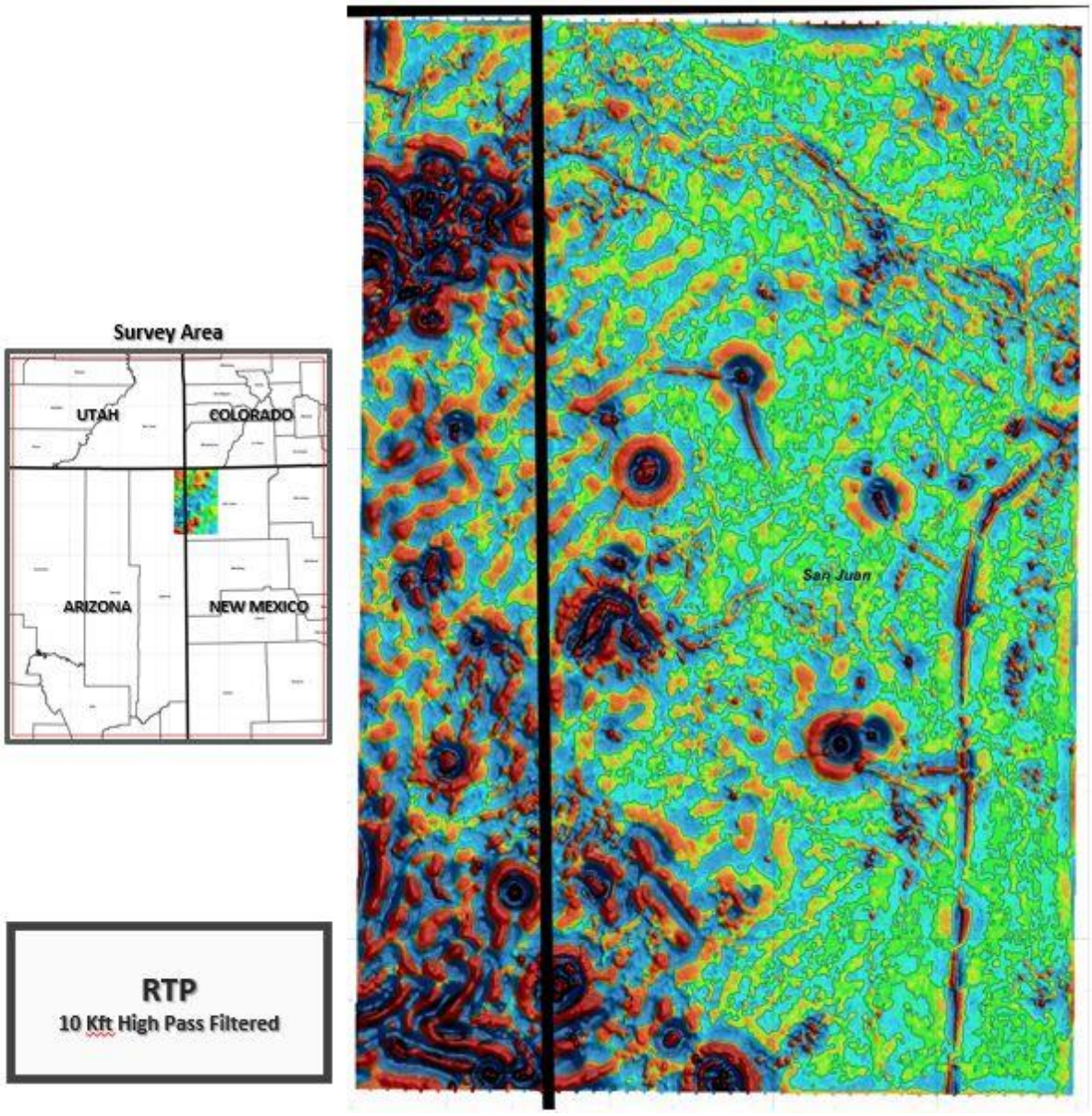


Figure 50. 10 kilo-feet (Kft) wavelength high pass filter of the High-Resolution magnetic RTP survey data. High pass filtering is useful in removing long wavelength anomalies from deep sources to enhance more subtle anomalies arising from shallower sources. The high-pass filtered RTP magnetic data is used qualitatively to help define basement faults and trends calculated using Werner deconvolution.

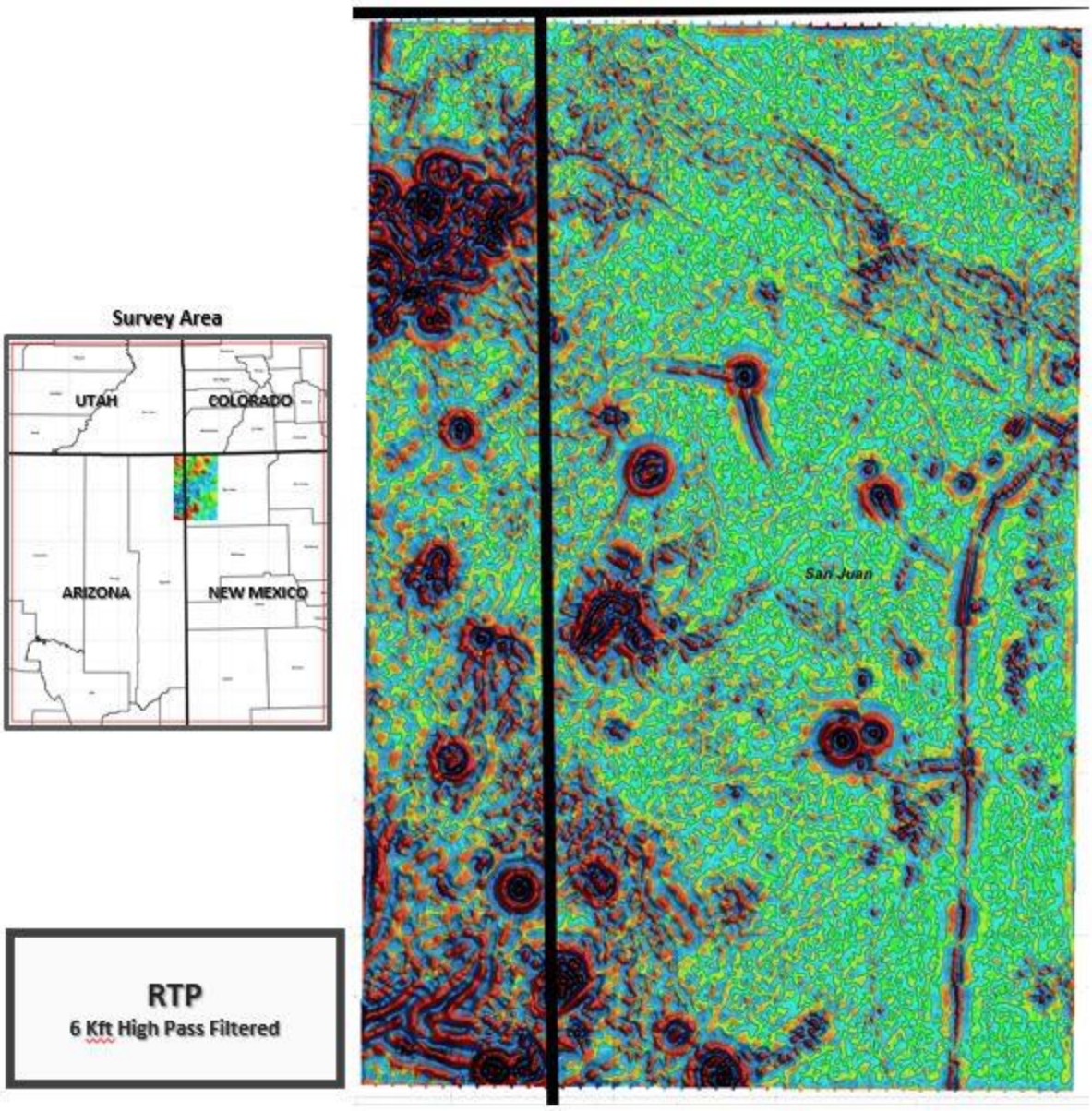


Figure 51. 6 kilo-feet (Kft) wavelength high pass filter of the High-Resolution magnetic RTP survey data. High pass filtering is useful in removing long wavelength anomalies from deep sources to enhance more subtle anomalies arising from shallower sources. The high-pass filtered RTP magnetic data is used qualitatively to help define basement faults and trends calculated using Werner deconvolution.

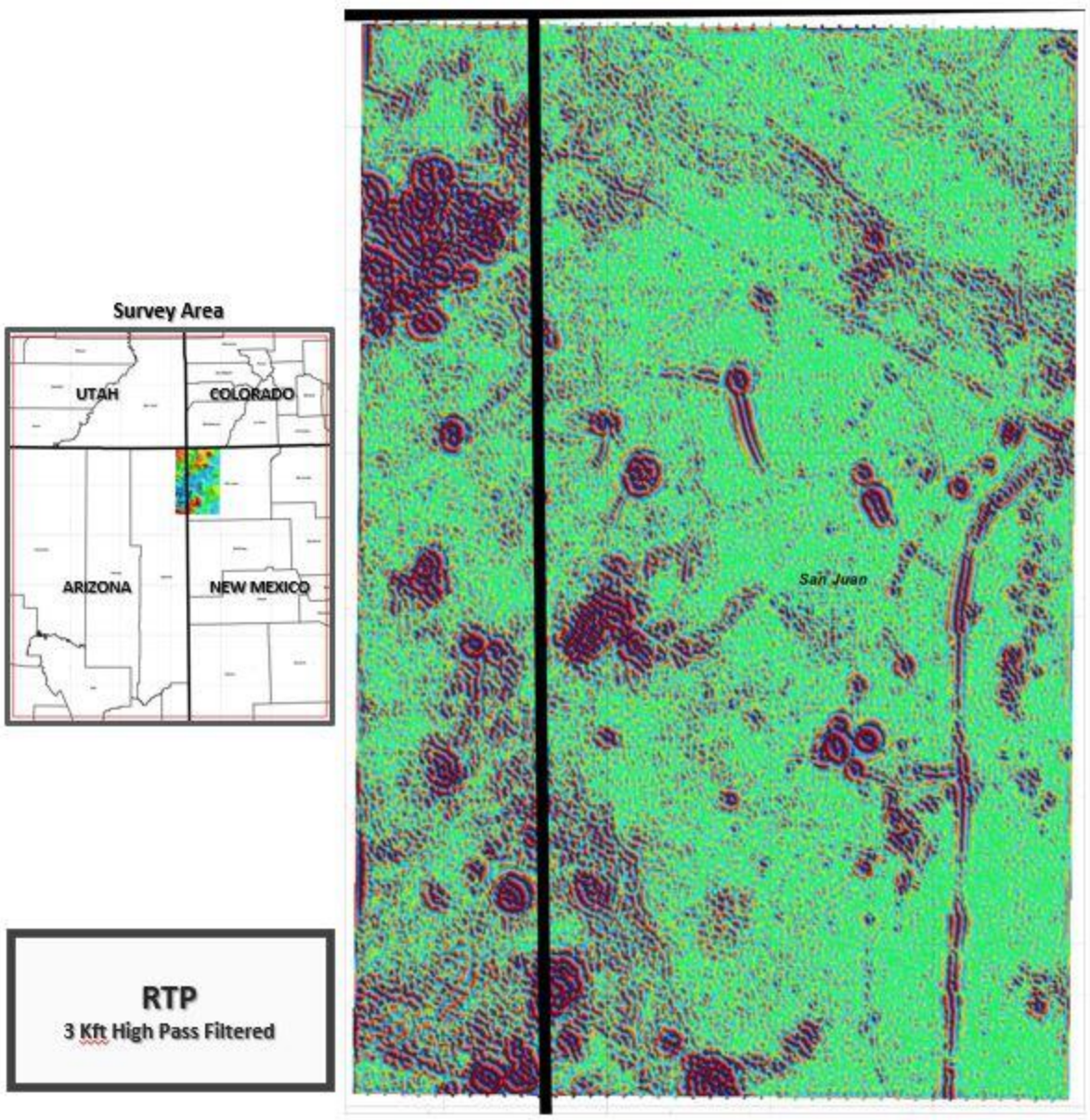


Figure 52. 3 kilo-feet (Kft) wavelength high pass filter of the High-Resolution magnetic RTP survey data. High pass filtering is useful in removing long wavelength anomalies from deep sources to enhance more subtle anomalies arising from shallower sources. The high-pass filtered RTP magnetic data is used qualitatively to help define basement faults and trends calculated using Werner deconvolution.

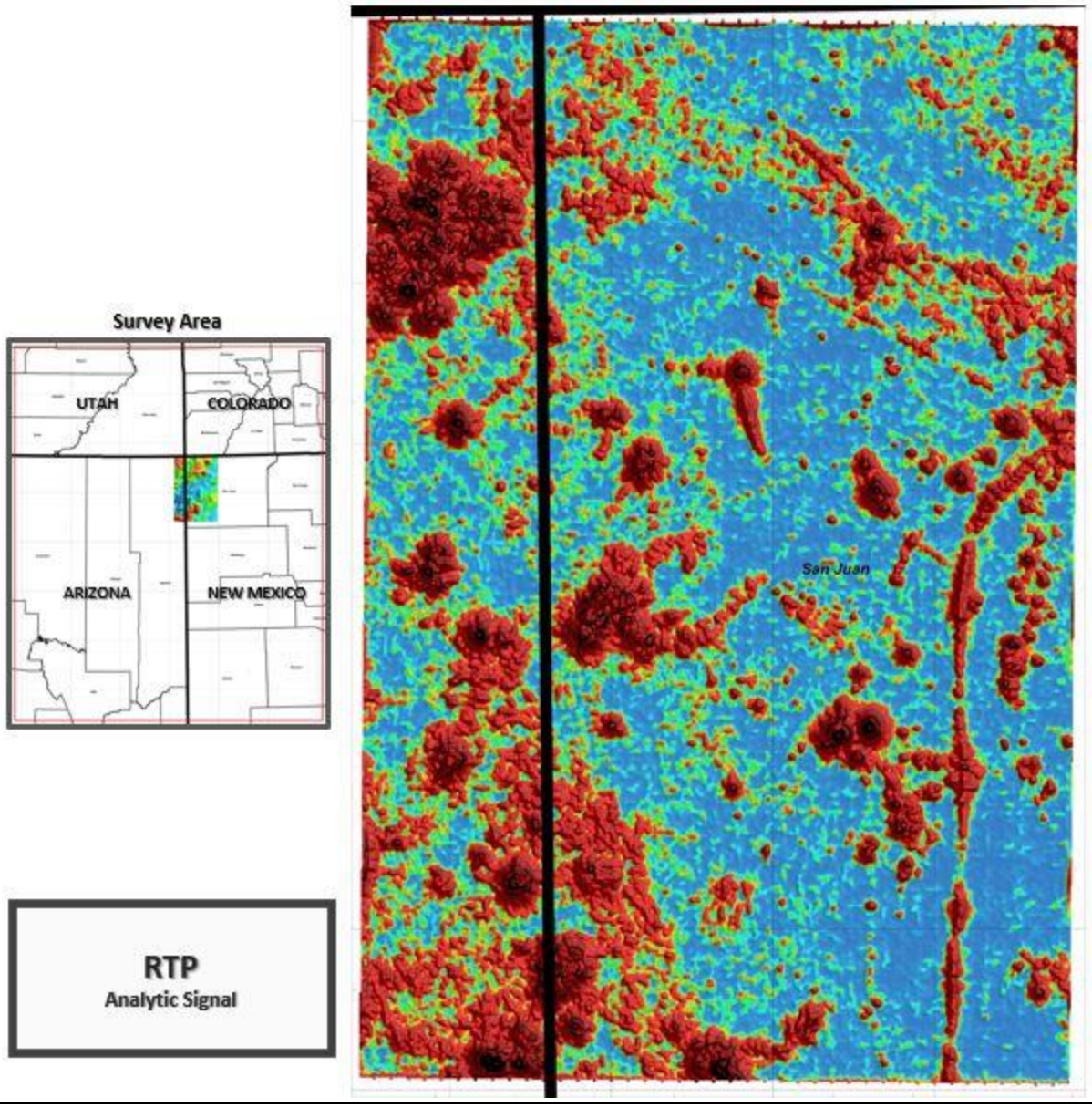


Figure 53. RTP Analytic Signal Map from the High-Resolution magnetic RTP survey data. The Analytic Signal technique enhances magnetic anomalies from subtle sources, at the expense of longer wavelength magnetic anomalies arising from deeper sources. The RTP Analytic signal map helps sharpen and focus over shallow bodies and thus better identifies shallow intrusive bodies.

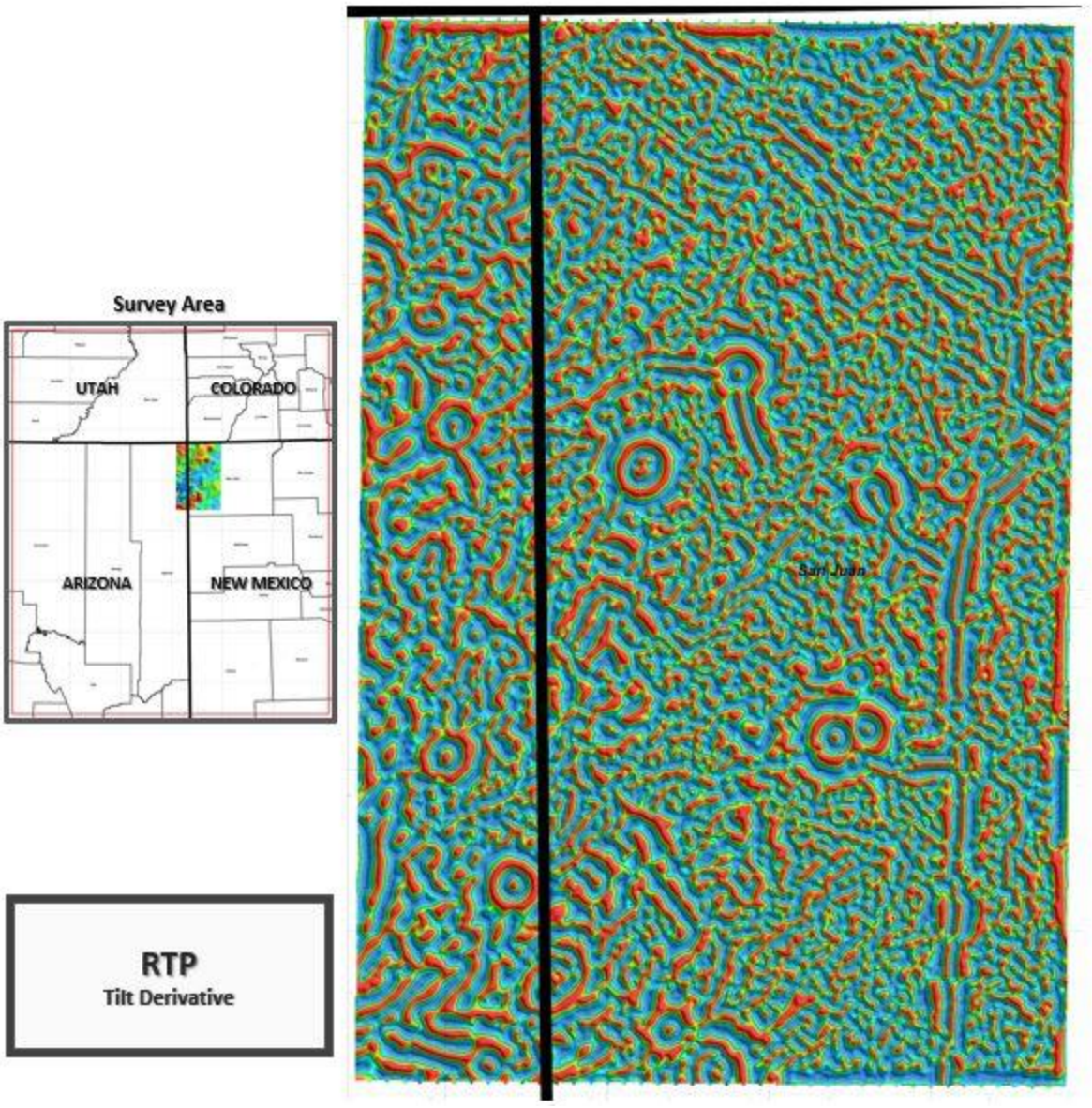


Figure 54. Tilt Derivative of the magnetic RTP data from the High-Resolution magnetic survey data. Tilt derivative enhances anomalies associated with lateral boundaries, i.e. lithologic changes and/or fractures & fault zones. The tilt derivative and the high-pass filtered RTP magnetic data are used qualitatively to help define basement faults and trends calculated using Werner deconvolution.

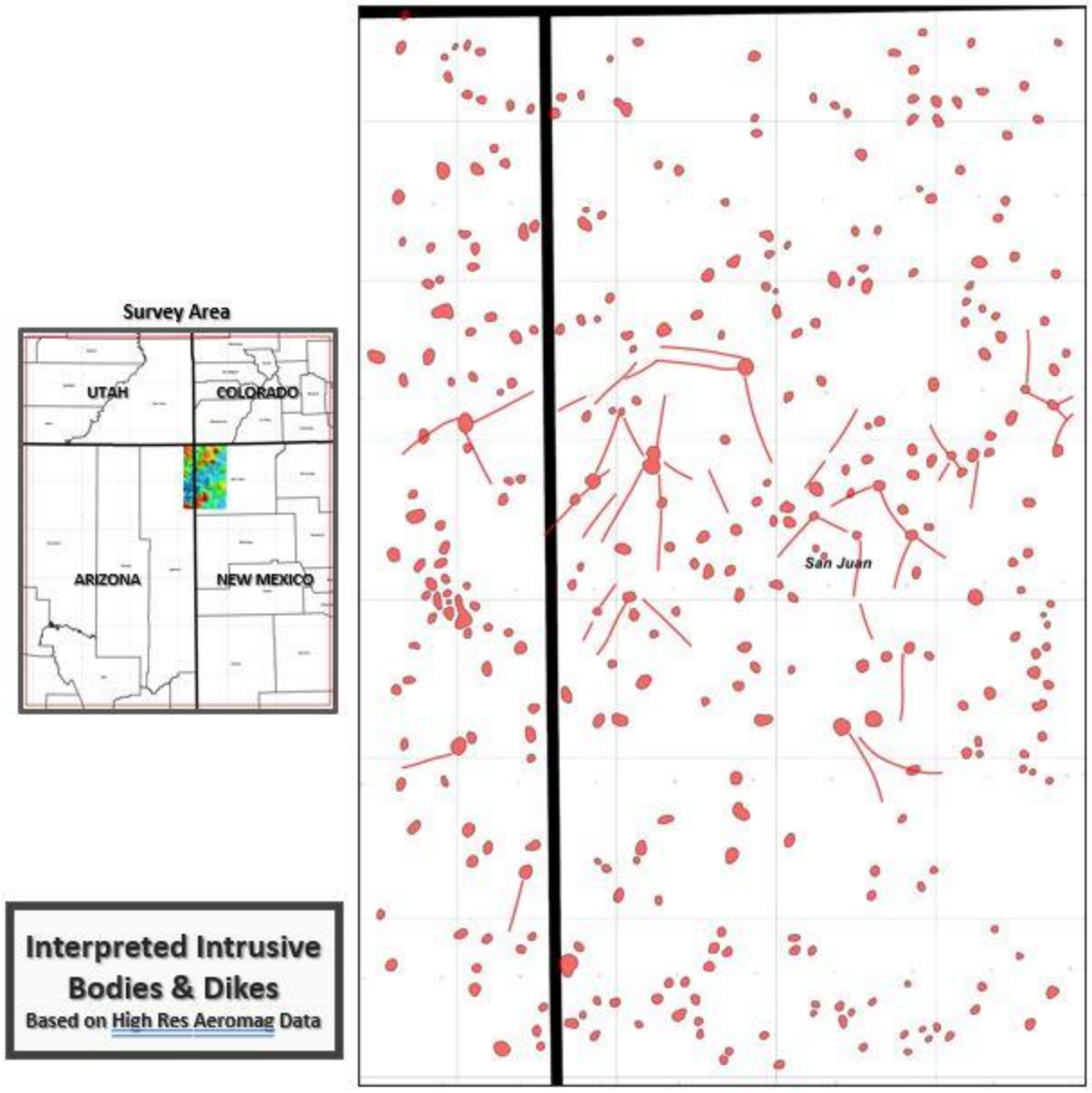


Figure 55. Locations of Igneous plutons, dikes, and sills interpreted from the High-Resolution magnetic survey data. These bodies have been identified using Werner Deconvolution depth estimation profiles, and from various filters and derivative maps of the magnetic data.

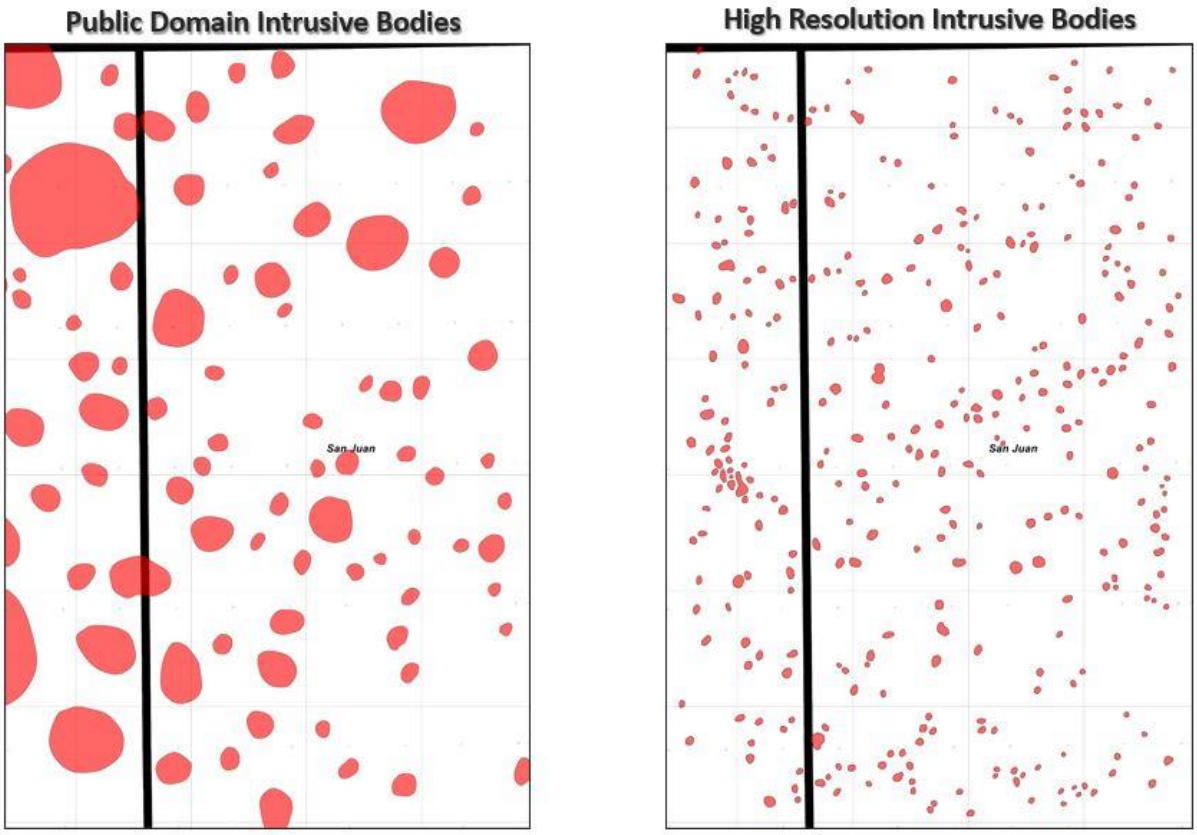


Figure 56. Comparison of locations of Igneous plutons, dikes, and sills (left image) interpreted from the regional 3mi x 9 mi grid of magnetic lines previously acquired and from the High-Resolution magnetic survey data (right image). The ¼ mile x 1 mile spacing of the new survey data has allowed the mapping of much smaller, more discrete igneous bodies that wasn't possible with the regional magnetic data.

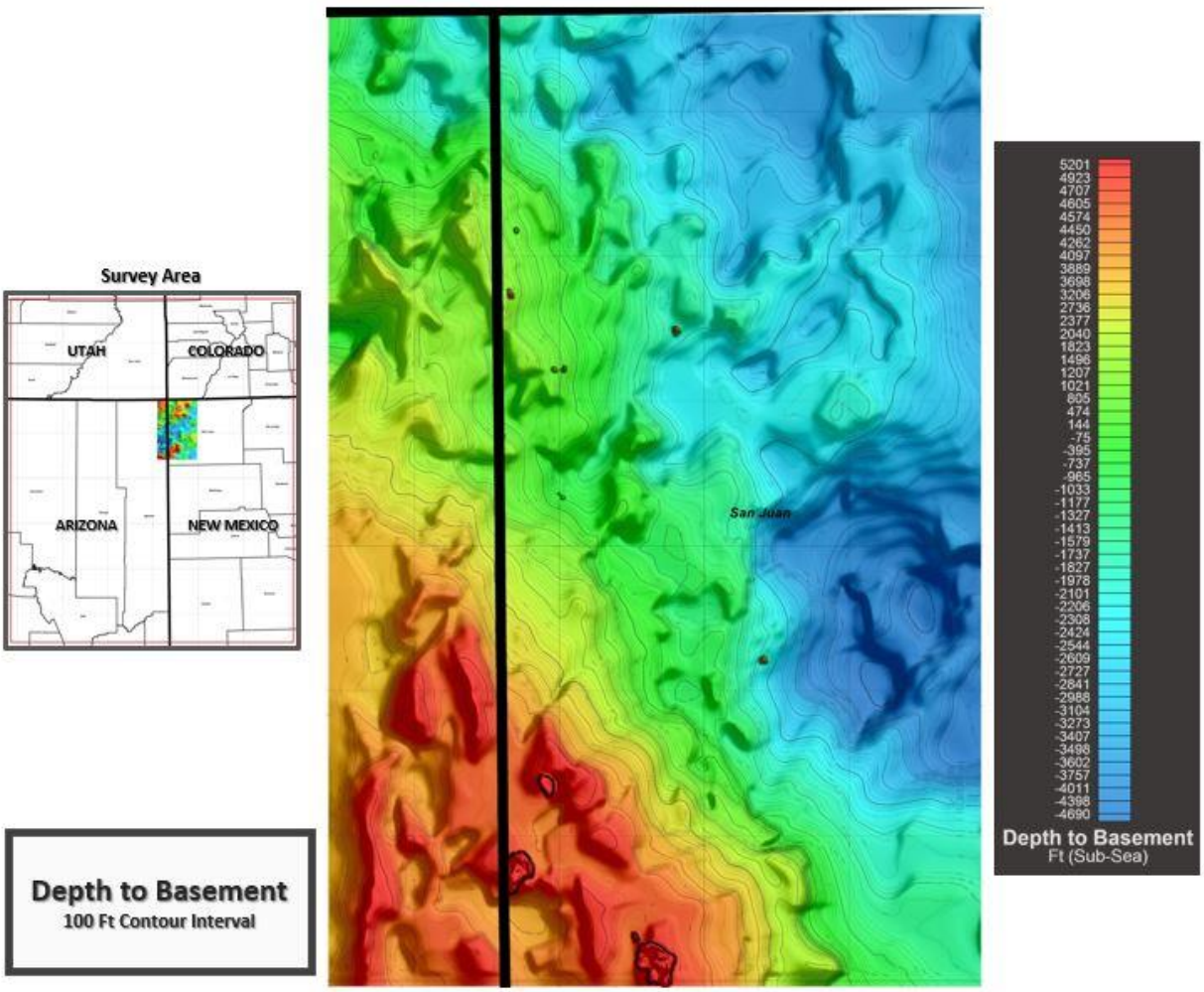


Figure 57. Interpreted Depth to Basement Map (without faults) made from the analysis of the High-Resolution magnetic survey data via quantitative depth to source analysis using Earthfield's proprietary Werner Deconvolution software.

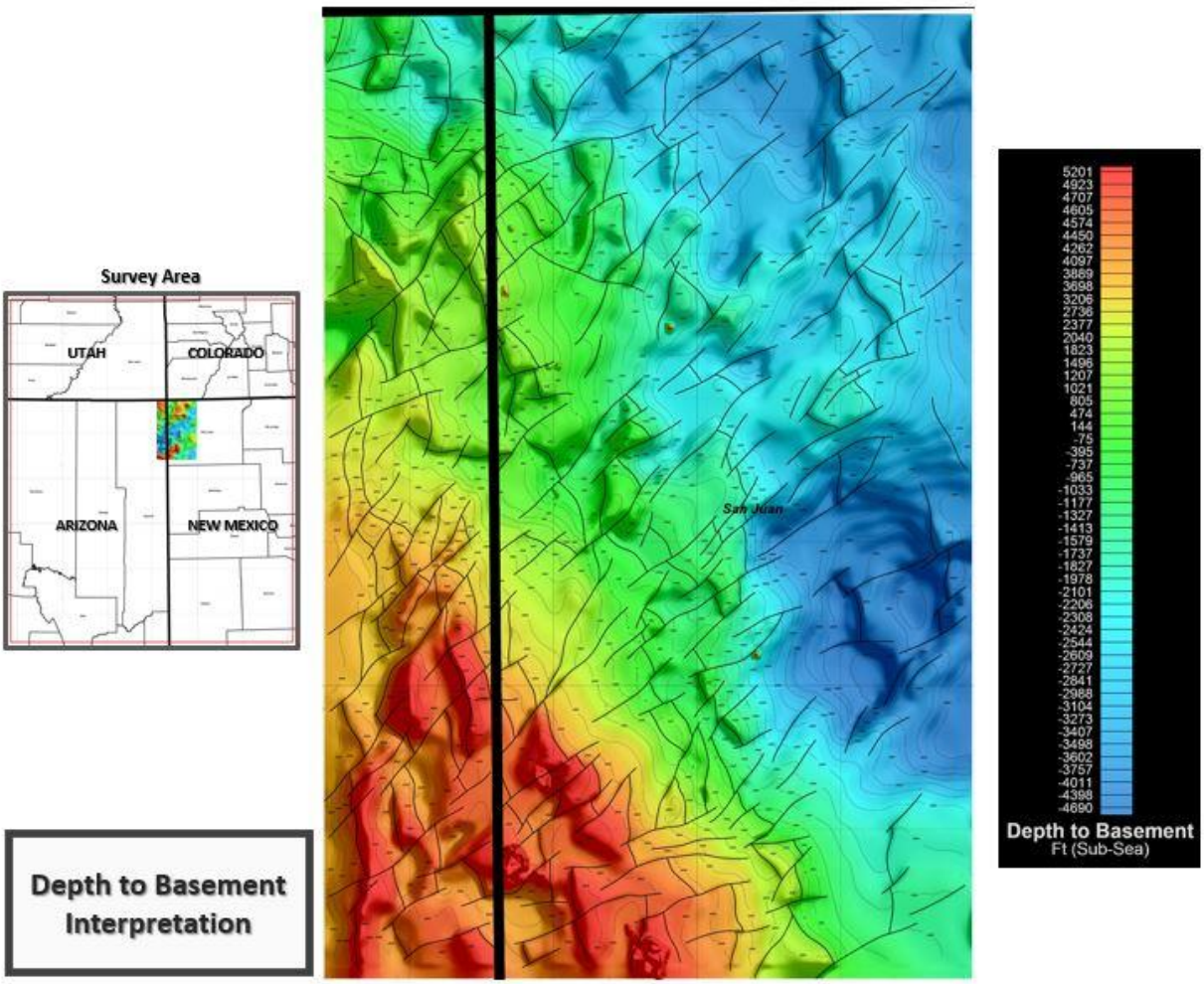


Figure 58. Interpreted Depth to Basement Map (with faults) made from the analysis of the High-Resolution magnetic survey data via quantitative depth to source analysis using Earthfield's proprietary Werner Deconvolution software.

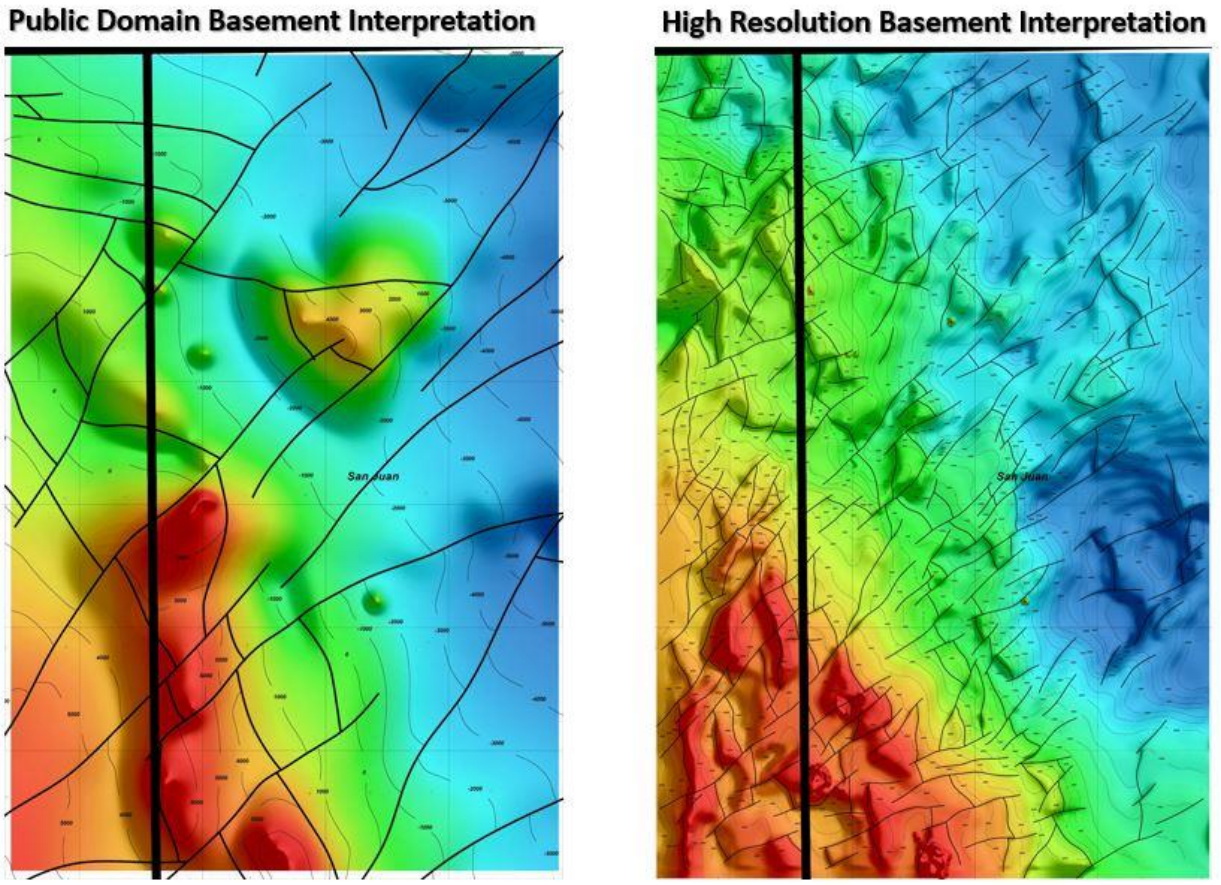


Figure 59. Comparison of Interpreted Depth to Basement surfaces interpreted from the regional 3mi x 9 mi grid of magnetic lines previously acquired (left image) and the detailed basement surface interpreted from the High-Resolution magnetic survey data (right image). The ¼ mile x 1 mile spacing of the new survey data has allowed the mapping of much smaller, more discrete structures/faults/fractures that wasn't possible with the regional magnetic data.

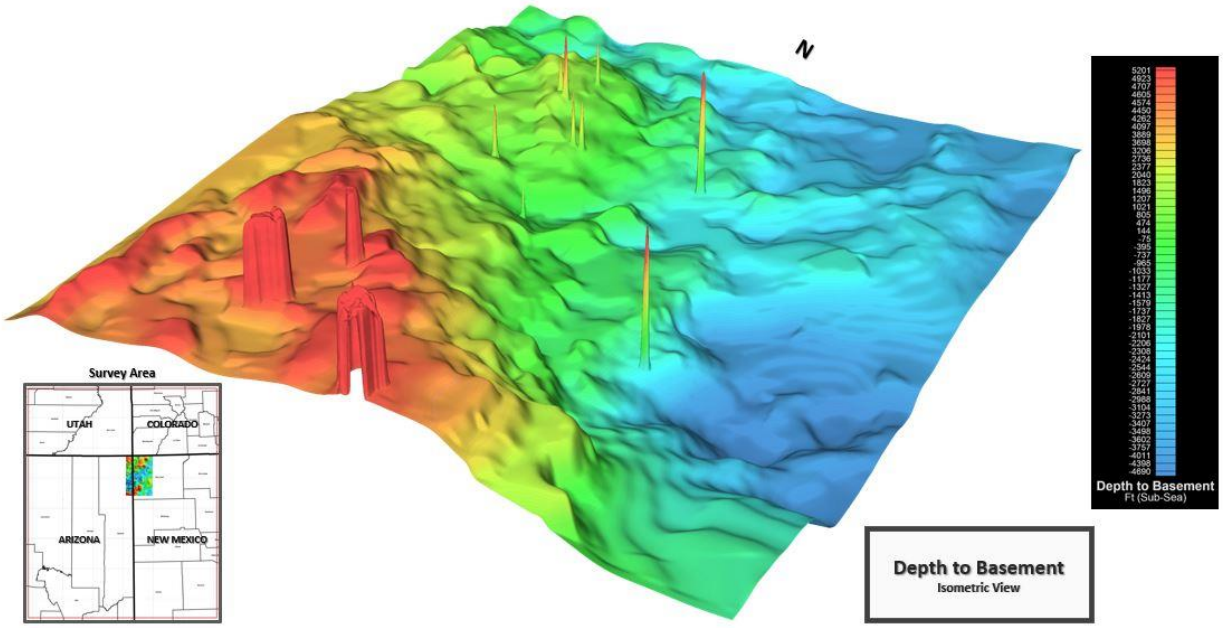


Figure 60. Isometric view (north is to the top of the image) of the interpreted Depth to Basement Map made from the analysis of the High-Resolution magnetic survey data via quantitative depth to source analysis using Earthfield's proprietary Werner Deconvolution software.

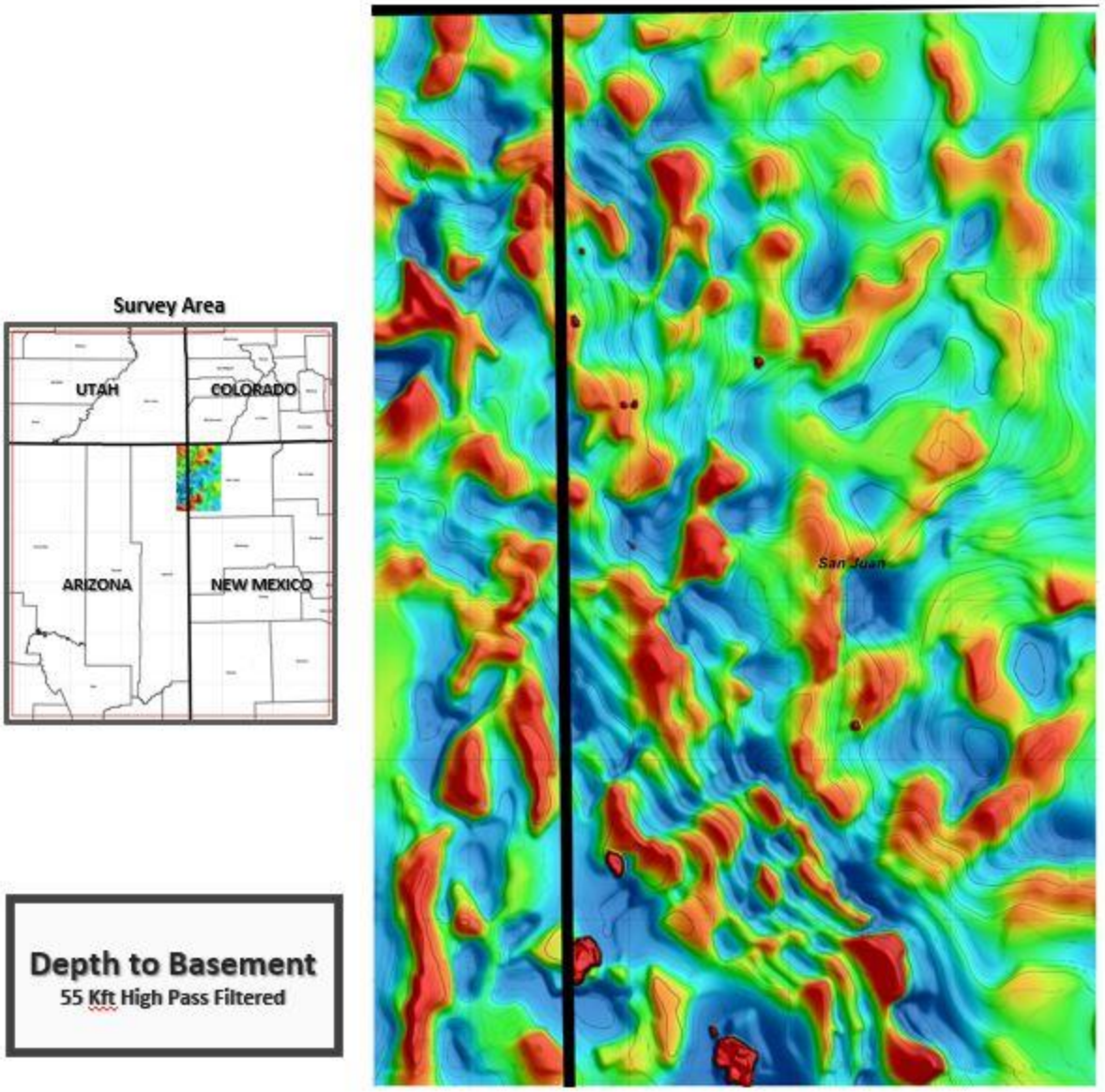


Figure 61. “Flattened” Interpreted Depth to Basement Map made from the analysis of the High-Resolution magnetic survey data via quantitative depth to source analysis using Earthfield’s proprietary Werner Deconvolution software. The interpreted basement surface has been high pass filtered (55 Kft wavelength), to remove regional dip from the basement surface, and to enhance subtle structures on the basement surface that are somewhat hidden on the original basement surface due to regional dip.

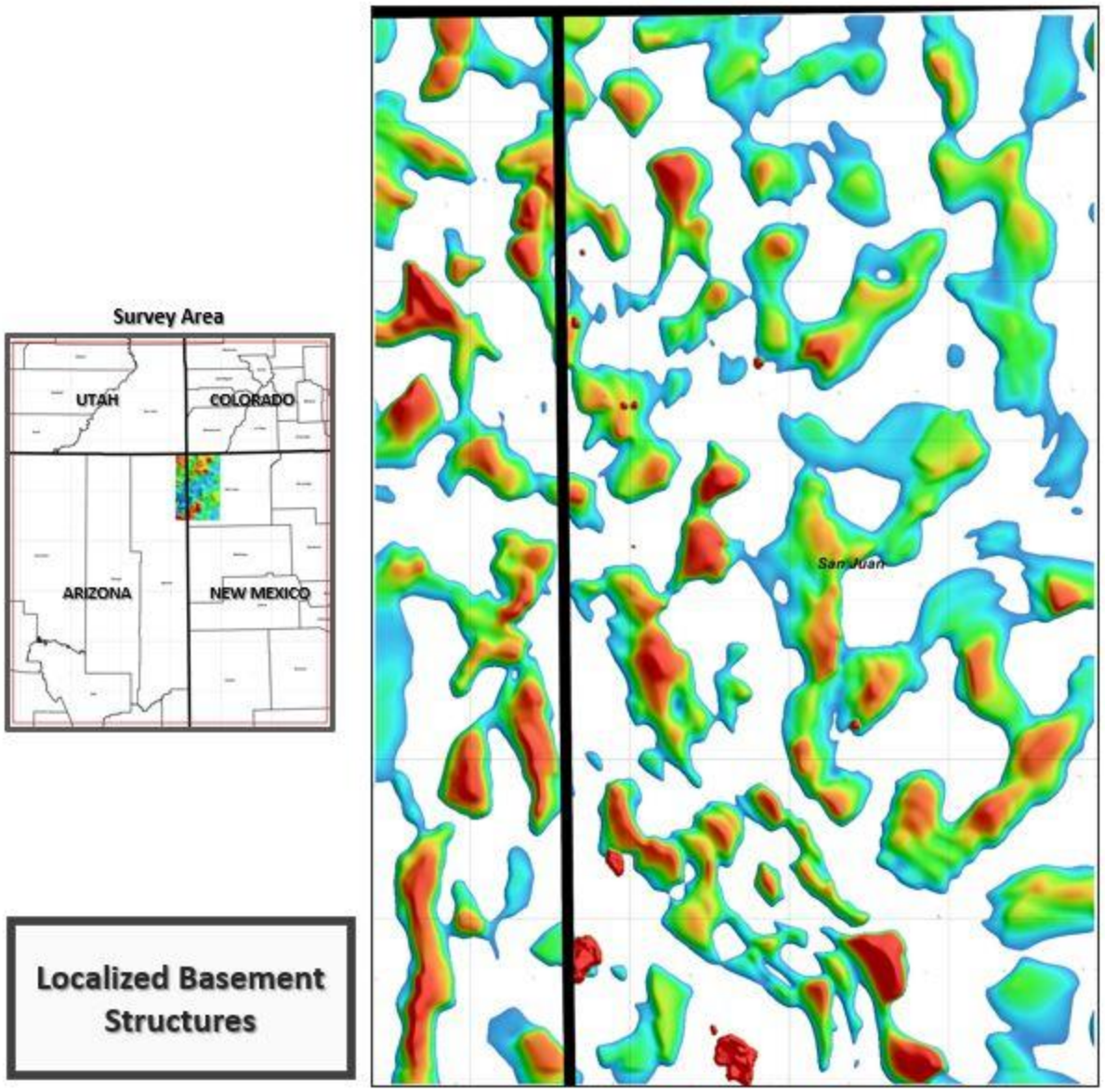


Figure 62. Localized Basement Structure Map. This map has been made by using the "Flattened" Interpreted Depth to Basement Map made from the analysis of the High-Resolution magnetic survey data via quantitative depth to source analysis using Earthfield's proprietary Werner Deconvolution software, and only displaying the local basement highs by removing local basement structural lows. The interpreted basement surface has been initially high pass filtered (55 Kft wavelength), to remove regional dip from the basement surface, and to enhance subtle structures on the basement surface that are somewhat hidden on the original basement surface due to regional dip.

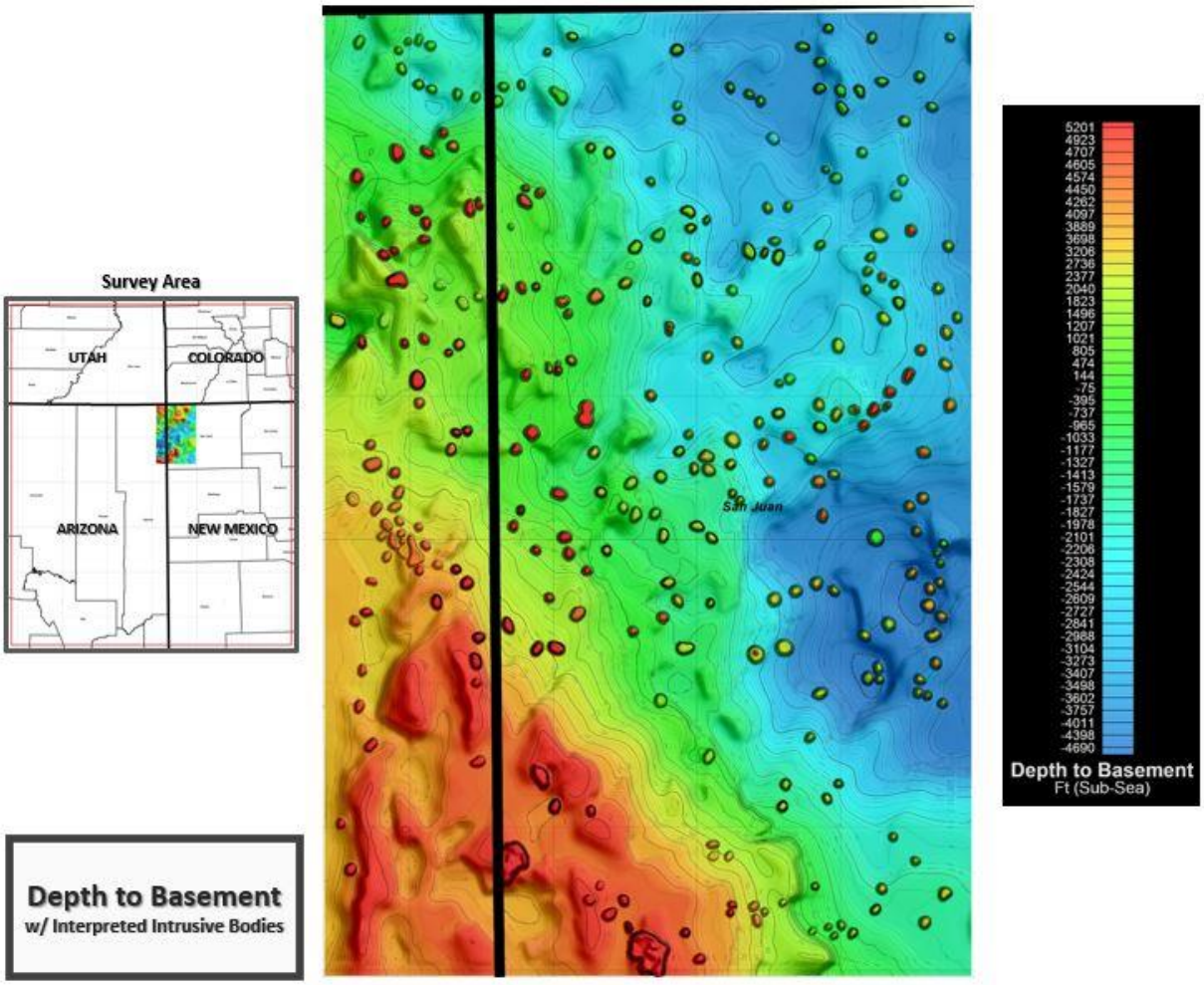


Figure 63. Interpreted Depth to Basement/younger Igneous Intrusive Bodies. This map was produced via the analysis of Werner Deconvolution profiles of magnetic profiles collected during the High-Resolution magnetic data survey. The profiles were analyzed twice. The first was to identify the Precambrian basement surface, and the second to identify the locations of younger, igneous intrusive bodies in the area. The products were merged to display the basement surface, and areas where younger intrusive bodies have breached the basement surface.

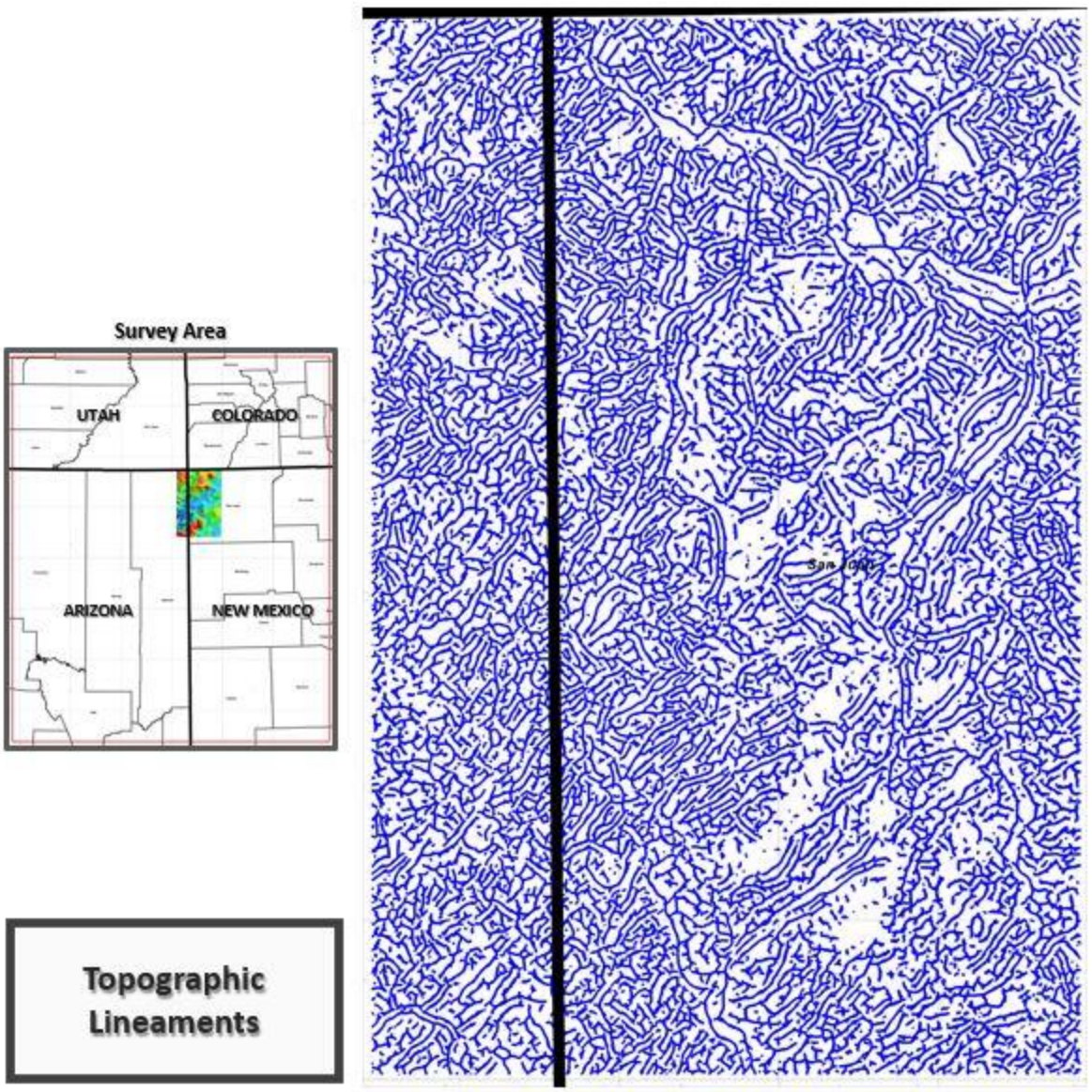


Figure 64. The Topographic Lineaments have been generated by using the gridded SRTM-30 topographic data. The topographic data were then used as input into Earthfield's proprietary Lineament Analysis software, that identifies sharp gradients in gridded data, and generates and connects lineaments at those positions.

These areas within the gridded data are associated with the sharpest gradients (slopes), and sharp slopes are often associated with faulting/fracturing.

These lineaments are considered quite detailed, as the underlying SRTM-30-meter topography data are considered to be excellent. These lineaments are used in the Lineament & Intersection Density map construction, are considered as ancillary data to the project.

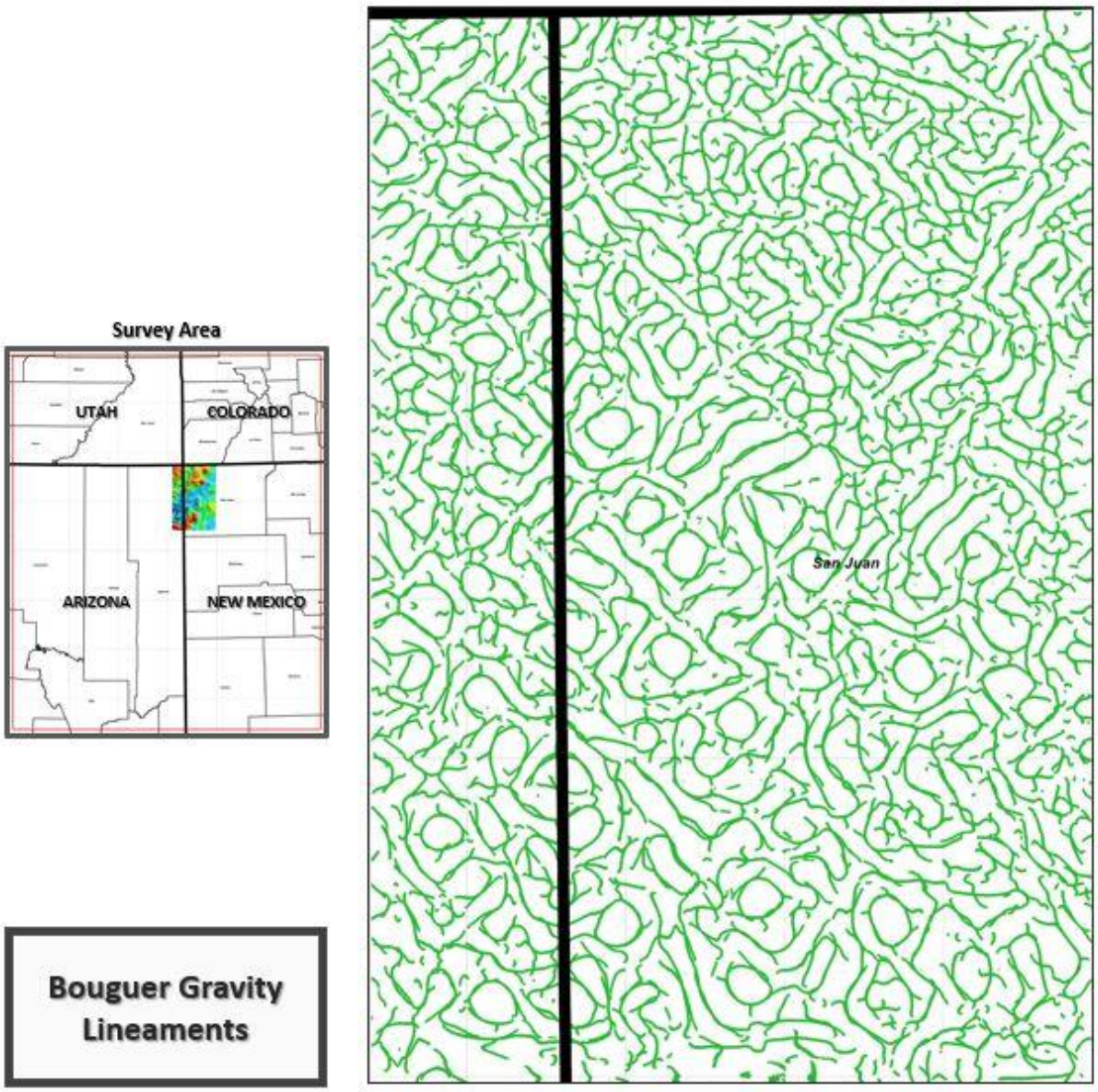


Figure 65. The Bouguer Gravity Lineaments have been generated by using the gridded Bouguer Gravity data. The Bouguer gravity data were then used as input into Earthfield's proprietary Lineament Analysis software, that identifies sharp gradients in gridded data, and generates and connects lineaments at those positions.

These areas within the gridded data are associated with the sharpest gradients (slopes), and sharp slopes are often associated with faulting/fracturing.

These lineaments are somewhat regional in nature (due to the underlying gravity data control), and can be greatly improved locally, with the addition of more detailed gravity data. These lineaments are used in the Lineament & Intersection Density map construction, are considered as ancillary data to the project.

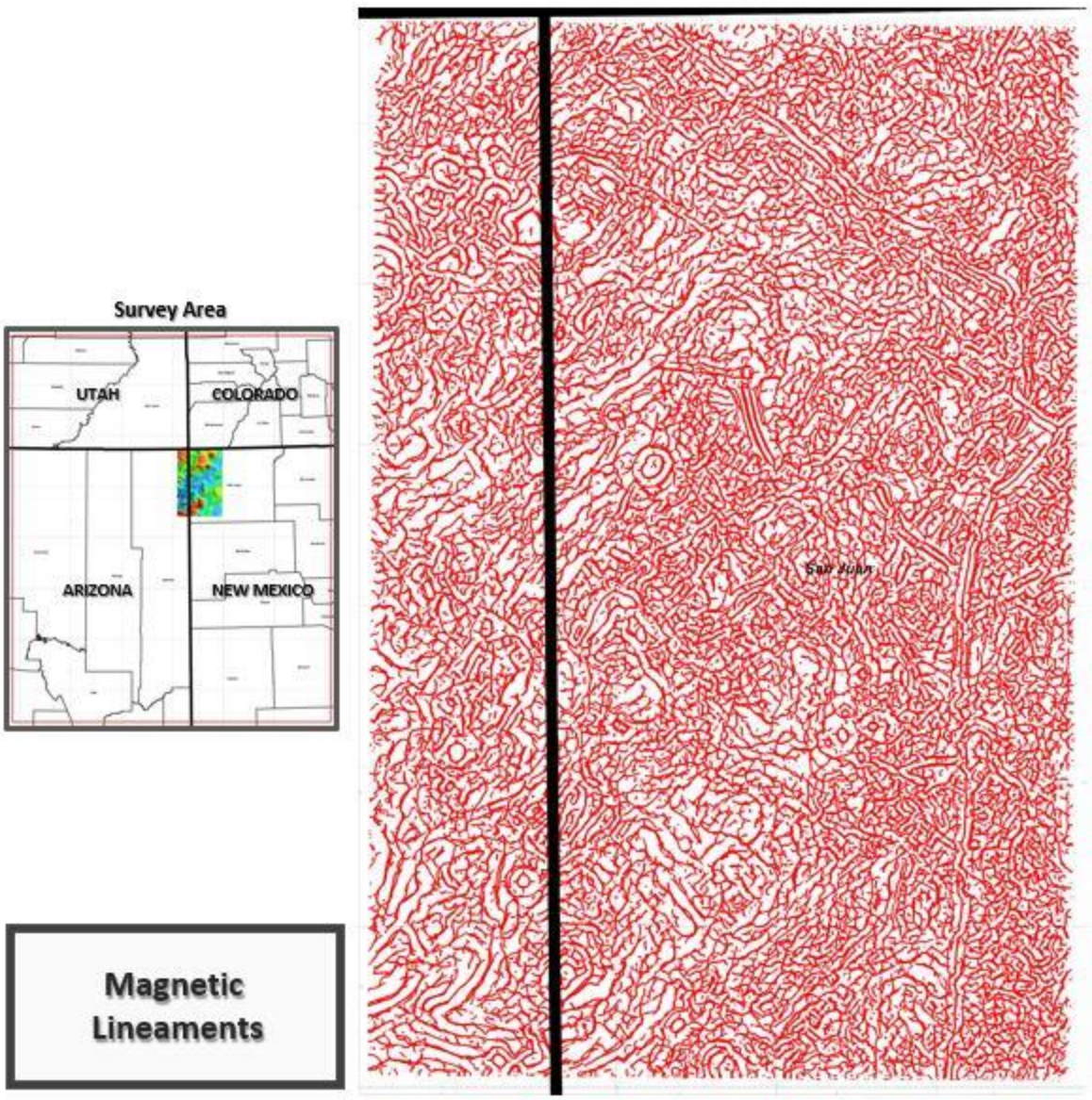


Figure 66. The RTP Lineaments have been generated by using the gridded RTP magnetic data. The RTP data were then used as input into Earthfield's proprietary Lineament Analysis software, that identifies sharp gradients in gridded data, and generates and connects lineaments at those positions.

These areas within the gridded data are associated with the sharpest gradients (slopes), and sharp slopes are often associated with faulting/fracturing.

These lineaments are used in the Lineament & Intersection Density map construction, are considered as ancillary data to the project.

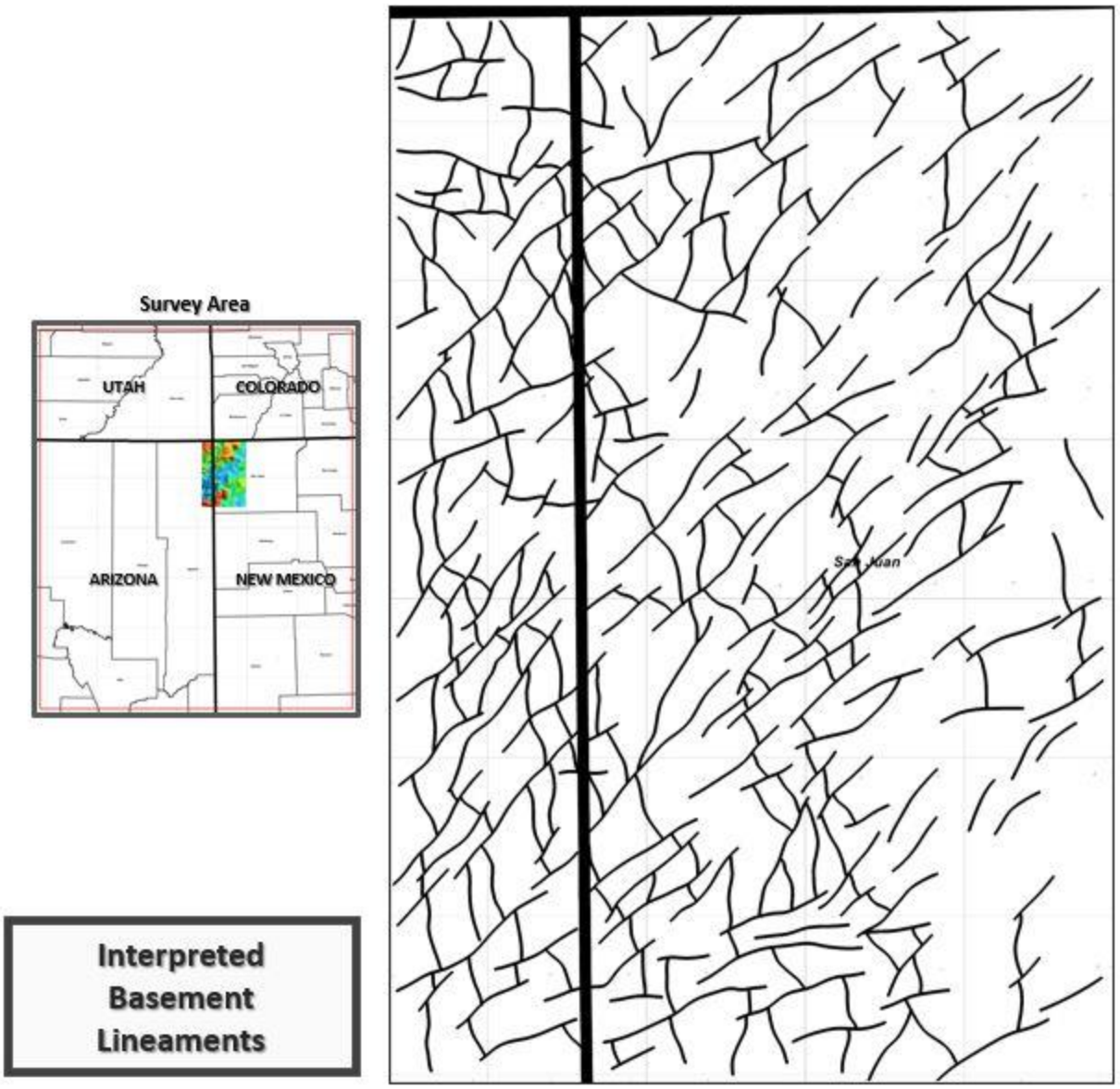


Figure 67. The Basement Lineaments have been generated during the Depth to Basement mapping, via the Werner Deconvolution analysis of the magnetic & gravity data. Basement faults have been interpreted where distinctive gradients in the magnetic and gravity data exist and have been identified. We believe these basement lineaments (faults/fracture zones), are very important to understanding possible traps, possible production hazards, and in outlining individual "containers" that might have slightly different fracturing trends and frequency.

These basement lineaments are used in the Lineament & Intersection Density map construction.

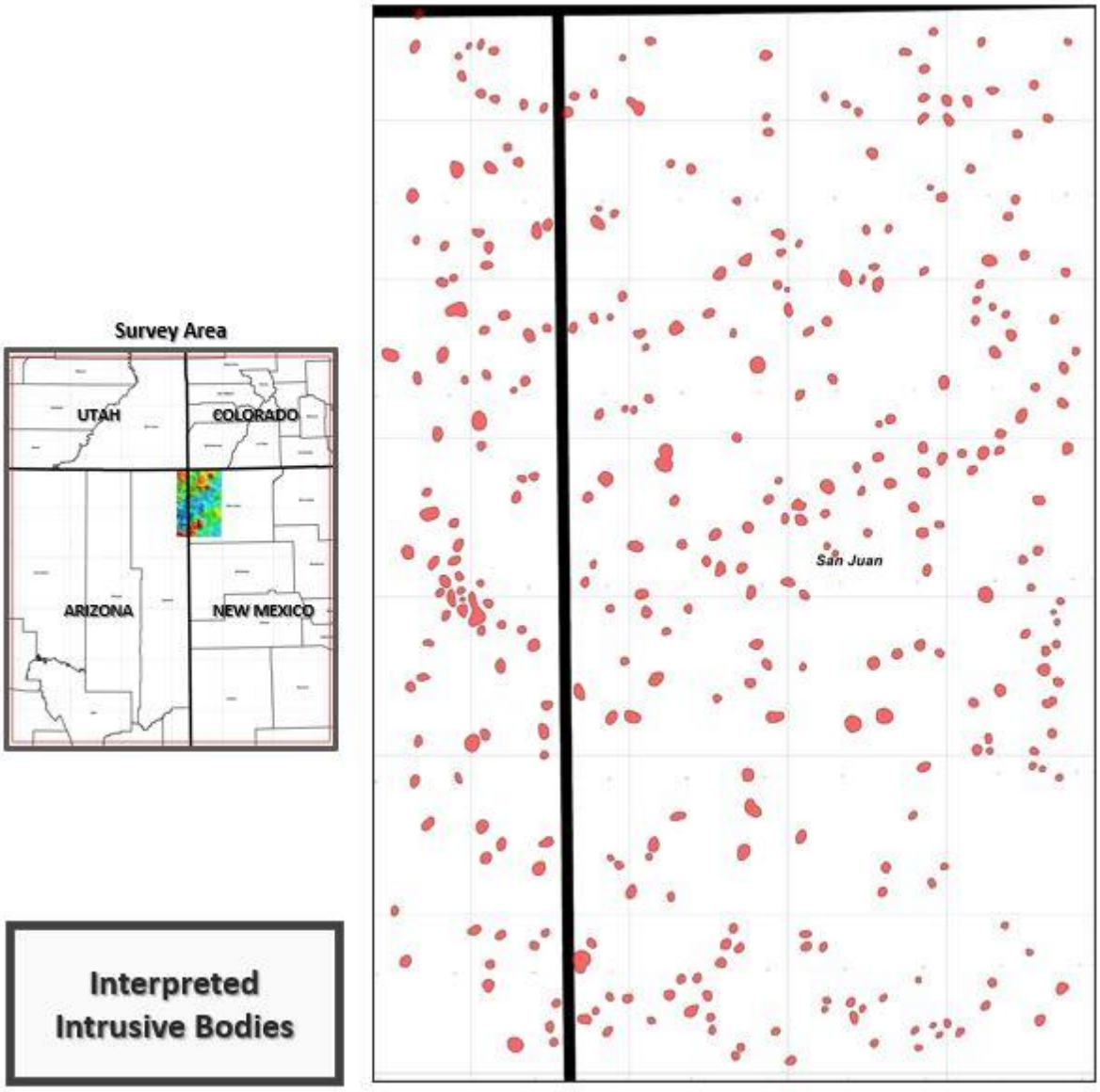


Figure 68. Locations of Igneous plutons, dikes, and sills interpreted from the High-Resolution magnetic survey data. These bodies have been identified using Werner Deconvolution depth estimation profiles, and from various filters and derivative maps of the magnetic data. The outlines of these interpreted igneous bodies have been used in the Lineament & Intersection Density map construction.

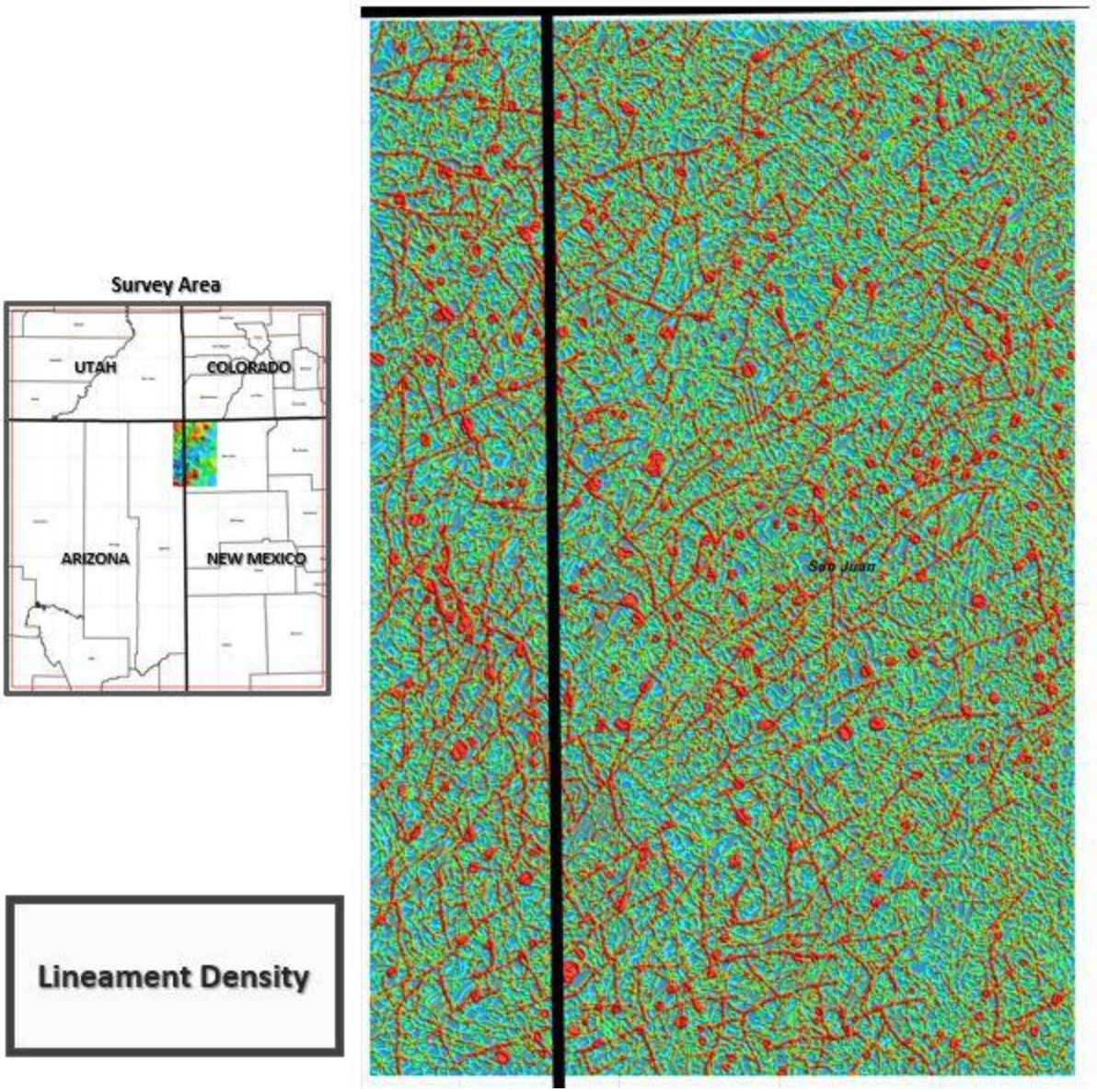


Figure 69. The Lineament Density Map has been constructed by combining all the various lineaments described in the prior pages. These lineaments have all been gridded (each lineament has a common number 1 value in the grid z field) and added through a Boolean grid process. Where the lineaments from the various datasets suggest a lineation, the z values are added together. In this fashion, the Lineament Density grid displays the number of the lineaments predicted at a particular location. The Lineament Density Map grid values are displayed in simple numerical units that correspond to the actual number of the datasets that suggest a lineation/possible fracture, at a given location.

This method of fracture prediction has proven to be a highly effective/inexpensive method of identifying zones of pervasive fracturing. These zones seem to increase natural porosity, and in some cases appear to identify zones of increased helium production.

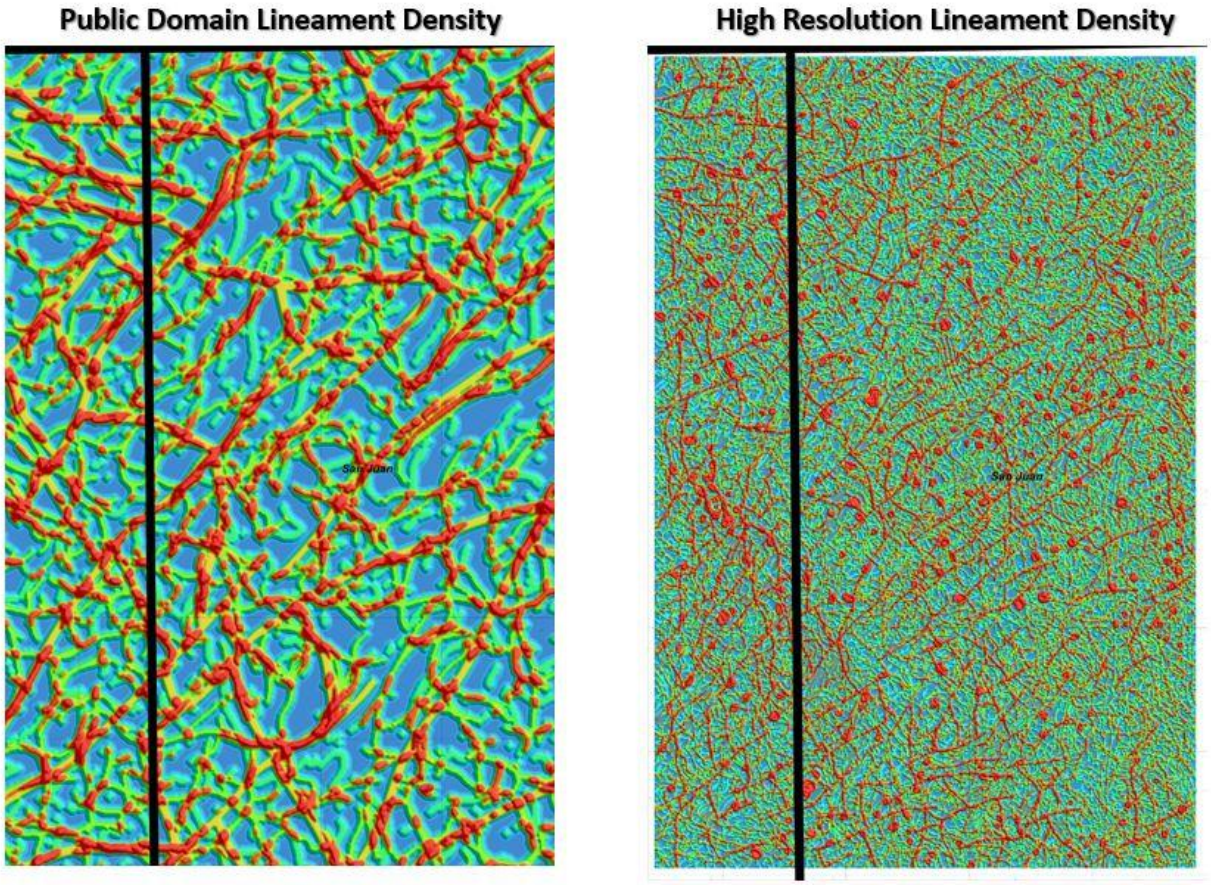


Figure 70. Comparison of Lineament Density Maps produced from the prior regional project (image on left), and from the High-Resolution magnetic survey data. Fracture networks are mapped in much greater level of detail using the High-Resolution magnetic survey data.

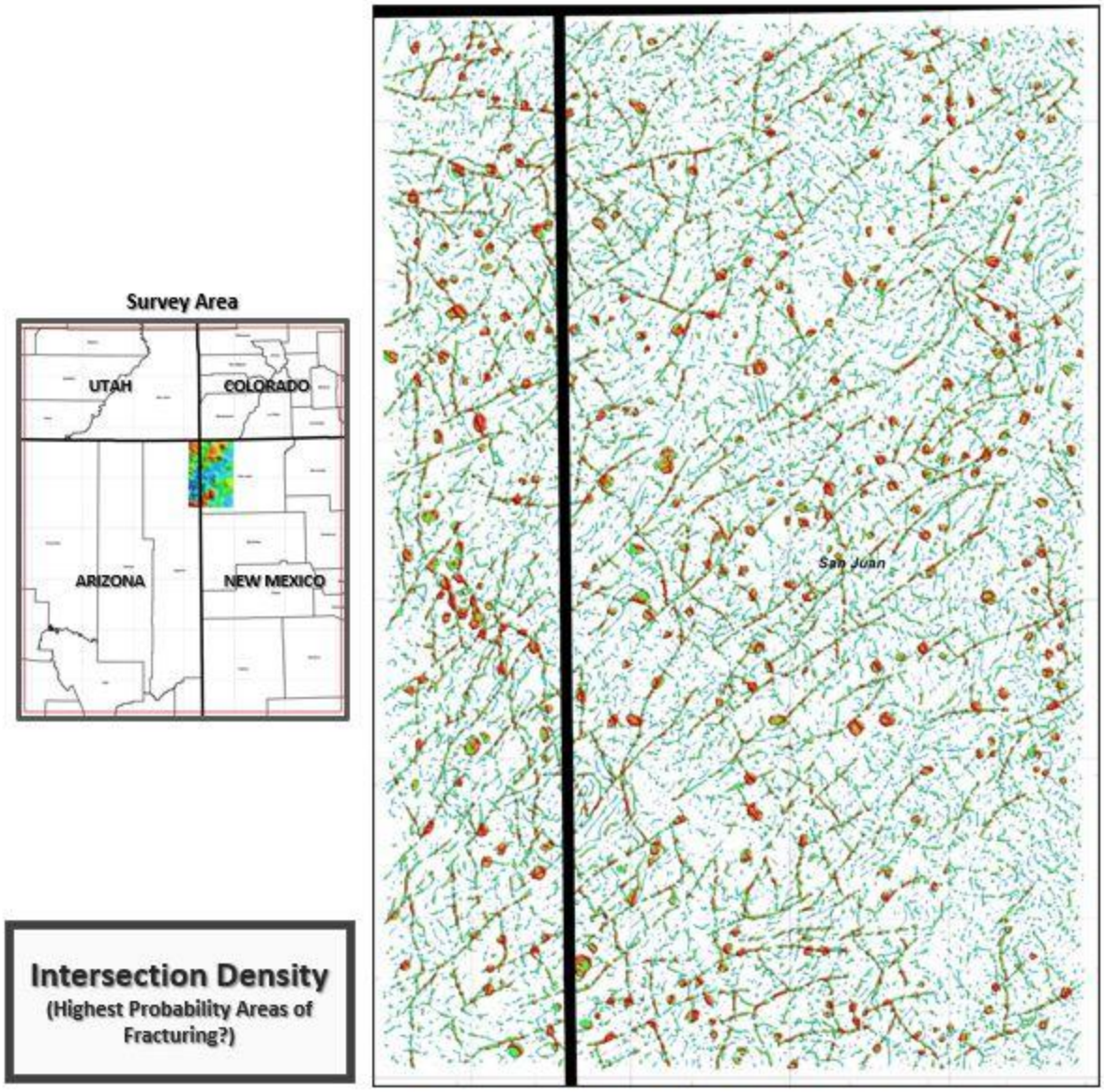


Figure 71. The Intersection Density Map is essentially the windowed version of the Lineament Density Map described on the prior page. The Intersection Density has been constructed by combining all the various lineaments described in the prior pages. These lineaments have all been gridded (each lineament has a common number 1 value in the grid z field) and added through a Boolean grid process. Where the lineaments from the various datasets suggest a lineation, the z values are added together. In this fashion, the Lineament Density grid displays the number of the lineaments predicted at a particular location. The grid values have then windowed to display only the areas where at least 3 of the datasets have identified lineaments.

This process thus displays only the areas with the most pervasive fractures. The Intersection Density Map grid values are displayed in simple numerical units that correspond to the actual number of the datasets that suggest a lineation/possible fracture, at a given location.

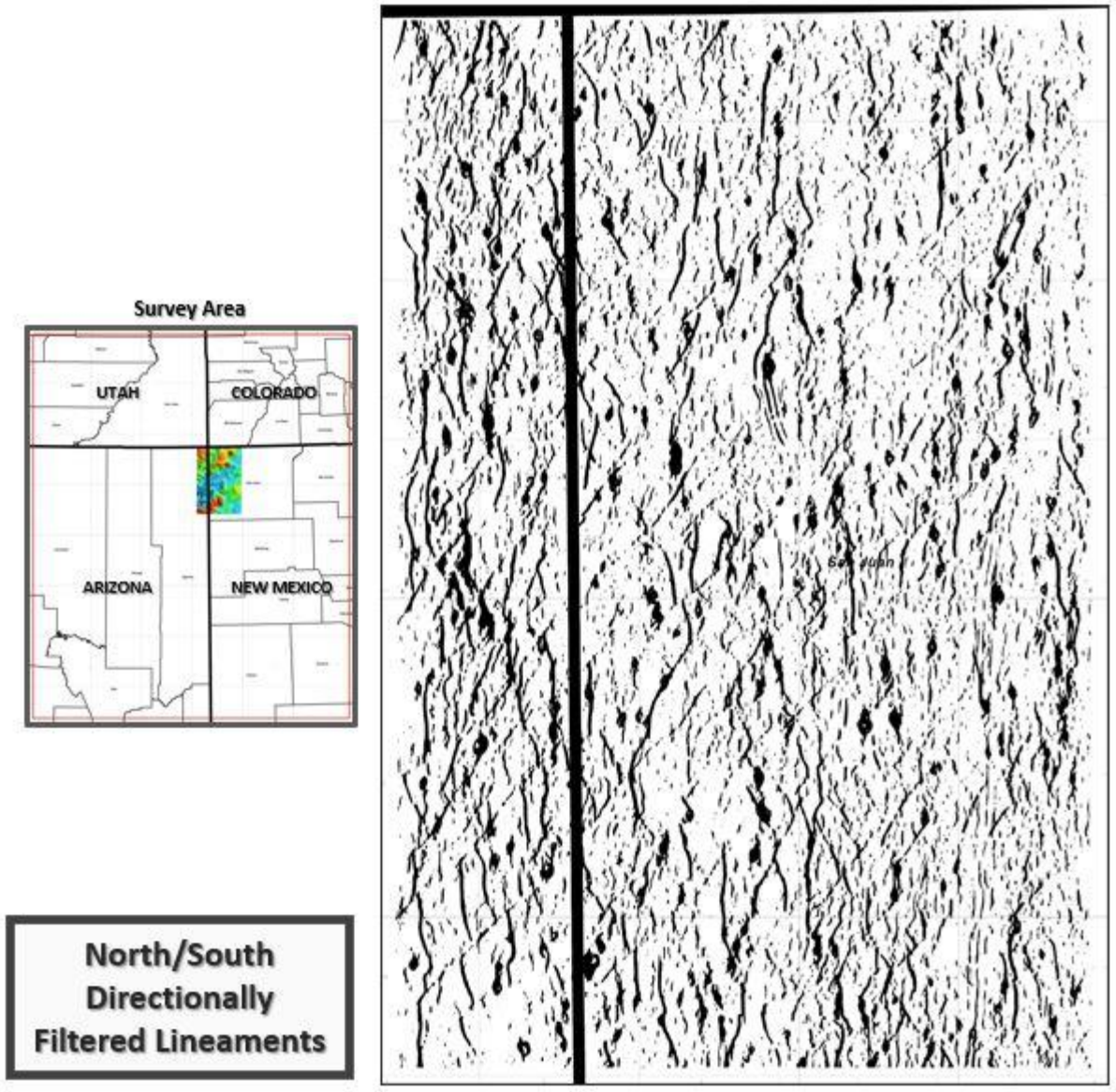


Figure 72. North-South directionally filtered Lineament Density Map. This map has been constructed by combining all the various lineaments described in the prior pages. These lineaments have all been gridded (each lineament has a common number 1 value in the grid z field) and added through a Boolean grid process. Where the lineaments from the various datasets suggest a lineation, the z values are added together. In this fashion, the Lineament Density grid displays the number of the lineaments predicted at a particular location. The Lineament Density data were then directionally filtered to capture lineaments in only the generally North-South orientations. This has been done to enhance structural trends in that direction to determine relationships with areas of increased helium production.

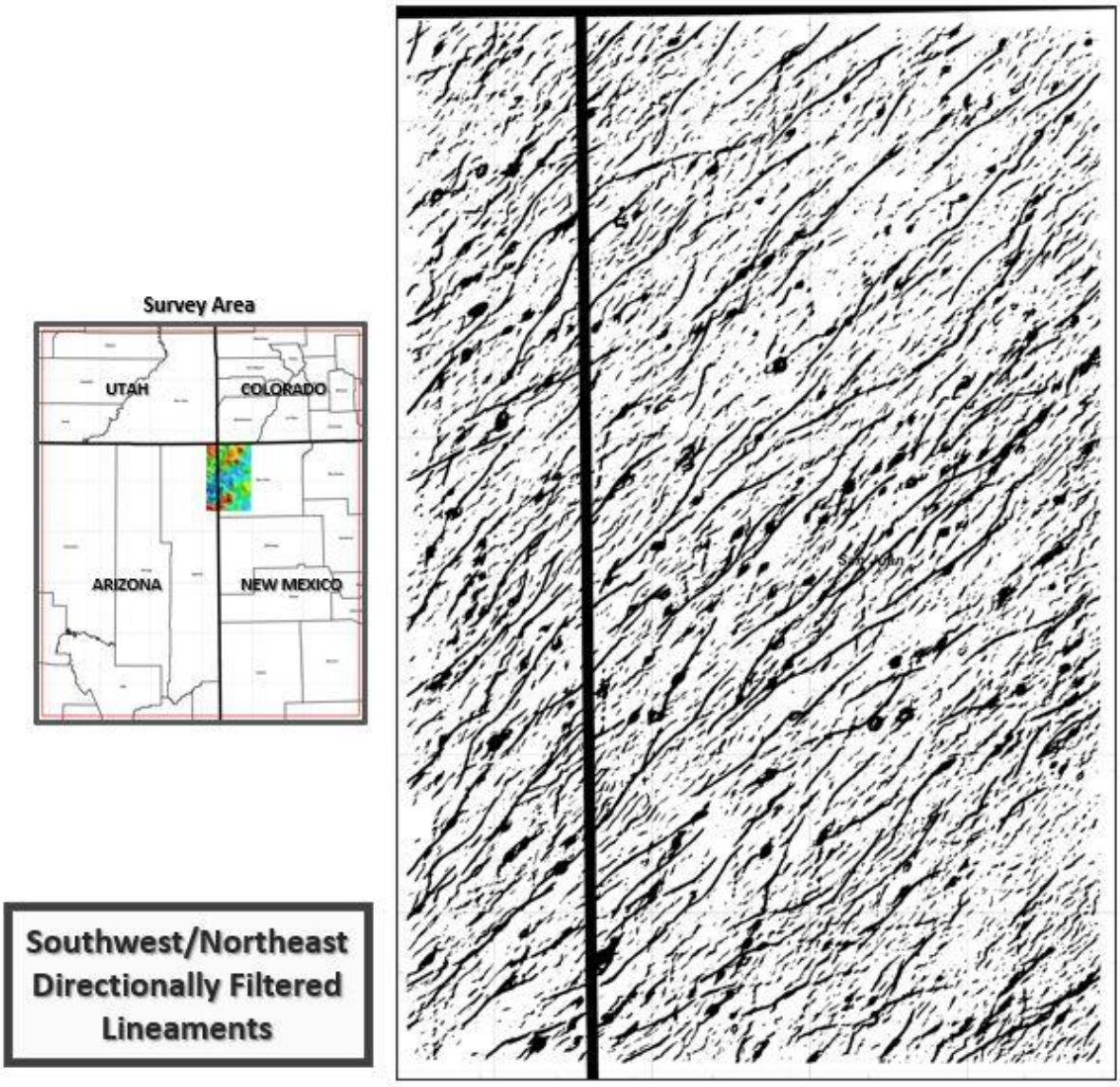


Figure 73. Southwest-Northeast directionally filtered Lineament Density Map. This map has been constructed by combining all the various lineaments described in the prior pages. These lineaments have all been gridded (each lineament has a common number 1 value in the grid z field) and added through a Boolean grid process. Where the lineaments from the various datasets suggest a lineation, the z values are added together. In this fashion, the Lineament Density grid displays the number of the lineaments predicted at a particular location. The Lineament Density data were then directionally filtered to capture lineaments in only the generally Southwest-Northeast orientations. This has been done to enhance structural trends in that direction to determine relationships with areas of increased helium production.

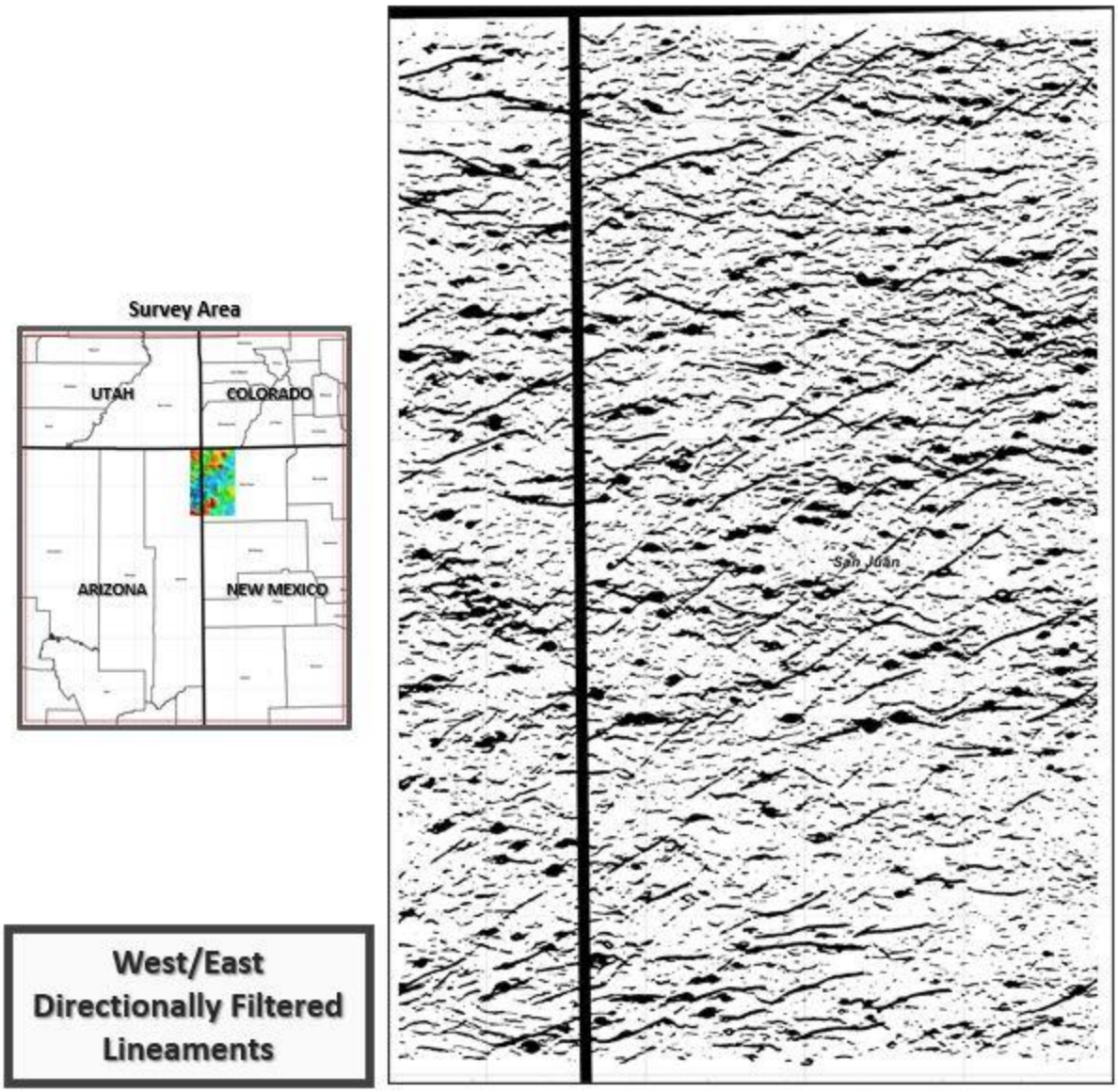


Figure 74. West-East directionally filtered Lineament Density Map. This map has been constructed by combining all the various lineaments described in the prior pages. These lineaments have all been gridded (each lineament has a common number 1 value in the grid z field) and added through a Boolean grid process. Where the lineaments from the various datasets suggest a lineation, the z values are added together. In this fashion, the Lineament Density grid displays the number of the lineaments predicted at a particular location. The Lineament Density data were then directionally filtered to capture lineaments in only the generally West-East orientations. This has been done to enhance structural trends in that direction to determine relationships with areas of increased helium production.

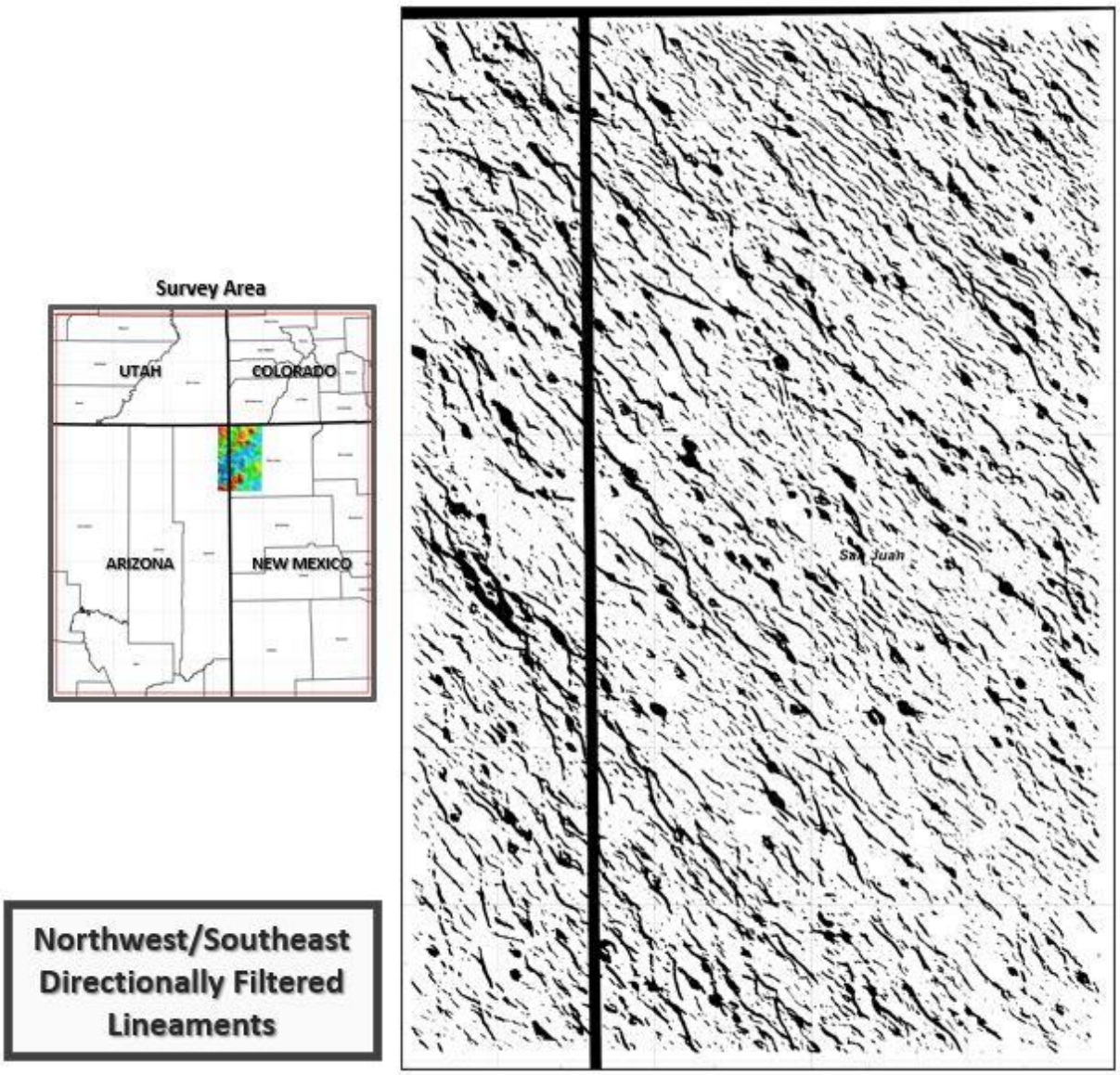


Figure 75. Northwest-Southeast directionally filtered Lineament Density Map. This map has been constructed by combining all the various lineaments described in the prior pages. These lineaments have all been gridded (each lineament has a common number 1 value in the grid z field) and added through a Boolean grid process. Where the lineaments from the various datasets suggest a lineation, the z values are added together. In this fashion, the Lineament Density grid displays the number of the lineaments predicted at a particular location. The Lineament Density data were then directionally filtered to capture lineaments in only the generally Northwest-Southeast orientations. This has been done to enhance structural trends in that direction to determine relationships with areas of increased helium production.

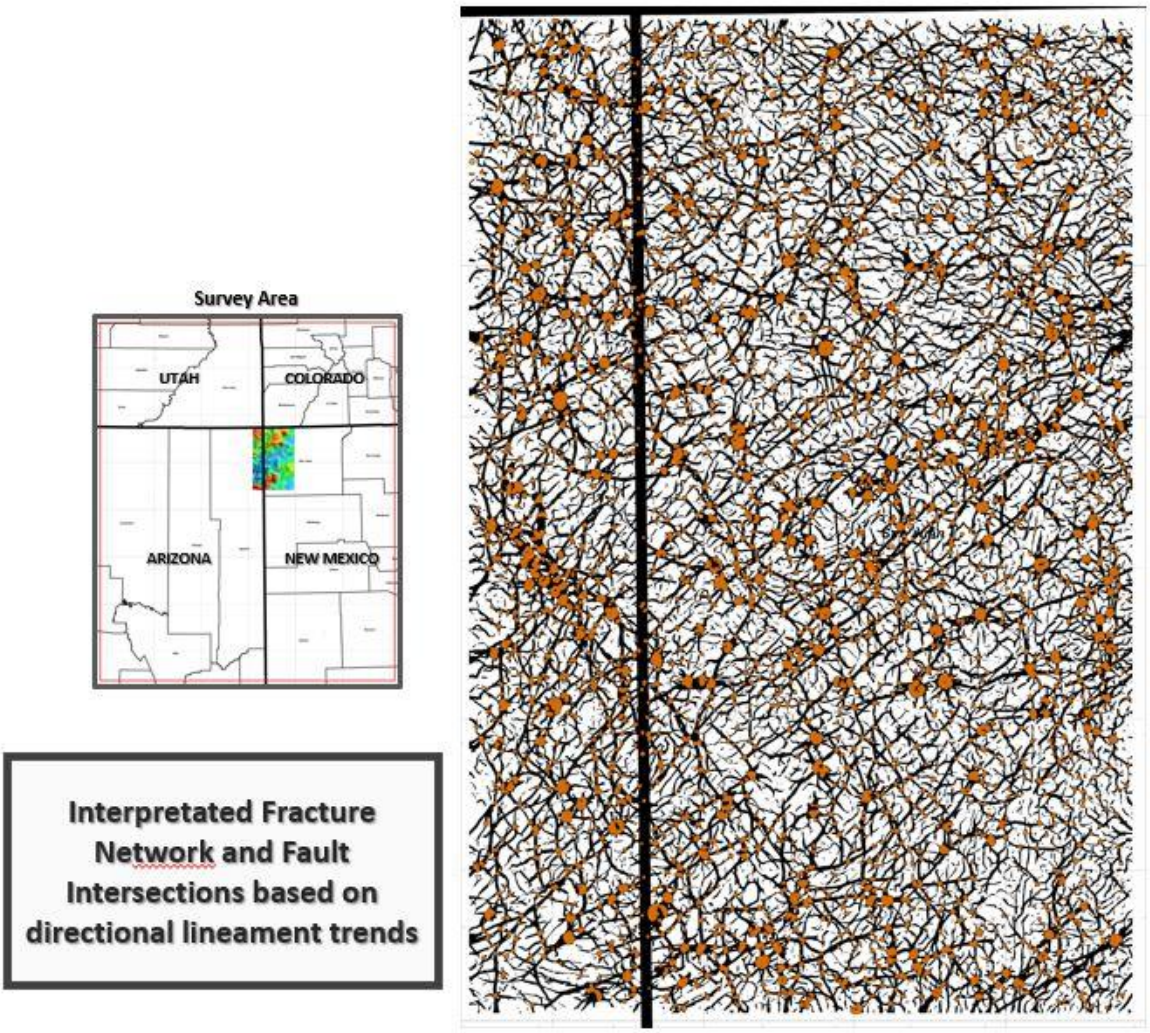


Figure 76. Interpreted Fracture Network Map & Intersections. The Fracture Network map was produced by combining the Directionally filtered Lineament data (see Figures 72-75), and by highlighting (orange features displayed on the map), areas where multiple interpreted lineaments intersect. Numerous projects have shown that these interpreted lineaments often indicate areas of increased natural porosity, and hence can be indicative of areas with increased helium production.

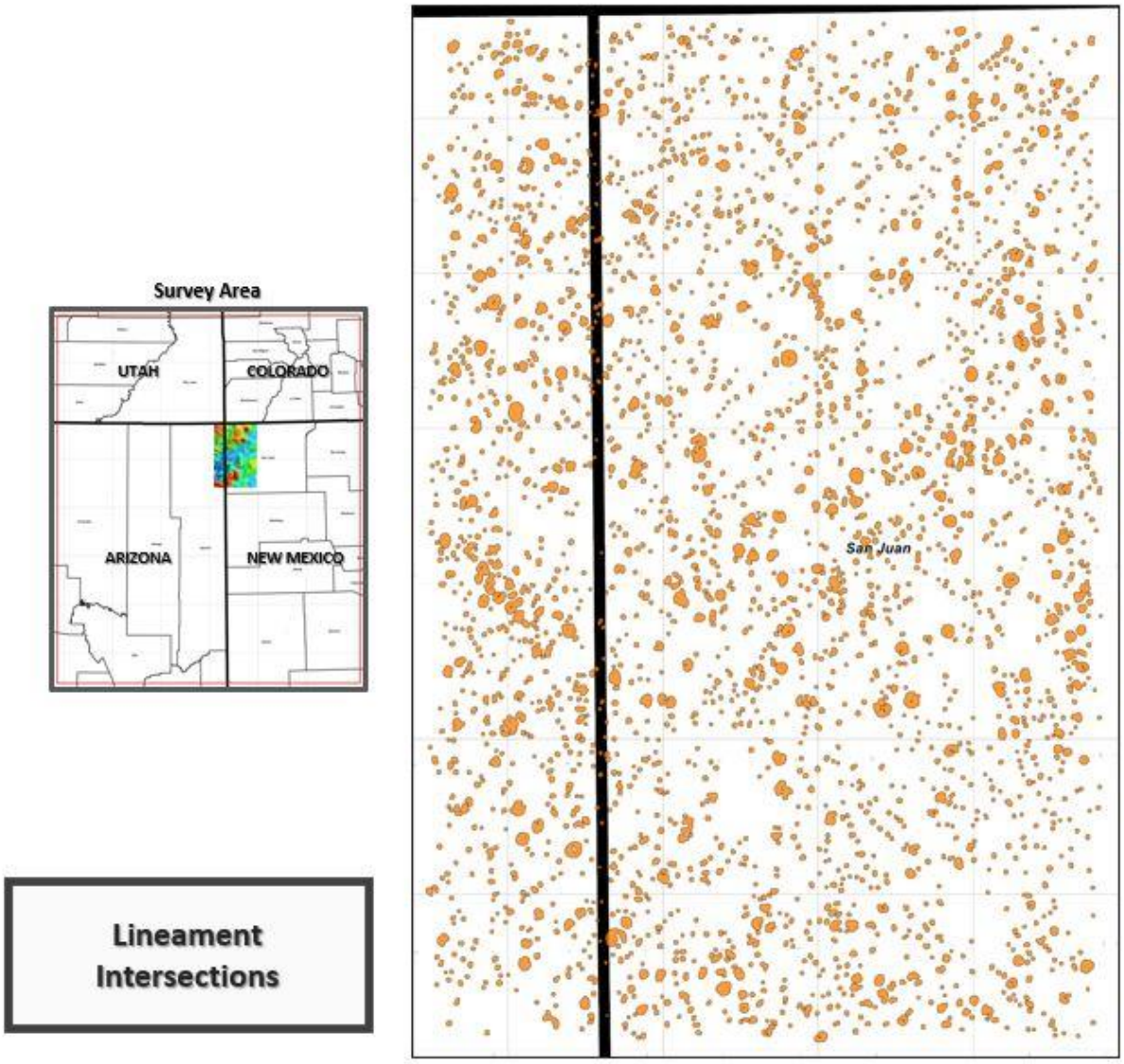


Figure 77. Interpreted Lineament Intersection Map. The interpreted Lineament Map was generated by extracting only areas of multiple lineament intersections shown on the Fracture Network map (Figure 76). The Fracture Network & Intersections map was produced by combining the Directionally filtered Lineament data (see Figures 72-75), and by highlighting (orange features displayed on the map), areas where multiple interpreted lineaments intersect. Numerous projects have shown that these interpreted lineaments often indicate areas of increased natural porosity, and hence can be indicative of areas with increase helium production.

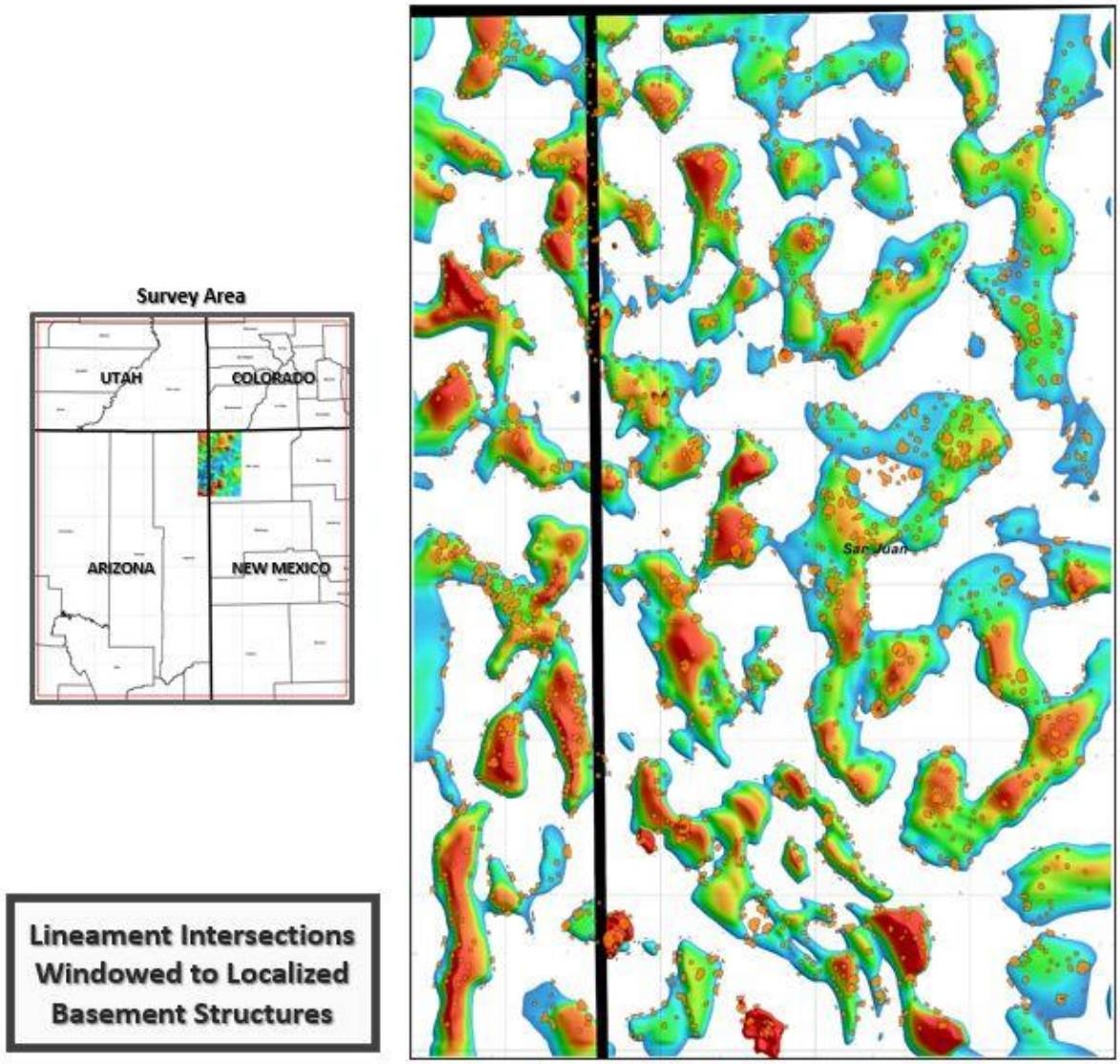


Figure 78. Lineament Intersections Windowed to Localized Basement Structures Map. This map was produced by utilizing the data shown on the Lineament Intersections Map (Figure 77), with the results shown on Localized Basement Structure Map (Figure 62). Helium appears to correlate well with Lineament Intersection areas, and with areas of local basement structural positive features. Areas that display local basement positive features AND Lineament Intersections are considered to have a higher probability of increased helium accumulation and should be investigated in more detail.

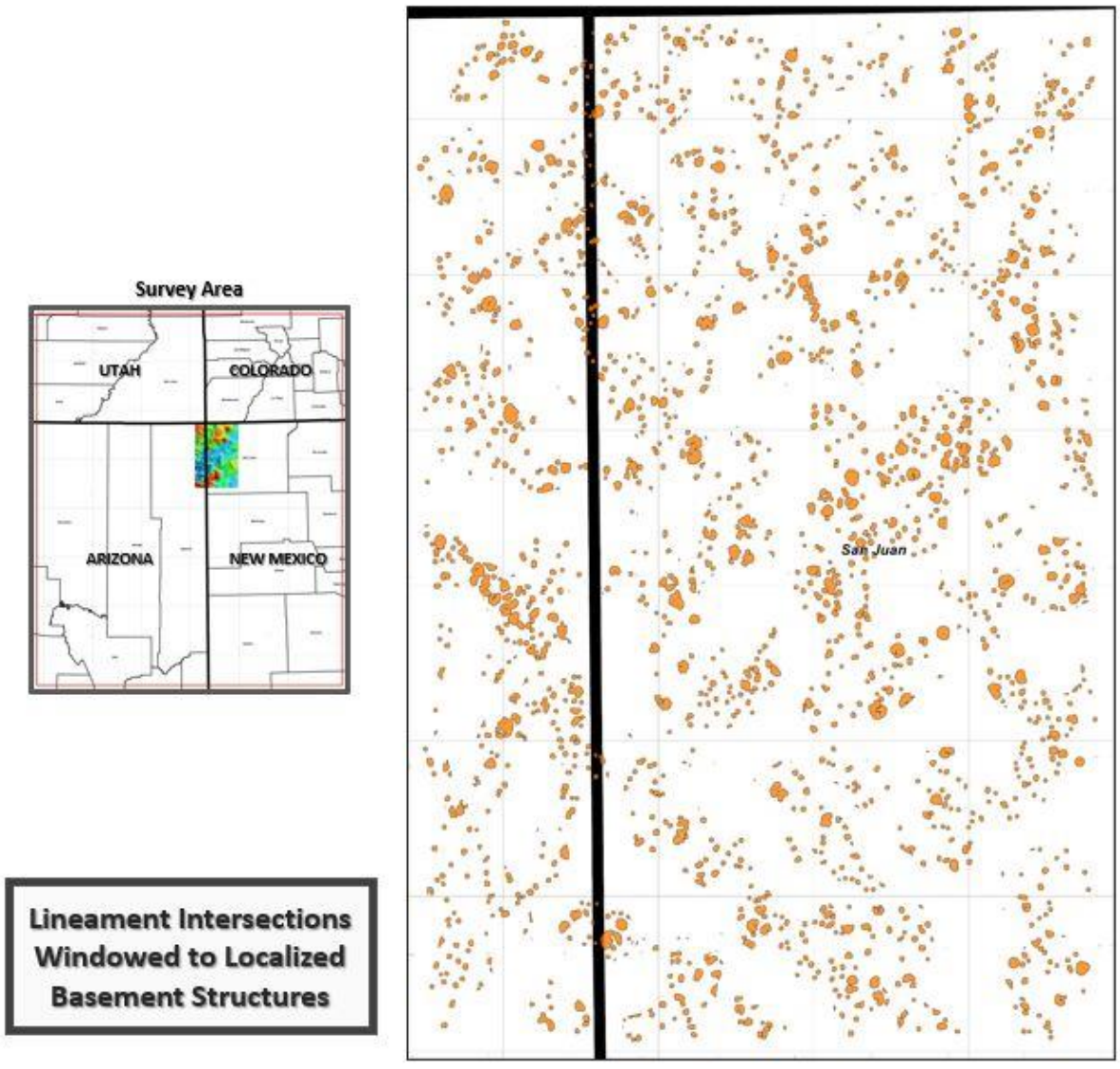


Figure 79. Lineament Intersections Windowed to Localized Basement Structures Map. This map was produced by utilizing the data shown on the Lineament Intersections Map (Figure 77), with the results shown on Localized Basement Structure Map (Figure 62). Only areas where both Lineament Intersections AND positive basement structures are present, are displayed on this map. Helium appears to correlate well with Lineament Intersection areas, and with areas of local basement structural positive features. Areas that display local basement positive features AND Lineament Intersections are considered to have a higher probability of increased helium accumulation, and should be investigated in more detail, and correlated with additional geologic/geochemical/geophysical datasets.

## Thermal Properties Study

### Summary

The objective of this study was to generate thermal property data in the Four Corners region to determine possible relationships with areas of increased helium generation. The various thermal properties that have been determined as part of this study include: Curie point, thermal conductivity, heat production, thermal gradients, basement temperature, and heat flow.

To accomplish the generation of the thermal properties for the Four Corners areas, Earthfield Technology, LLC has developed a proprietary 12-step workflow that uses a combination of publicly available data with new geologic/geophysical analyses of the basement/Moho.

In general, we can derive the various thermal properties of the Four Corner's area, in boot-strap fashion, by combining two basic heat flow equations and an empirical relationship with Earthfield Technology's depth to basement interpretation using magnetic and gravity data, and several open-file data: grids, stations, and results from published sources.

Fourier's Law, Equation 1: $Q_0 = k \times (\Delta T/\Delta z)$ where $Q_0$ is heat flow ($m \cdot W/m^2$), k is thermal conductivity ($W/m \cdot K$), $\Delta T$ is the temperature difference (°C) over distance $\Delta z$ (km) – the equation assumes sources or sinks do not exist within $\Delta z$.

Heat flow from continental crust includes flow from radiogenic sources in the basement, Equation 2: $Q_{TOT} = Q_{BG} + A_0D$ where $Q_{TOT}$ is total heat flow ($m \cdot W/m^2$), $Q_{BG}$ is background heat flow (also called reduced heat flow), $A_0$ is heat produced by basement rocks ($\mu W/m^3$), D is thickness of the heat producing basement layer (km). Note that the product $A_0D$ is flux (heat flow), which can be expressed as $m \cdot W/m^2$.

Pollack and Chapman (1977) determined the empirical relationship that, on average, $Q_{BG}$ and $A_0D$ are 3/5 and 2/5 of total heat flow ($Q_{TOT}$) respectively.

Using these formulas and relationships, Earthfield has been able to determine the current temperatures at several key geologic horizons: 1). The topographic surface; 2). The basement surface; 3). Curie Point/Moho. Using the variations in temperature with depth of these temperature horizons allows the generation of thermal gradients for the basin (topographic surface to basement surface), the magnetic layer (top of basement to Curie point), and background (Curie point to the Earth's core). Ultimately allowing for the calculation of temperature at any depth, and the calculated heat flow for the basin, heat flow from the magnetic layer, background heat flow, and total heat flow.

## Thermal Properties Definitions

- **Heat Flow**: $m \cdot W/m^2$

= milli-Watts per square meter. **Heat flow is flux, or flow through unit area**.

- **Heat Production**: $\mu W/m^3$

= micro-Watts per cubic meter. **It is the heat produced per unit volume of material.**

- *Note that when heat production is multiplied by the heat producing layer thickness (Equation 2 in this study), the product becomes heat per unit area, and it can then be added to the background heat flow.*

**Thermal Conductivity**: $W/m \cdot K$

= Watts per meter Kelvin. **It is a linear, distance-temperature measure energy transport.**

**Thermal gradient** ($\Delta T/\Delta z$)

**= The rate of temperature increase within the earth as a function of depth**

**. It is simply the change in temperature (°C) over a given depth interval (m).**

Below is a summary of all the data used & products produced during the thermal properties study of the Four Corners area. An image of each of the products delivered are included in the following figures (Figures 80-114). A description of each of the products, along with the utility of the product is included in the captions for each figure.

Data: 1) Earthfield Technology basement interpretations from regional magnetic data
2) Open-file stations: heat flow, heat production, thermal conductivity, seismic refraction
3) Open-file grids: topography, gravity, magnetics, Curie depth point

Methods: 1) Heat flow equations and empirical relation
2) 3D modeling: basement magnetic susceptibility
3) Basement terrane mapping (from published sources)

Products: 1) Topography, gravity, magnetics (3)
2) Basement and Curie Point Depth (2)
3) Heat flow (5): measured, background, heat production (basin and basement), final calculated heat flow
4) Thermal conductivity (2): basin, magnetic layer
5) Basement temperature (1)
6) Thermal gradients (2): basin, magnetic layer
7) Magnetic susceptibility (1)
8) Magnetic layer heat production and thickness (2)
9) Stations (4): heat flow, heat production, thermal conductivity, seismic refraction
10) Shapefiles (2): basement terranes and major orogenic boundaries

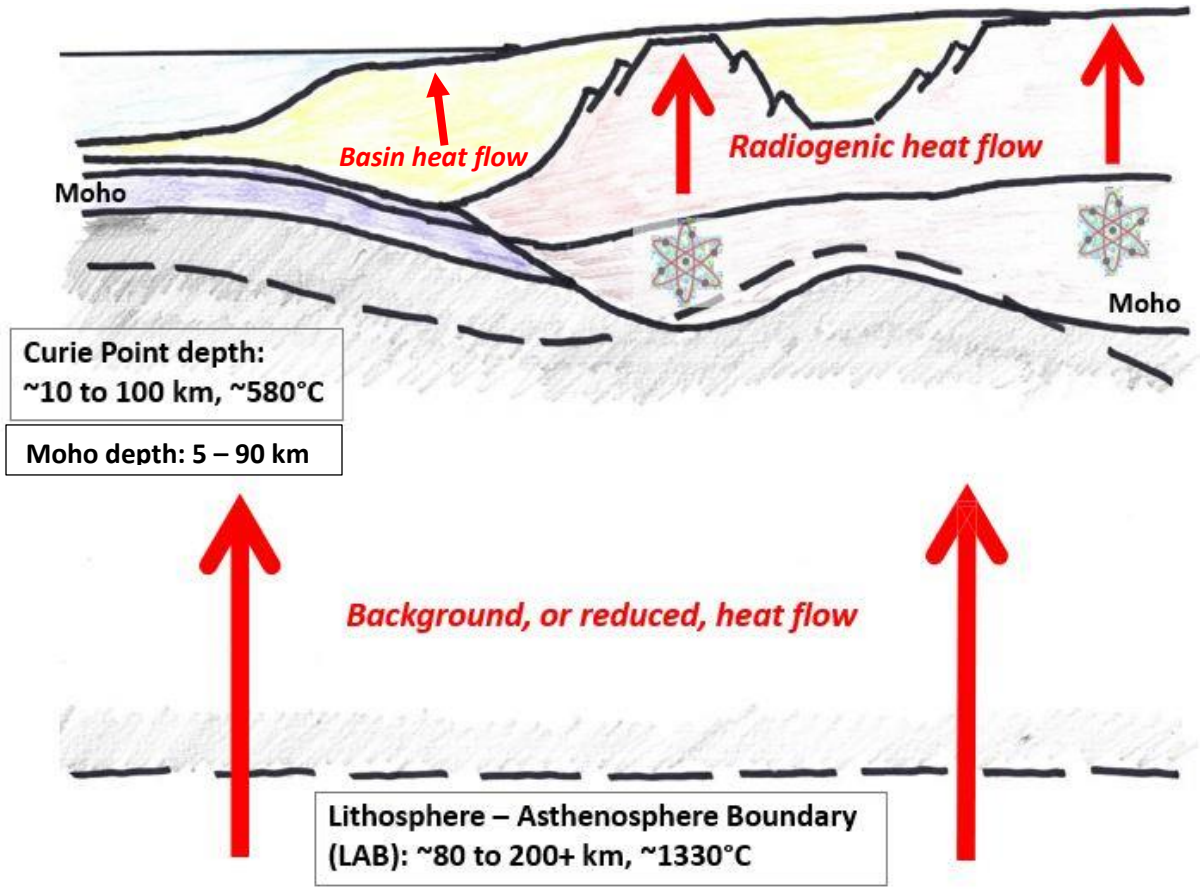


Figure 80. Illustration of the three components of heat flows: 1) background heat flow which is the heat flow from the Moho and below, including the Mantle and the Core, 2) radiogenic heat flow which is the heat flow from the igneous basement to the Moho, and 3) basin heat flow which is the relatively insignificant heat flow contribution from the sedimentary column.

The radiogenic heat flow is produced by the radioactive decay of primarily Uranium, Potassium, and Thorium within the crystalline igneous rocks between the top of the basement and the Curie Point: 580 °C (called the magnetic layer), which is a close approximation of the Moho in continental basement settings. The Curie point is temperature at which rocks/minerals lose their magnetism. The radiogenic heat flow is thus affected by the total amount of radioactive elements within the igneous rocks beneath the study area and thickness of that layer. Continental granitic rocks in general have much higher concentrations of these radioactive elements than mafic or ultramafic rocks. Sedimentary rocks (basin) contribute little of overall heat flow, but are still included in our calculations.

It is therefore critical to determine the basement depth, and lithology to infer the amount of radioactive elements present. The amount of radioactive elements present control the heat

production capacity for a given rock type, and heat production is used in formulas to calculate the various thermal properties.

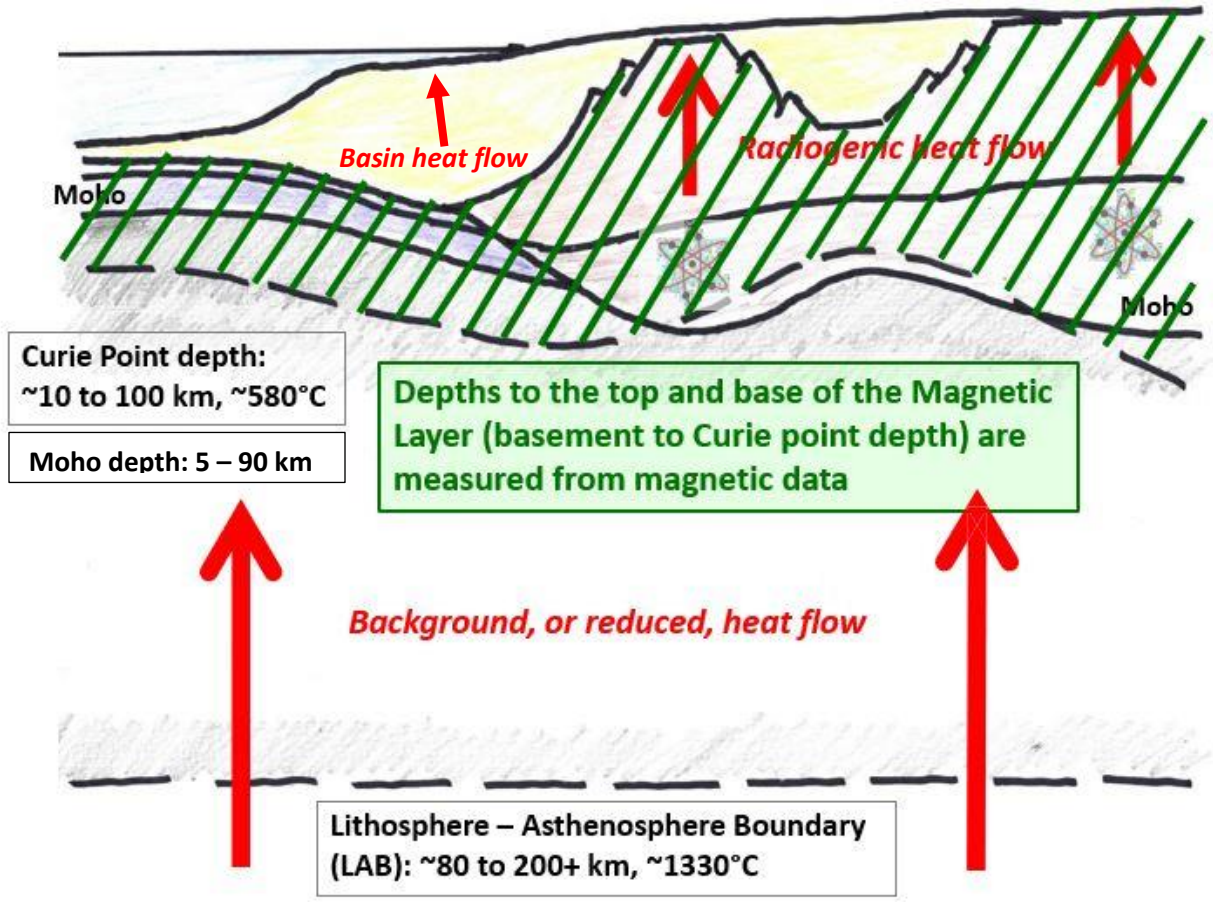


Figure 81. Illustration of Magnetic Layer Heat Flow. The magnetic layer exists from the top of the basement (crust) to the Curie point depth which is defined at the isotherm point of 580 °C where all rocks lose their magnetism and roughly is equal to the thickness of the radiogenic layer.

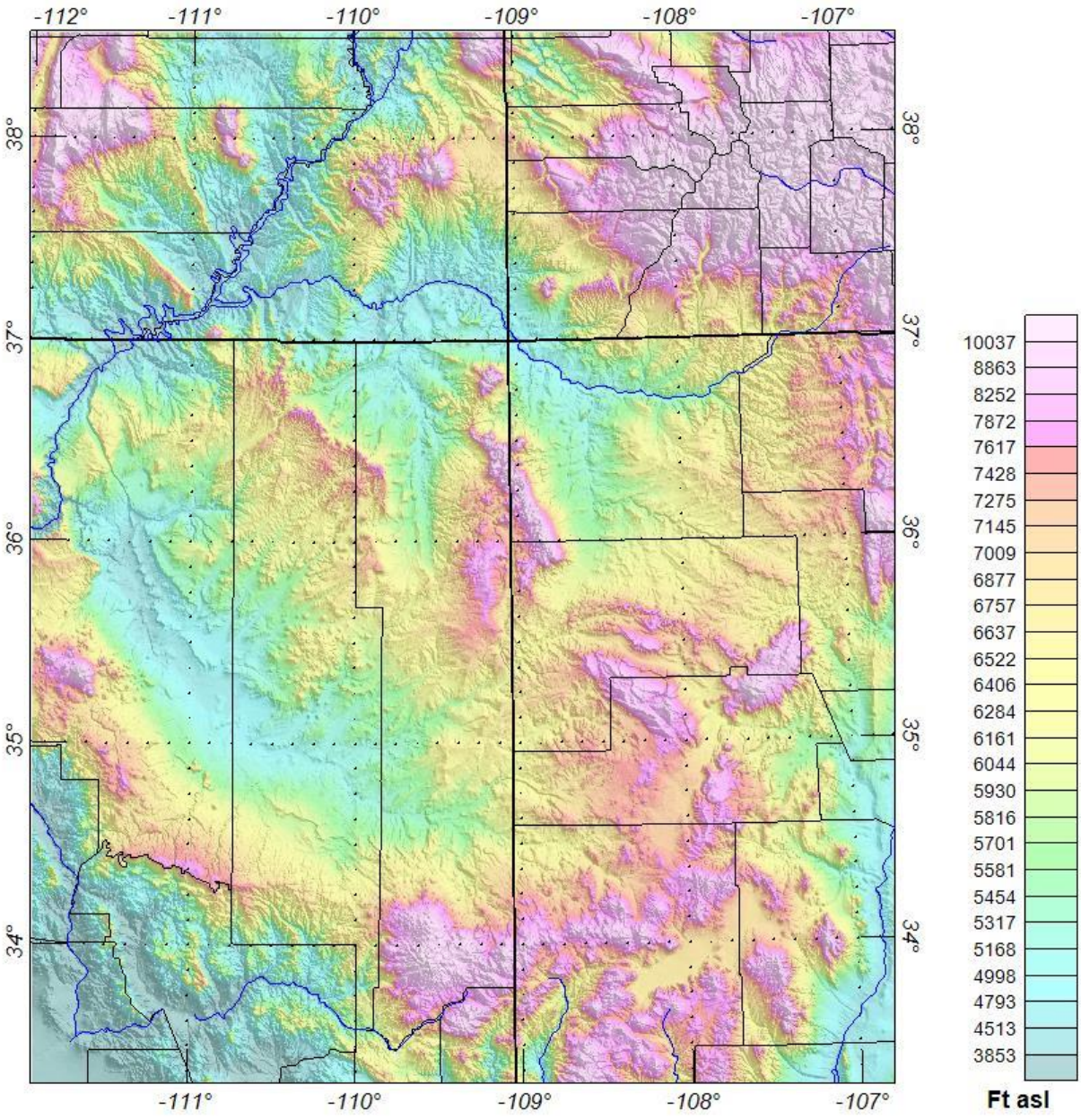


Figure 82. Study area, and SRTM 30 Topographic data used in thermal properties study. The topography data has been used in the thermal properties calculations to define the first thermal horizon (defines top of basin).

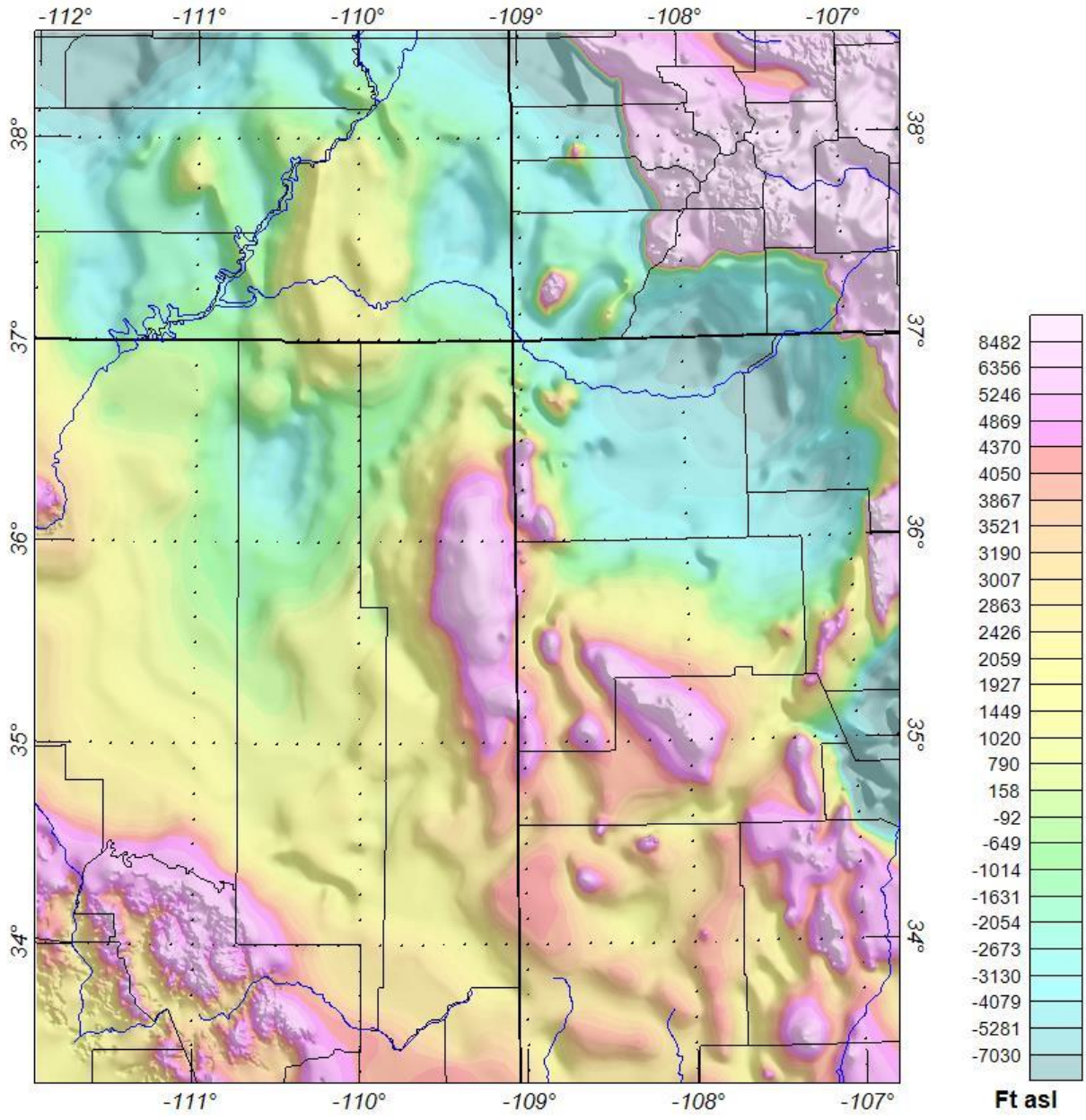


Figure 83. Earthfield Technology's interpreted basement structure from 3 x 9 mile regional aeromagnetic grid. The interpreted basement surface has been used to define the second thermal horizon used in our calculations. This surface defines the top of the radiogenic/magnetic layer.

The basement surface also is used to calculate the magnetic susceptibility changes within the basement, and thus determine the lithology of various basement terranes beneath the study area. Using the basement surface as starting control, 3D inversions of the magnetic data yield changes in magnetic susceptibilities. Different rock lithologies contain different magnetic characteristics, and can thus be used to predict the lithology, and by extension, the heat production values, and ultimately heat flow.

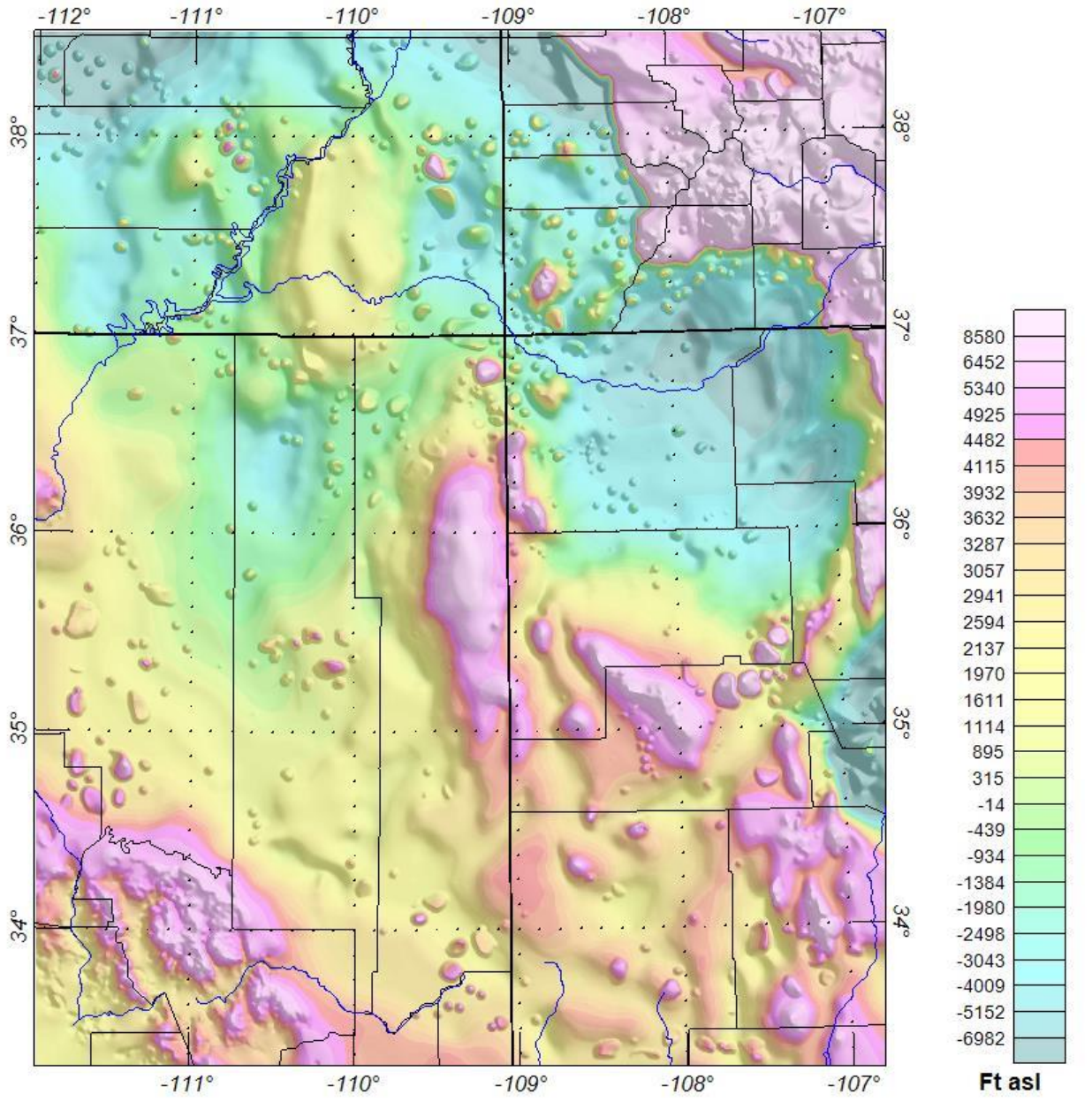


Figure 84. Earthfield Technology's interpreted basement & shallower igneous body structure map from 3 x 9 mile regional aeromagnetic grid. Numerous small intrusive bodies have been identified in the area, and these interpreted mafic intrusions may affect the overall heat flow of the radiogenic/magnetic layer, and were included in our calculations.

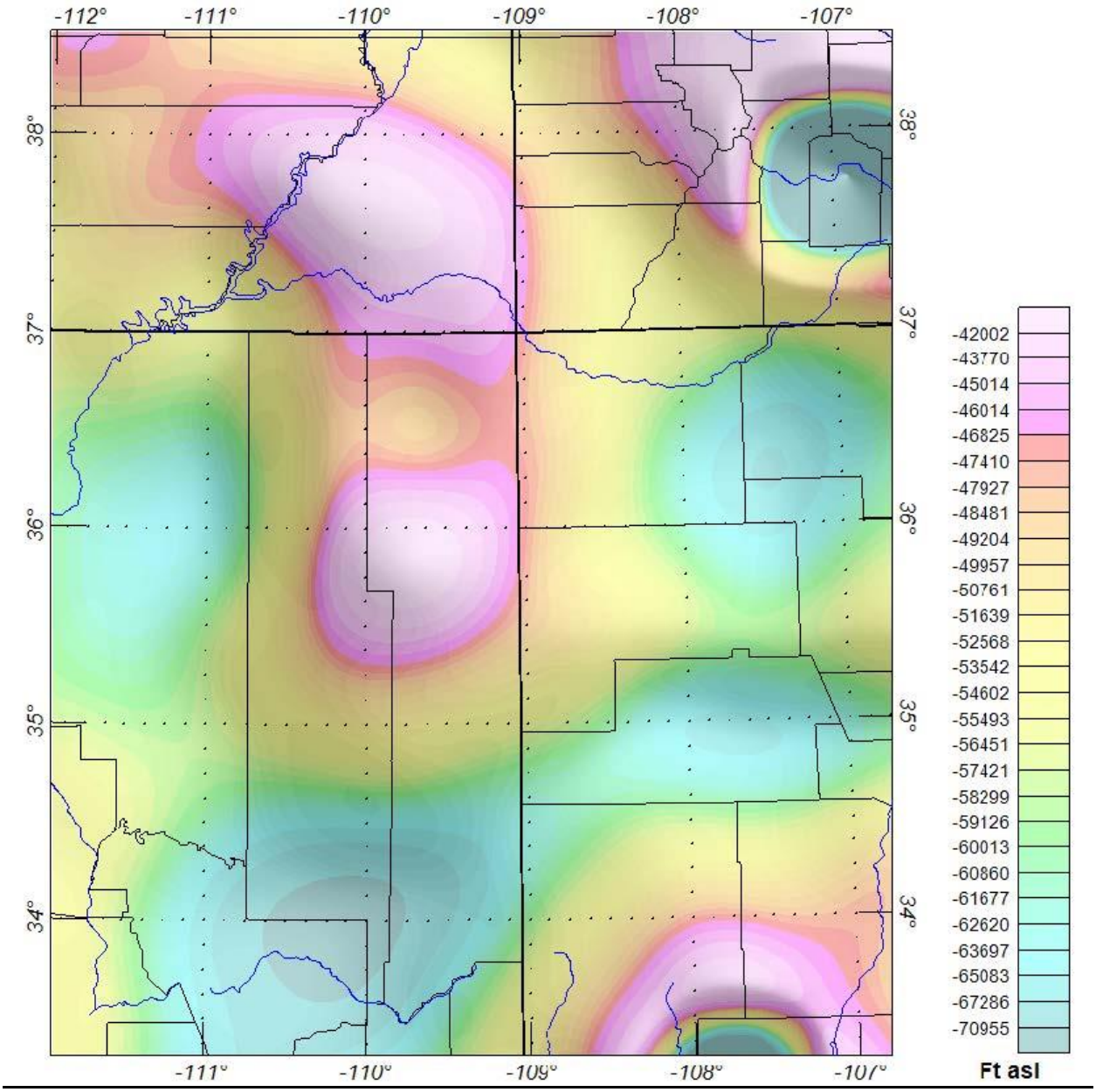


Figure 85. Calculated Curie point depth surface. The calculated Curie point has been generated from several refraction seismic points in this area that define the Moho/Curie point. The Curie point is where rocks lose their magnetism. This horizon marks the third thermal horizon (base of radiogenic/magnetic layer), that we are able to determine from geophysical data, and allows for the calculation of thermal gradients for the radiogenic/magnetic layer, and thus computation of temperature & heat flow using Fourier's Law equation.

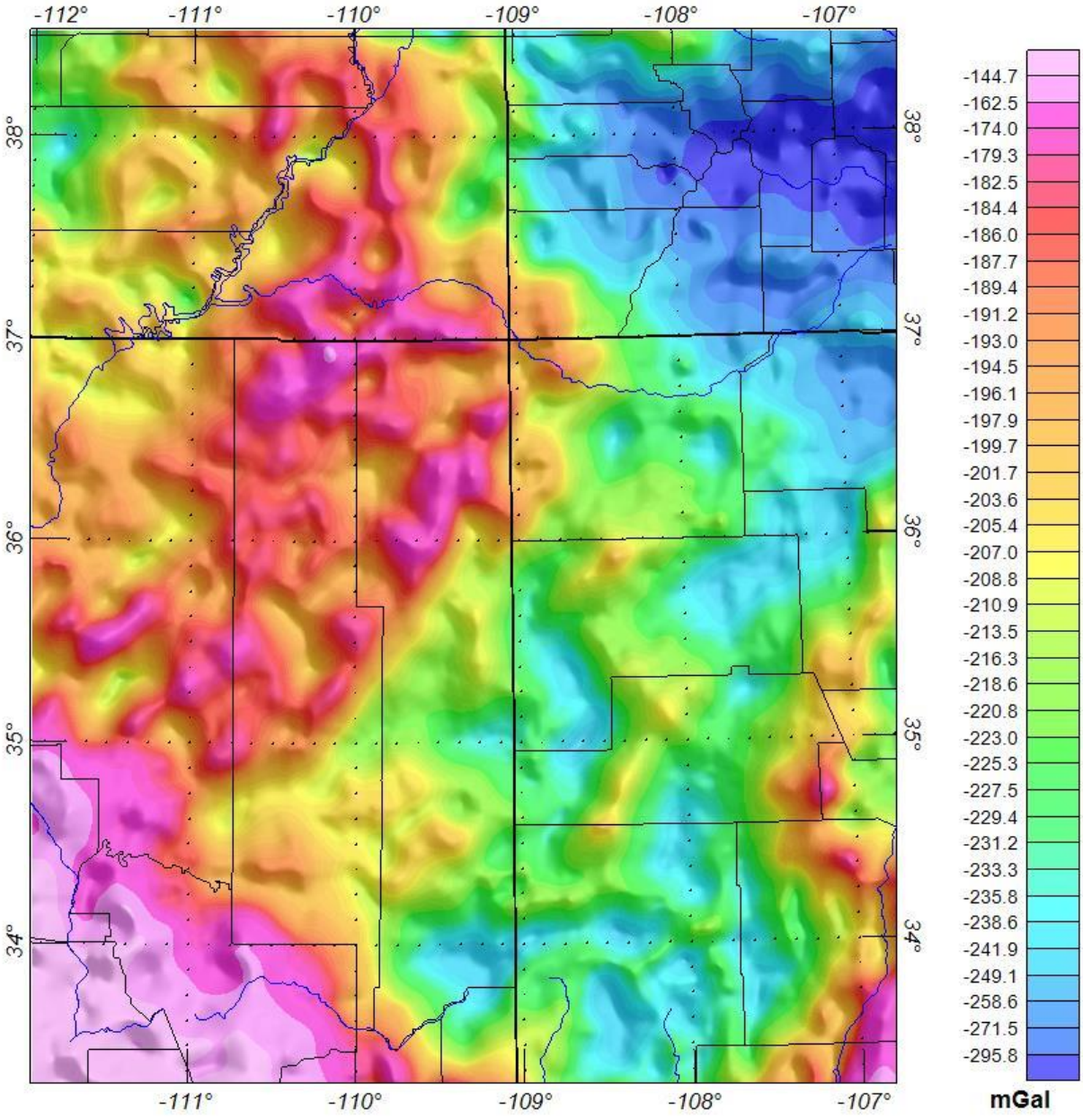


Figure 86. Bouguer gravity anomaly grid used in Thermal Properties Study. Used to help define the density of the basement, and hence basement lithology of the radiogenic/magnetic layer.

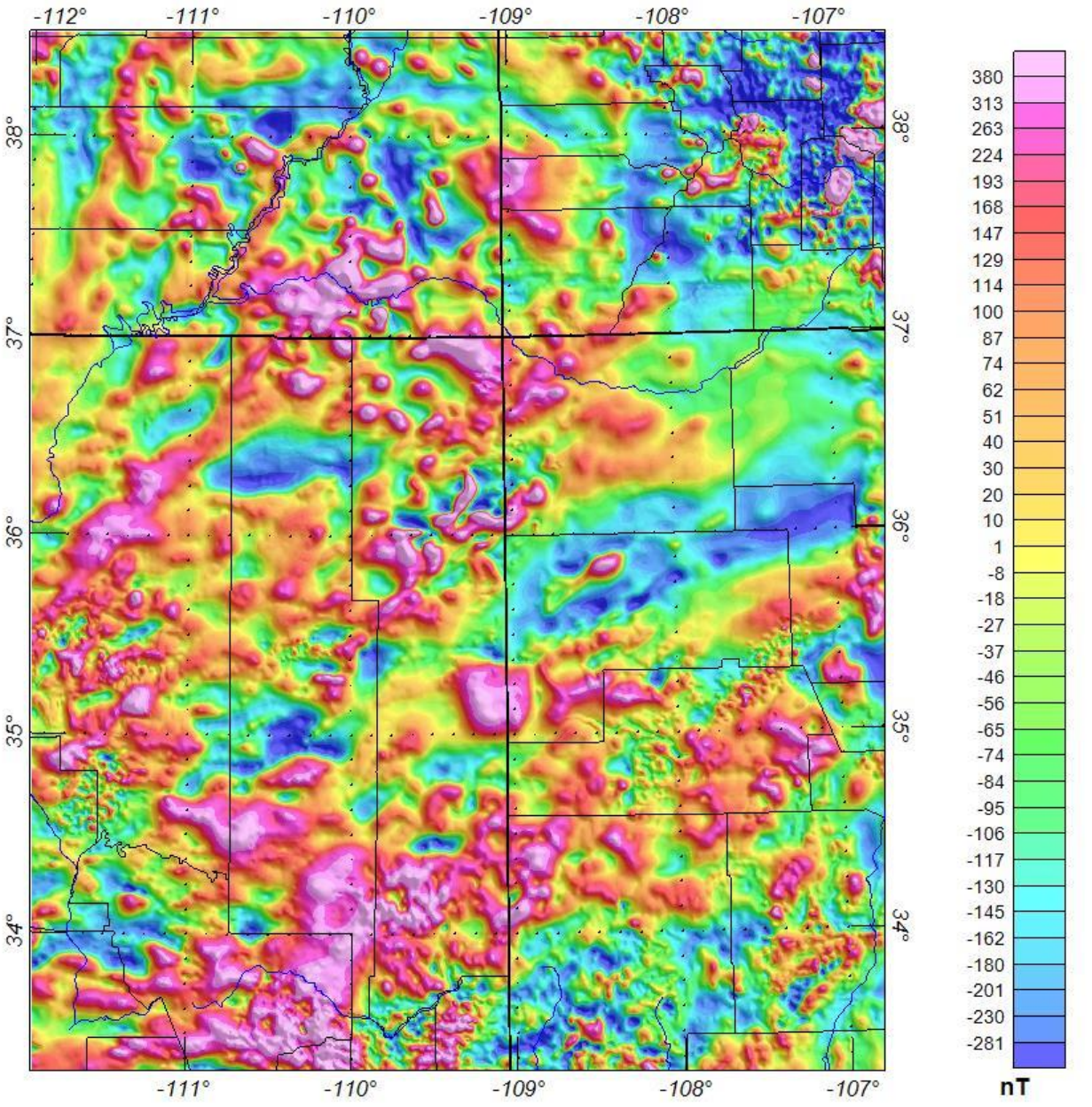


Figure 87. Total magnetic intensity (TMI) anomaly grid used in Thermal Properties Study. The magnetic data were used to help define the magnetic susceptibility of the basement, and hence basement lithology of the radiogenic/magnetic layer, by producing a 3D magnetic susceptibility inversion that used the interpreted basement surface (Figure 83), as a constraint.

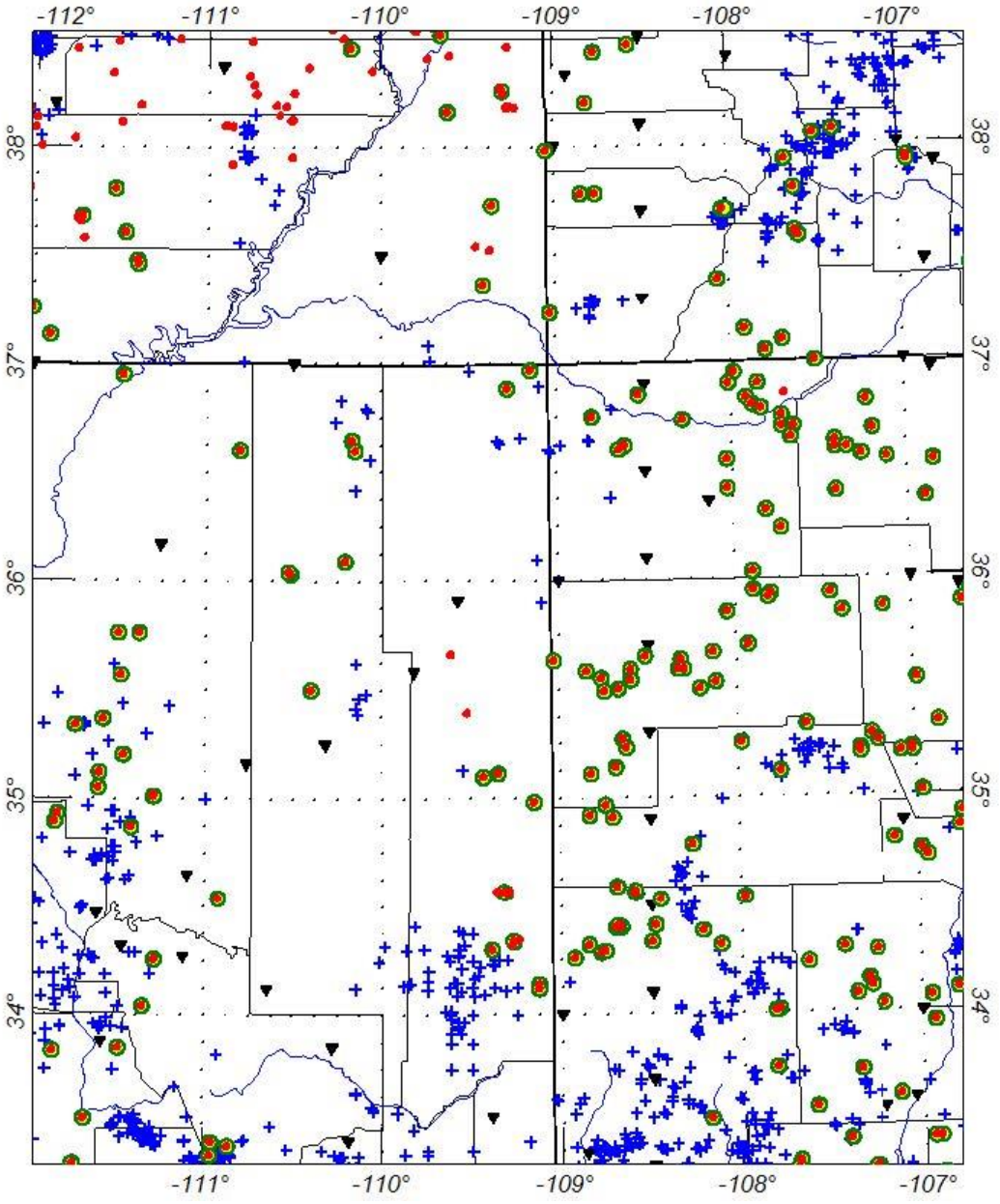


Figure 88. Thermal and seismic refraction stations used in Thermal Properties Study. These points from public domain sources, have been used to provide measured control points for temperatures at various well depths, measured heat flow in the shallow section, basin thermal conductivity, and for determination of the Moho/Curie point in the area.

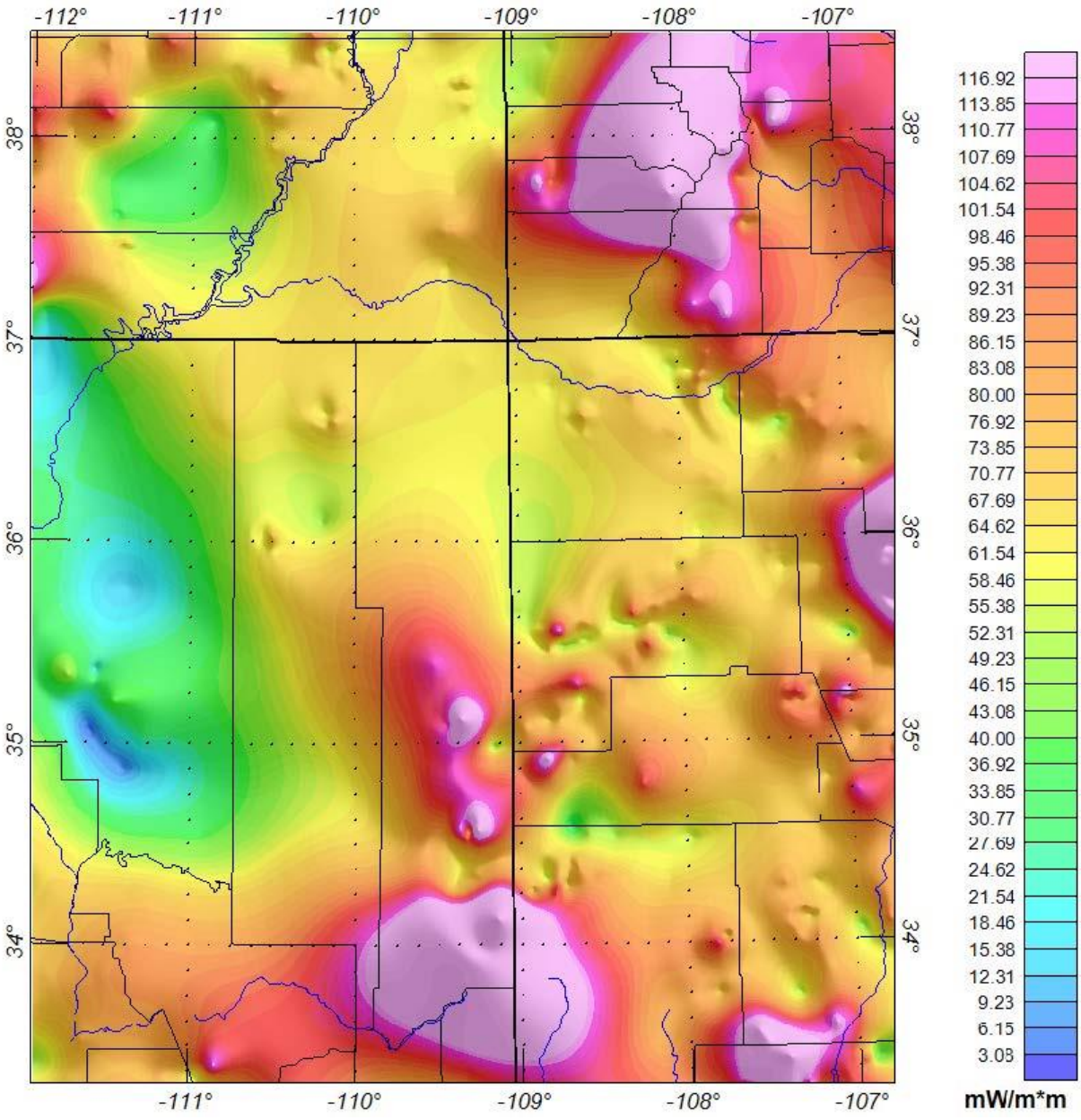


Figure 89. Measured heat flow stations used in Thermal Properties Study. These values were obtained from the public domain heat flow stations of various shallow wells within the study area. These data thus provide measured values of the heat flow that have been used to constrain the heat flow calculations produced in the current study.

Below is a summary of the data used, and the calculation method of the near surface temperature horizon:

1. Many heat flow stations include minimum and maximum temperature measurement depths.
2. Medians values were gridded and corrected for conflicts with topography and basement horizons.
3. The temperature of this horizon was then calculated from SMU BHT and surface temperatures.

SMU BHT and Near surface temperature horizon:

- Southern Methodist University's (SMU) Borehole temperature (BHT) database
    - SMU BHT database includes well depths and temperatures, drilling dates, etc. and is free to use: https://www.smu.edu/Dedman/Academics/Departments/Earth-Sciences/Research/GeothermalLab
- University of Delaware Terrestrial air temperature and precipitation
    - Global grids of monthly and annual air temperature and precipitation are free to download for years 1900 through 2017: http://climate.geog.udel.edu/~climate/html_pages/README.ghcn_ts2.html
- Approach
    - Surface temperature is assumed to equal average air temperatures. Examination of global air temperature grids reflect effects of latitude and elevation support this assumption.
    - Mean and 1st standard deviation of spud and completion dates of SMU BHT wells in the Four Corners study area range in dates from 1968 to 1986, therefore surface temperature grids were averaged together over this time frame.
    - Thermal gradients were calculated, for each corrected bottom hole temperature, between the near surface (deeper than 21 m) and well depth temperatures.
    - Median heat flow depth measurements were gridded – 21 m is the shallowest depth.

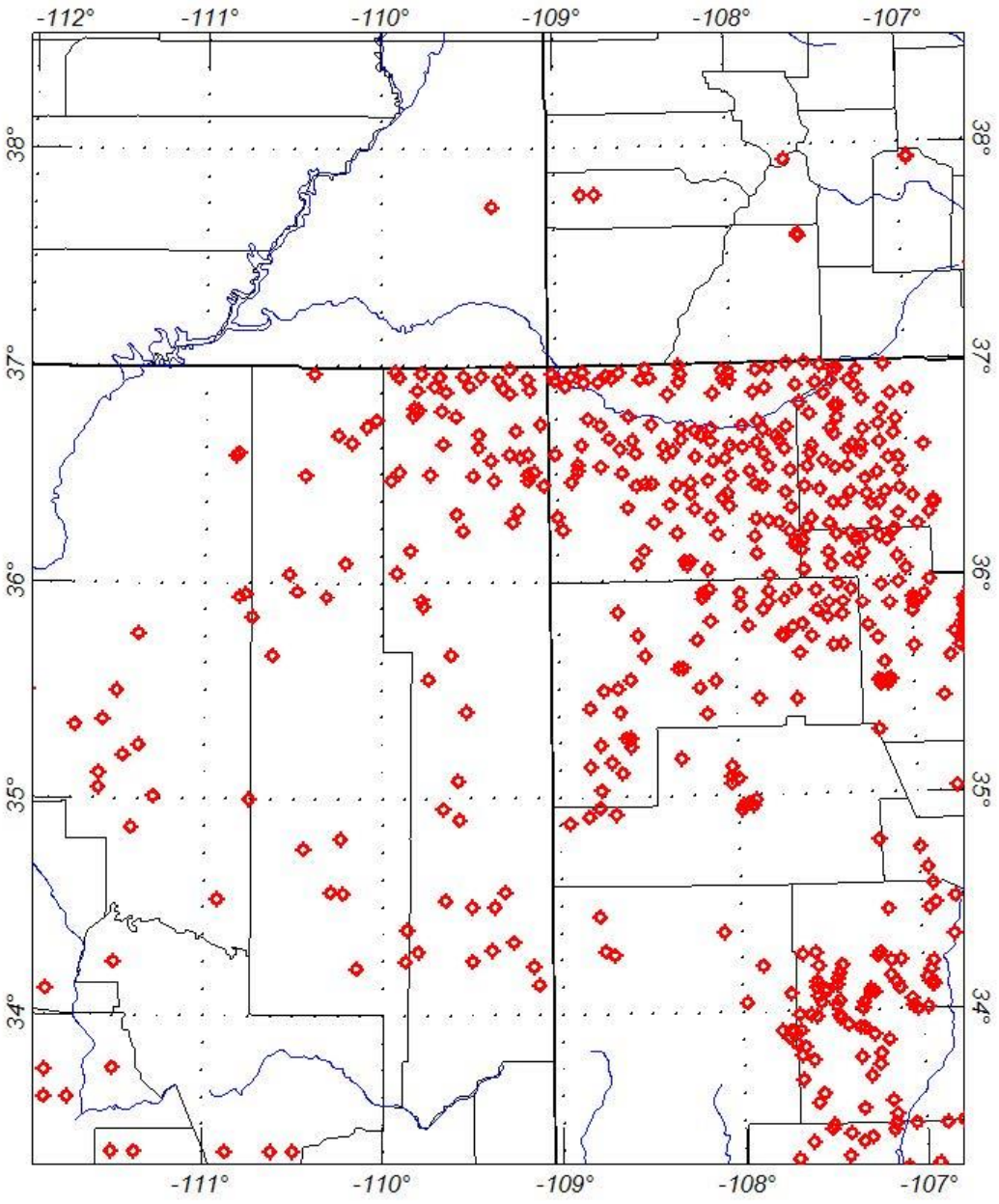


Figure 90. Measured public domain borehole temperature well locations used in Thermal Properties Study. Used as control for determining the shallow thermal characteristics of the area, and as constraints for our thermal calculations of the basin, and determinations of thermal gradients in the area.

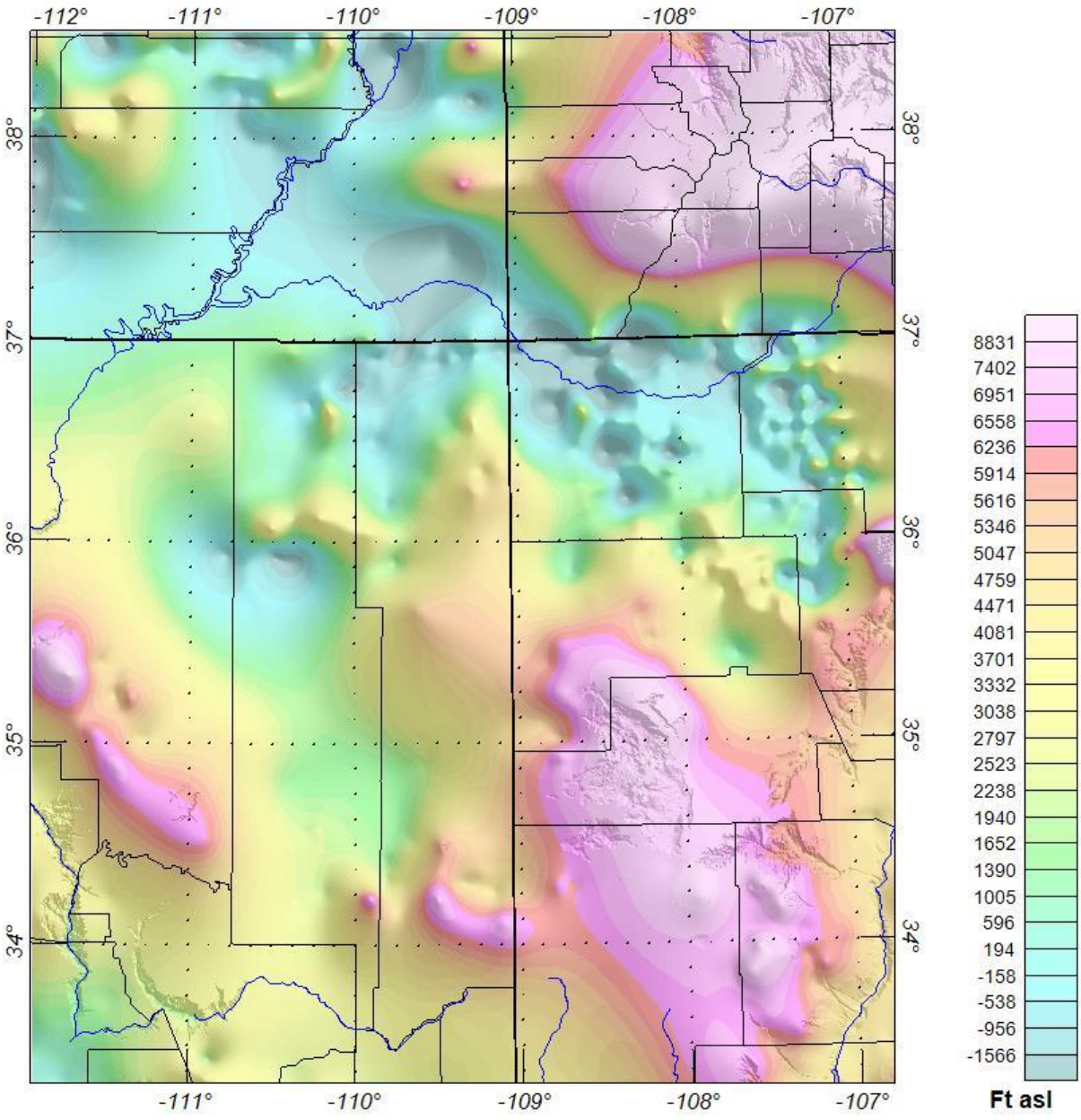


Figure 91. Grid of measured borehole temperature subsea depth of measurement from data samples shown on Figure 90.

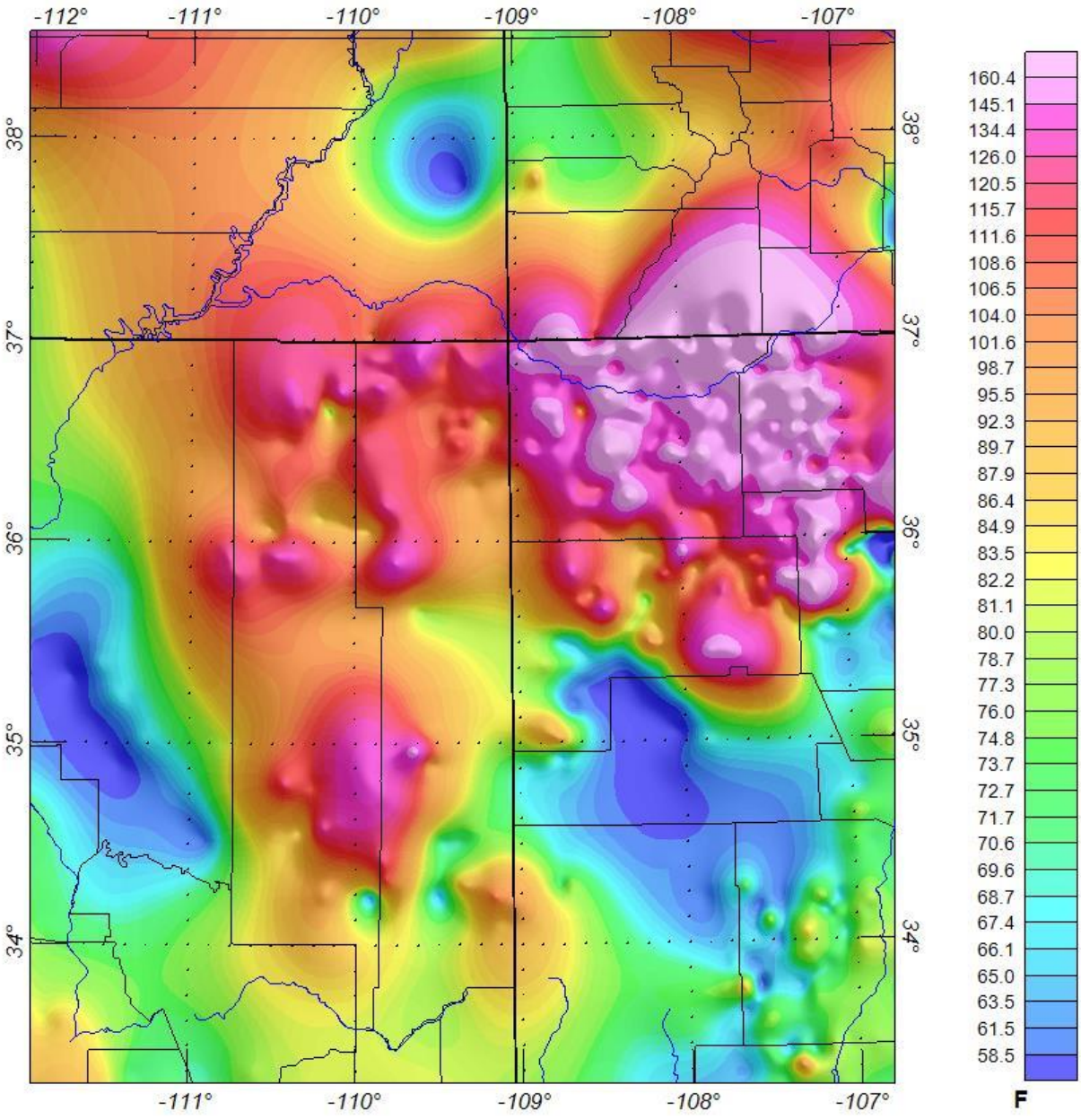


Figure 92. Calculated corrected borehole temperatures in °F. These values have been determined using the data shown on Figure 91.

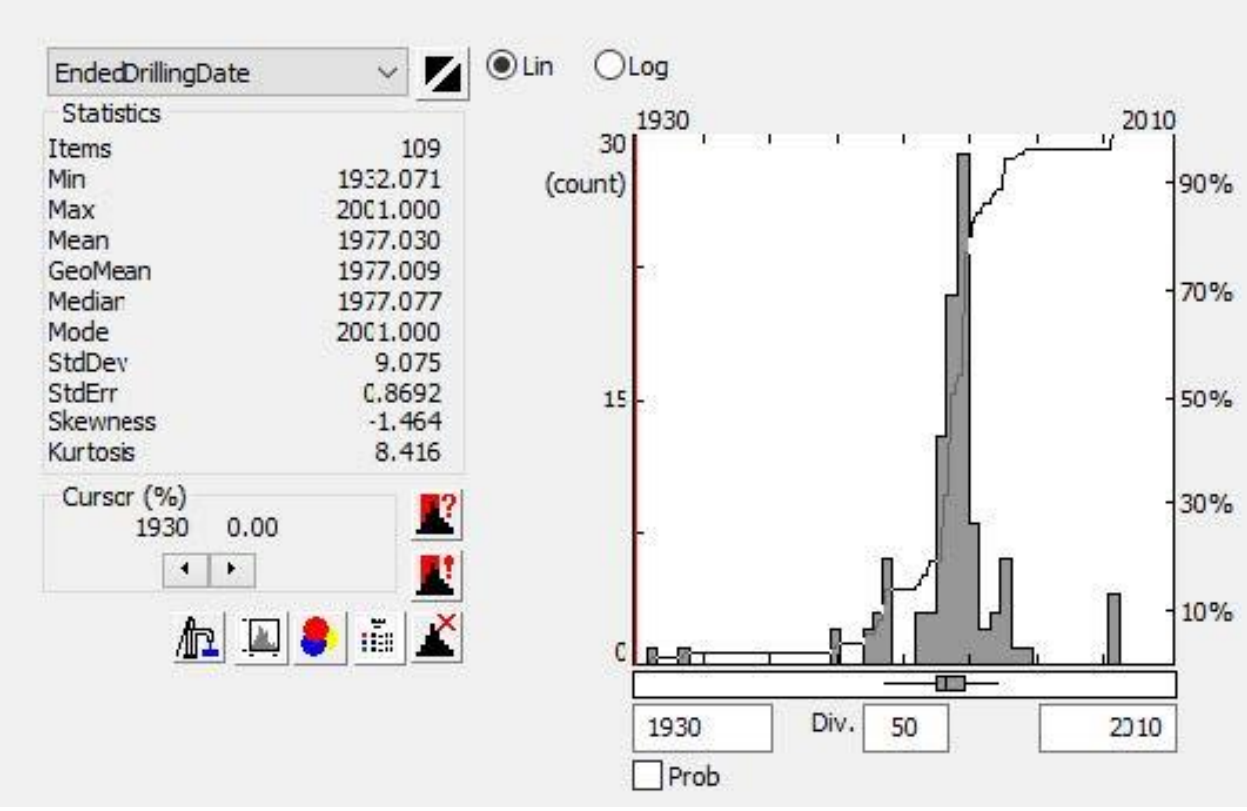


Figure 93. Borehole temperature well drilling dates. These drill dates have then been used to calculate the dates to use in the extraction of historical public domain temperature values for the period of the actual drilling of the wells. We have thus been able to accurately determine the average surface temperature for our study area. This provides the 1st temperature horizon (top of basin layer) and used in the calculations of thermal gradients (Fourier's Law), and thus heat flow for the basin, radiogenic/magnetic layer, and background layers.

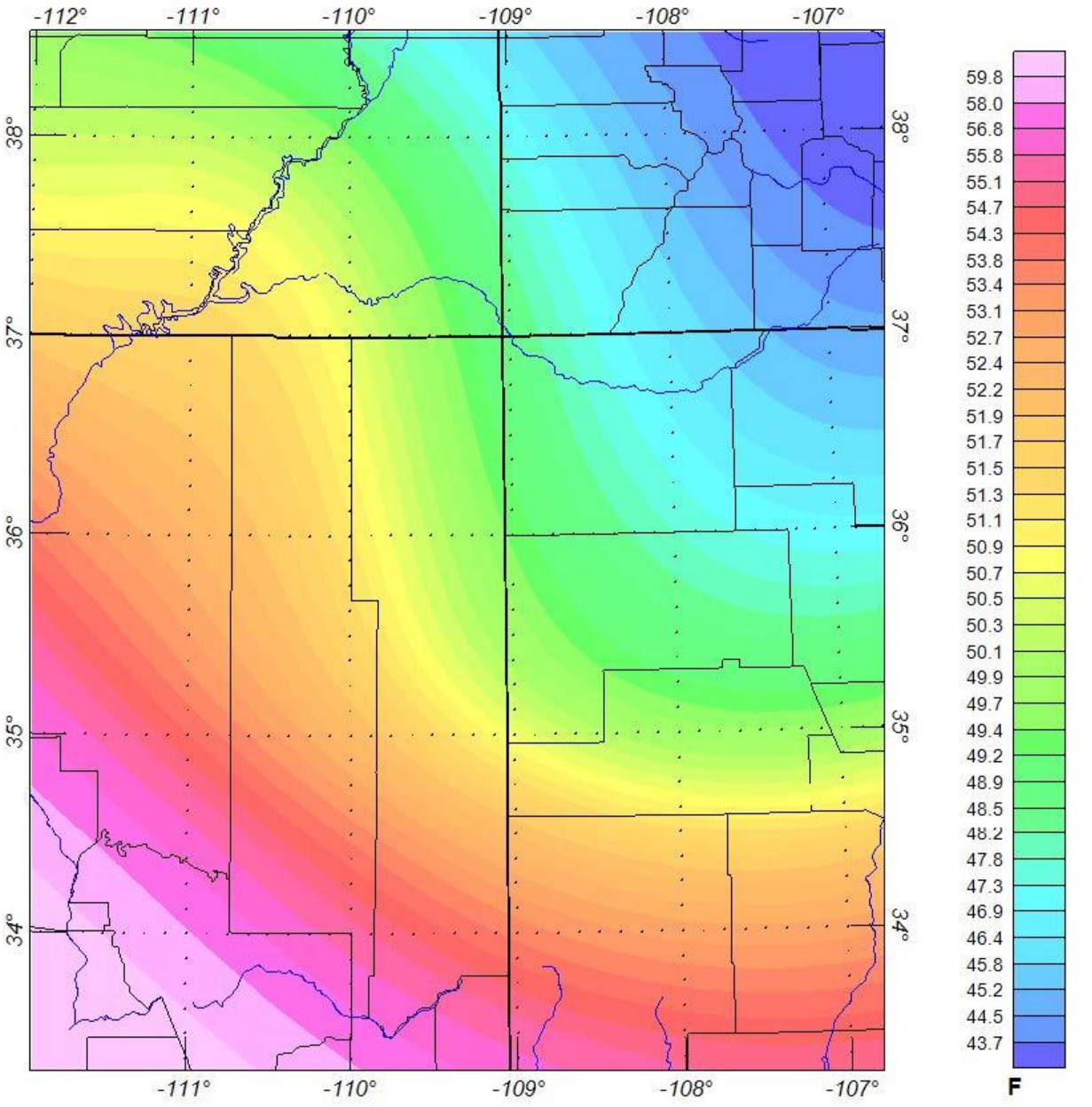


Figure 94. Average measured air temperature 1968-1986 from historic, public domain temperature measurements. These data have been used in the calculation of thermal gradients, and ultimately heat flow.

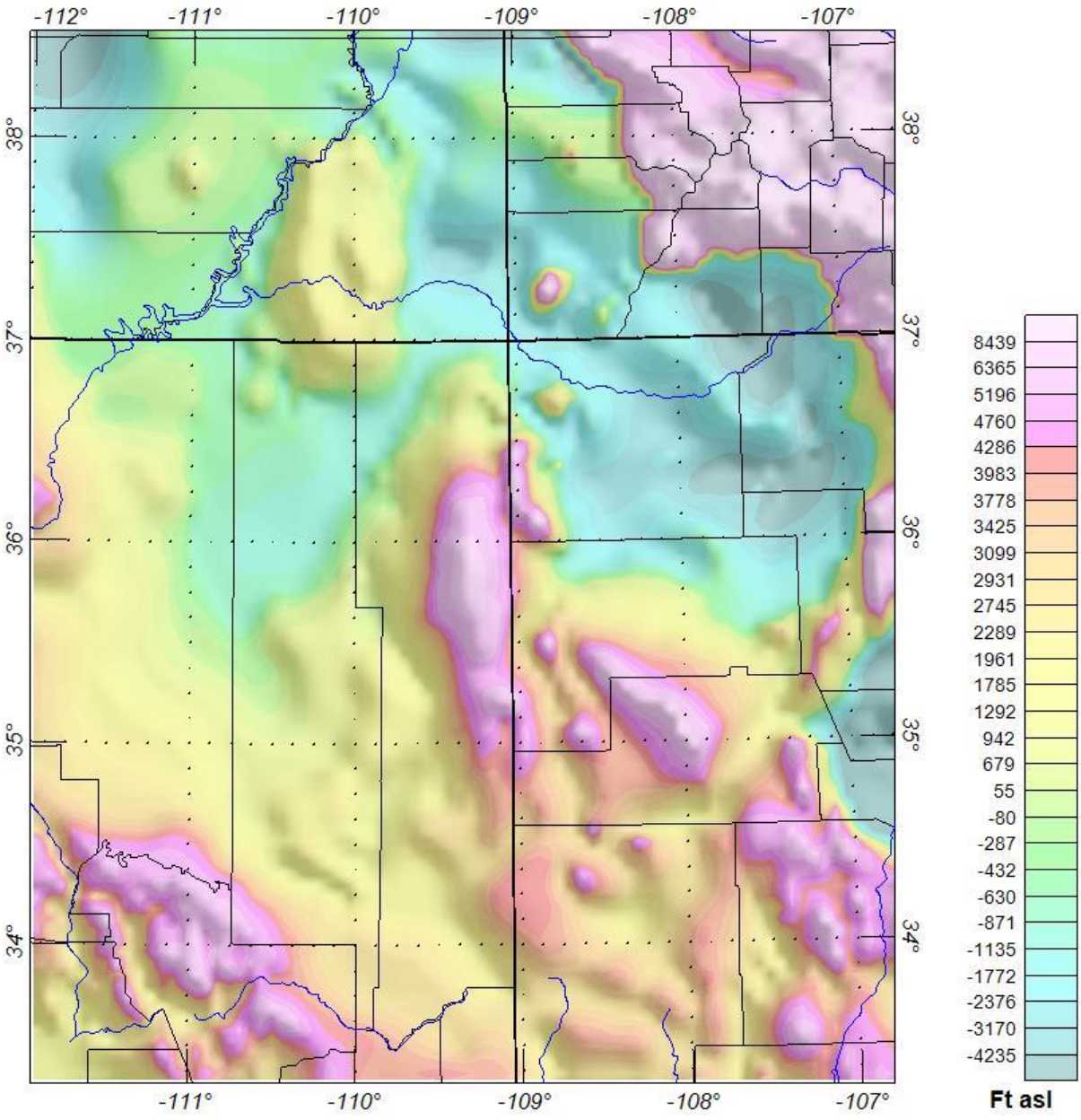


Figure 95. Near surface horizon – heat flow measurements taken from public domain borehole data shown on Figure 90 and used as calibration for the heat flow calculations produced in this study.

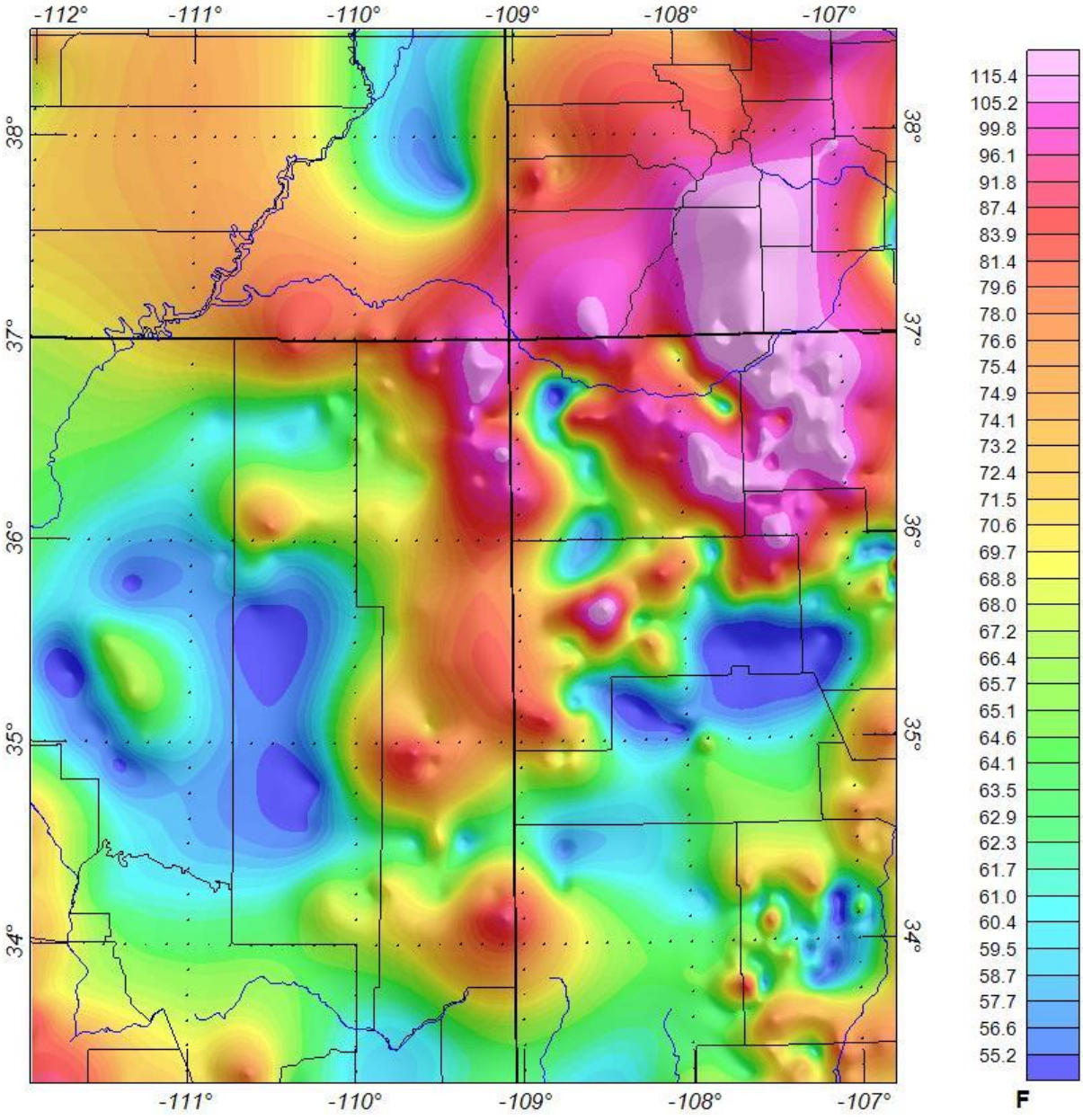


Figure 96. Near surface temperature from the public domain temperature data and used to define the temperature of the surface (first temperature horizon used in our thermal gradient & heat flow calculations).

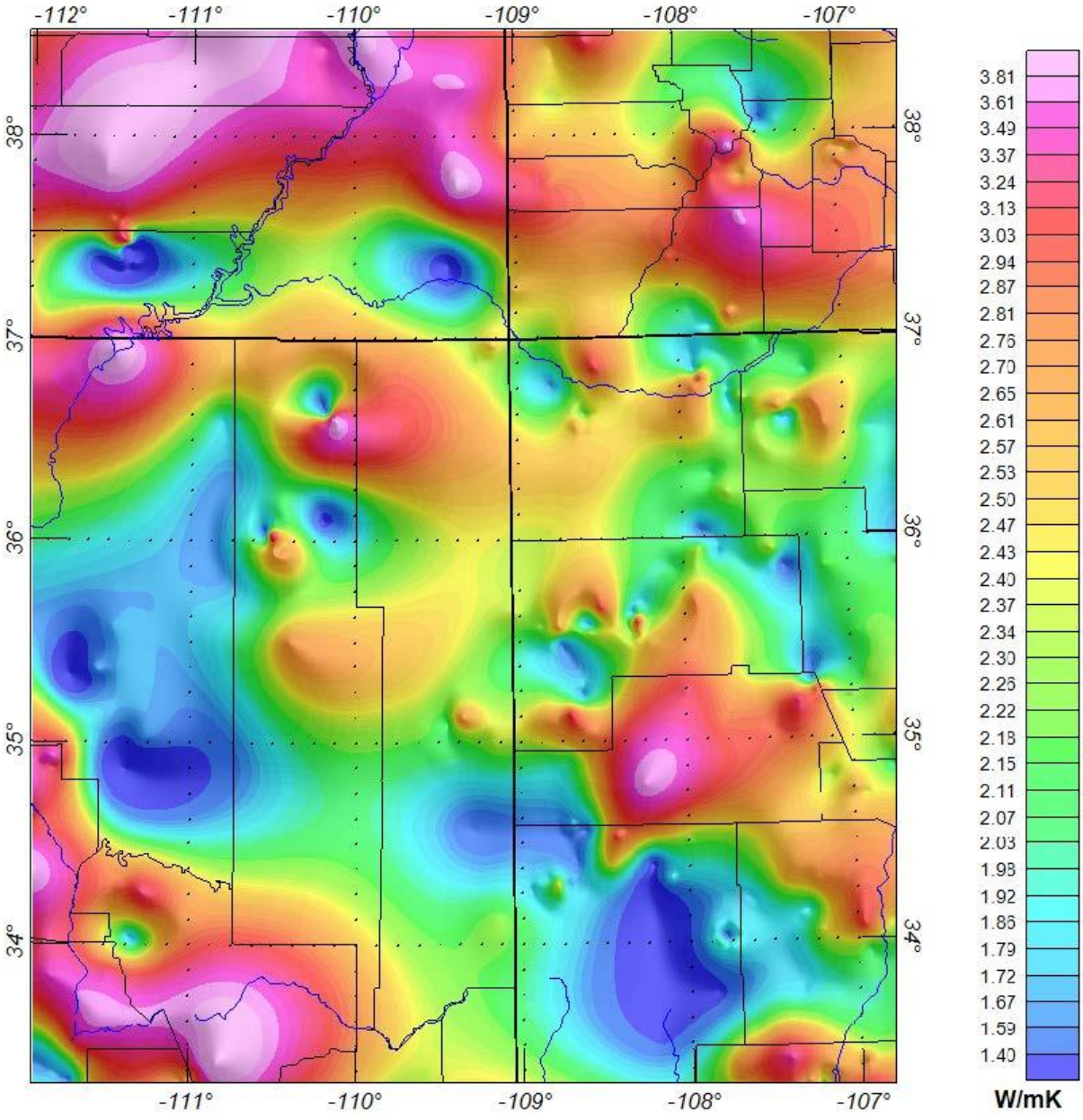


Figure 97. Measured basin thermal conductivity from the borehole data points displayed on Figure 90 and used in the calculation of heat flow using Fourier's Law.

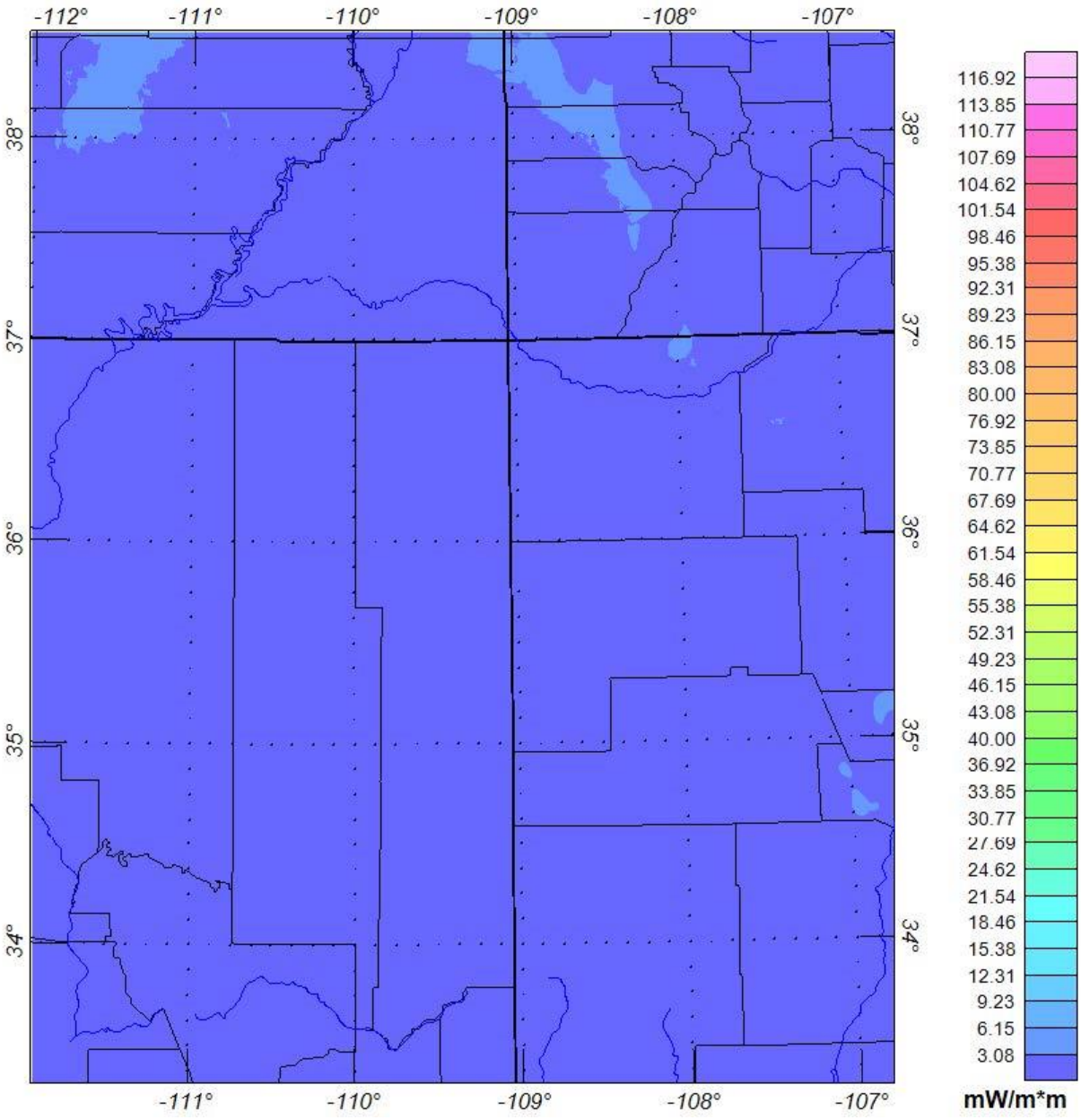


Figure 98. Calculated basin heat production values using Fourier's Law, and the borehole temperature/heat production/heat flow points shown on Figure 90.

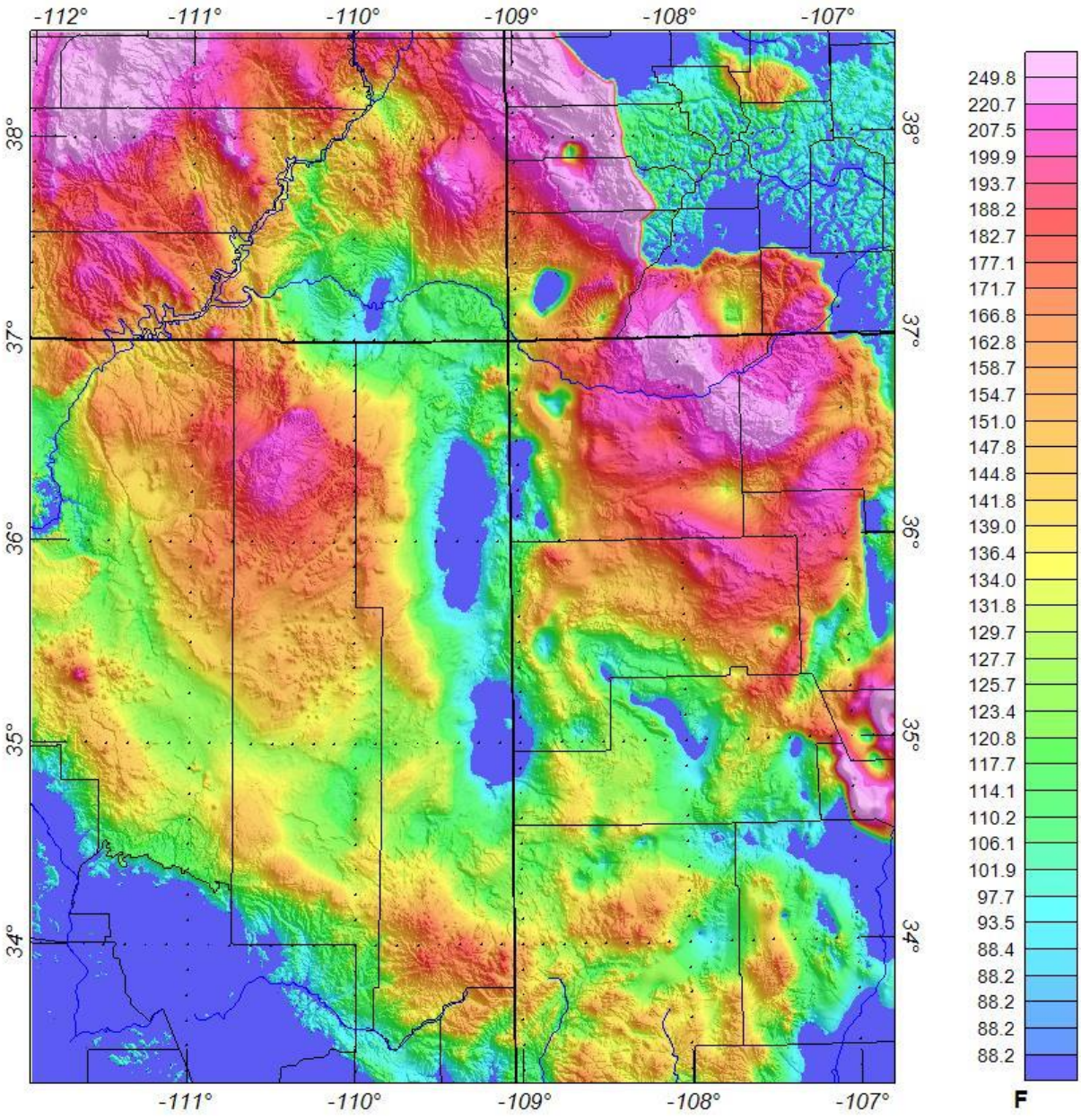


Figure 99. Calculated basement temperature. Using Fourier's Law, and the computation of the thermal gradient of the basin from the borehole data shown on Figures 88 and 90, the temperature to the interpreted basement surface has been determined.

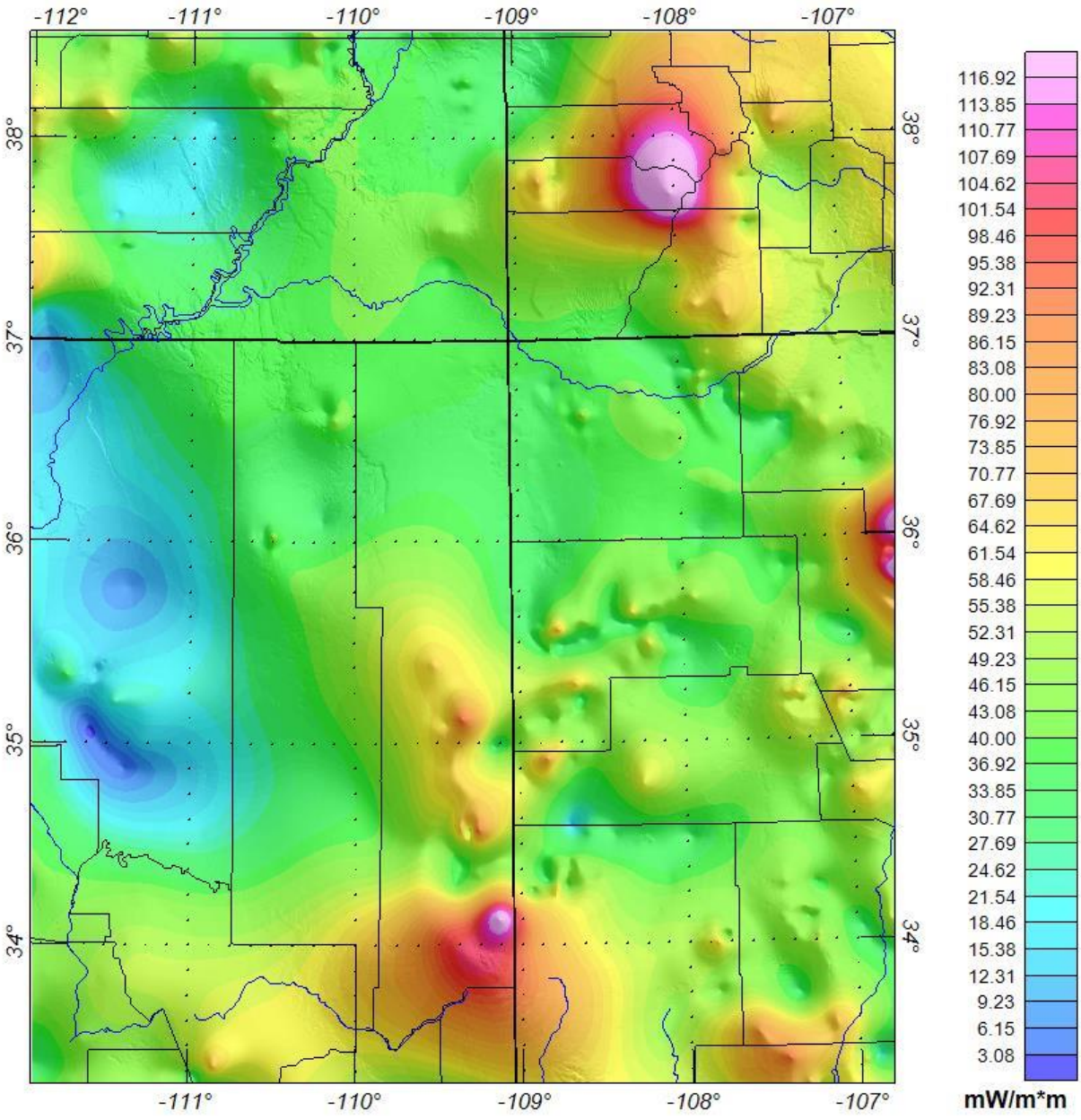


Figure 100. Calculated background heat flow. Using Fourier's Law, the heat flow of the background layer has been calculated.

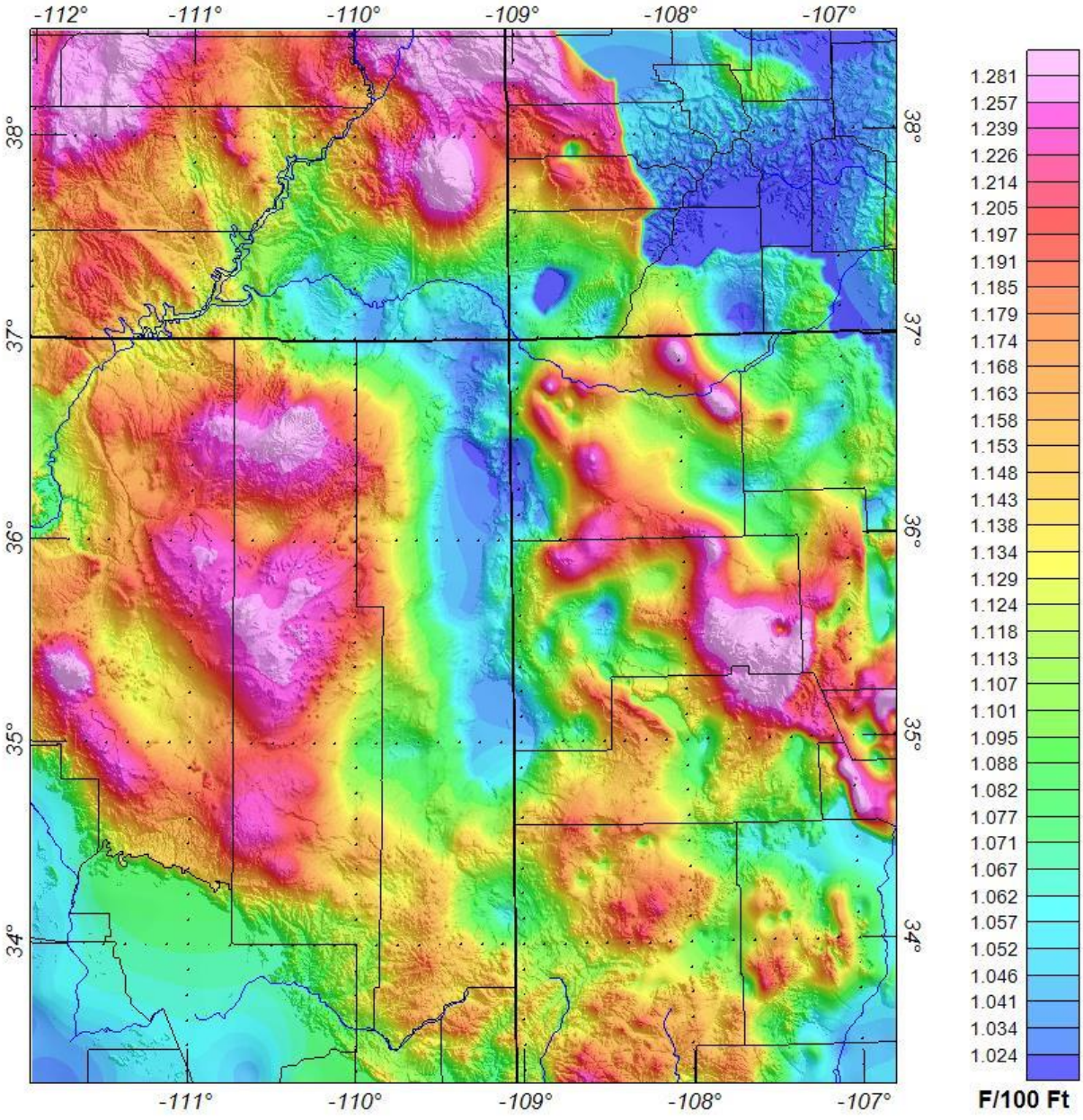


Figure 101. Calculated basin Thermal Gradient. The basin thermal gradient has been calculated used the public domain borehole data shown on Figure 90 since measurements of temperature have been determined at the surface (top of basin), and at various depths within the borehole data. These calculated data are then used as part of the calculation of the basin heat flow, and total heat flow.

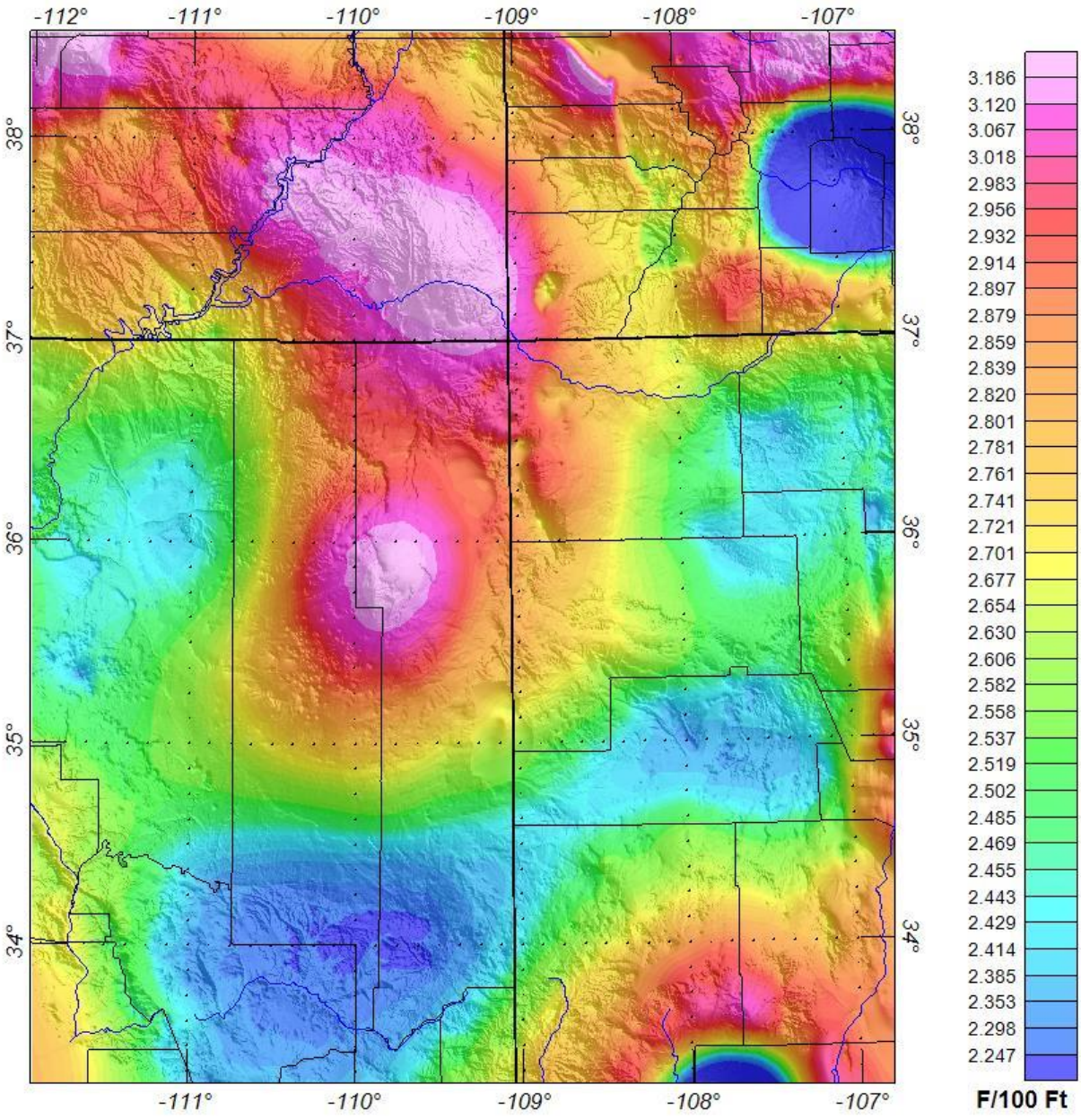


Figure 102. Calculated magnetic layer thermal gradient. The magnetic layer thermal gradient has been calculated using the public domain borehole data shown on Figure 90, along with the magnetic & gravity depth to basement surface & calculated Curie point. These calculated data are then used as part of the calculation of the magnetic layer heat flow, and total heat flow.

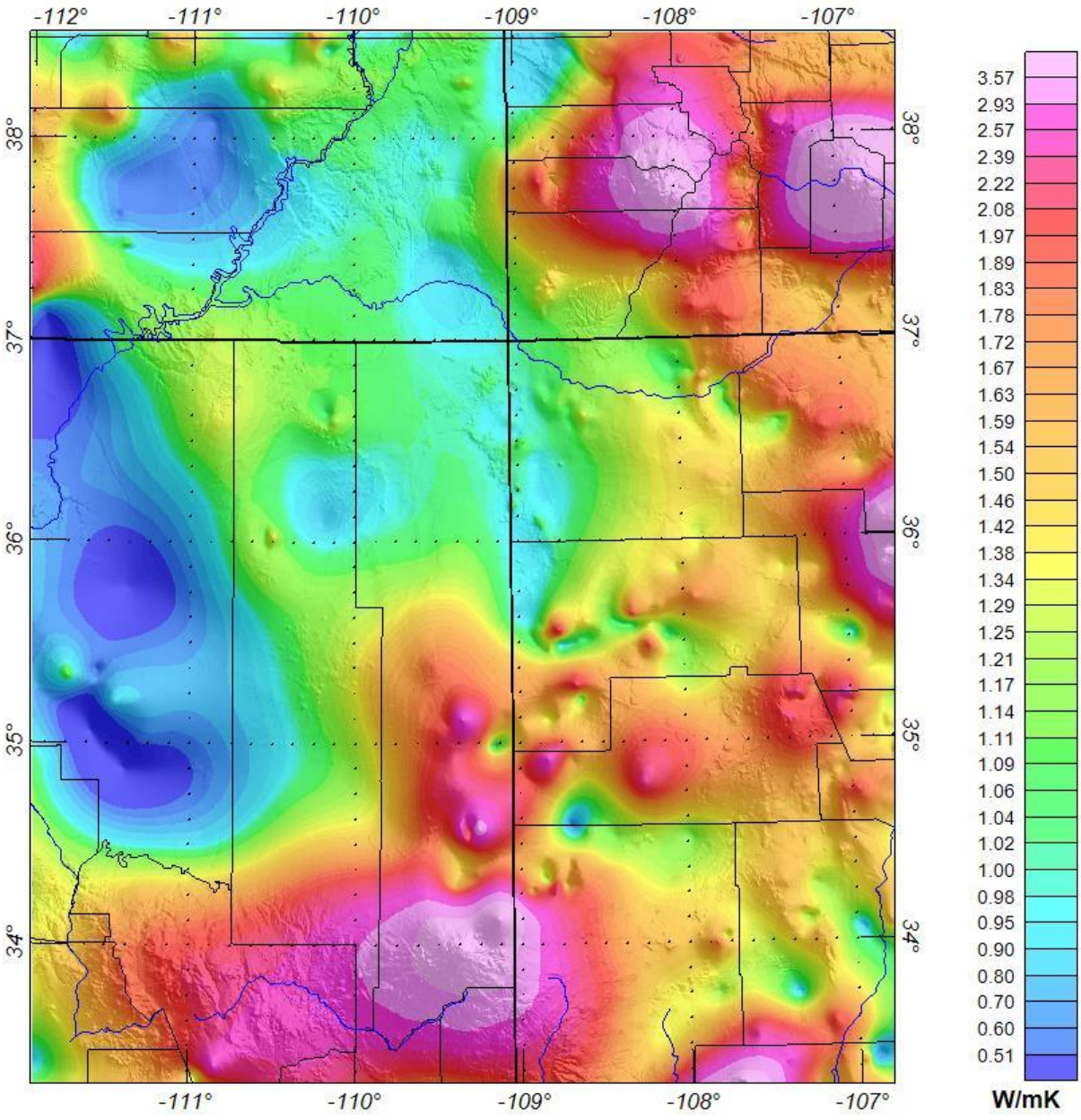


Figure 103. Calculated magnetic layer thermal conductivity. Using Fourier's Law, magnetic layer thermal conductivity has been calculated using the calculated background heat flow, calculated magnetic layer thickness, and calculated temperature at the magnetic layer interface, and temperature of the Curie point (80 °C). The resultant magnetic layer thermal conductivity is then used as part of the equation to calculate magnetic layer heat low (Figure 104).

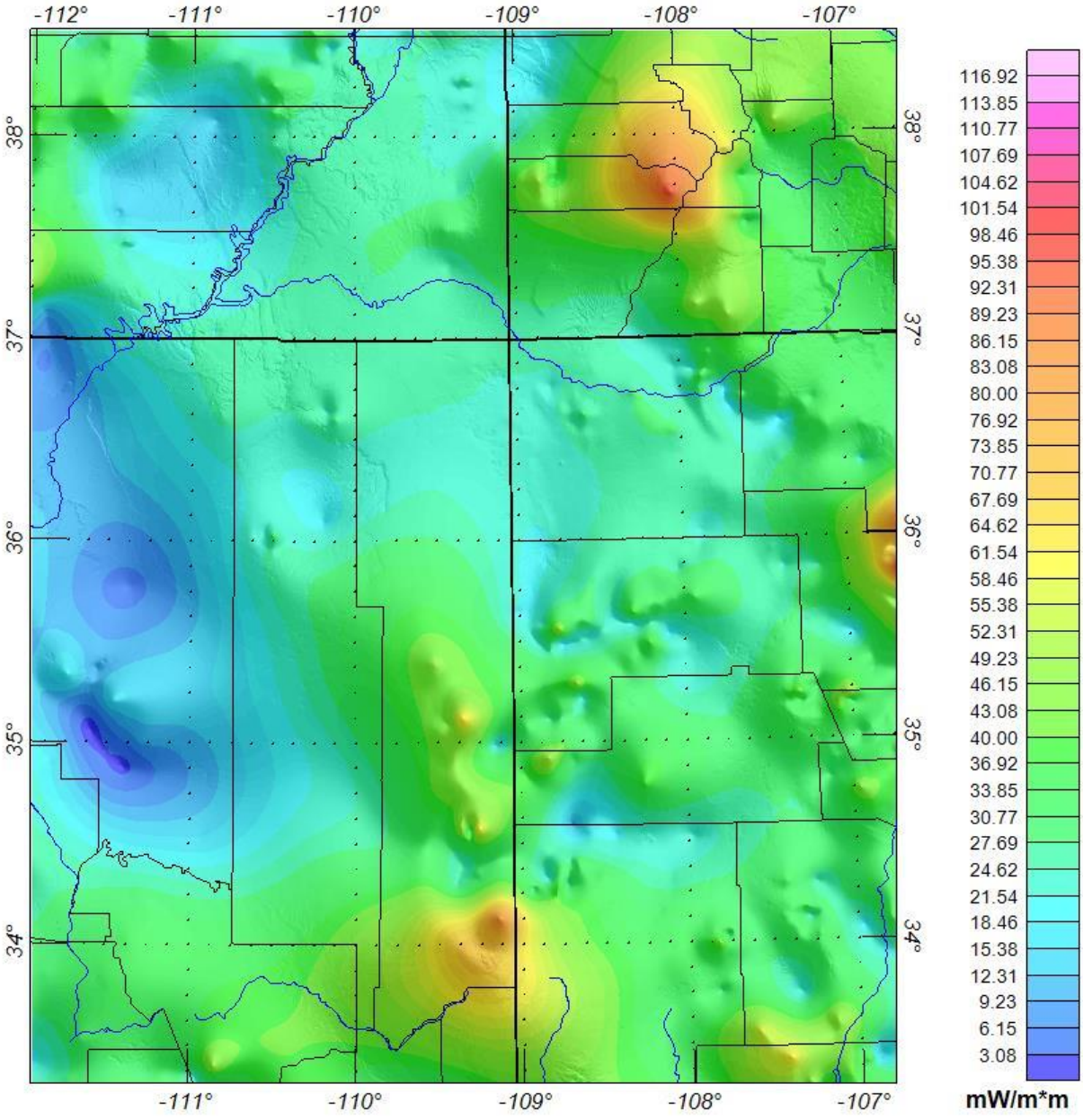


Figure 104. Calculated magnetic layer heat flow. The calculated magnetic layer thermal conductivity has been used in Fourier's Law to calculate the magnetic layer heat flow.

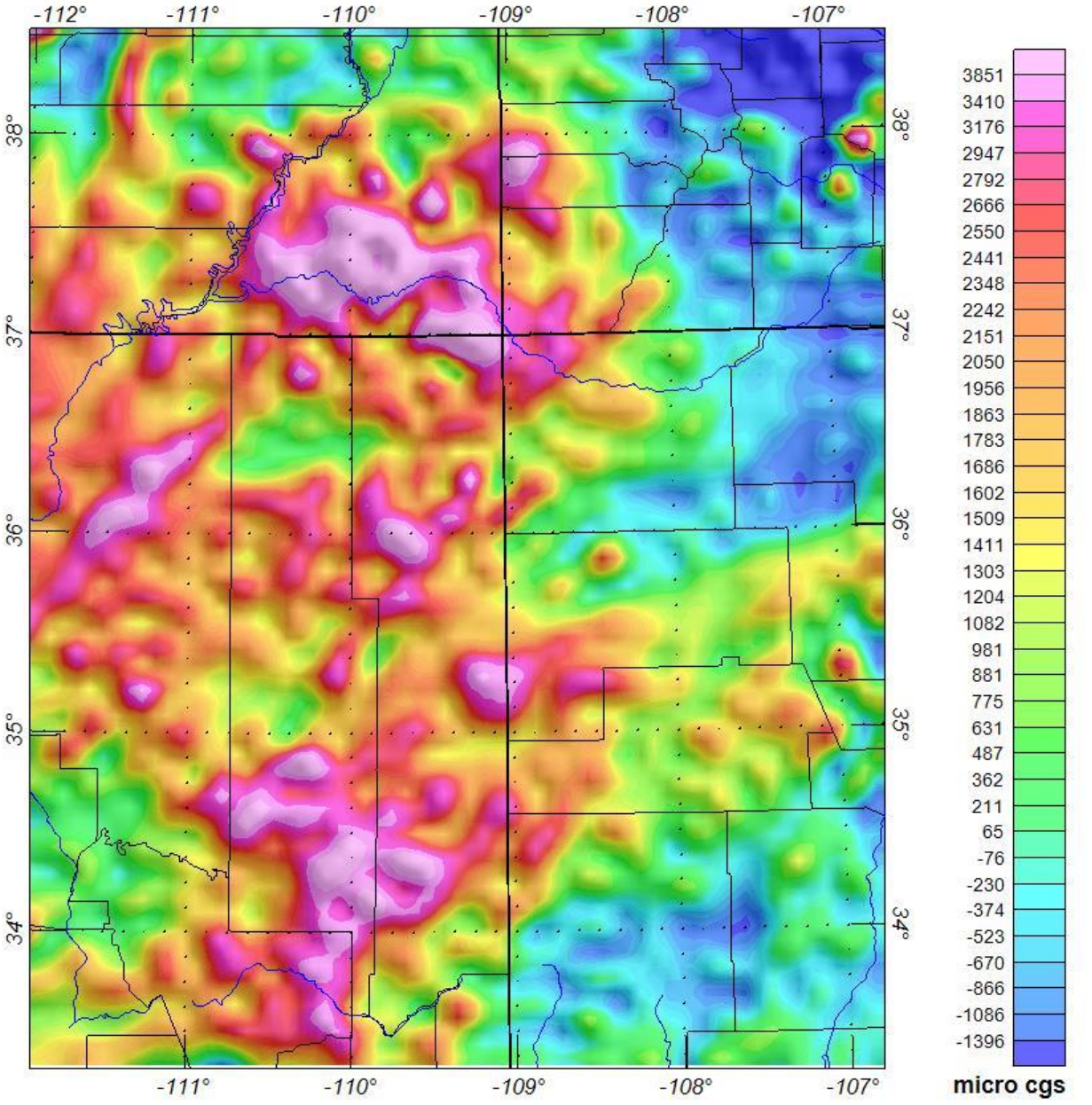


Figure 105. Calculated magnetic susceptibility 3D inversion – Basement to Curie point depth (Magnetic Layer). The calculated magnetic susceptibility has been generated from the 3D inversion of the magnetic data, using the interpreted basement surface to calculate the magnetic susceptibility of the magnetic layer. Variations in the calculated magnetic susceptibility of the magnetic layer indicates areas where the basement (magnetic layer) lithology changes exist. The resultant magnetic susceptibility data were then used along with published basement information to produce the interpreted basement (magnetic layer) terrane map (Figure 106).

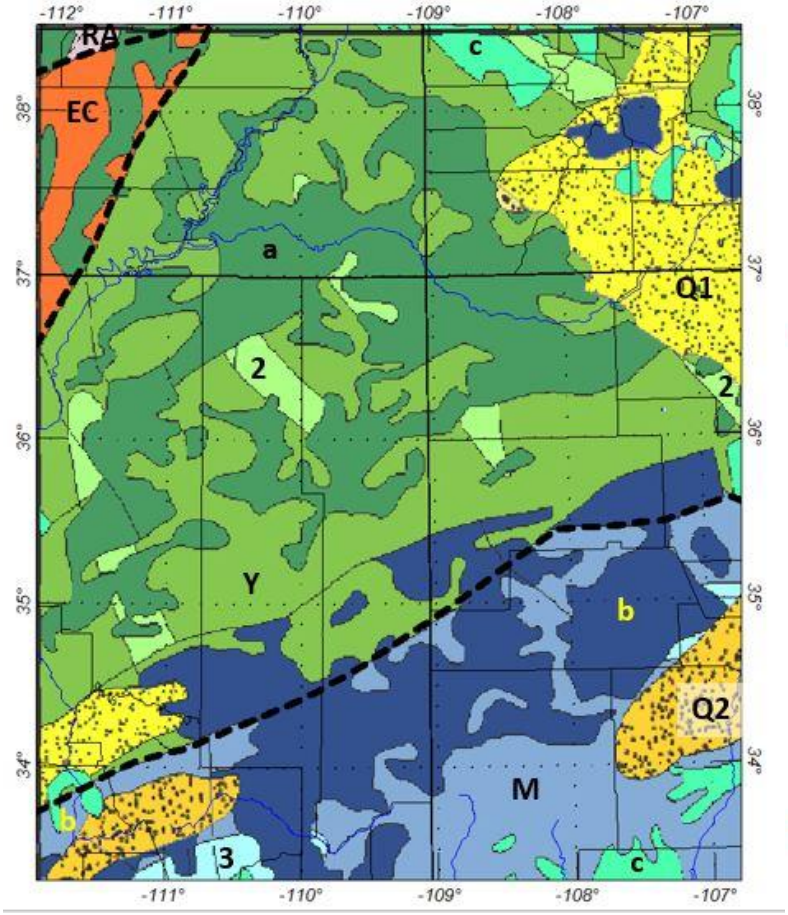


Figure 106. Interpreted Basement (magnetic layer) Terranes – Major crustal boundaries interpreted from the calculated magnetic susceptibility (Figure 105), and published basement terrane information of North America. The resultant basement (magnetic layer) terrane map is the used to calculate variations in heat production of the basement (magnetic layer).

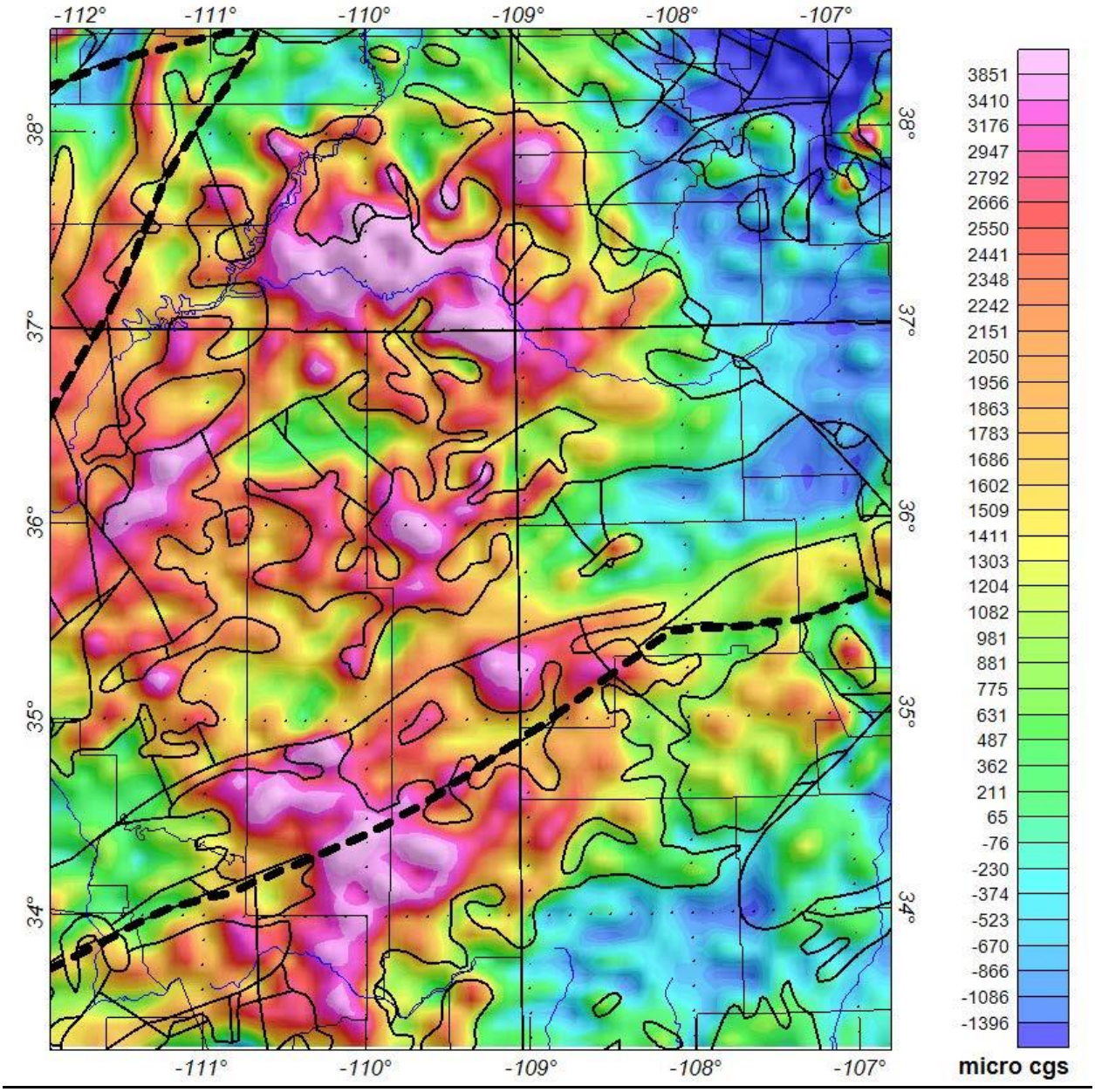


Figure 107. Calculated magnetic susceptibility 3D inversion (Magnetic layer) with basement terranes overlain for reference.

**CRUST terranes (heavy dashed lines):**
**RA:** Reworked Archean (pink), 1.9-1.8 Ga (Trans-Hudson orogeny) **2**
**Y:** Yavapai (olive green), 1.76-1.72 Ga, juvenile **4**
**M:** Mazatzal (purple), 1.69-1.65 Ga, juvenile **6**

**ARC terranes:**
**EC:** Elves Chasm Gneiss (orange), 2.0-1.8 Ga, juvenile arc **1**
**2:** 1.80-1.76 Ga (green), juvenile **3**
**3:** 1.72-1.68 Ga (blue), juvenile **5a**

**GRANETOID intrusions:**
a. 1.72-1.68 Ga (dark green) **5b**
b. 1.65-1.60 Ga (dark blue) **7a**
c. 1.45-1.35 Ga (aqua) **8**

**QUARTZITE deposits:**
**Q1:** ca. 1.70 Ga (yellow stipple) **5c**
**Q2**: ca. 1.65 Ga (orange stipple) **7b**

**Red** = oldest to youngest

Heat production stations were sorted and averaged by the basement terrane regions, then gridded to generate the heat production grid.

| | Age | Terrane | µW/m³ |
|---|---|---|---|
| 1 | 2.00 – 1.80 Ga | Arc (Elves Chasm) | **1.930** |
| 2 | 1.90 – 1.80 Ga | Crust (reworked Archean) | **2.150** |
| 3 | 1.80 – 1.76 Ga | Arc | **2.860** |
| 4 | 1.76 – 1.72 Ga | Crust (Yavapai) | **2.570** |
| 5a | 1.72 – 1.68 Ga | Arc | **3.090** |
| 5b | 1.72 – 1.68 Ga | Granitoid intrusions | **3.050** |
| 5c | 1.70 Ga | Quartzite deposits | **2.860** |
| 6 | 1.69 – 1.65 Ga | Crust (Mazatzal) | **2.841** |
| 7a | 1.65 – 1.60 Ga | Granitoid intrusions | **2.750** |
| 7b | 1.65 Ga | Quartzite deposits | **2.700** |
| 8 | 1.45 – 1.35 Ga | Granitoid intrusions | **3.197** |

Figure 108. Interpreted basement terranes heat production. The heat production values have been determined by using the various interpreted basement terrane/lithologies from the magnetic susceptibility calculations, and published heat production values of various crystalline basement lithologies from around the world. These values are then applied to the interpreted basement terrane map (Figures 106 & 107), and used to calculate the magnetic layer heat production (Figure 109).

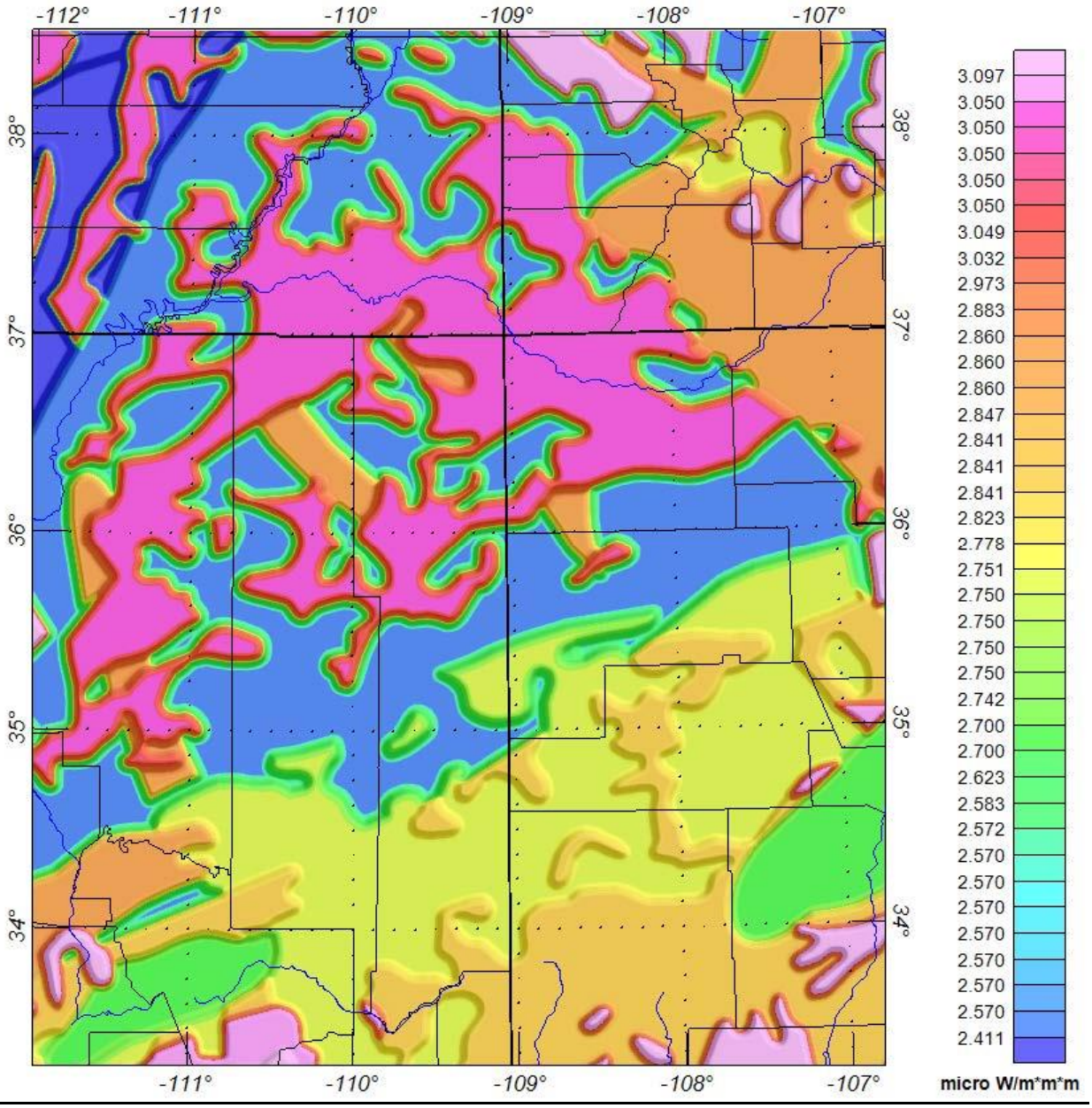


Figure 109. Calculated magnetic layer heat production. This grid was produced using the interpreted basement terrane map, and interpreted basement heat production values. Using Fourier's Law, it is then possible to calculate the total heat flow for the area, after calculating and using the magnetic layer thickness (Figure 110).

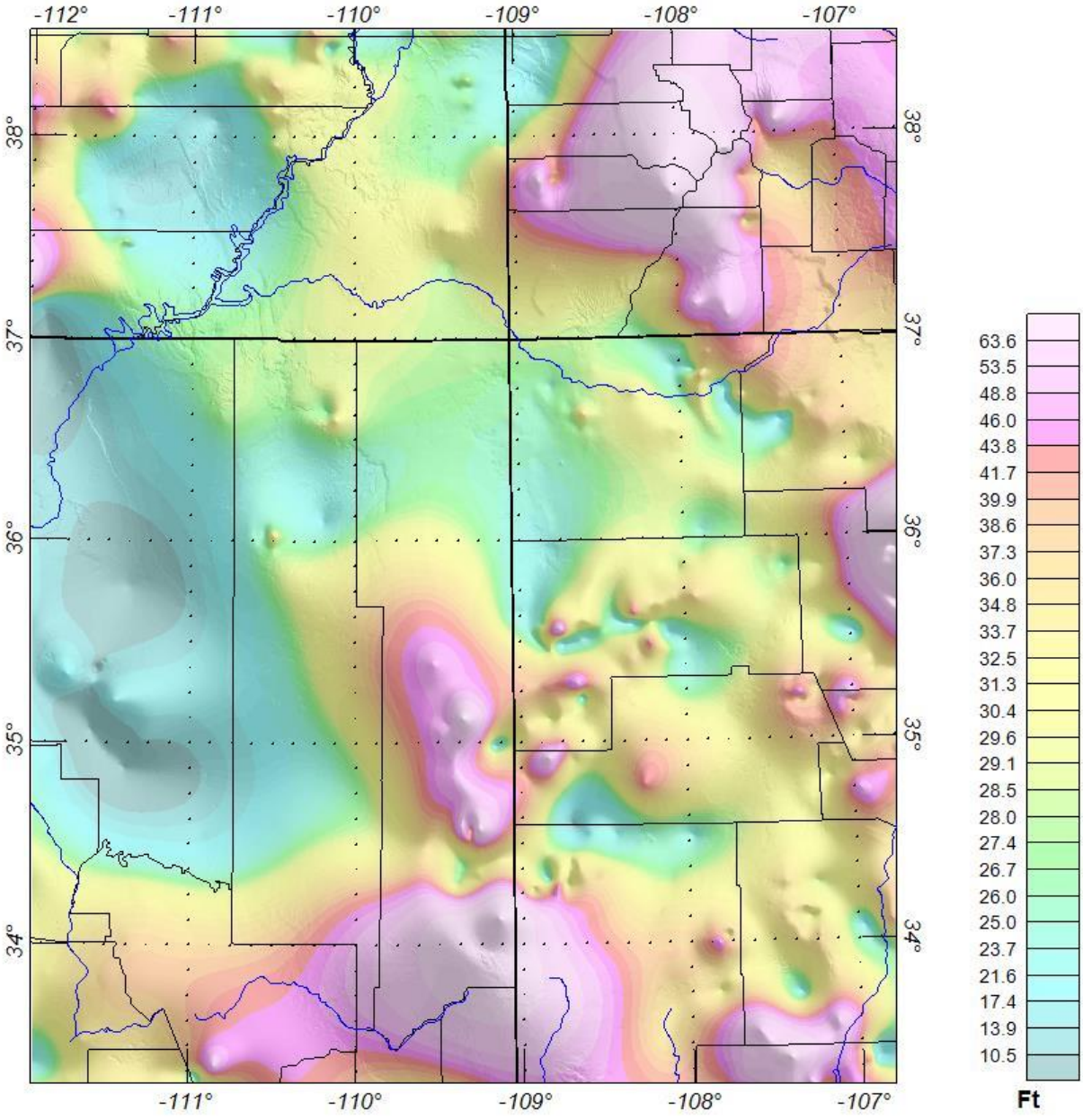


Figure 110. Calculated heat production layer thickness. Calculated using the top of the magnetic layer, and the Curie point/Moho surface. When combined with the magnetic layer heat production, and again using Fourier's Law, it is possible to calculate the total heat flow of the area (Figure 111).

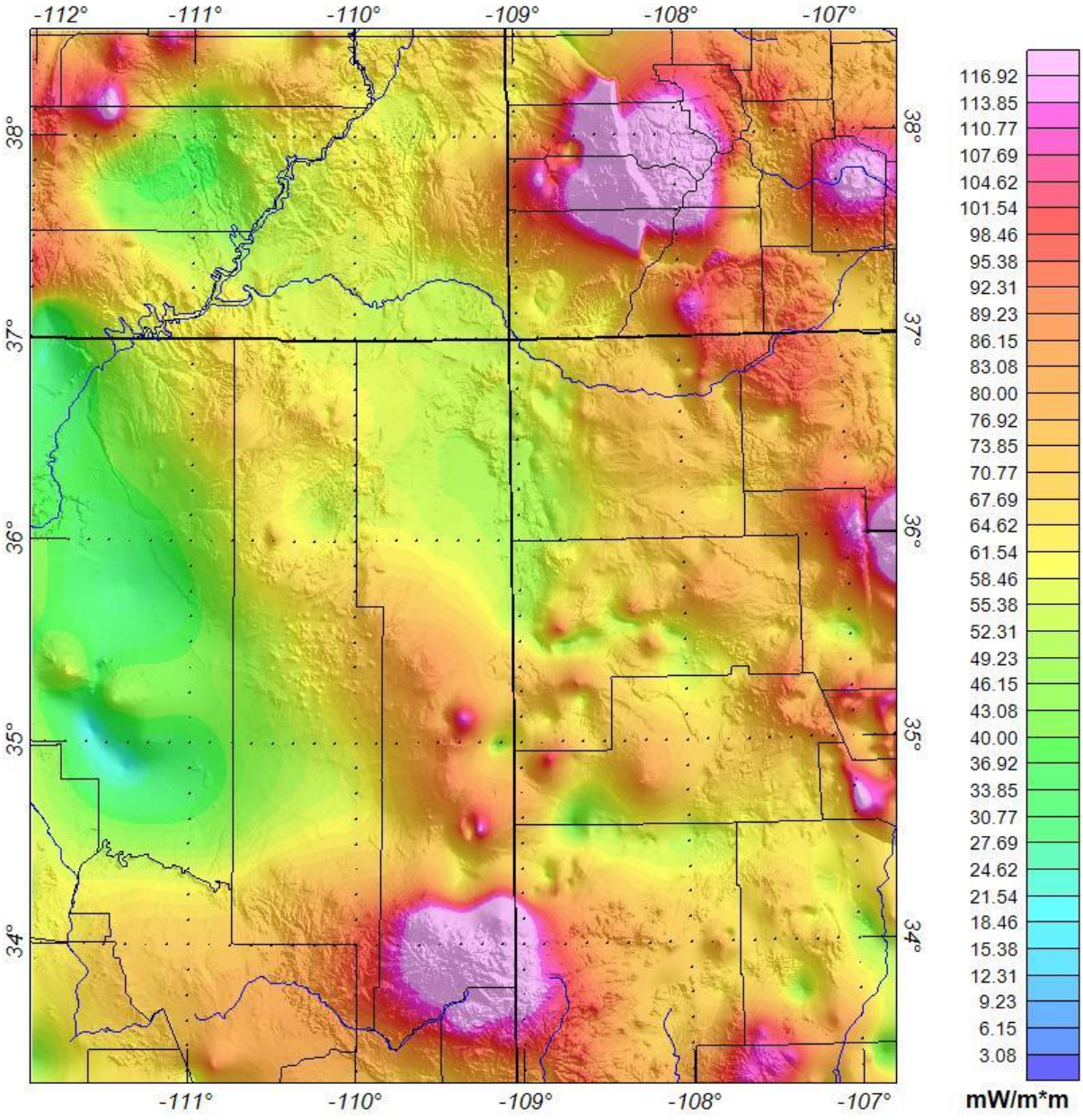


Figure 111. Calculated final total heat flow. The total heat flow has been calculated utilizing the magnetic layer heat production, and magnetic layer thickness as inputs into Fourier's Law. The total heat flow grid displays areas of increased heat flow, which may have relationships to increased helium generation.

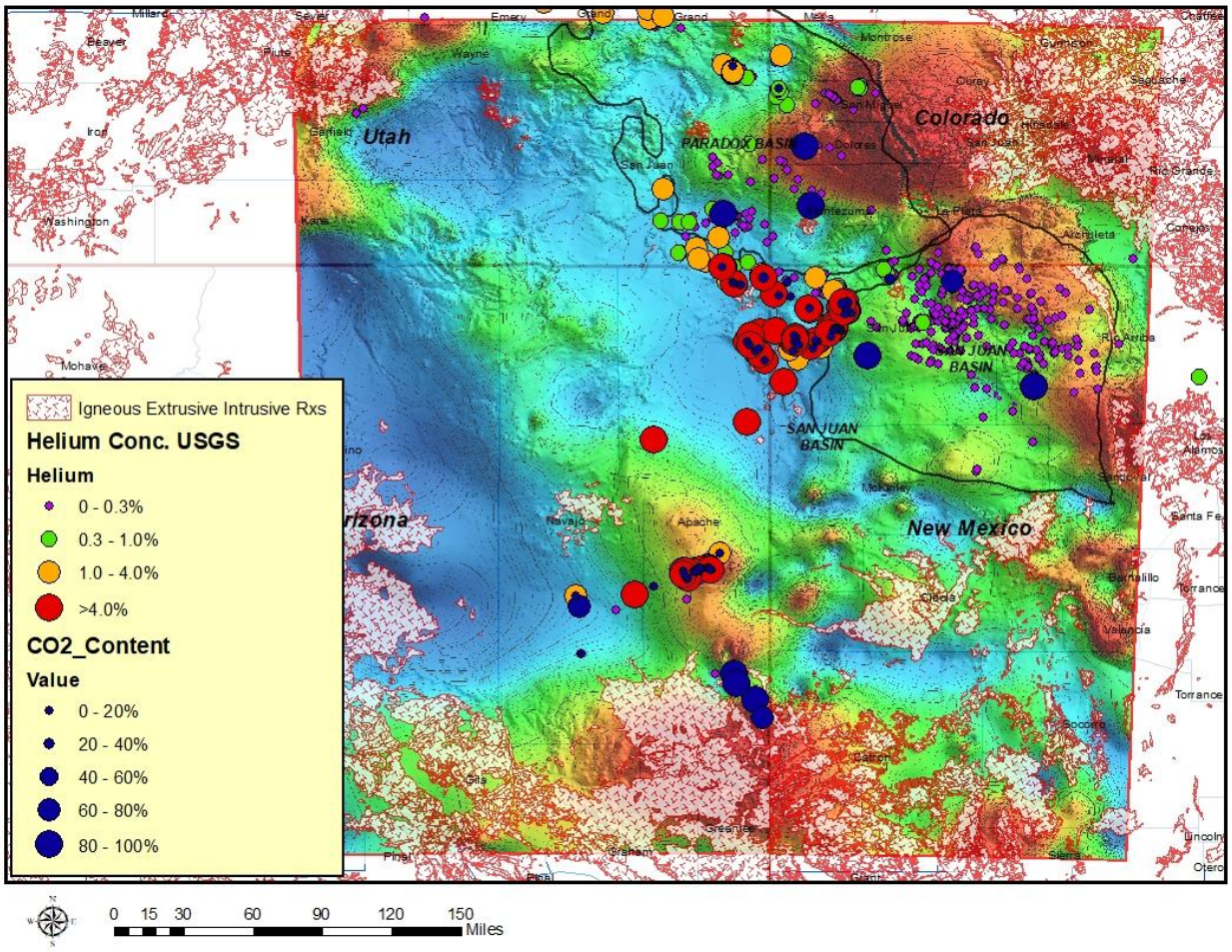


Figure 112. Calculated final Heat Flow and distribution of helium and $CO_2$ concentrations. The final calculated heat flow represents present-day conditions and areas of high heat flow (red areas) do not correspond to areas of high helium concentrations. Instead, the high heat flow areas correspond to recent volcanic activity of the Basin and Range extension and the Rio Grande rifting. $CO_2$ distribution correlates well with areas on high heat flow and has migrated and filled the San Juan and Paradox basins diluting and displacing any previous high helium deposits.

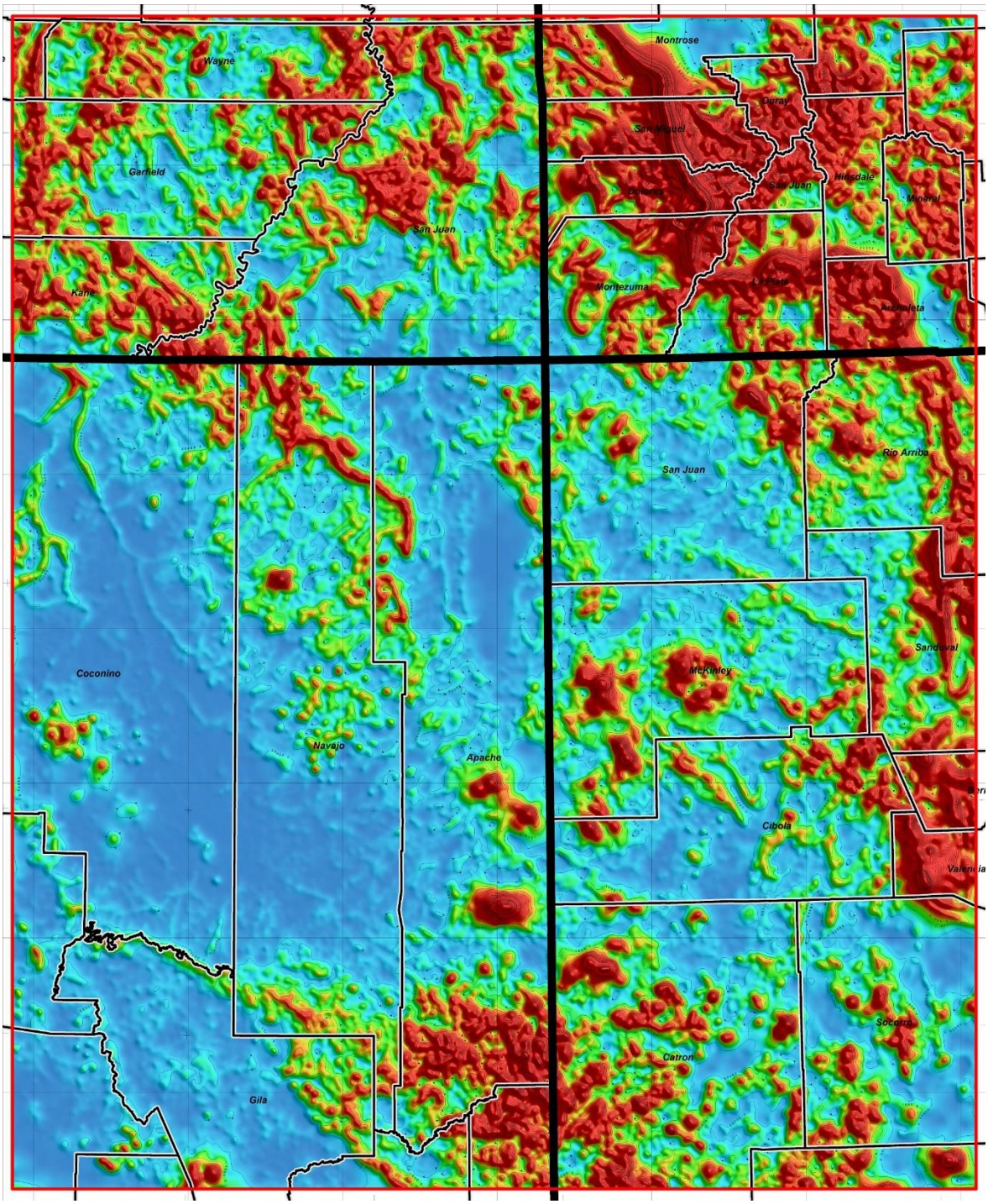


Figure 113. Calculated Analytic Signal of the calculated final Heat Flow. The analytic signal of the heat flow is defined as the square root of the sum of the squares of the vertical and the two horizontal derivatives of the calculated heat flow. The analytic signal is useful in locating the edges of heat flow source bodies, particularly where subtle heat flow anomalies are difficult to identify when inspecting the total heat flow. The resultant grid displays areas where local heat flow exists, possibly identifying subtle heat flow differences produced from intrusive bodies.

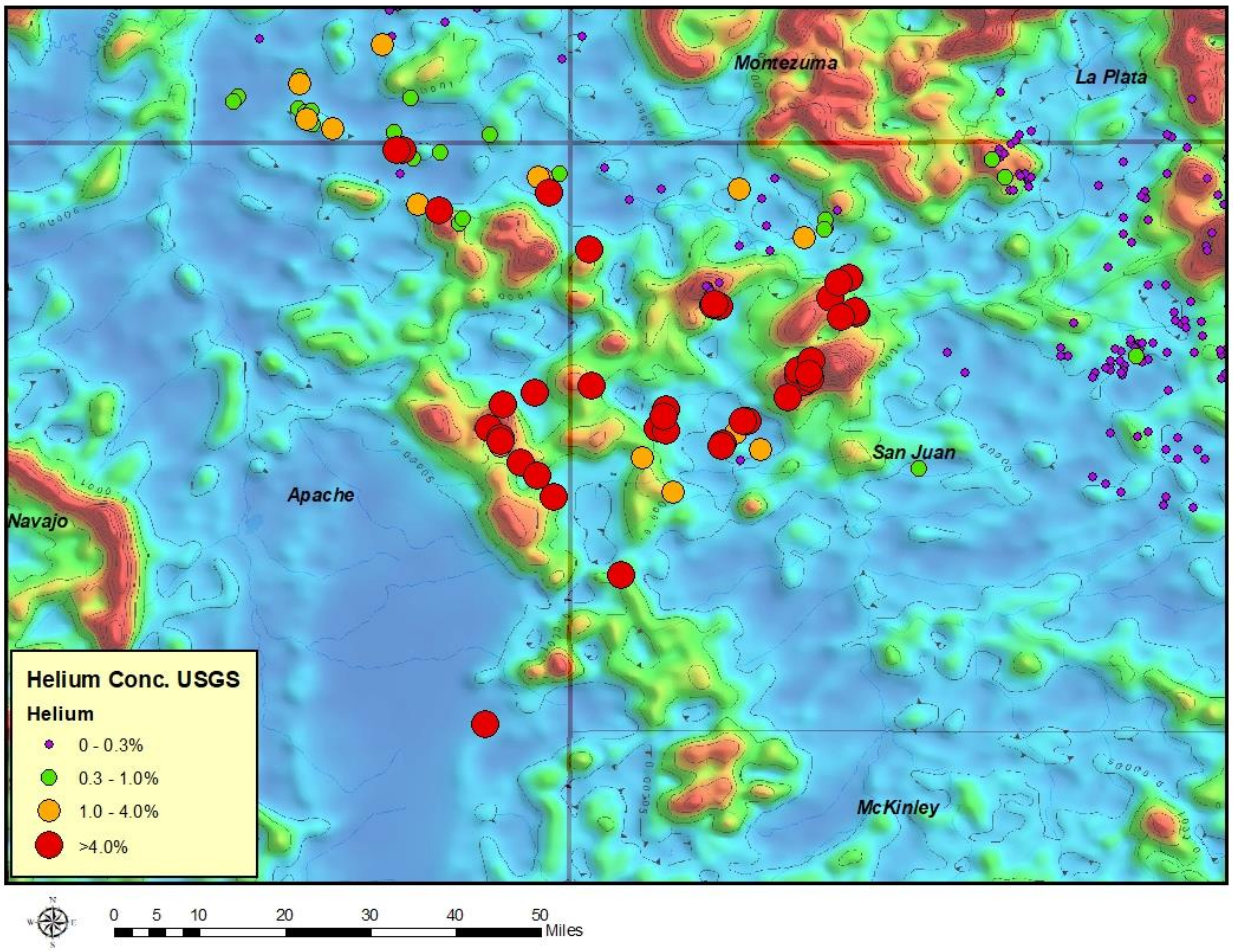


Figure 114. Calculated final Heat flow analytic signal and distribution of helium in the Four Corners. Analytic signal (filtered heat flow) shows some relationship between residual heat flow related to the Navajo Volcanic field and high helium concentrations.

## Helium soil gas concentration measurements

Measuring helium content in soils has been used as a technique for uranium exploration since the early 1980's (Hinkle and Kilburn, 1980, Reimer and Bowles, 1983, Been et al., 1984). The technique has also been used to map the extent of subsurface helium deposits (Roberts, 1981). Some of the main problems with exploring for helium are that migration pathways that the helium-enriched gas took from the source via fractures are complex and difficult to predict. Identifying a structural trap doesn't mean that it is charged with helium-rich gases nor the degree of trap fill. The viability of measuring helium soil gas concentrations to identify subsurface helium accumulations is based on the assumptions that helium, given its extremely small atomic size and high diffusion coefficient, will continuously migrate through any sealing lithology that is trapping a gas accumulation and make its way to the surface in time. Helium is

also being continuously emitted from the Earth's surface at an average concentration of 5.240 ppm representing a background helium concentration while the subsurface helium deposits being explored generally range from 40,000 – 80,000 ppm. Anomalous soil helium concentrations should occur within soils directly overlying a helium-rich gas deposit, regardless of depth. Helium leakage through a seal is a function of the capillary entry pressure of the sealing horizon. When the reservoir pressure of the helium-rich accumulation exceeds the capillary entry pressure, helium can escape (Rice, 2022) (Figure 115). Gas will continue to escape until the reservoir pressure falls below the capillary entry pressure of the seal.

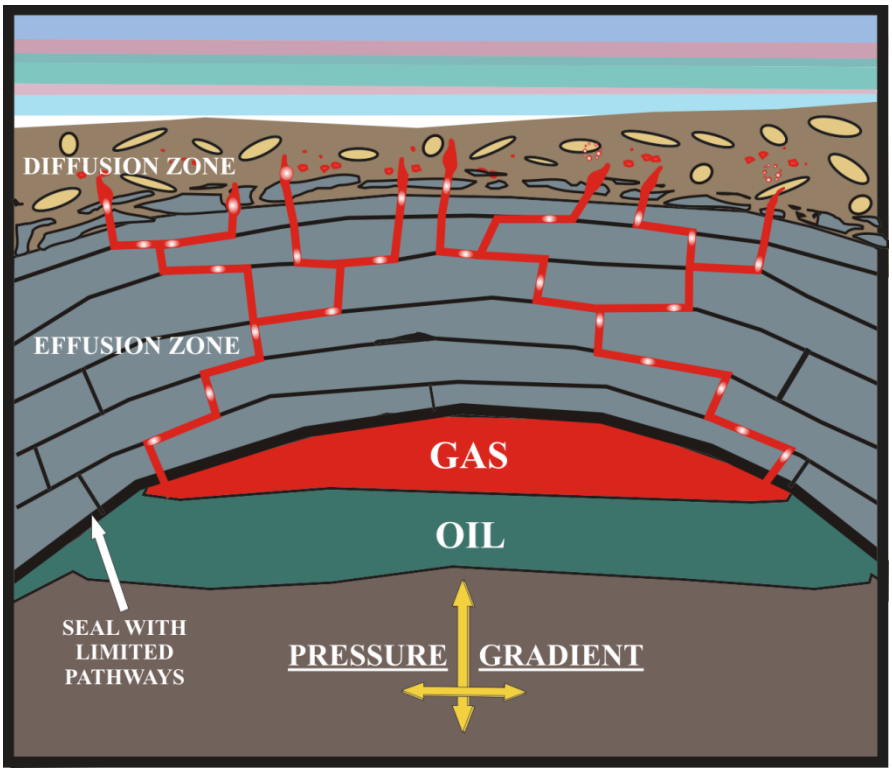


Figure 115. Illustration of buoyancy-driven vertical migration depicting migration of gases from the reservoir to the surface (Rice, 2022).

**Field Sampling**

The helium soil gas samples were collected over seven possible helium deposits (Figure 116). Surveys ranged in size from four to ten square miles and with sampling points every 1/8 mile (660 ft). Helium soil gas samples are collected from 1.5 to 3-foot depths. Rock outcrop was encountered in all the sampling locations at a depth of 1-3 feet. One area previously sampled by the USGS in Bisti, De-Na-Zin, and Ah-Shi-She-Pah wilderness areas was included in the study to help establish the helium soil gas background concentrations (Been et al., 1984).

Helium soil gas sample collection will be done using a modified soil auger as a probe and operated using a two-cycle engine powerhead. Trained, local Navajo contractors were used to

collect the helium soil gas samples. Safety precautions were exercised when using a soil gas probe. Safety glasses are recommended. With all moving parts there is a chance that struck materials could fracture and be forcefully displaced. Care was taken to be sure body parts were not in the way of the rotating soil auger probe or the powerhead engine. Care was also taken to locate and avoid any potential buried utility lines such as water, electricity, phone lines, etc.

At the beginning of each day and prior to any sample collection, the septum at the end of the sample collection port on the sample probe is replaced with a new one and the probe is leak tested to ensure no atmospheric air contamination can occur during sampling. Also, either the first sample or sometime during the day, an atmospheric gas sample is collected to help establish background atmospheric helium concentration levels. Once at a sample location, the powerhead engine is started, and the soil auger probe is drilled to a maximum depth of three feet (Figure 117). After the probe is at the desired depth, gas samples were collected by the following steps:

1. Using the syringe, withdraw 20 cc of soil gas and discard. The 20-cc volume is one 1.5 times the internal sample volume of the probe. Discarding this volume flushes any previous sample from the probe.
2. Collect 20 cc of soil gas using the syringe (Figure 118).
3. Inject all the 20 cc of soil gas into an evacuated sample bottle provided by GeoFrontiers (Figure 119). The evacuated bottles have an internal volume of about 12 cc. Approximately 8-10 cc of gas will be forced into the bottle by atmospheric pressure. The remaining sample will be forced into the bottle by pressing the syringe plunger. The sample in the vial will be above atmospheric pressure.
4. Sample bottle is then labeled with a unique sample number and the sample location is recorded using GPS.
5. Gas samples will be shipped every two weeks to the GeoFrontier lab in Dallas for analysis.

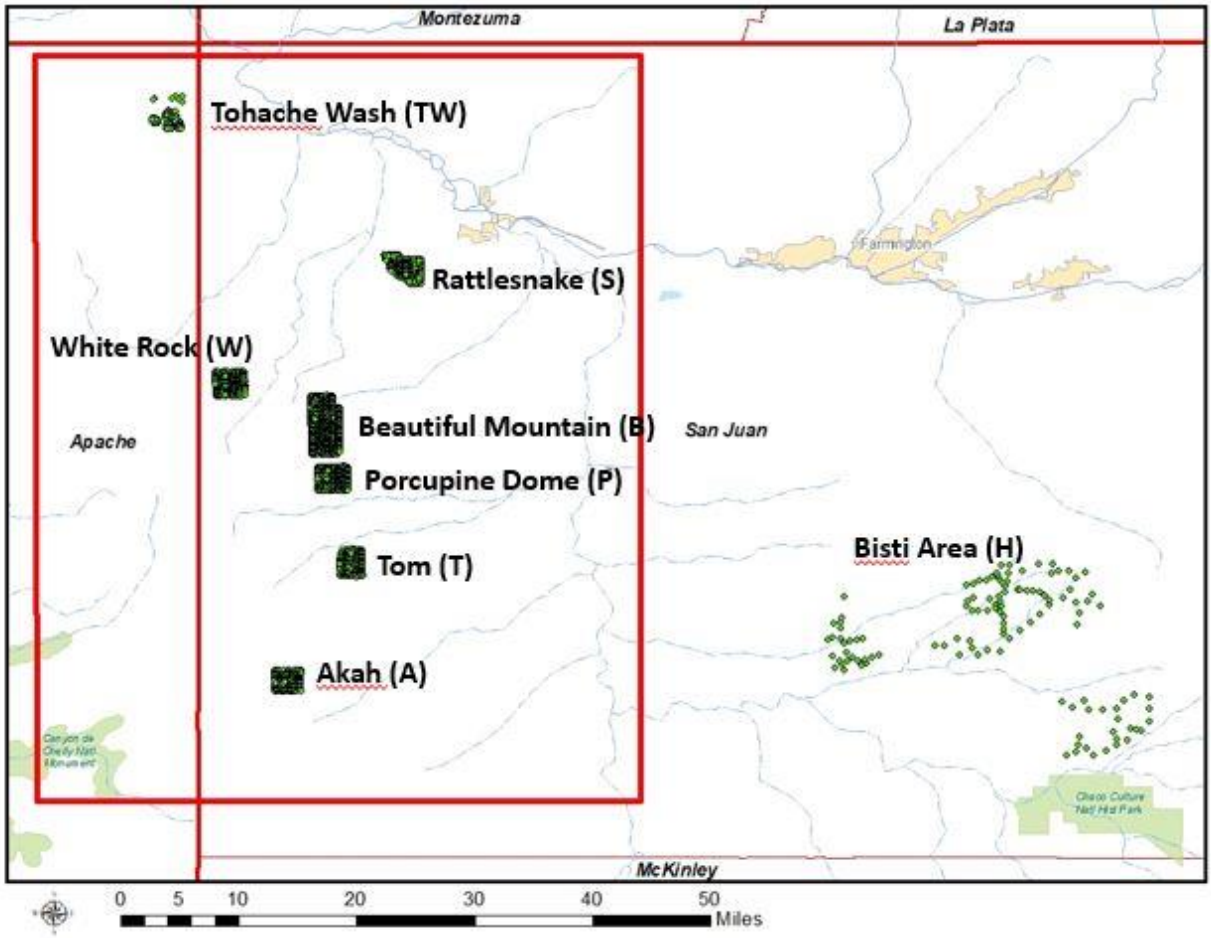


Figure 116. Location of the seven helium soil gas sampling areas with the area of the high-resolution aeromagnetic survey (red box). Data from the Bisti area collected by the USGS in 1984 was also included in the study to help establish background helium soil gas concentrations.

Figure 117. Helium soil gas probe in operation. Figure 118. Soil gas collection from probe.

Figure 119. Soil gas sample being placed in sample vial.

## LABORATORY ANALYSIS OF SOIL GAS SAMPLES

### Helium Analyzer General Description

Equipment selection was prior to the NNOGC program. While several commercial mass spectrometers can perform helium analysis with varying sensitives, their initial costs are significant, and performance is uncertain at low concentrations. An important requirement of any exploration technique is cost effectiveness to address the coverage versus cost problem. Expensive techniques suffer from limited coverage that complicates interpretation. Low-cost techniques, e.g., gas chromatography, may not provide the sensitivity and reproducibility needed for exploration interpretation.

GeoFrontiers' solution was to start by using mass spectrometer technology proven for helium analysis by the USGS (Friedman and Denton, 1976; Reimer, 1976). USGS technology started with a commercially available mass spectrometer that was popular as a part of a leak detector and therefore readily available. Data from literature showed sufficient resolution and reproducibility for helium exploration.

This equipment could help achieve the sub-$25 per sample (in large quantities) goal allowing sufficient coverage for interpretation at reasonable cost.

A Model 120SSA mass spectrometer was part of a leak detector manufactured by DuPont and sold under several brands. GeoFrontiers redesigned the inlet system and replaced the output electronics with a modern analog-to-digital converter and digital data processor. The fixed mass to charge ratio (m/z) of this instrument allows continuous measurement of helium-4 in the entire sample injected instead of short scan times divided among several gases as in scanning instruments.

### Sample Management

Soil gas samples were received at GeoFrontiers in pre-evacuated glass vials with internal volumes about 12 cc. Most vials were filled with 20 cc of gas during sample collection so that the vials contained positive pressures during shipping. Upon arrival samples were inventoried, compared with field records, and discrepancies, if any, were reported.

In most cases, unique laboratory IDs were assigned to each sample vial. After analysis, laboratory IDs were translated back to field-assigned IDs by computer software.

### Sample Analysis

A small aliquot of soil gas was injected into the analyzer inlet. After passing through a liquid nitrogen cooled trap to remove water vapor, carbon dioxide, and other impurities, the sample entered the mass spectrometer. Helium and most other gases were ionized by an electron beam. All ionized gases were separated according to their m/z (mass divided by charge) as

shown in Figure 120. Only helium-4 passed through a slit to a detector where the positive helium ions picked up an electron at the detector producing a current proportional to the number of ions contacting the detector plate. Therefore, detector current is proportional to helium-4 concentration in the soil gas sample.

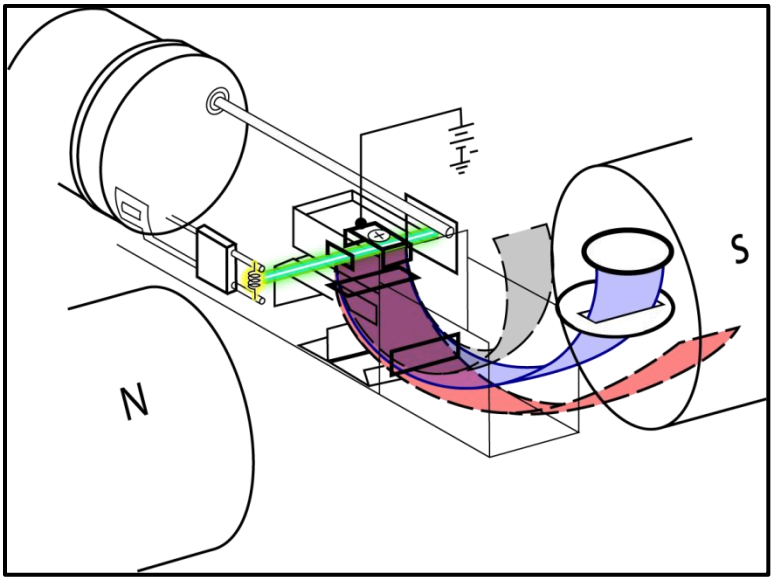


Figure 120. Ion detector diagram. Modified from Manual for 120 SSA Leak Detector, DuPont Instruments Company, 1979, by Paula Fleischmann.

The way the mass spectrometer works is illustrated in the simplified diagram in Figure 121. Colors in Figure 2 correspond to ion beam colors in Figure 1. Radius $r_1$ is a path taken by an ion lighter than m/z=4 which could be $H_2^+$ from hydrogen or from water. Radius $r_3$ is a path taken by an ion heavier than m/z=4. Radius $r_2$ is a path taken by an ion with an m/z=4 which matches that of $He^+$. Ions following radius $r_2$ pass through the ion selection slit to the collector where they are counted electronically.

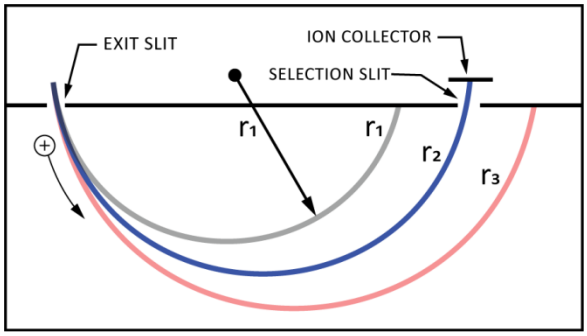


Figure 121. Ion detector principles of operation. Modified from Manual for 120 SSA Leak Detector, DuPont Instruments Company, 1979, by Paula Fleischmann.

**Data Output**

Helium data from the detector are converted to a voltage and amplified before going to an analog to digital converter (ADC). The ADC sums small slices of output peaks in a process called integration to calculate peak areas. Peak areas are proportional to helium concentrations. Helium sample peak areas are compared with peak areas from standards containing known helium concentrations which were used to calculate soil gas helium concentrations for each sample.

**Concentration Calculation**

To get the highest precision at low concentrations, GeoFrontiers bracketed each sample run with standard gas mixtures at known concentrations (Holland, 1984). This technique is illustrated by the example in Figure 122 which shows actual data from analysis of sample TW3 in the Tohache Wash area. A sample peak in the center of the chart was bounded on each side by standard peaks. Interpolating between the two standards mitigates small amounts of instrument drift thereby increasing precision.

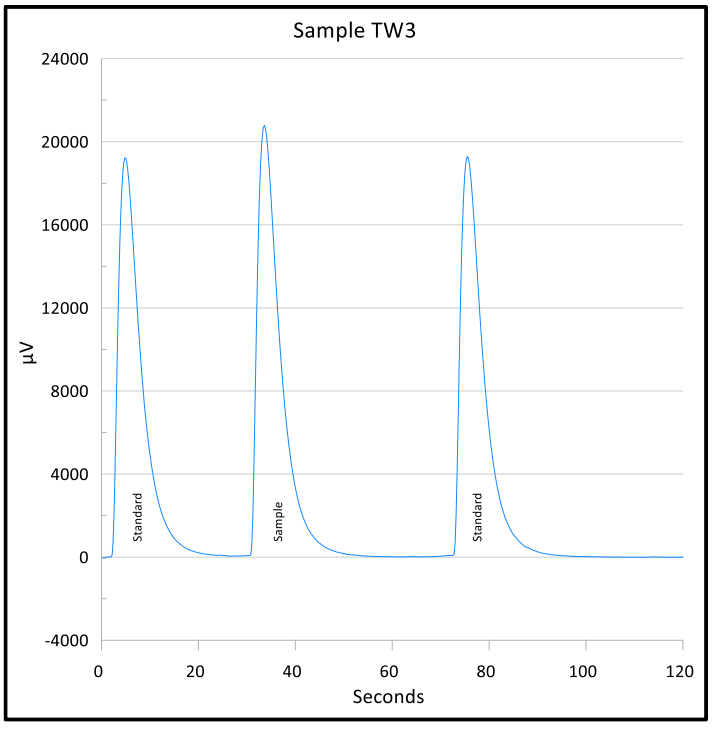


Figure 122. Mass Spectrometer Raw Data.

A discerning eye can see a very small difference in peak heights of the two standards. A more discerning eye would notice the first peak width is slightly larger than the last peak width. Peak

areas of the two standards are 106.75 on the left and 106.72 on the right which is a difference of only 0.028%. Many helium analysis instruments measure signal maxima (equivalent to peak heights). Instead of using peak heights, using peak areas to measure concentrations further improved precision.

These precision improvements combined with numerous modifications and adjustments lead to a conservatively estimated helium precision of 20 ppb.

**Helium Soil Gas Sampling Results**

Soil gas samples were collected and analyzed for helium content in seven areas deemed either prospective for a subsurface helium-rich gas deposit or to establish the response for a depleted helium deposit. Two thousand one hundred-eleven (2,111) soil gas samples and 30 air samples were collected over about a three-month period (October-December 2021). An additional 121 samples from the Bisti et al. wilderness areas were used in this study to help establish background helium soil gas levels (Been at al., 1984). Atmospheric samples were taken each day over the sample areas and used to determine true helium background concentrations. Atmospheric helium concentrations were found to range from 5.24 – 5.40 ppm with an average value of 5.33 ppm (Figure 123). The average atmospheric helium value of 5.33 ppm was used in this study as the background and all soil gas measurements were evaluated in terms of ppb (parts per billion) above this background level. Since the atmospheric range extended to a maximum of 5.40 ppm, only helium soil gas readings of >50 ppb over background were considered anomalous.

The helium soil gas concentrations found in the 2,232 samples used in this study ranged in value from 5.0 ppm to slightly over 6.0 ppm (Figure 124). As mentioned previously, only samples with >50 ppb above the helium background level of 5.33 ppm were considered anomalous and mapped. Figure 125 shows a comparison of the range and median helium soil gas values by sample area.

| Sample# | He ppm |
|---|---|
| P86-AIR | 5.24 |
| W234-AIR | 5.27 |
| W213-AIR | 5.29 |
| T237-AIR | 5.29 |
| A220-AIR | 5.30 |
| S73-AIR | 5.31 |
| T95-AIR | 5.31 |
| A213-AIR | 5.31 |
| T99-AIR | 5.31 |
| S280-AIR | 5.32 |
| S5-AIR | 5.32 |
| B629 AIR | 5.32 |
| TW3-AIR | 5.33 |
| T16-AIR | 5.33 |
| P63-AIR | 5.33 |
| P208-AIR | 5.33 |
| S238-AIR | 5.34 |
| S279-AIR | 5.34 |
| W243-AIR | 5.34 |
| T114-AIR | 5.35 |
| W231 AIR | 5.35 |
| S96-AIR | 5.35 |
| W44 AIR | 5.35 |
| S3-AIR | 5.36 |
| W120 AIR | 5.36 |
| W114 AIR | 5.36 |
| TW22-AIR | 5.38 |
| P188 AIR | 5.38 |
| A43-AIR | 5.39 |
| P81-AIR | 5.40 |
| | |
| **Average** | **5.33** |

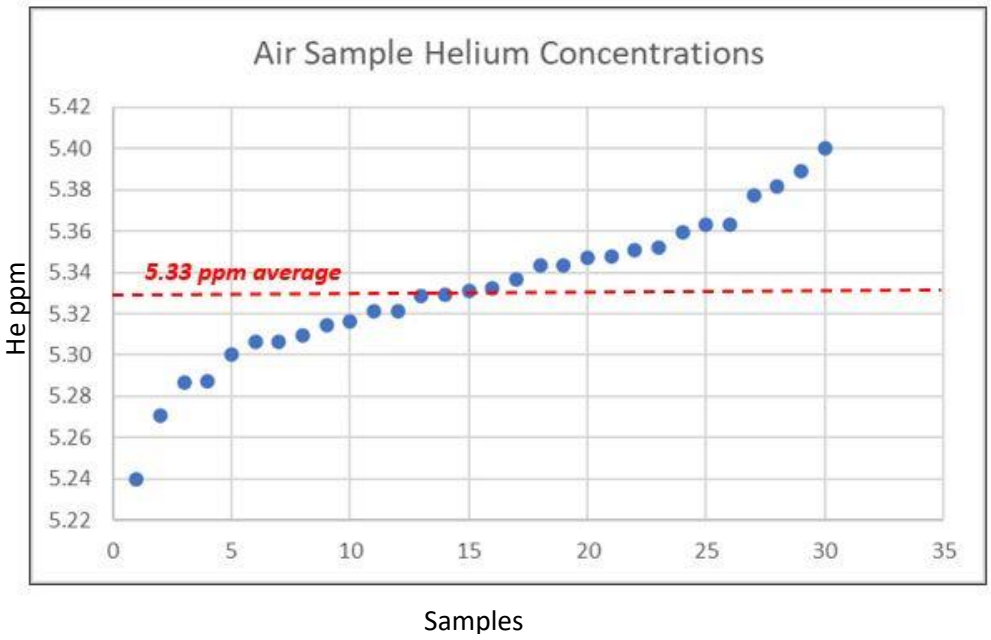


Figure 123. Helium concentrations from atmospheric samples collected during the study in the seven collection locales. Helium air concentrations range from 5.24 – 5.40 ppm with an average of 5.33 ppm, slightly higher than the global average of 5.24 ppm. The 5.33 ppm level was used as the background helium concentration to compare the helium soil gas sample results in this study.

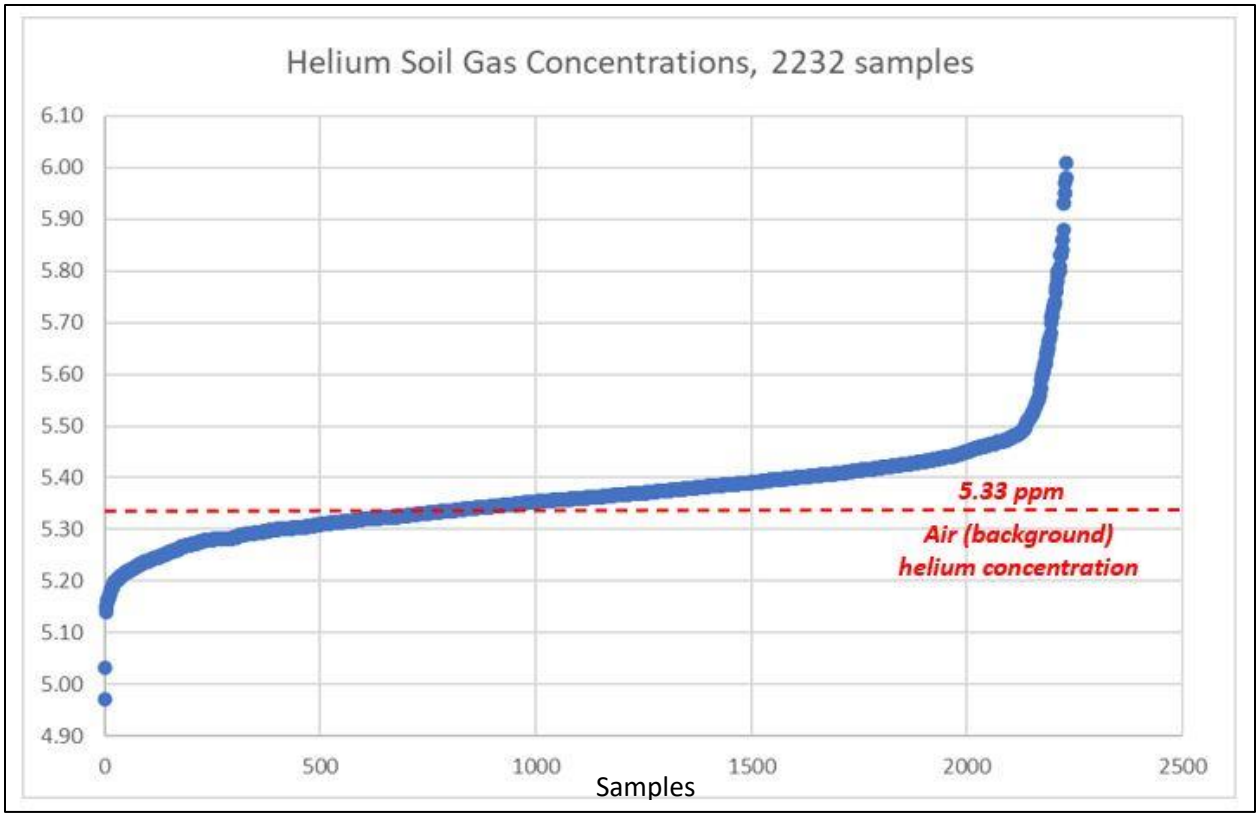


Figure 124. Helium soil gas concentration values for the 2232 samples collected in seven areas in the study. The values from the Bisti area collected by Been et al. (1984) are also included in the data. Helium soil gas concentrations in the study area ranged from 5 to over 6 ppm.

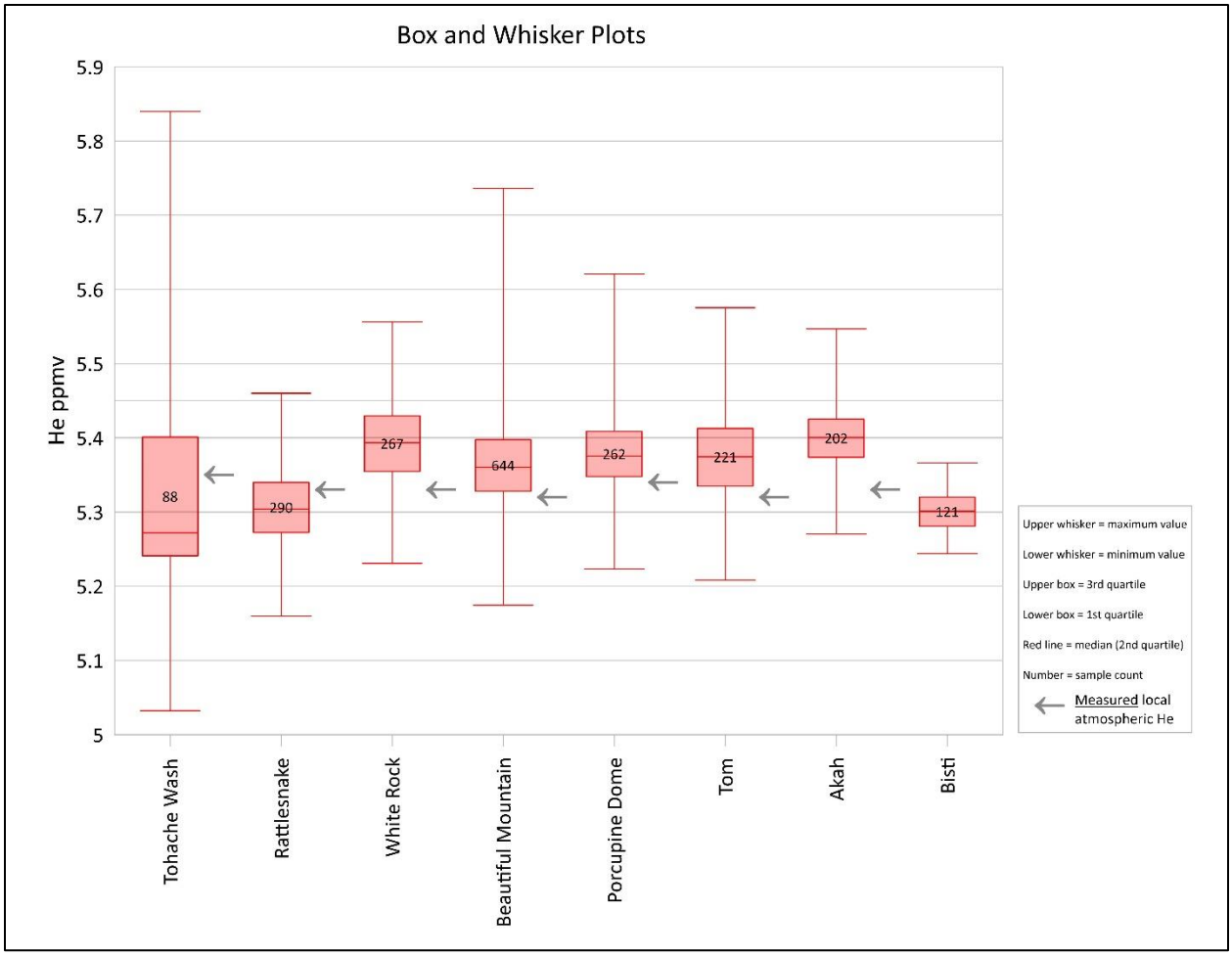


Figure 125. Comparison of the range and median helium soil gas values by sample area. Arrows on the graph show the average atmospheric helium concentrations collected at that particular sample area.

## Tohache Wash Sample Area

The Tohache Wash sample area is in the far northwestern corner of Apache County, Arizona near the border with New Mexico and Utah. Two hundred twenty-five (225) soil gas samples were collected in the sample area in and around the Navajo-Z well helium discovery. The Navajo-Z well was drilled and completed by Texaco in 1967. The Navajo-Z well encountered 64 feet of gas pay at 6500 feet in the Leadville limestone with a gas composition of 6.08% helium, 47.5% nitrogen, and 25.3% $CO_2$. Texaco completed the Z well and produced 386 MMcfg over 1.5 years. In 2015, NNOGC re-entered the Navajo-Z well and found the Leadville reservoir had 3500 psi of pressure and significant remaining gas reserves. The Navajo-Z well was an ideal candidate for helium soil gas sampling since it would establish what a helium soil gas response would be over a known helium accumulation.

NNOGC also had access to six 1950's vintage Gulf Oil single fold seismic lines that were used to map the 170-acre closure on the Leadville limestone structure trapping the helium in the Navajo-Z. As seen in Figure 126, there is good correspondence between the Navajo-Z Leadville closure and the anomalous helium soil gas readings ranging from 50 to over 500 ppb (parts per billion) over the background helium level of 5.33 ppm.

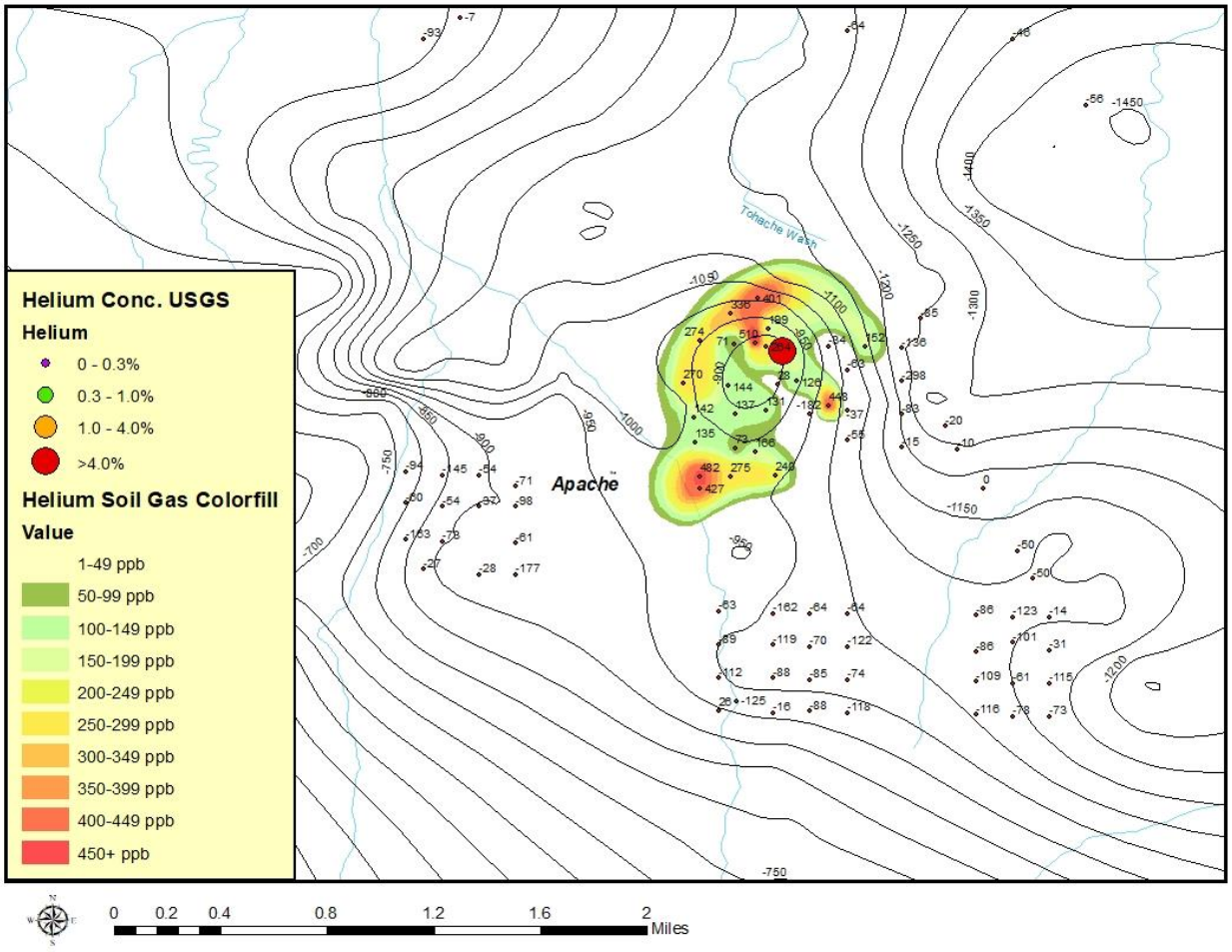


Figure 126. Helium soil gas sampling locations and values in the Tohache Wash (TW) sample area. Helium values are in ppb (parts per billion) above the background helium level of 5.33 ppm. A structure map on the top of the Leadville limestone (Mississippian) is also shown. The Navajo-Z well, identified by the red dot, is a well re-entered by NNOGC in 2015 and tested significant gas volumes containing 6.08% helium at 6500 ft depth and 3500 psi pressure from the Leadville limestone. Note the excellent correspondence between anomalous helium soil gas readings (which exceed 500 ppb over background) and the location of the Navajo-Z structure on the Leadville.

**Beautiful Mountain Sample Area**

Beautiful Mountain is a large north-south oriented structurally closed anticline located along the east side of the Defiance Monocline in San Juan Co., New Mexico. Oil production with significant helium content was produced from the Mississippian Leadville limestone starting in 1975 in Beautiful Mountain. Starting in 1979, the Pennsylvanian Barker Creek limestones produced minor amounts of oil and gas. Seven of the older wells in Beautiful Mountain were recompleted for helium production from the Permian Organ Rock formation beginning in 1981. All wells in Beautiful Mountain field were plugged and abandoned by 2011.

The Mississippian Leadville limestone produced 2.58 BCFG of gross gas with approx. 0.19 BCF helium and 16.3 MBO from four wells. Analyzed gas composition for the Leadville reservoir in the Navajo 1-5 well yielded 87.83% nitrogen, 7.14% helium, 3.41% hydrocarbons, and 1.62% $CO_2$. Calculated drainage areas for the four producing Leadville wells range from 21 to 820 acres. The Permian Organ Rock sandstone produced 3.18 BCFG of gross gas with approx. 0.17 BCF helium from seven wells. Helium content averaged 5.35% in the Organ Rock. Calculated drainage areas for the seven producing Organ Rock wells range from 3 to 93 acres. The variable and lower drainage areas are the result of highly discontinuous fluvial depositional environment of the sandstones. This also suggests that there are large, undrained volumes of helium bearing gas remaining in Beautiful Mountain. Three wells produced 0.26 BCFG gross gas and 10.7 MBO from the Pennsylvanian Barker Creek limestone with 5.93% helium. Helium bearing gas with a concentration of 4.05% helium was tested in the Devonian McCracken sandstone from the structurally crestal Navajo Tract 381-1 well, although the McCracken was never produced.

Beautiful Mountain was chosen as a soil gas sampling area because of the potential for undrained volumes of helium-rich gas, particularly in the discontinuous Permian Organ Rock sandstones. In addition, good seismic and well control allowed for mapping of the Leadville and Organ Rock reservoirs. Six hundred forty-four (644) soil gas samples were collected over a 9.5 sq. mi. area at a sample spacing of every 660 feet (1/8$^{th}$ mile) over the Beautiful Mountain anticline (Figure 127). The results of the helium soil gas results over Beautiful Mountain are reflective of a partially depleted helium field (Figure 128). Anomalous helium soil gas readings ranging from 50 to over 400 ppb over helium background of 5.33 ppm are concentrated on the flanks of the structure over potentially undrained portions of the field, particularly in the Permian Organ Rock sandstone.

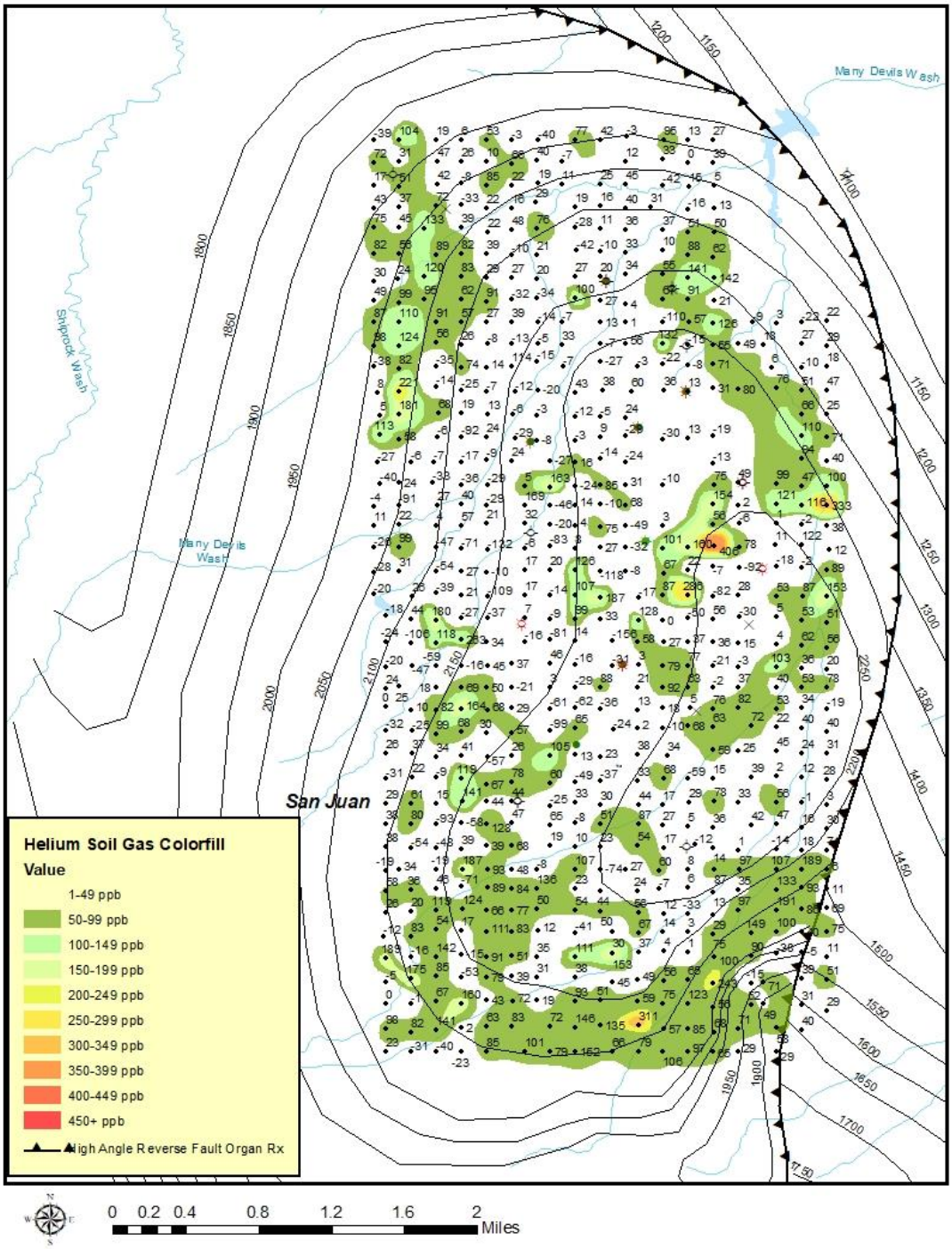


Figure 127. Helium soil gas sampling locations and values in the Beautiful Mountain (B) sample area. Helium values are in ppb (parts per billion) above the background helium level of 5.33 ppm. A structure map on the top of the Organ Rock formation (Permian) is also shown. The Beautiful Mountain field produced 3.18 Bcfg from the Permian Organ Rocks sandstones with 5.35% helium from 7 wells at an average depth of 3700 ft. The Leadville limestone (Mississippian) also produced 2.58 Bcfg + 16.3 MBO from 4 wells with 7.0% helium at an average depth of 5900 ft. All wells were plugged and abandoned in the field between 2005 – 2011.

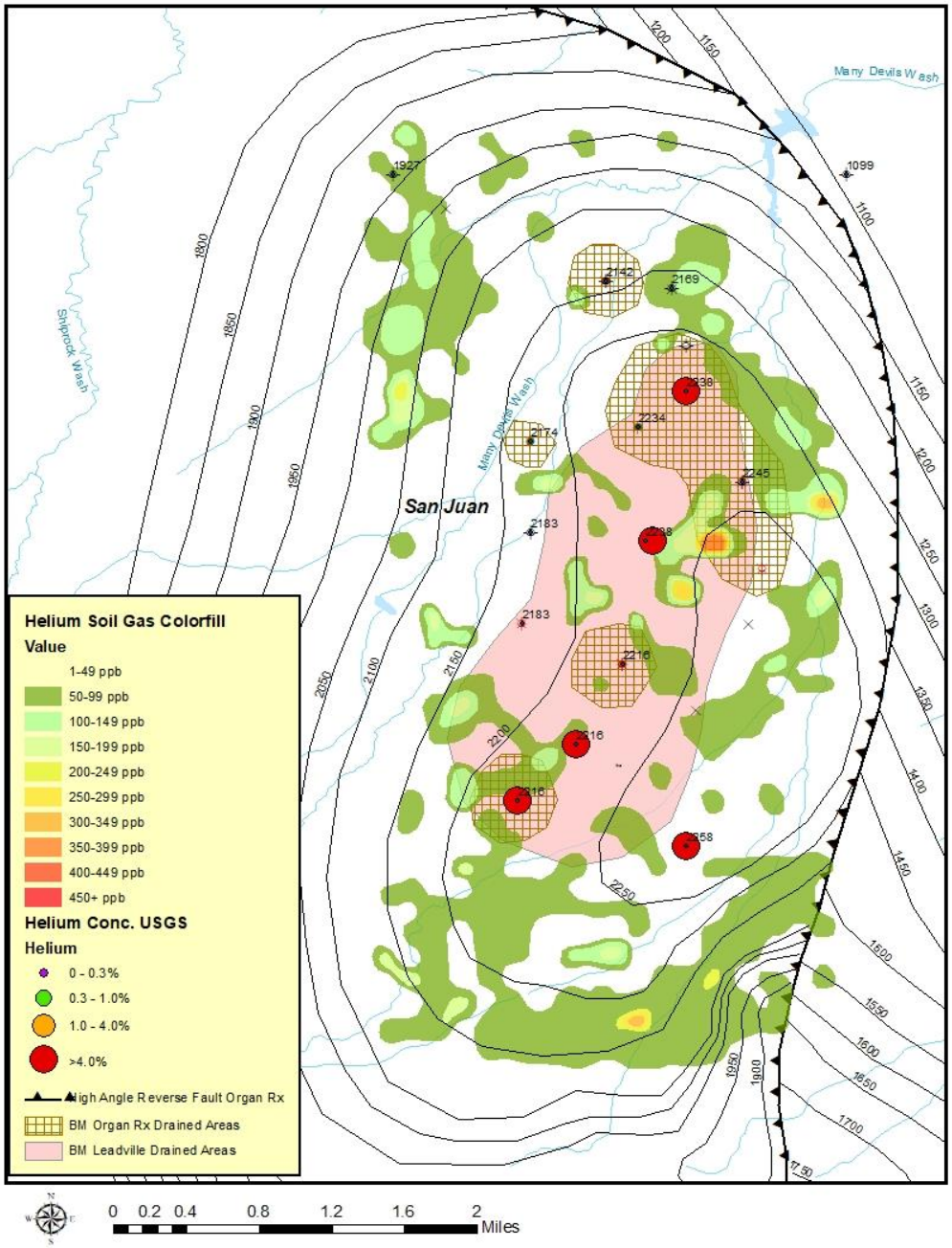


Figure 128. Anomalous helium soil gas readings relative to the depleted, produced areas of the Organ Rock and Leadville reservoirs at Beautiful Mountain. Leadville produced areas in pink, Organ Rock produced areas in checkered pattern. Leadville reservoir is a fractured limestone with a drainage area approx. 600 acres while the Organ Rock sandstones are discontinuous fluvial deposits with a less than 60-acre average drainage radius. Helium soil gas anomalies occur on the potentially undrained portions

of the field on the flanks of the structure. Red dots represent wells that tested helium from the USGS helium database.

**Porcupine Dome Sample Area**

The Porcupine Dome sample area is located approximately 2 miles south the Beautiful Mountain helium field in San Juan County, New Mexico. A structural closure on the Leadville limestone and Organ Rock sandstones was mapped by NNOGC used 2D seismic acquired in 2020. Two hundred sixty-two (262) soil gas samples were collected over a 4 mile$^2$ area at a sample spacing of every 660 feet (1/8$^{th}$ mile) over the Porcupine Dome anticline and surrounding area (Figure 129). High helium soil gas readings (50 – 250+ ppb above background) occur over the structural closure, over a three-way closure on the downthrown block east of the closure, and along the thrust fault separating the blocks. A well drilled by Apache in 1970 tested 3.5 MMcfgpd from the Leadville but was abandoned. Helium concentration from this test is unknown but the Leadville contains 7% helium two miles to the north in Beautiful Mountain field.

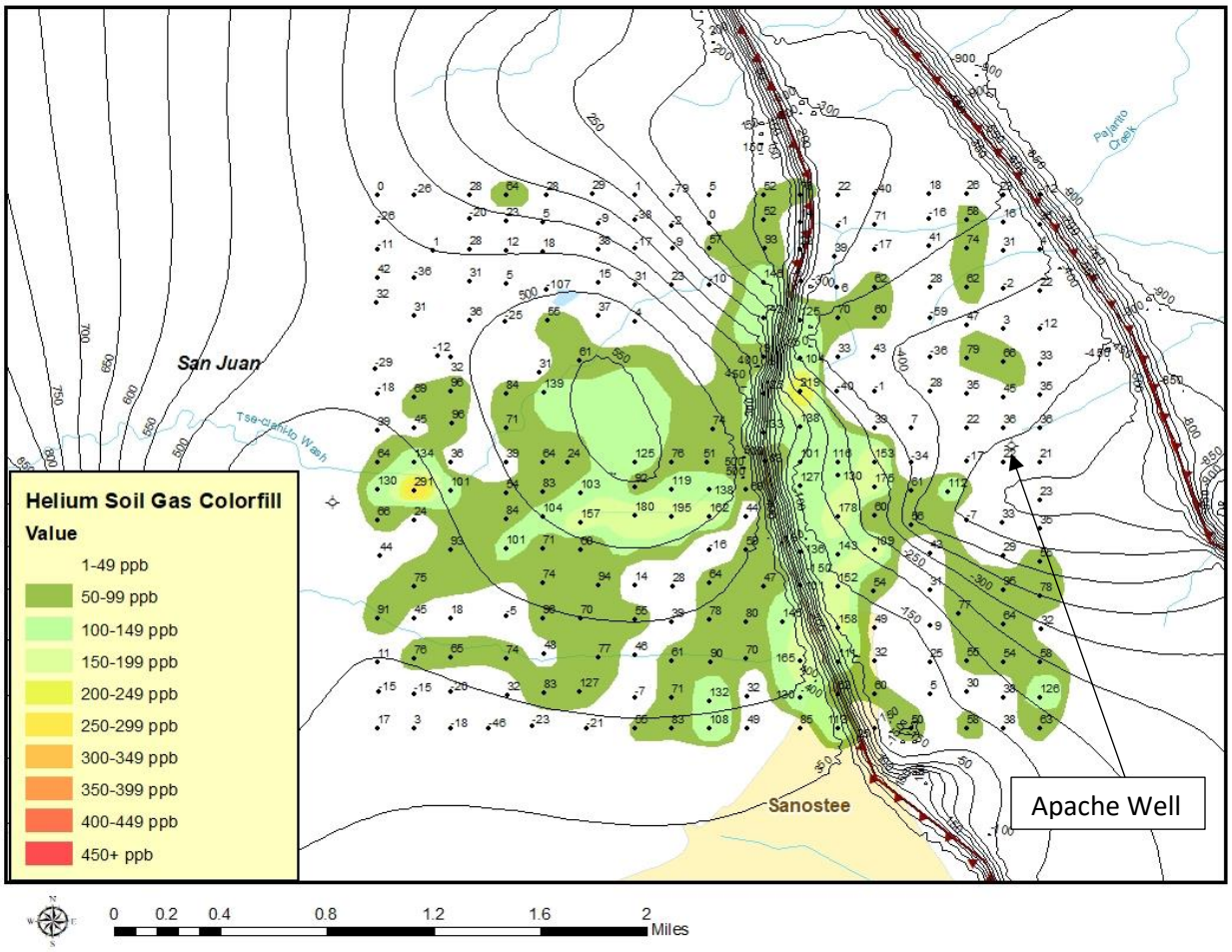


Figure 129. Helium soil gas sampling locations and values in the Porcupine Dome (P) sample area. Helium values are in ppb (parts per billion) above the background helium level of 5.33 ppm. A structure map on the top of the Leadville limestone (Mississippian) is also shown. High helium soil gas readings (50 – 250+ ppb above background) occur on a Leadville closure in the center of the map, on a three-way closure on the downthrown block east of the closure, and along the thrust fault separating the blocks. The Apache well identified on map tested 3.5 MMcfgpd from the Leadville and was abandoned. Helium concentration from this test is unknown but the Leadville contain 7% helium 2 miles to the north in Beautiful Mountain field.

## Tom Sampling Area

The Tom sampling area is located about five miles to the south of the Porcupine Dome sample area in San Juan County, New Mexico. A structural closure on the Leadville limestone was suggested by a 2D seismic line (acquired by NNOGC, 2020) oriented NW-SE over the structure. Two hundred twenty-one (221) soil gas samples were collected over a 4 mile$^2$ area at a sample spacing of every 660 feet (1/8$^{th}$ mile) over the Tom feature and surrounding area (Figure 130). Tom was selected as a sampling location because of the occurrence of an apparent structure, proximity to wells testing high helium concentrations in the Devonian and Mississippian sections ranging from 2.9 to 7% helium, and the existence of a 1976 oil & gas well producing

from the Devonian McCracken sandstone formation (a known helium-bearing reservoir in the area). High helium soil gas readings (50 – 200+ ppb above background) occur on and along the flanks of the closure. There is not a strong correspondence of high helium soil gas readings and structure in the Tom sample area, but this could be because the location of the structure is not well defined by seismic.

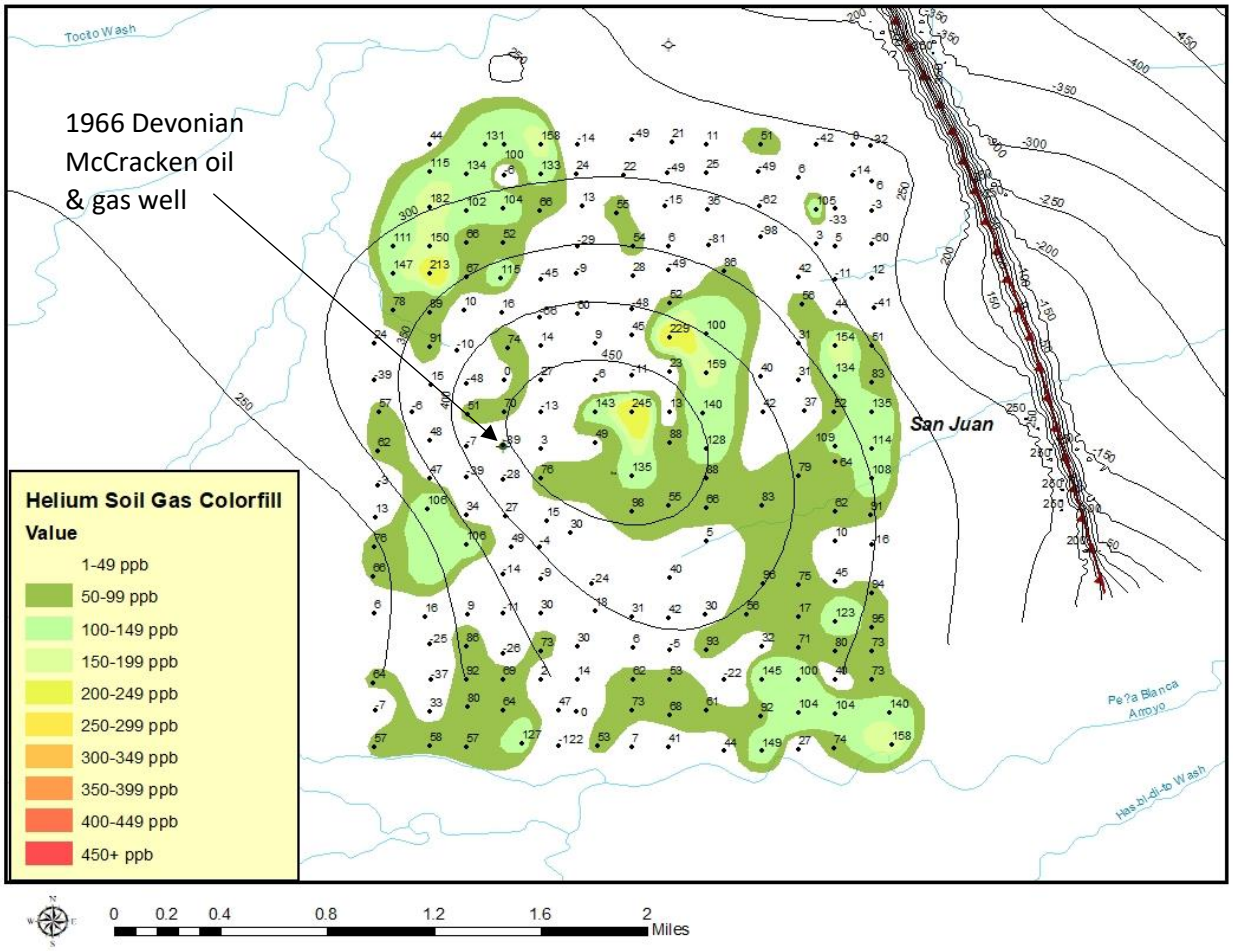


Figure 130. Helium soil gas sampling locations and values in the Tom (T) sample area. Helium values are in ppb (parts per billion) above the background helium level of 5.33 ppm. A structure map on the top of the Leadville limestone (Mississippian) is also shown. High helium soil gas readings (50 – 200+ ppb above background) occur on and along the flanks of the Leadville closure in the center of the map. There is not a strong correspondence of high helium soil gas readings and structure in the Tom sample area. Potential helium reservoirs in this area include the Mississippian Leadville limestone, the Devonian McCracken sandstone, and the Permian Organ Rock sandstones.

## Akah Sampling Area

The Akah sampling area is located about nine miles to the southwest of the Tom sample area in San Juan County, New Mexico. Structural control is very poor, but an apparent closure is suggested based on basement structure from the high-resolution aeromagnetic survey acquired

for this study. Two hundred two (202) soil gas samples were collected over a 4 sq. mi. area at a sample spacing of every 660 feet (1/8th mile) over the Akah area (Figure 131). Akah was selected as a sampling location because of the occurrence of a possible structure at the Precambrian basement level, the occurrence of 5.5% helium tested from the Devonian McCracken sandstone approximately three miles to the NW of the sample area, and the existence of two oil & gas wells (1967, 1970) producing from the McCracken sandstone formation. Helium presence or concentration is unknown in the two McCracken oil and gas wells. High helium soil gas readings (50 – 200+ ppb above background) occur within the sample area and correspond generally well to the Precambrian closure even with a weakly-controlled structure.

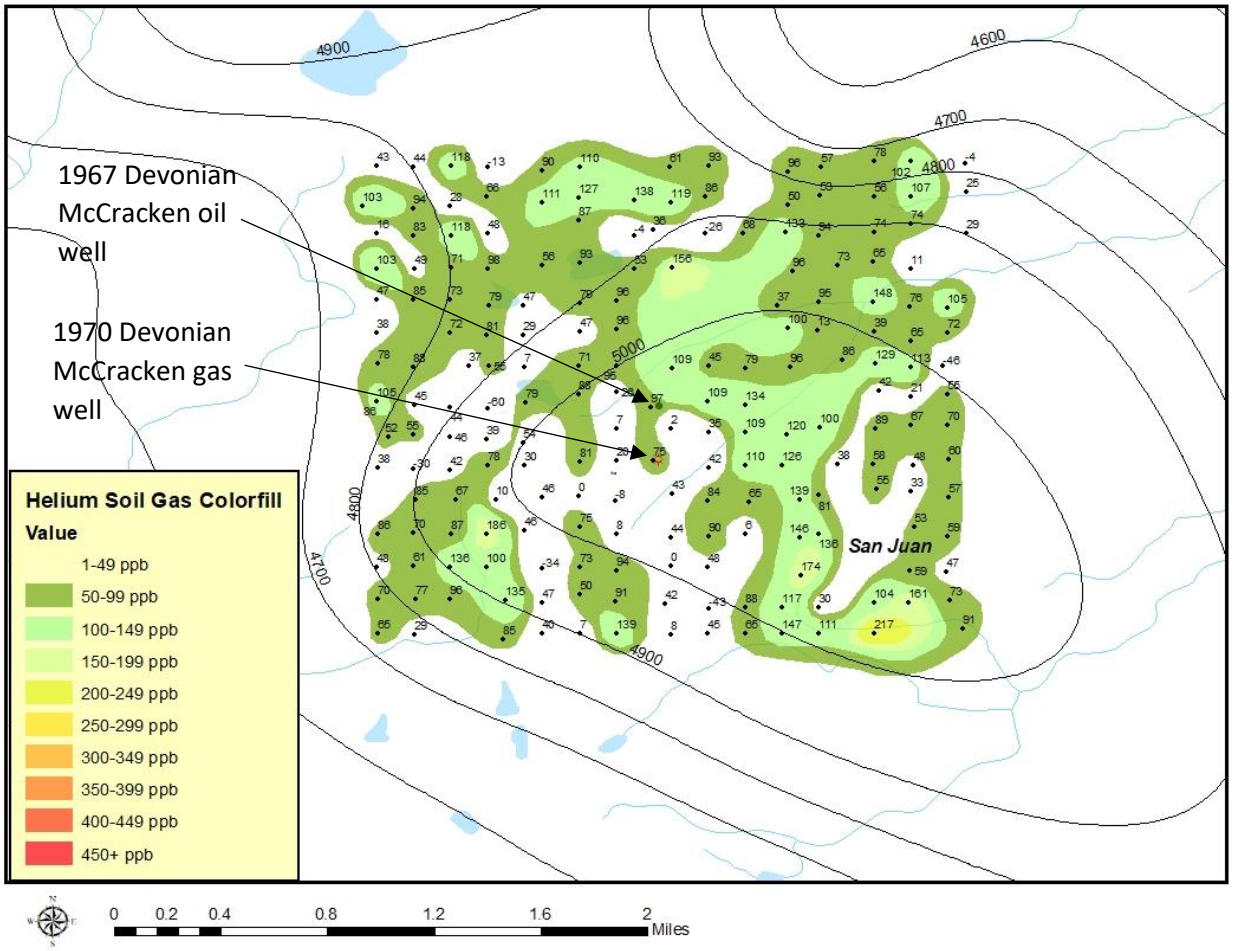


Figure 131. Helium soil gas sampling locations and values in the Akah (A) sample area. Helium values are in ppb (parts per billion) above the background helium level of 5.33 ppm. Structure map on the top of the Precambrian granite as determined by the high-resolution aeromagnetic survey is also shown. Correspondence of high helium soil gas readings (50 – 200+ ppb above background) to structure is generally good. The Devonian McCracken sandstone would be the likely helium reservoir in this area.

**White Rock Sampling Area**

The White Rock sampling area is in San Juan County, New Mexico about five miles to the northwest of the Beautiful Mountain sample area and about 1 mile east of the Arizona/New Mexico border. Structural control is very poor, and no closure is suggested based on the basement structure from the high-resolution aeromagnetic survey acquired for this study. Two hundred sixty-seven (267) soil gas samples were collected over a 4 sq. mi. area at a sample spacing of every 660 feet (1/8$^{th}$ mile) over the White Rock area (Figure 132). White Rock was selected as a sampling location because of the occurrence of a 1966 gas well that tested 7.8% helium from the Precambrian and 5.2% helium from the Pennsylvanian Barker Creek carbonate. High helium soil gas readings (50 – 200+ ppb above background) occur within the sample area, but with no apparent relationship to the Precambrian structure. Structural control is very poor and the existence of small closures within the sample area cannot be ruled out. Slightly elevated helium soil gas readings (75 – 140 ppb above background) occur around the old 1966 helium-rich dry well.

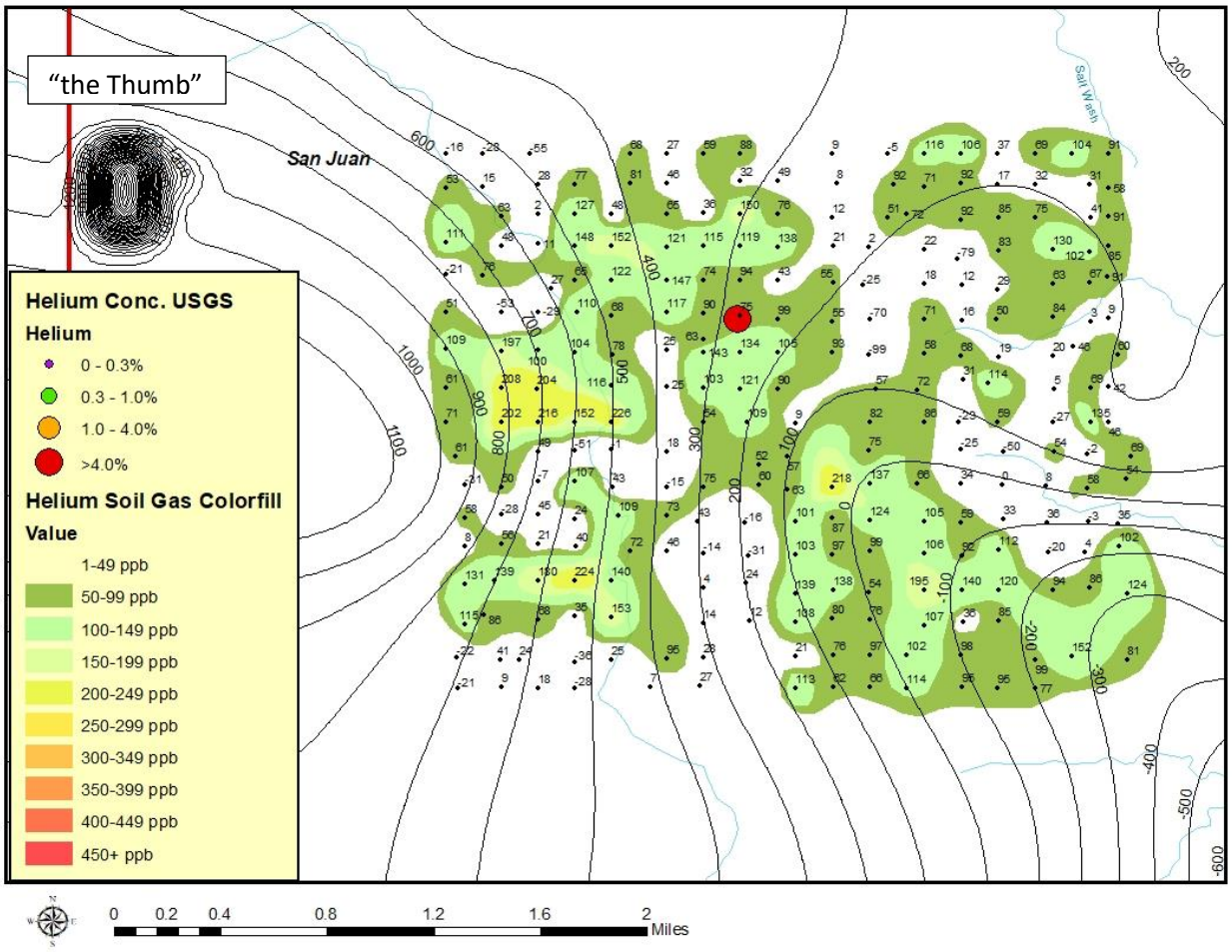


Figure 132. Helium soil gas sampling locations and values in the White Rock (W) sample area. Helium values are in ppb (parts per billion) above the background helium level of 5.33 ppm. Structure map on the top of the Precambrian granite as determined by the high-resolution aeromagnetic survey is also shown. No defined structure on the Precambrian is apparent and it is unclear what the high helium soil gas readings (50 – 200+ ppb above background) are responding to. The 1966 dry well (red dot) drilled in the center of the study area tested 5.2% helium in the Pennsylvanian Barker Creek and 7.8% helium from the Precambrian. Just to the west of the sample area lies a Navajo Volcanic field diatreme known as "the Thumb".

## Rattlesnake Sampling Area

Rattlesnake is a large northwest-southeast trending anticline located about seven miles southwest of the town of Shiprock in San Juan Co., New Mexico. Oil was discovered on the Rattlesnake structure in the Cretaceous Dakota sandstone in 1924 and followed in 1929 with oil being found in the Pennsylvanian Hermosa formation. In 1942, helium-rich gas was discovered in the Mississippian Leadville-Devonian Ouray dolomites. Gas analysis from the Leadville-Ouray reservoir yielded 7.6% helium, 72.6% nitrogen, 14.2% methane, and 2.8% $CO_2$. Initial reservoir pressure was 3,605 psia at a depth of 7,100 feet. The helium-rich field was developed by two wells, one well, the Continental Navajo #1, encountered high porosity (8-12.9%) dolomites and

tested at a rate of 30,000 Mcfgpd. The second well, the Rattlesnake 1-G located 0.5 miles to southwest of the Navajo #1 well, encountered a very tight (<3%) porosity dolomites and tested only 17 Mcfgpd. Within less than 2 years, water production overtook the two wells and the Leadville-Ouray helium field was abandoned after only producing between 1-2 Bcfg of gross gas.

Rattlesnake was chosen as a soil gas sampling area to establish the soil helium response over a depleted field. Two hundred eighty-nine (289) soil gas samples were collected over an approximate 4 sq. mi. area at a sample spacing of every 660 feet (1/8$^{th}$ mile) over the helium field portion of the Rattlesnake field (Figure 133). The results of the helium soil gas results over Rattlesnake are reflective of a totally depleted helium field. Almost the entire sample area is represented by background helium soil gas readings. Scattered anomalous helium soil gas pockets ranging up to only slightly over 100 ppb over helium background of 5.33 ppm are concentrated on the southwestern flank of the structure where the Leadville-Ouray reservoir was found to be very tight and may represent residual helium-rich gas or liquids (Figure 134).

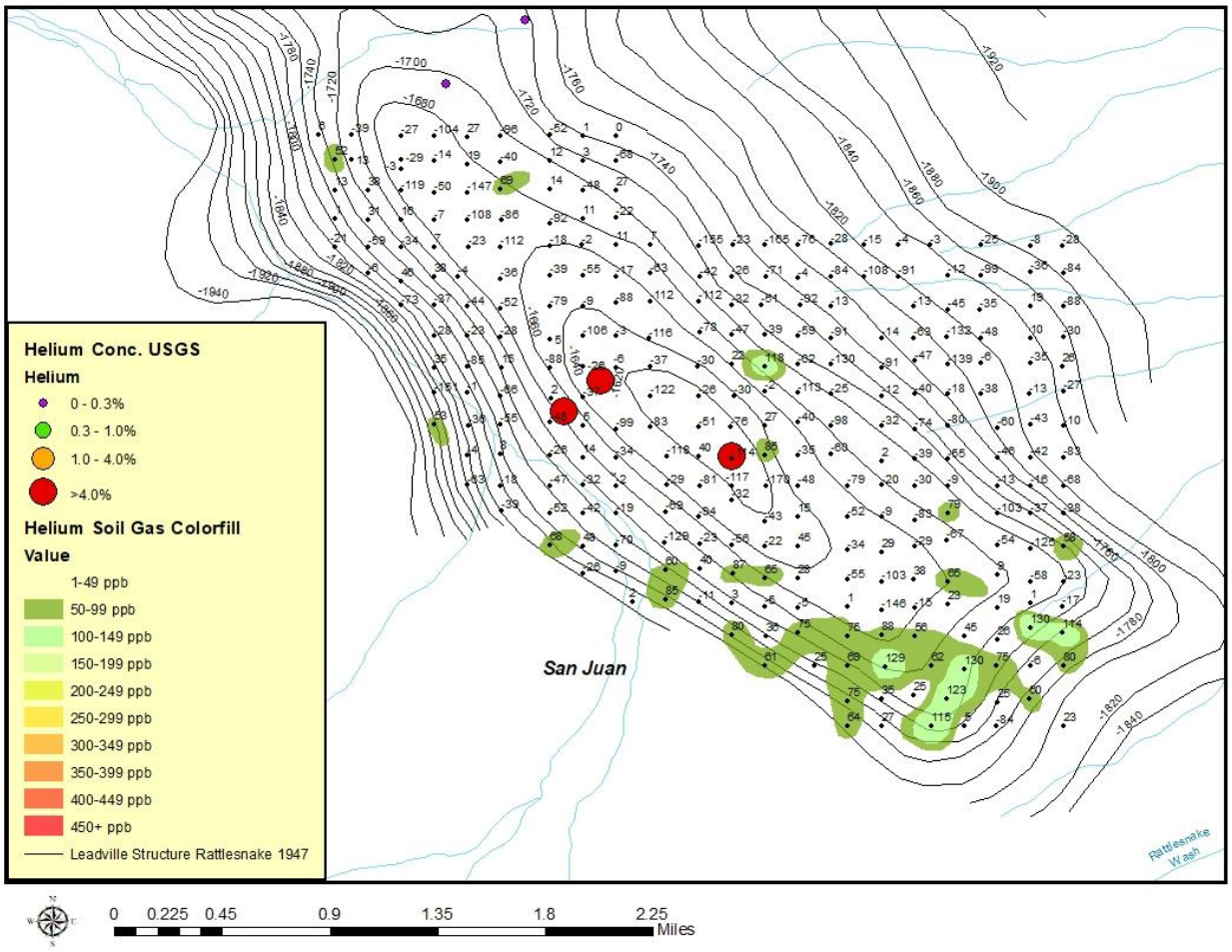


Figure 133. Helium soil gas sampling locations and values in the Rattlesnake (S) sample area. Helium values are in ppb (parts per billion) above the background helium level of 5.33 ppm. Structure map on the top of the Devonian Ouray Carbonate (Hinson, 1947) is also shown. The Rattlesnake helium field produced helium-rich gas (7.6%) from two wells for less than 2 years in the 1940's before being depleted and overrun by water production. The helium soil gas readings across almost the entire sample area are at helium background levels. Slightly anomalous helium soil values were found on the southwest portion of the structure and may represent residual helium-rich gas pockets.

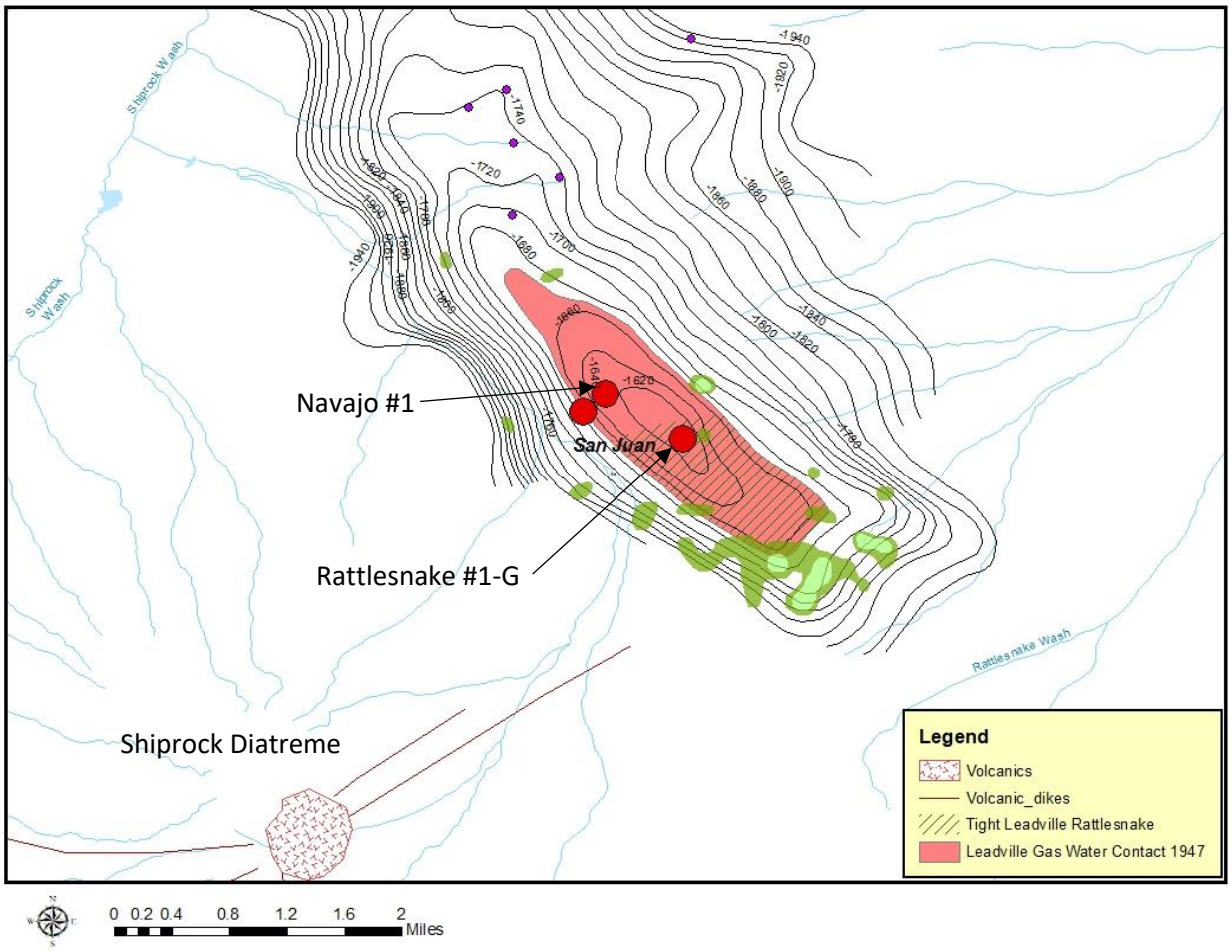


Figure 134. Weakly anomalous helium soil gas readings in relation to the original gas-water contact in the Leadville-Ouray carbonate reservoir and to the tight reservoir areas in the southwest part of Rattlesnake field.

## Other Helium Soil Gas Surveys used in the study

Two additional helium soil gas surveys previously gathered by others were included in this study to assist in the interpretation of the soil gas readings from our study area. The first survey was from the Bisti, De-Na-Zin, and Ah-Shi-Sle-Pah wilderness areas in southeastern San Juan County, New Mexico collected by the USGS in 1984 (Been et al., 1984) (Figure 135). This area is outside of the helium fairway on and around the Defiance uplift and was used in this study to help establish the helium soil gas background readings. The atmospheric helium readings collected during our sampling found the average helium concentration to be 5.33 ppm with a range of 5.24 – 5.40 ppm. The helium soil gas readings in the Bisti et al. wilderness areas recorded helium concentrations of ±50 ppb (parts per billion) from the atmospheric helium average of 5.33 ppm. This data supported our decision to only consider helium readings >5.40 ppm to be anomalous.

The other survey was over the Harvey Dome helium field in Grand County, Utah (Roberts, 1981). Harvey Dome is a small helium-rich Jurassic Entrada field (7% helium) that is very shallow (950-1000 feet) and also exhibits very high helium soil gas readings (>3500 ppb over background or >8.74 ppm) (Figure 136). The Tohache Wash sample area that was over a known helium deposit at 6500 feet in the Leadville limestone and recorded helium soil gas readings of >500 ppb over background was the only one that was close to the Harley Dome results. The helium soil gas results at both Tohache Wash and Harley Dome suggests that helium soil gas is a viable method to identify helium-rich gas accumulations in the subsurface. There also may be a relationship between the depth of the subsurface deposit and the strength of the helium soil gas anomaly but more data over other helium fields are needed to prove this theory.

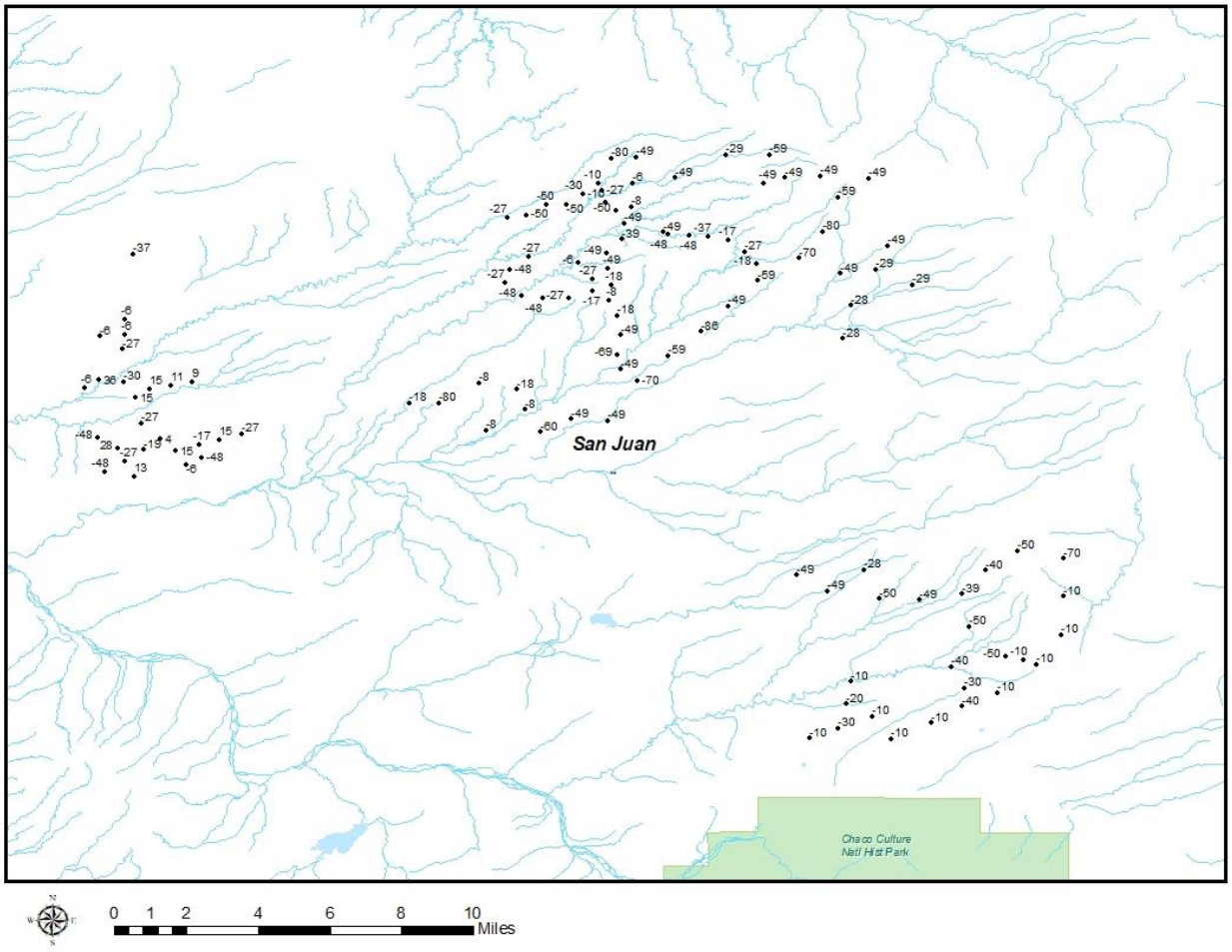


Figure 135. Helium soil gas samples from the Bisti, De-Na-Zin, and Ah-Shi-Sle-Pah wilderness areas in San Juan County, New Mexico collected by Been et al. (1984) of the USGS. Helium values are in ppb (parts per billion) above the background helium level of 5.33 ppm. This area was included in the report because in is outside of the helium fairway around the Defiance uplift and represents background helium soil gas values.

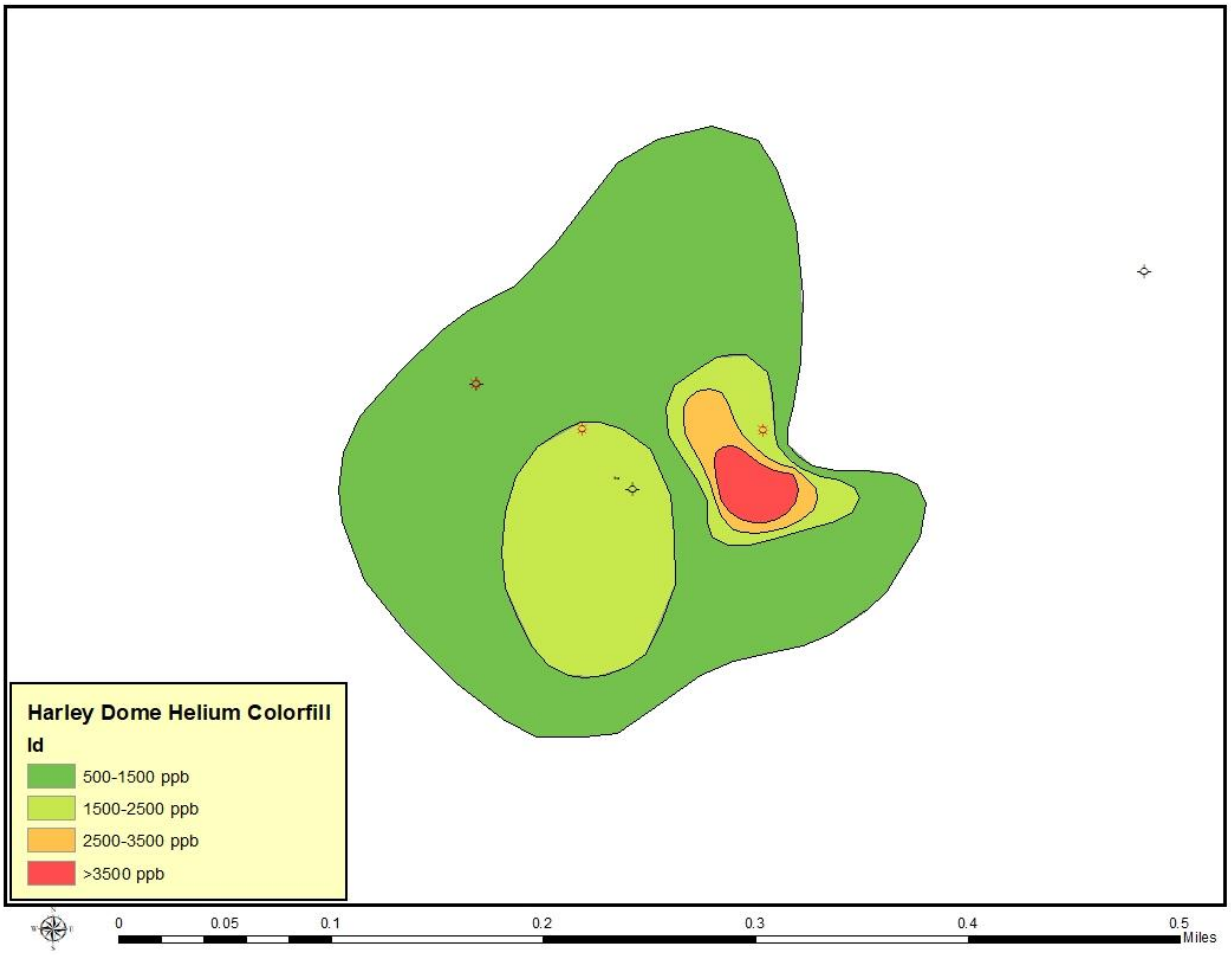


Figure 136. Helium soil gas results from Harley Dome, Grand County, Utah (from Roberts, 1981). Extremely high helium soil gas readings (up to >3500 ppb over background) were recorded over a helium field with 7% helium at 950-1000 ft. in the Jurassic Entrada sandstone.

## Integration and interpretation of the study data and analytical results

### Occurrence of known high helium wells with high-resolution aeromagnetic survey results and identification of new potential helium deposits

Forty-eight (48) wells that tested between 1 – 8% helium occur within the high-resolution aeromagnetic survey area of the study. Forty-one (41) or 85% of these high helium wells lie on Precambrian basement highs as defined by the aeromagnetic data (Figures 137 and 138).

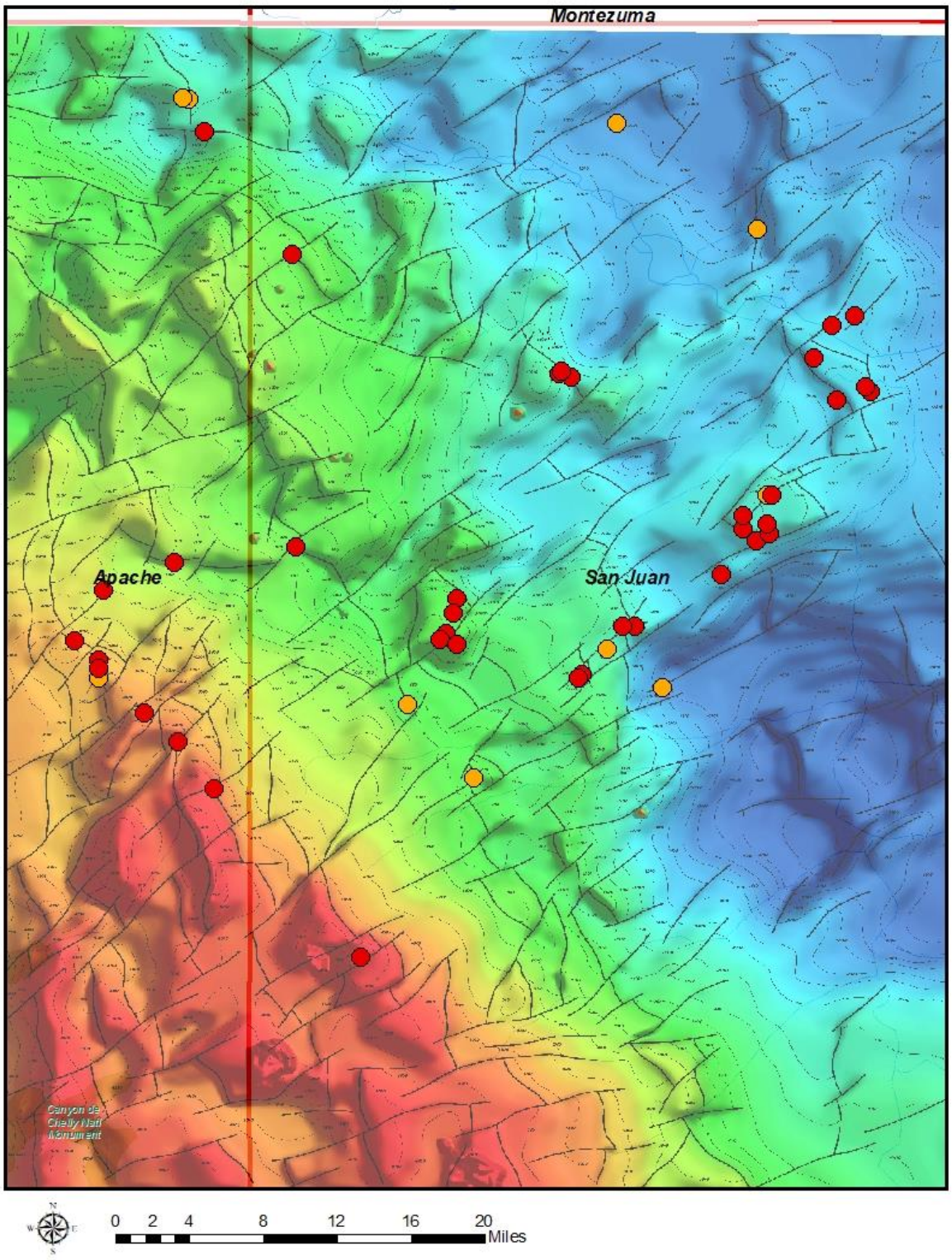


Figure 137. Location of 48 helium wells that tested greater than 1% helium relative to Precambrian structure as defined by the aeromagnetic data. Red colored dots are wells that tested greater than 4% helium while orange-colored dots are those wells that tested 1-4% helium. 41 of the 48 wells (85%) that tested >1% lie on Precambrian highs.

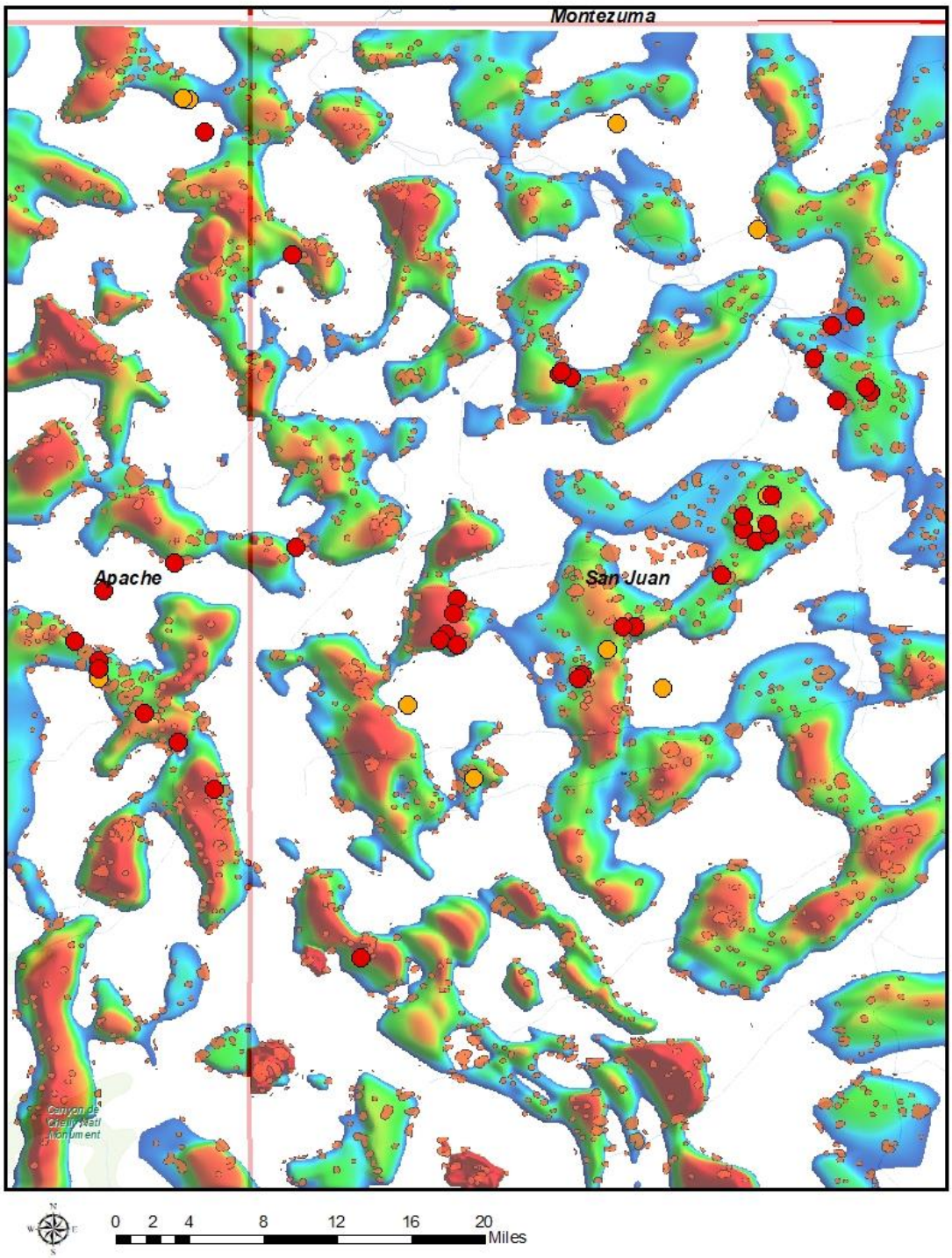


Figure 138. Location of 48 helium wells that tested greater than 1% helium relative to the filtered Precambrian structure as defined by the aeromagnetic data. The filtered Precambrian structure removes regional dip and accentuates the high areas. Red colored dots are wells that tested greater than 4% helium while orange-colored dots are those wells that tested 1-4% helium. 41 of the 48 wells (85%) that tested >1% lie on Precambrian highs.

Lineament density, which is derived using proprietary software by Earthfield Technology, identifies where lineaments overlie one another from topographic, magnetic, gravity, interpreted basement and interpreted intrusive bodies trends (Figure 139). Lineament density defines areas where fracturing is most probable. Lineaments colored in red (refer to Figure 139) define areas where four or more trend surfaces overlie each other and identify areas of highest fracture probably. Of the 48 high helium wells (>1% helium) within the high-resolution aeromagnetic study area, all of them (100%) lie on lineaments where four or more lineament trends correspond.

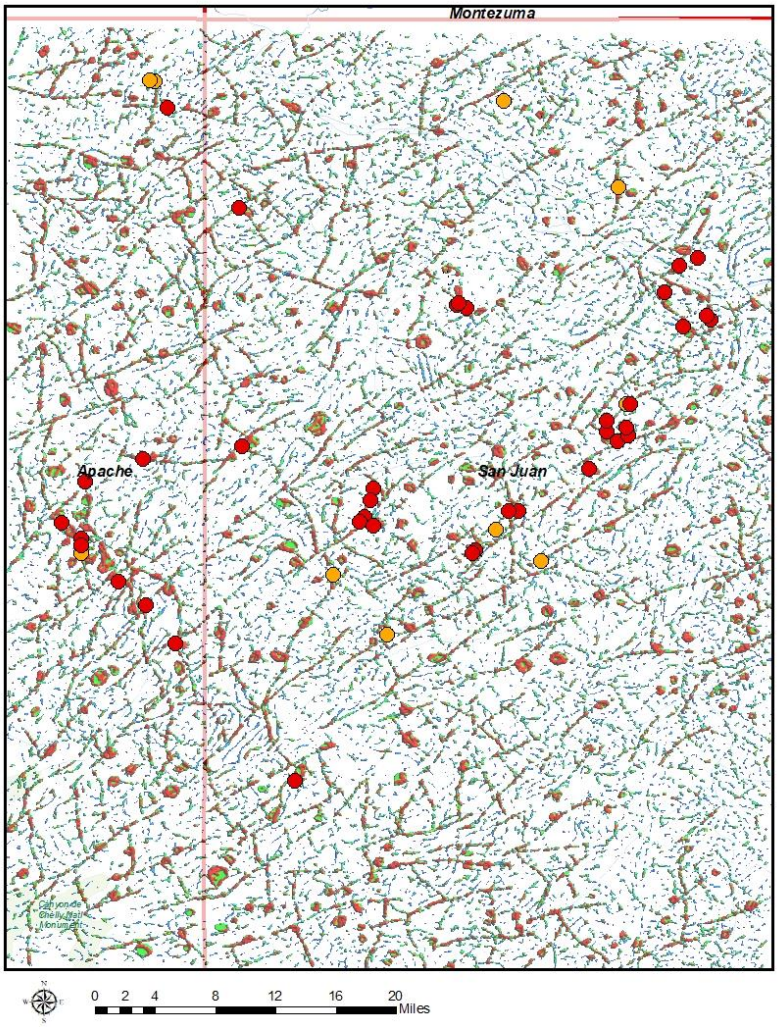


Figure 139. Location of 48 helium wells that tested greater than 1% helium relative to lineament density. Lineament density is derived from the combination of topographic, magnetic, gravity, and interpretated basement lineaments and interpreted intrusive bodies. Lineament density defines areas that have the highest probably of fracturing. Red colored lineaments are areas where 4 or more lineament trends overlie one another. Red colored dots are wells that tested greater than 4% helium while orange-colored dots are those wells that tested 1-4% helium. 48 of the 48 wells (100%) that tested >1% lie on high fracture probably lineaments.

Lineament intersections can also be derived from areas where lineaments trending at different orientations (N-S, E-W, NW-SE, and NE-SW) converge (Figure 140). These lineament intersections would also represent areas of high fracture probability. Again, all the 48 high helium wells (>1% helium) within the high-resolution aeromagnetic study area (100%) lie on lineament intersections. The occurrence of high helium wells also appears related to the location of intrusive bodies interpreted from the high-resolution aeromagnetic data (Figure 141). Intrusive bodies are probably largely responsible for both the release of helium from the basement source and for creating the migration pathways by generating both radial and concentric fractures.

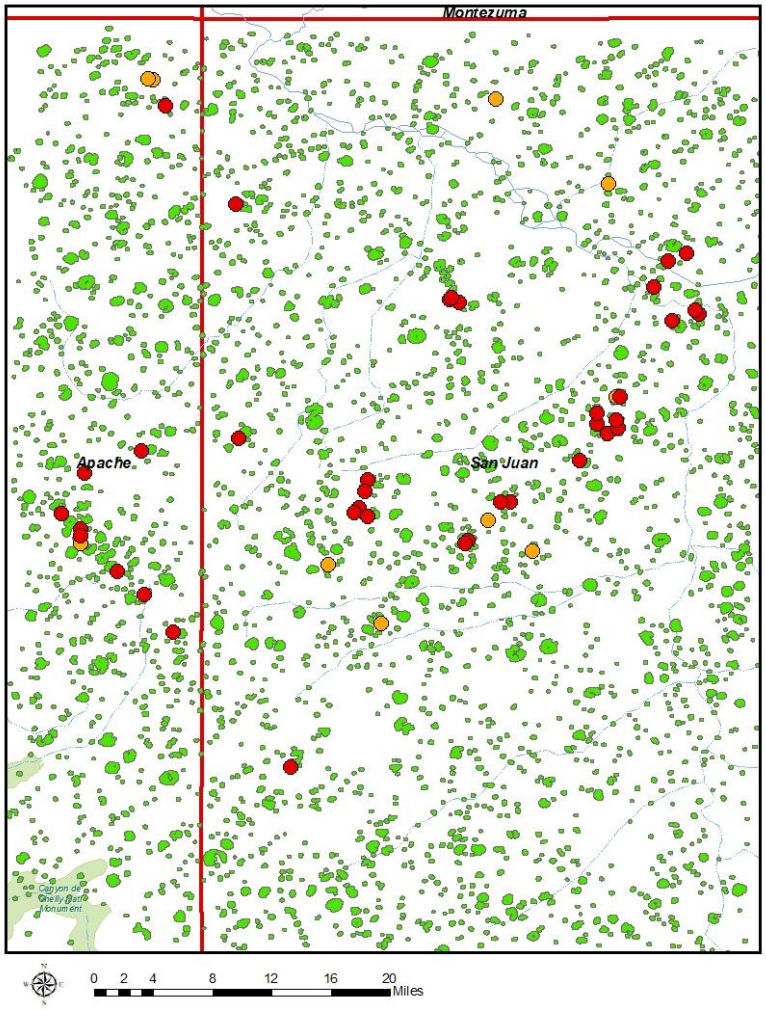


Figure 140. Location of 48 helium wells that tested greater than 1% helium relative to lineament intersections. Lineament density are areas where lineament trends of different orientations intersect and are interpreted as areas of highest fracture probably. Red colored dots are wells that tested greater than 4% helium while orange-colored dots are those wells that tested 1-4% helium. 48 of the 48 wells (100%) that tested >1% lie on lineament intersections.

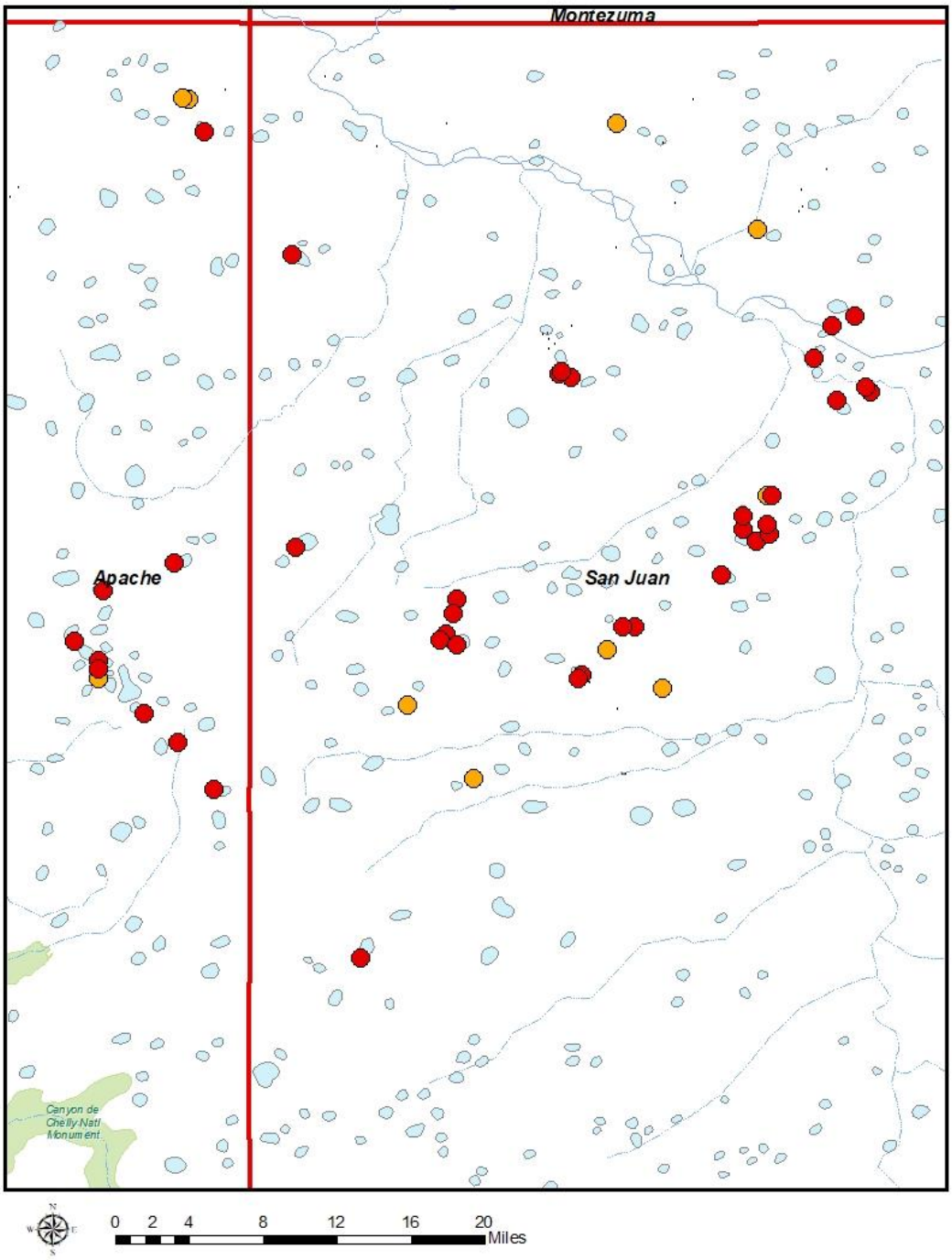


Figure 141. Location of 48 helium wells that tested greater than 1% helium relative to intrusive bodies as interpreted from the high-resolution aeromagnetic data. Intrusive bodies are probably largely responsible for both the release of helium from the basement source and for creating the migration pathways by generating both radial and concentric fractures. Red colored dots are wells that tested greater than 4% helium while orange-colored dots are those wells that tested 1-4% helium. 48 of the 48 wells (100%) that tested >1% lie on or within <0.5 miles of an intrusive body.

Areas most prospective for future helium discoveries are defined by where lineament intersections lie either on or adjacent to intrusive bodies based on the above observations (Figure 142). Over 250 prospective helium locations have been identified within the high-resolution aeromagnetic study area excluding areas that had previously been tested or where surface volcanics occur. The success rate for finding helium is very high on locations where lineament intersections overlie intrusive bodies (Figure 143). Thirty-five wells (35) have previously tested these overlap areas and resulted in sixteen (16) helium producers, ten (10) wells that tested helium but were not completed as a producer, and nine (9) dry holes. These well tests yield a 74% probability of finding helium (POSg) and 62% probability of making a helium producer (POSc) from the POSg population. Helium content can also be predicted by merging a grid of helium concentrations from the USGS helium database over the study area with the fracture network from the directional lineament trends (Figure 144). Prospects are then overlain on the resultant predicted helium concentration grid to estimate the prospects helium content.

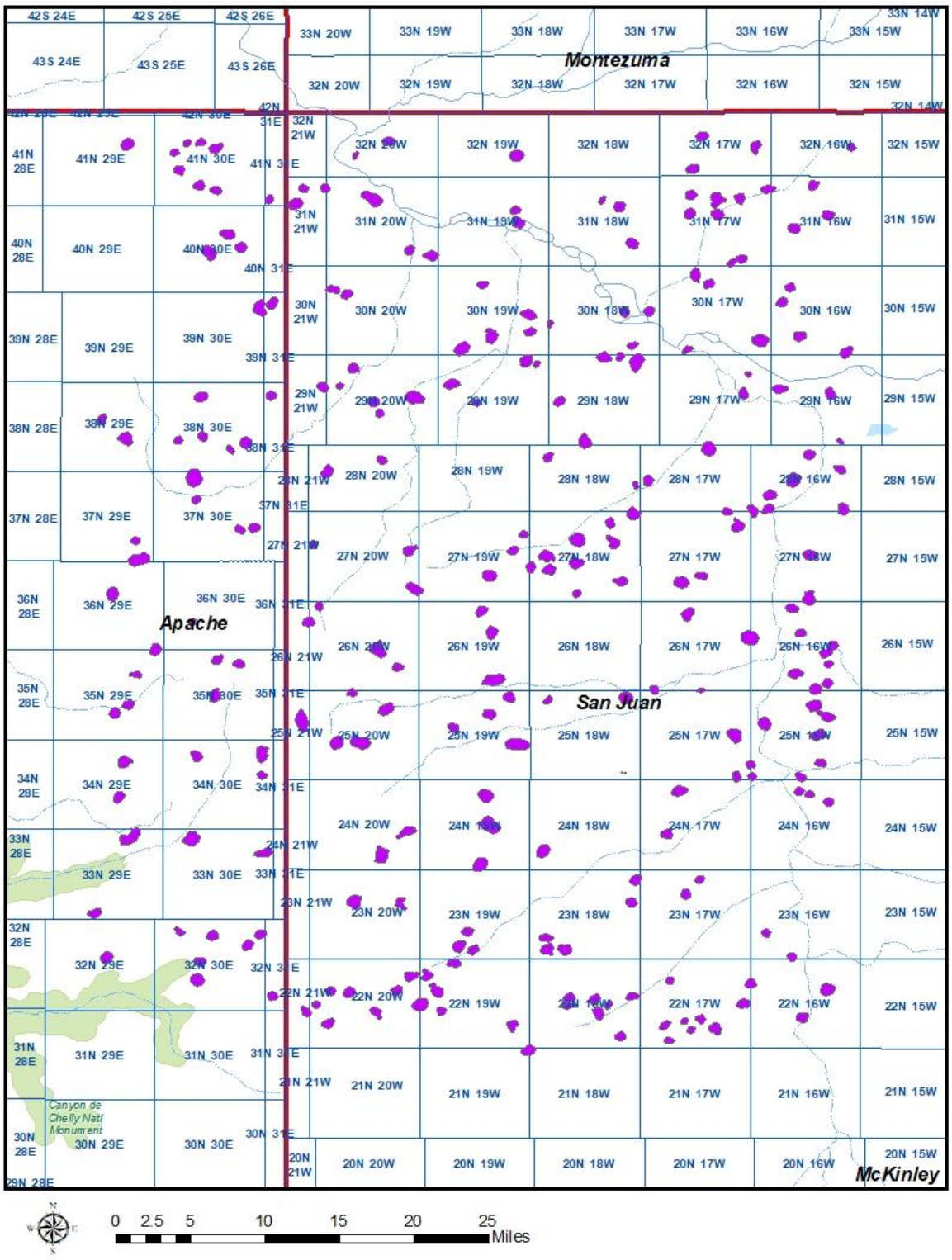


Figure 142. Helium prospective areas (253) identified where lineament intersections lie on or adjacent to intrusive bodies as defined by the high-resolution aeromagnetic survey data. Lineament intersections and intrusive body overlaps that have either previously been tested of represented by surface volcanics have been excluded.

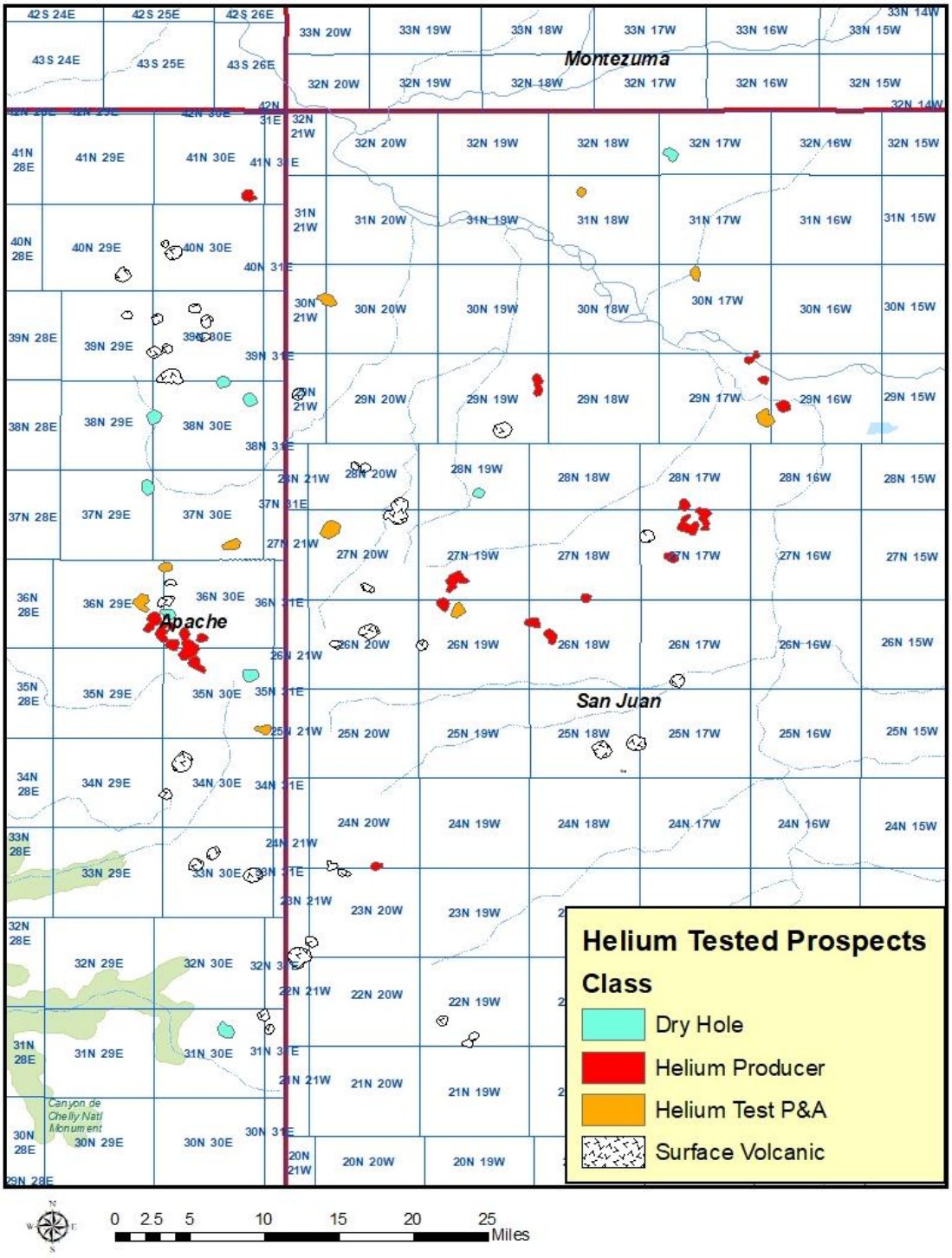


Figure 143. Lineament intersection and intrusive body overlap areas that had been previously tested or represented by surface volcanics. Thirty-five wells (35) that previously tested these overlap areas resulted in sixteen (16) helium producers, ten (10) wells that tested helium but were not completed as a producer, and nine (9) dry holes. These well tests yield a 74% probability of finding helium (POSg) and 62% probability of making a helium producer (POSc) from the POSg population. Thirty-nine (39) of the overlap areas were surface volcanics.

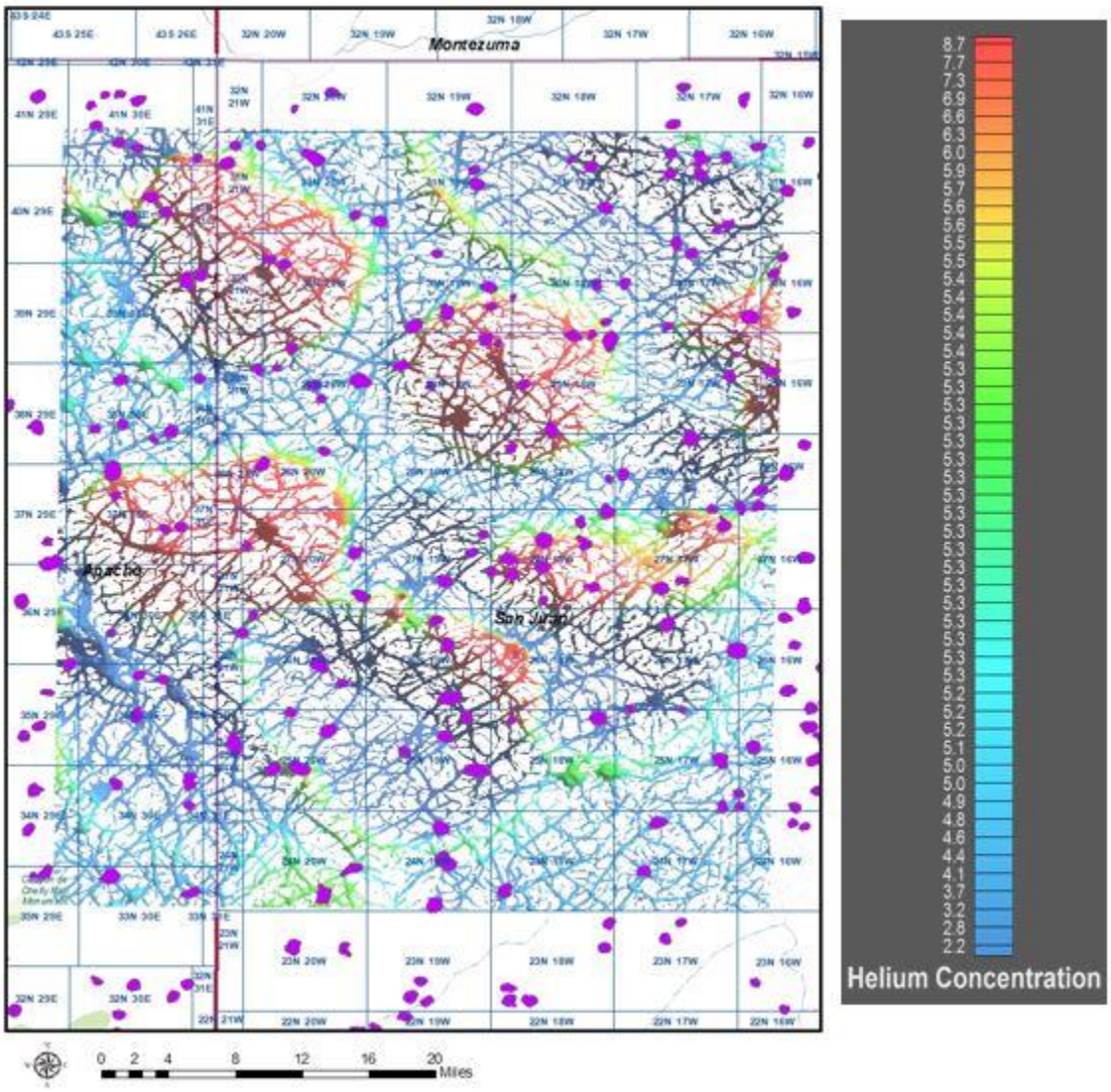


Figure 144. Helium prospects identified in this study and their predicted helium concentrations.

## Interpretation of helium soil gas data with high-resolution aeromagnetic survey results

Interpretation of the helium soil gas results was previously discussed based solely on relationships between the soil gas results and structural and/or well control. The seven helium soil gas areas are now interpreted based on the any observations and relationships observed after integrating the high-resolution aeromagnetic data results. The helium soil gas sample areas include Tohache Wash, Beautiful Mountain, Porcupine Dome, Tom, White Rock, Akah, and Rattlesnake. Figures 145-158 discuss the comparison of anomalous helium soil gas

concentrations (>50 ppb above background helium of 5.33 ppm) from the seven sample areas with lineament density, lineament intersections, interpretated intrusive bodies, and interpretated basement lineaments based on the high-resolution aeromagnetic data collected in this study. Overall, the agreement between all these datasets is very good.

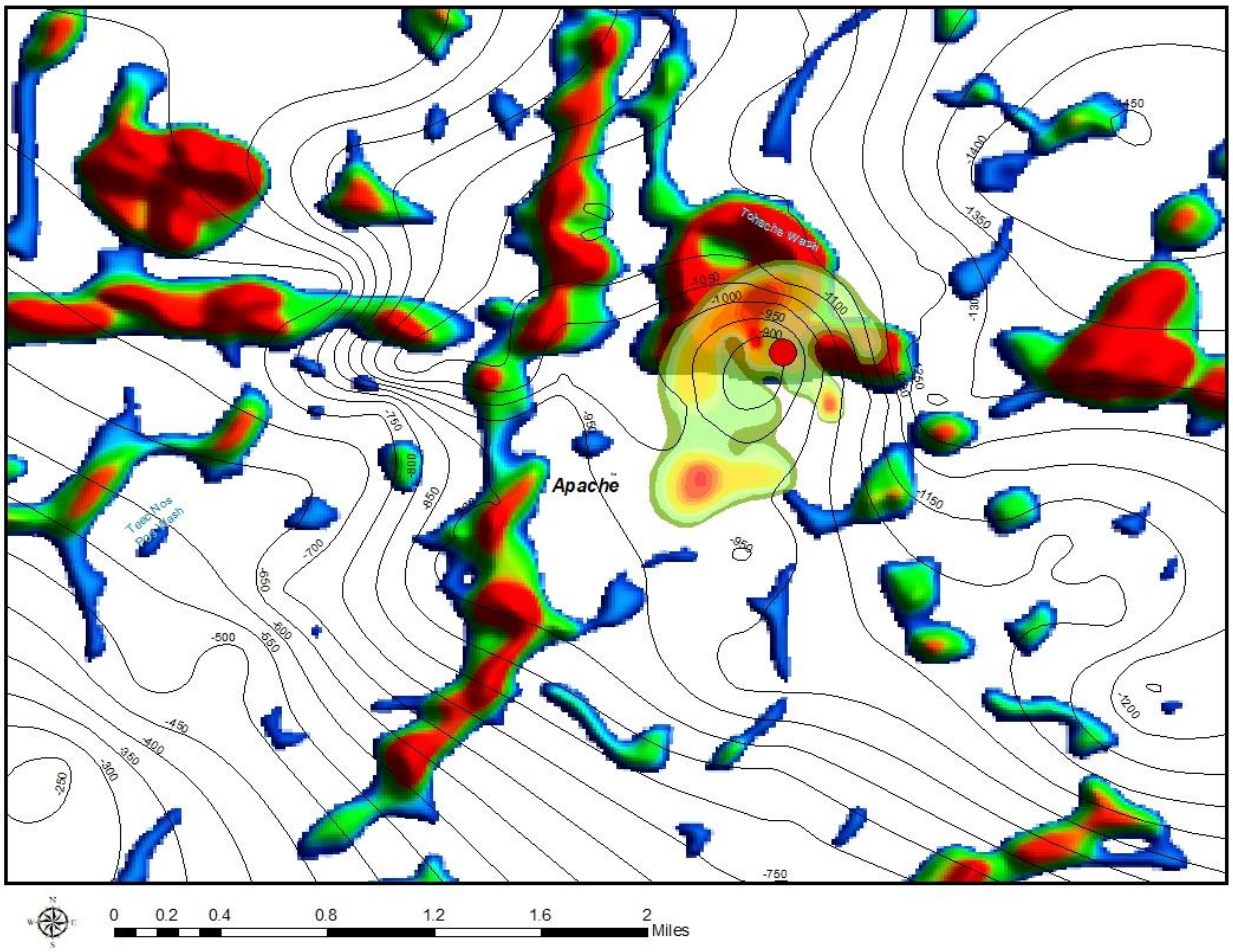


Figure 145. Integration of helium gas data from the Tohache Wash sample area with lineament density derived from the high-resolution aeromagnetic data. Leadville structure is also shown on the map. The Navajo-Z well helium discovery (red dot) and the northern half of the anomalous helium soil area and the Leadville seismic structure correspond well to areas of highest lineament trend correspondence (red areas) and areas of highest fracture probably.

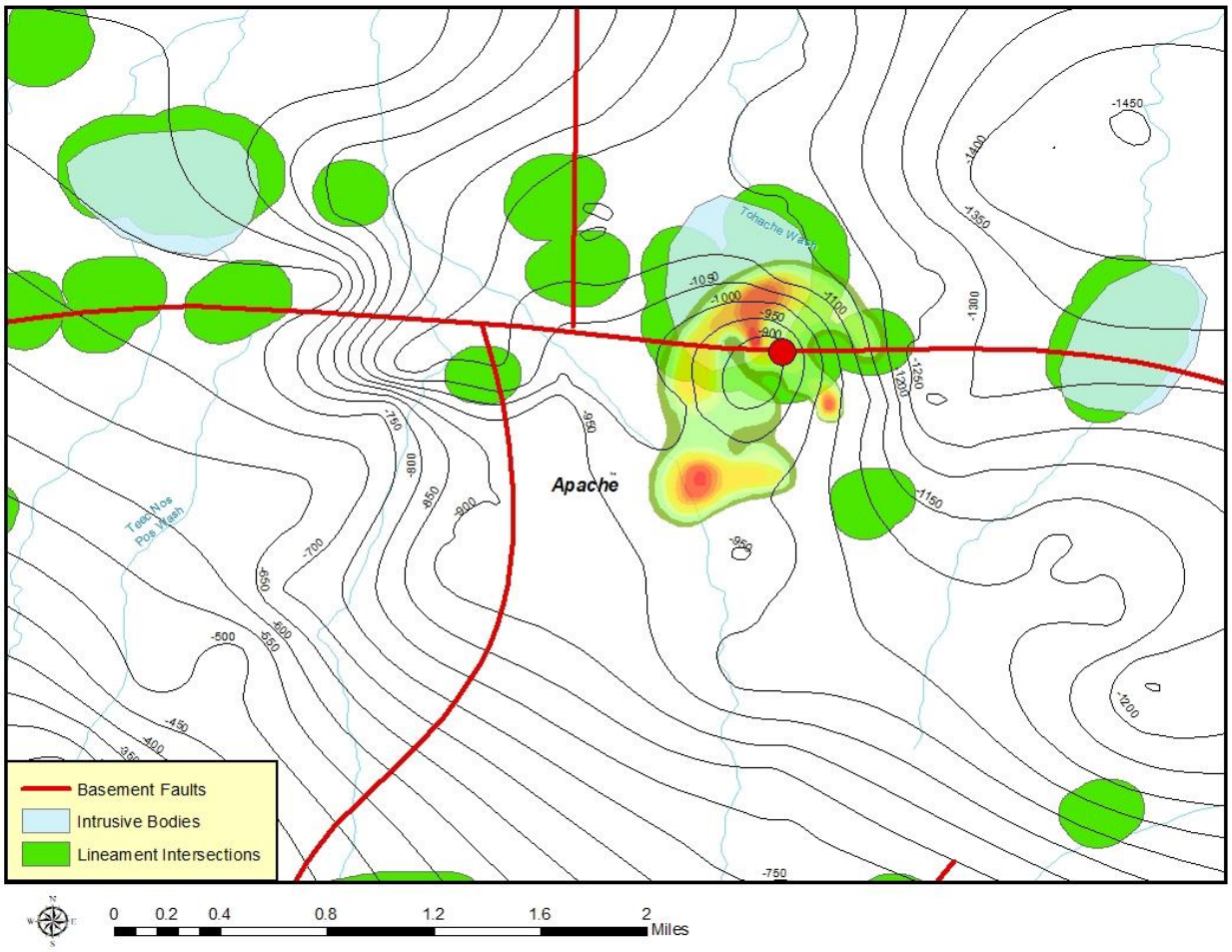


Figure 146. Comparison of helium gas data from the Tohache Wash sample area with the location of lineament intersections (green-colored areas) and intrusive bodies (light blue colored areas). Note excellent agreement between the locations of lineament intersections, intrusive bodies, basement lineaments (red lines), anomalous helium soil gas readings, and the Leadville structural closure.

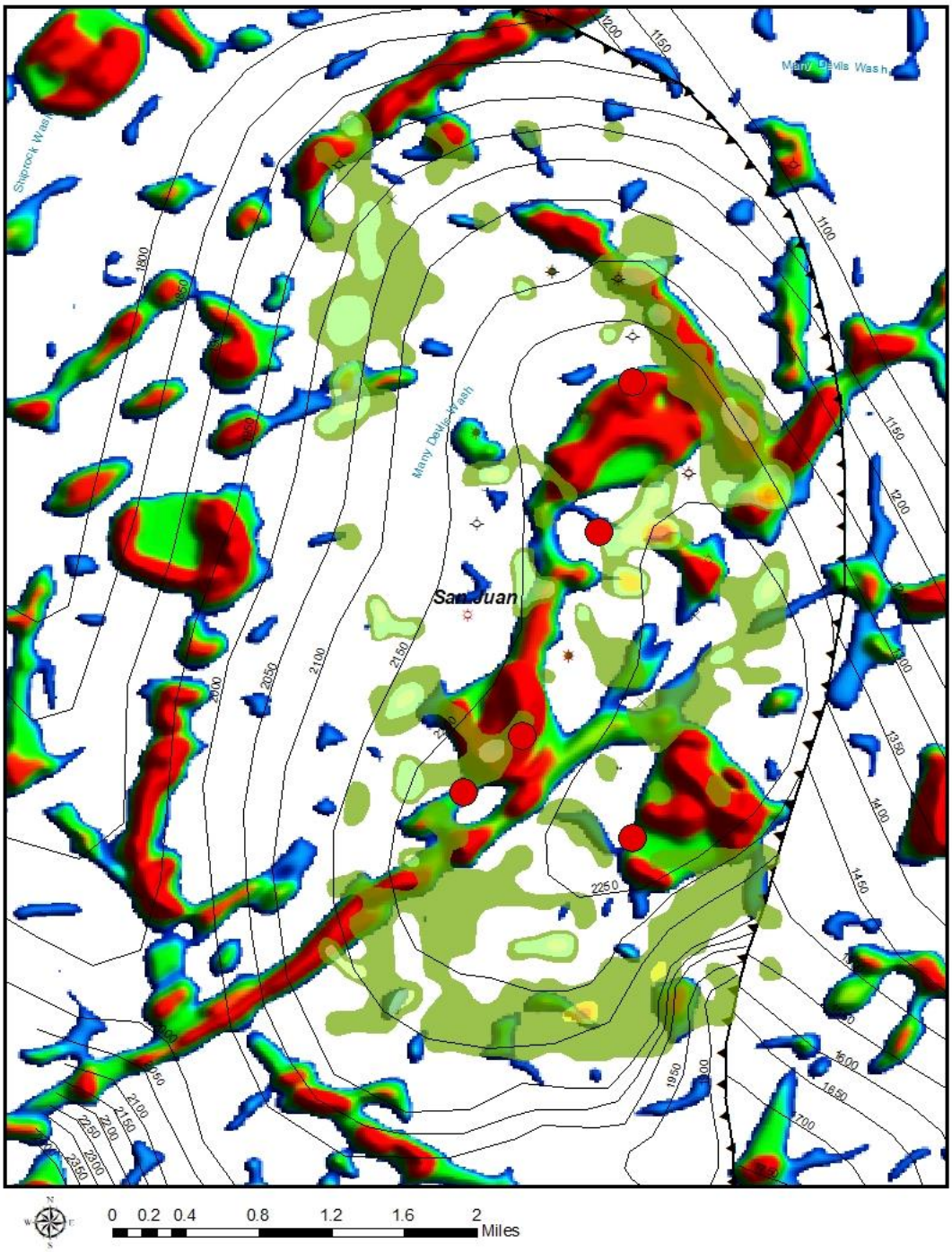


Figure 147. Integration of helium gas data from the Beautiful Mountain sample area with lineament density derived from the high-resolution aeromagnetic data. Permian Organ Rock structure is also shown on the map. Red dots represent wells that tested >4% helium in either the Organ Rock or Leadville (Mississippian) limestone and occur in areas of high lineament density (red areas) and highest fracture probably. Anomalous soil gas areas correspond in part to areas of high lineament density. Since the Organ Rock and Leadville helium deposits were previously produced, the highest lineament

density areas in the center of the field do not show anomalous helium soil gas readings and most likely due to depletion.

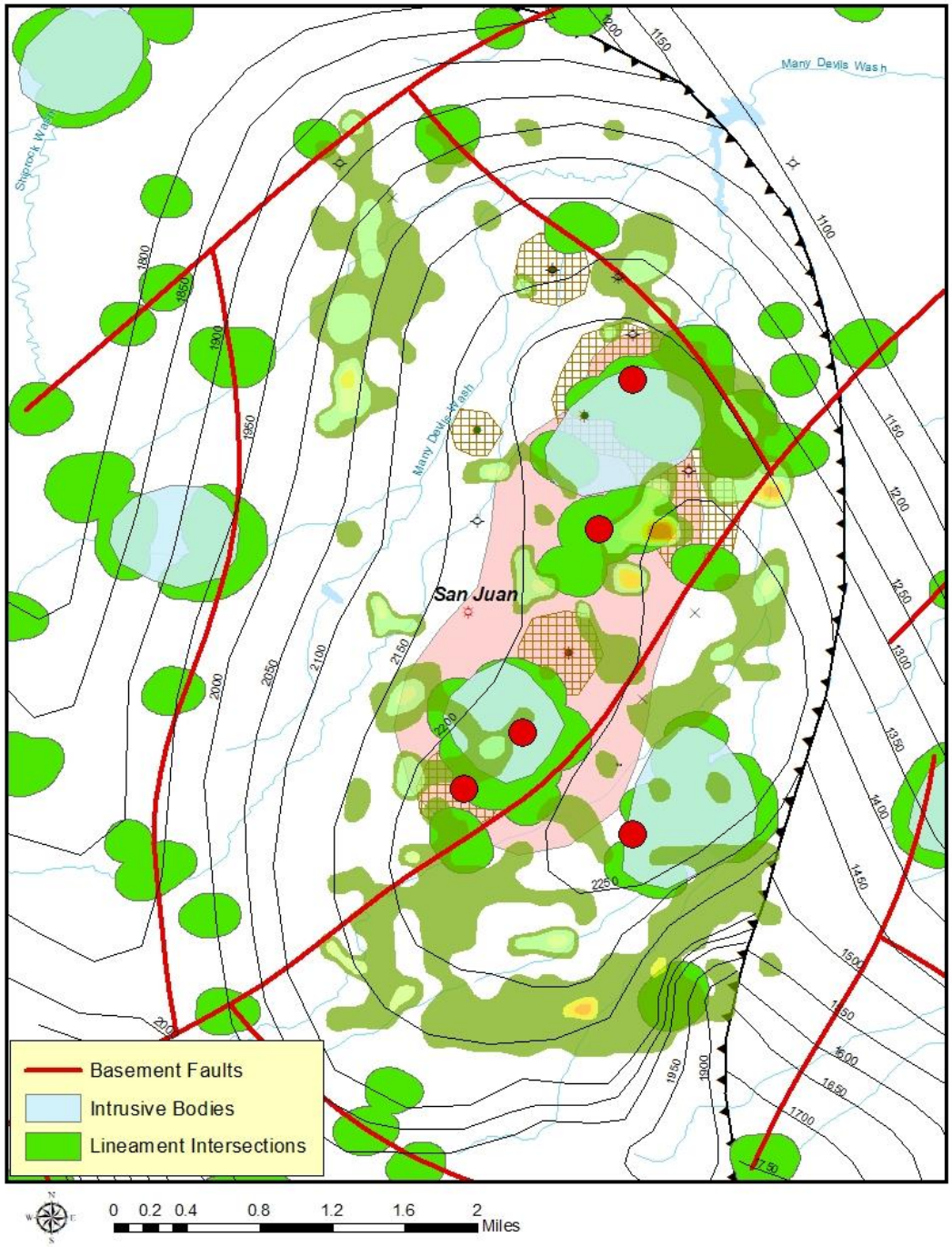


Figure 148. Comparison of helium gas data from the Beautiful Mountain sample area with the location of lineament intersections (green-colored areas) and intrusive bodies (light blue colored areas). Basement lineaments are shown as red lines. Wells that tested >4% helium (red dots) all occur on lineament intersections and mostly on intrusive bodies. Leadville helium produced areas are shown in pink color and Organ Rock helium produced areas are shown in cross-hatched pattern. Prospective

remaining helium areas lie either along basement lineament and intersections on northeast side of structure or in areas not corresponding to basement lineaments or lineament intersections to the south and northwest portions of the structure.

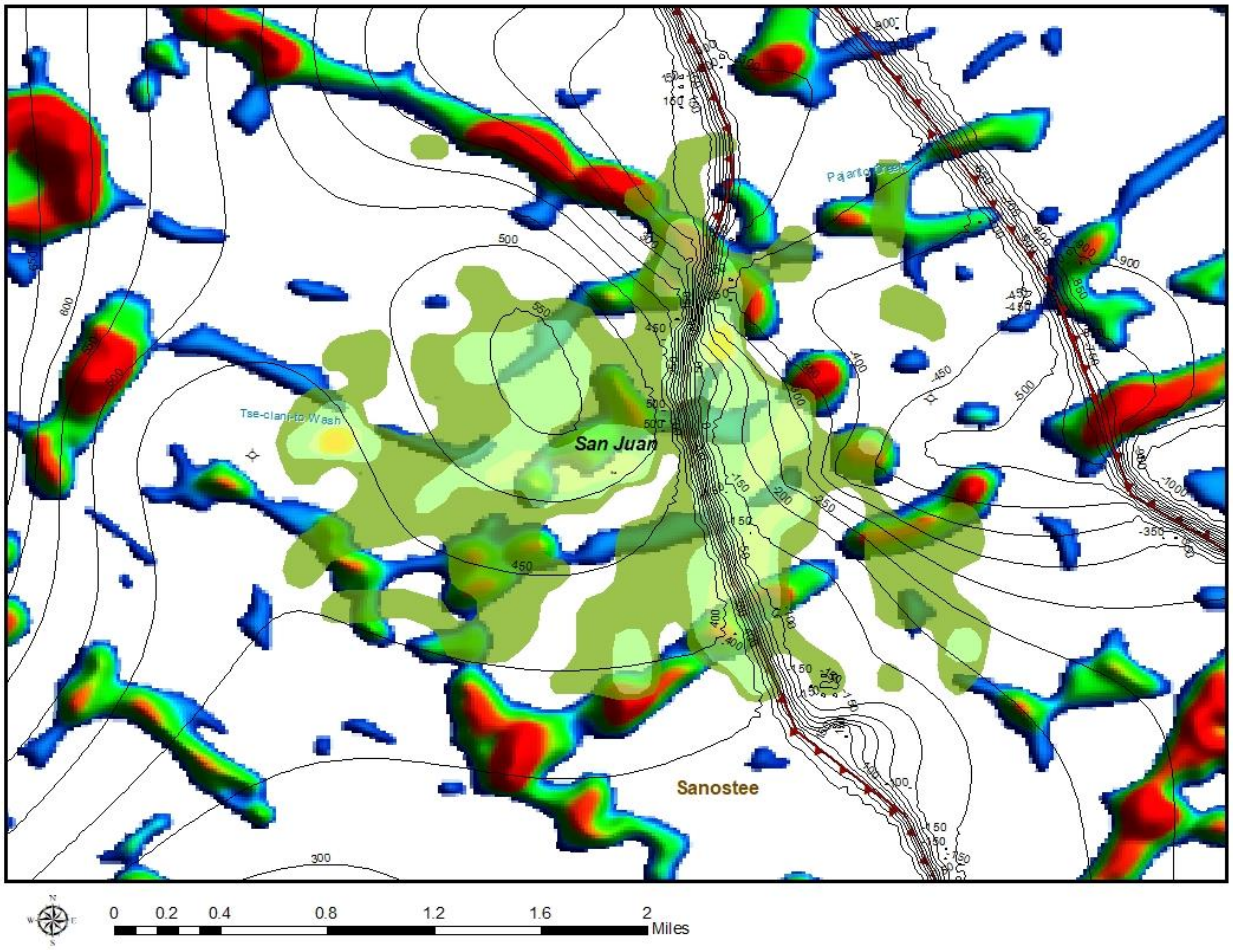


Figure 149. Integration of helium gas data from the Porcupine Dome sample area with lineament density derived from the high-resolution aeromagnetic data. Mississippian Leadville structure is also shown on the map. Anomalous helium soil gas readings correspond generally well with either strong lineament density trends (red area) to the north and east portions of the sample area or in weak lineament density features (blue and green colored areas) around the Leadville closure in the center of the map.

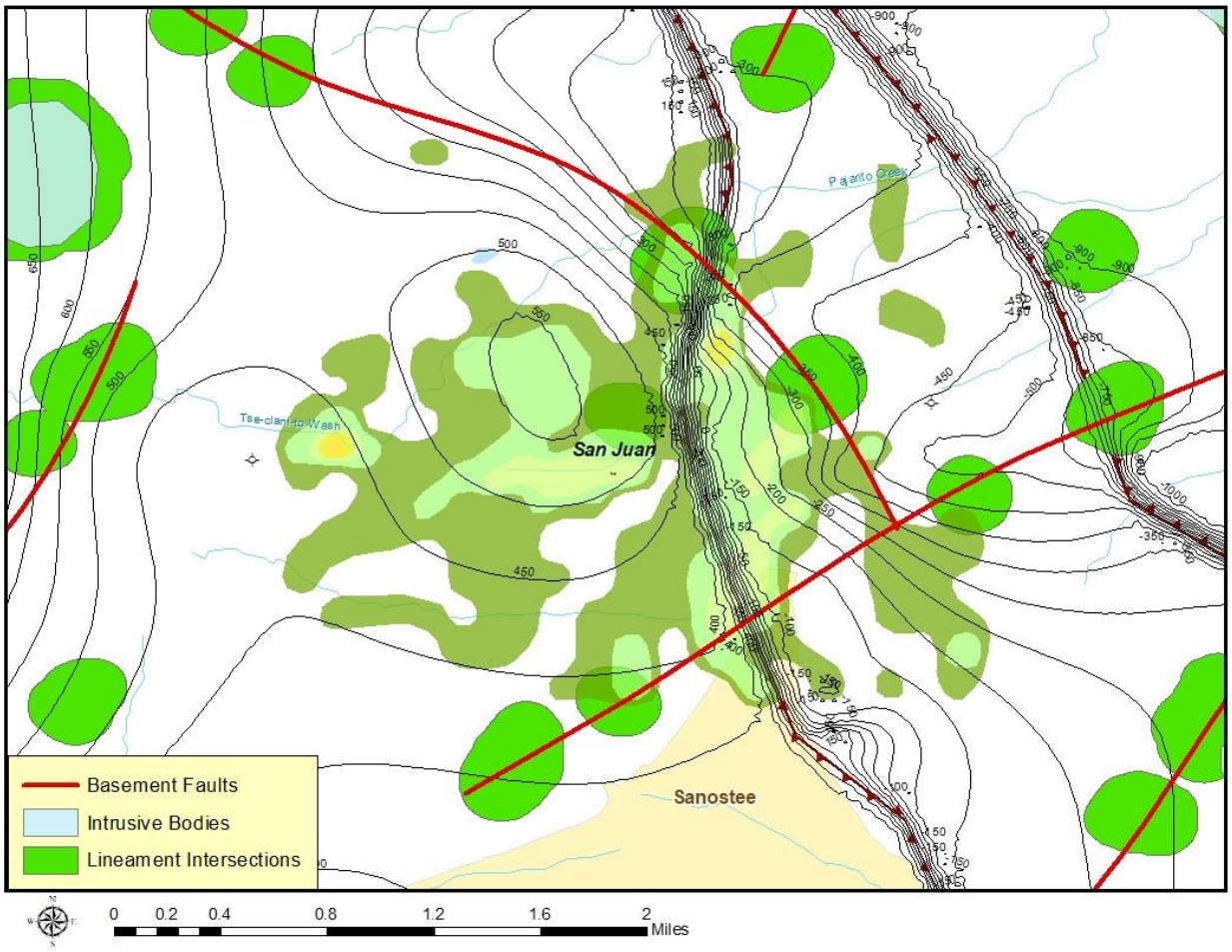


Figure 150. Comparison of helium gas data from the Porcupine Dome sample area with the location of lineament intersections (green-colored areas) and intrusive bodies (light blue colored areas). Basement lineaments are shown as red lines. No intrusive bodies occur within the helium soil sample area, but anomalous helium soil gas areas do tend to correspond to lineament intersections and basement lineaments.

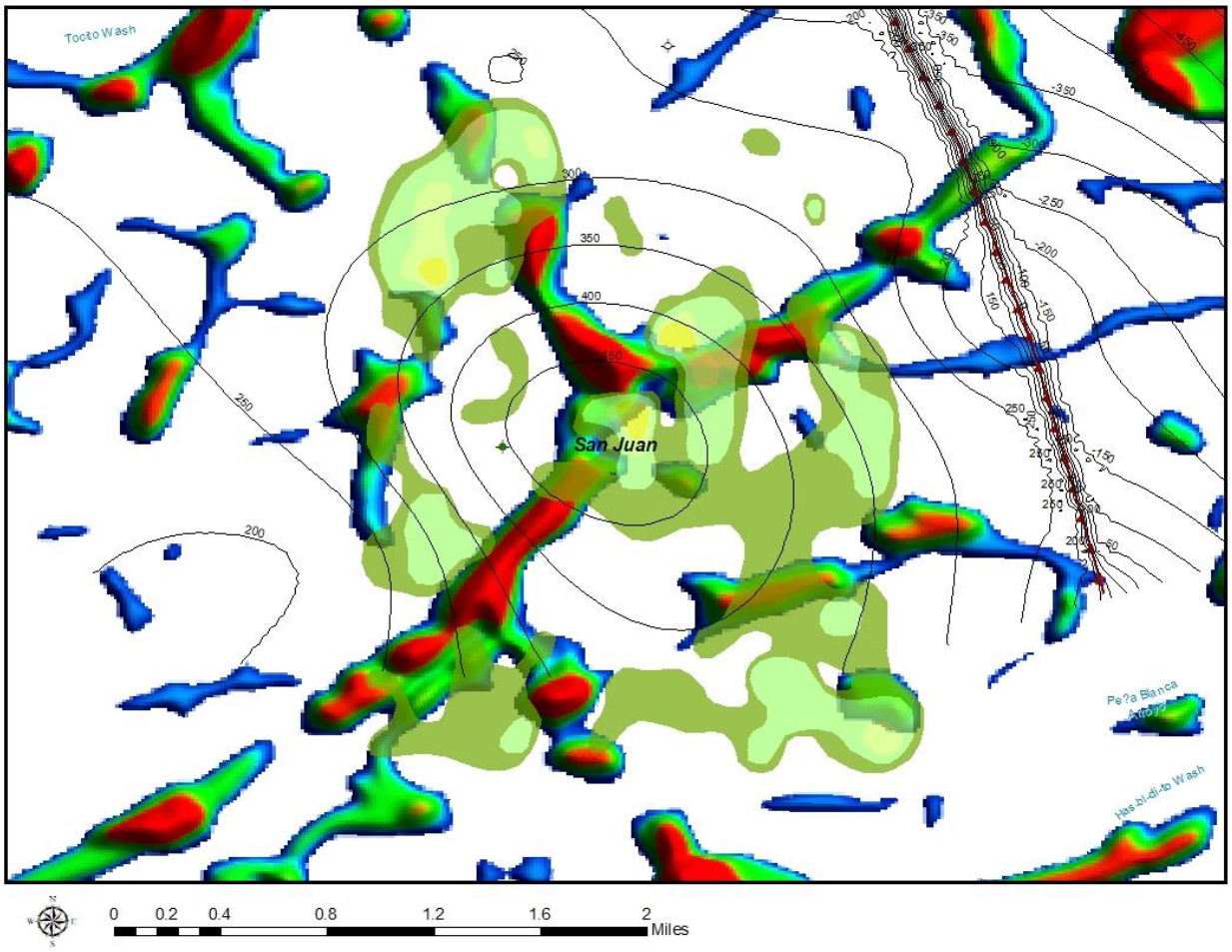


Figure 151. Integration of helium gas data from the Tom sample area with lineament density derived from the high-resolution aeromagnetic data. Mississippian Leadville structure is also shown on the map. Anomalous helium soil gas readings correspond generally well with either strong lineament density trends (red area) that cross the Leadville closure in the center of the map or ring the closure on the flanks of the structure.

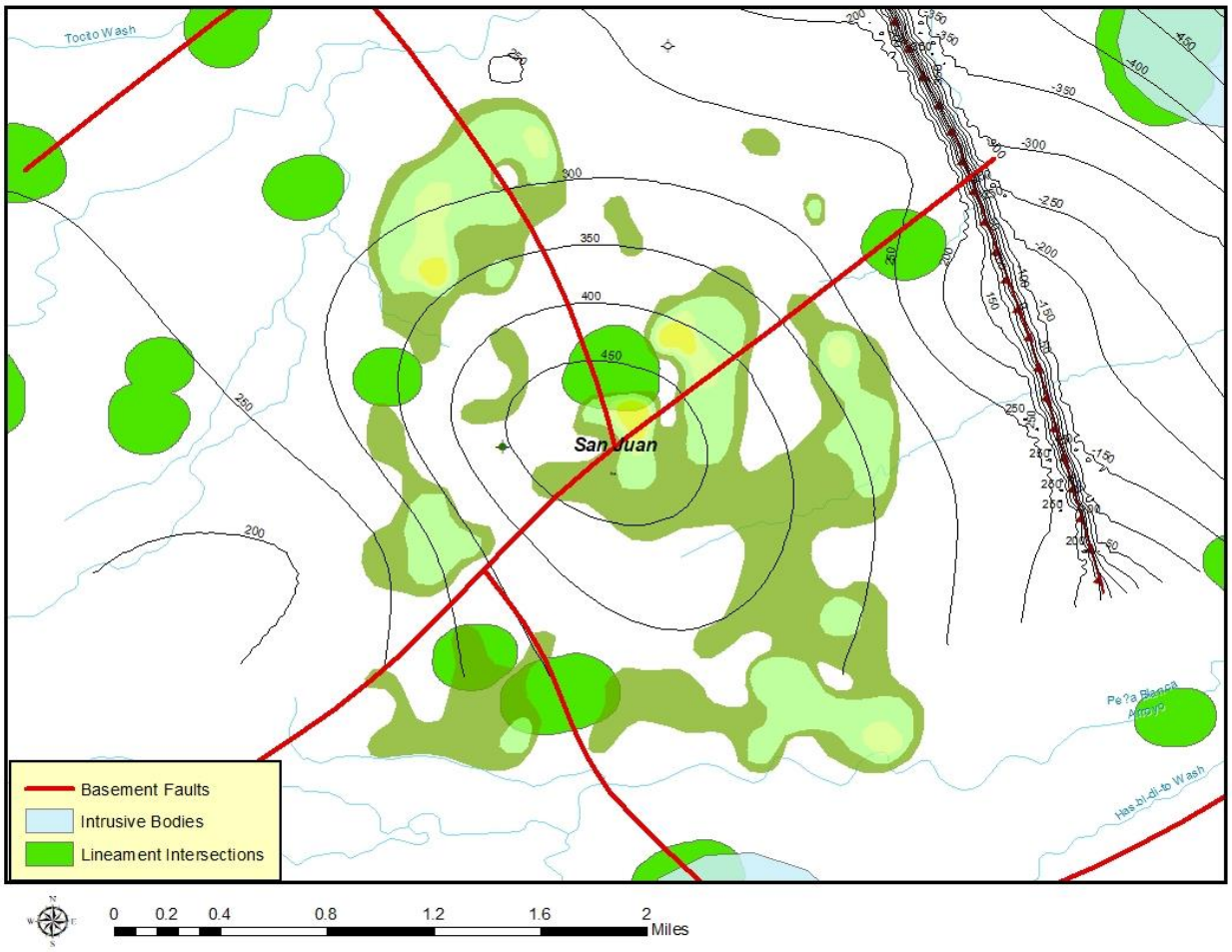


Figure 152. Comparison of helium gas data from the Tom sample area with the location of lineament intersections (green-colored areas) and intrusive bodies (light blue colored areas). Basement lineaments are shown as red lines. No intrusive bodies occur within the helium soil sample area and anomalous helium soil gas areas do not, for the most part, correspond to lineament intersections.

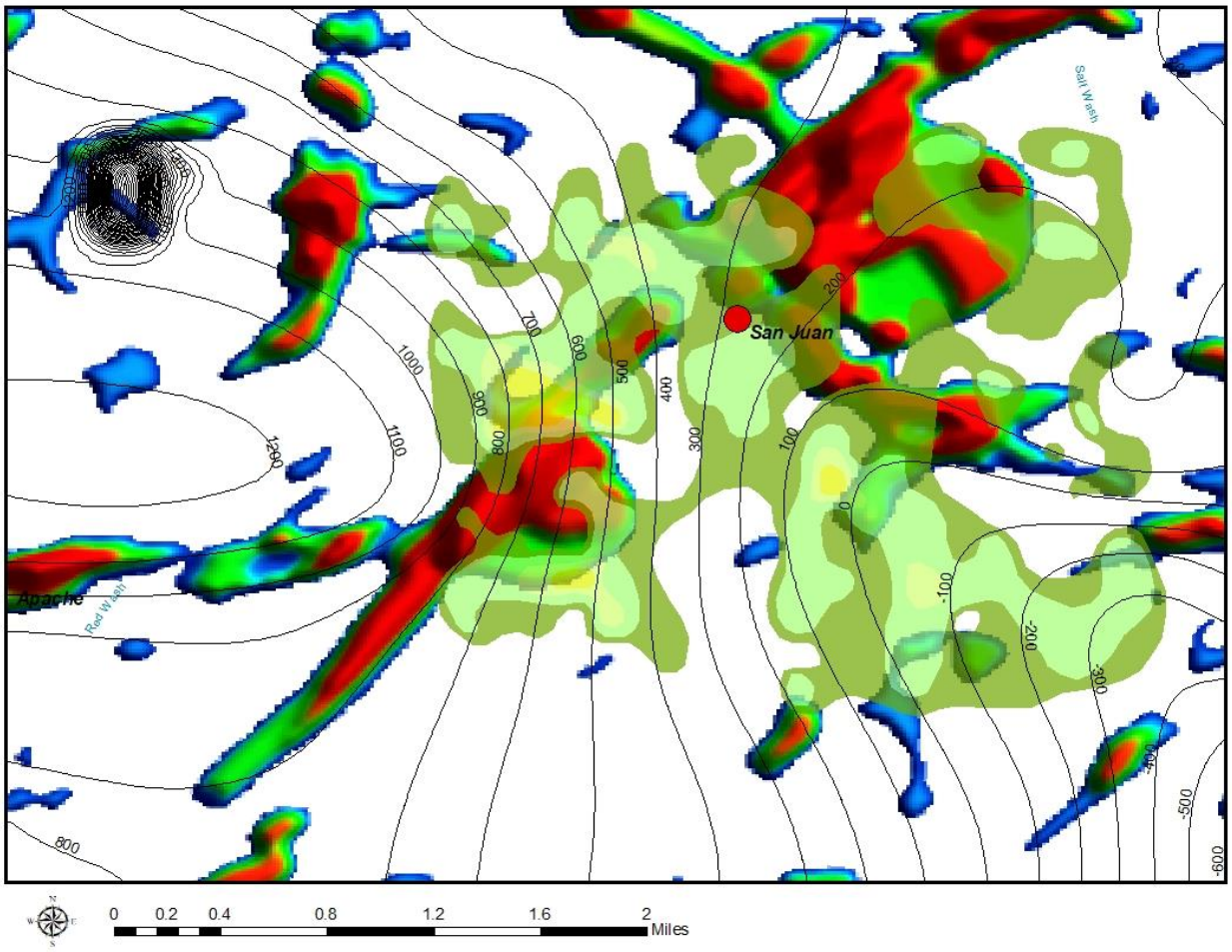


Figure 153. Integration of helium gas data from the White Rock sample area with lineament density derived from the high-resolution aeromagnetic data. Precambrian structure derived from the high-resolution aeromagnetic data is also shown on the map. Anomalous helium soil gas readings correspond generally well with either strong lineament density trends (red area) in the sample area. A 1966 dry well that tested 5.2% helium from the Pennsylvanian Barker Creek and 7.8% helium from the Precambrian is shown as a red dot in center of sample area.

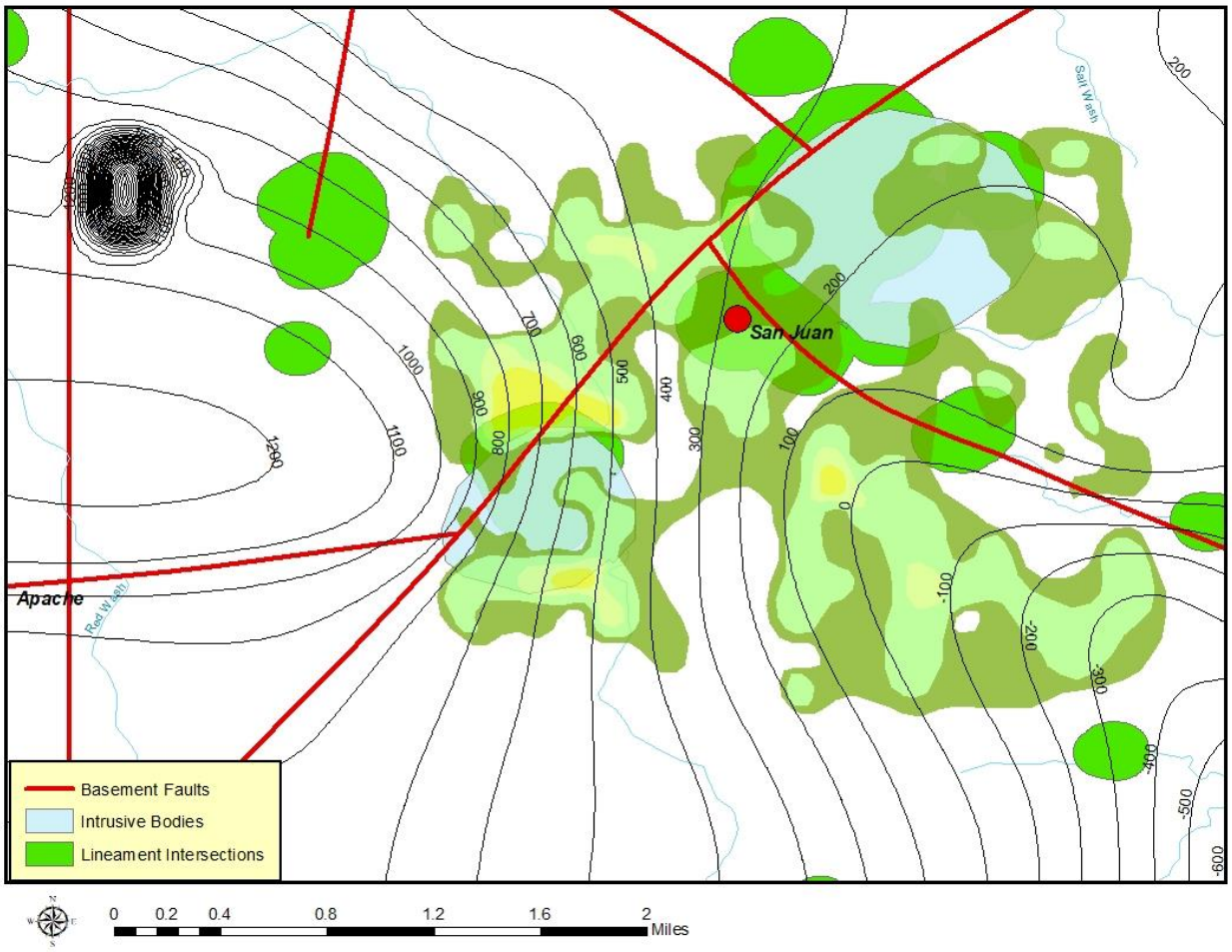


Figure 154. Comparison of helium gas data from the White Rock sample area with the location of lineament intersections (green-colored areas) and intrusive bodies (light blue colored areas). Basement lineaments are shown as red lines. There is a generally good agreement between anomalous helium soil gas areas and the location of lineament intersections, intrusive bodies, and basement lineaments (red lines). Note how intrusive bodies correspond to basement lineament intersections.

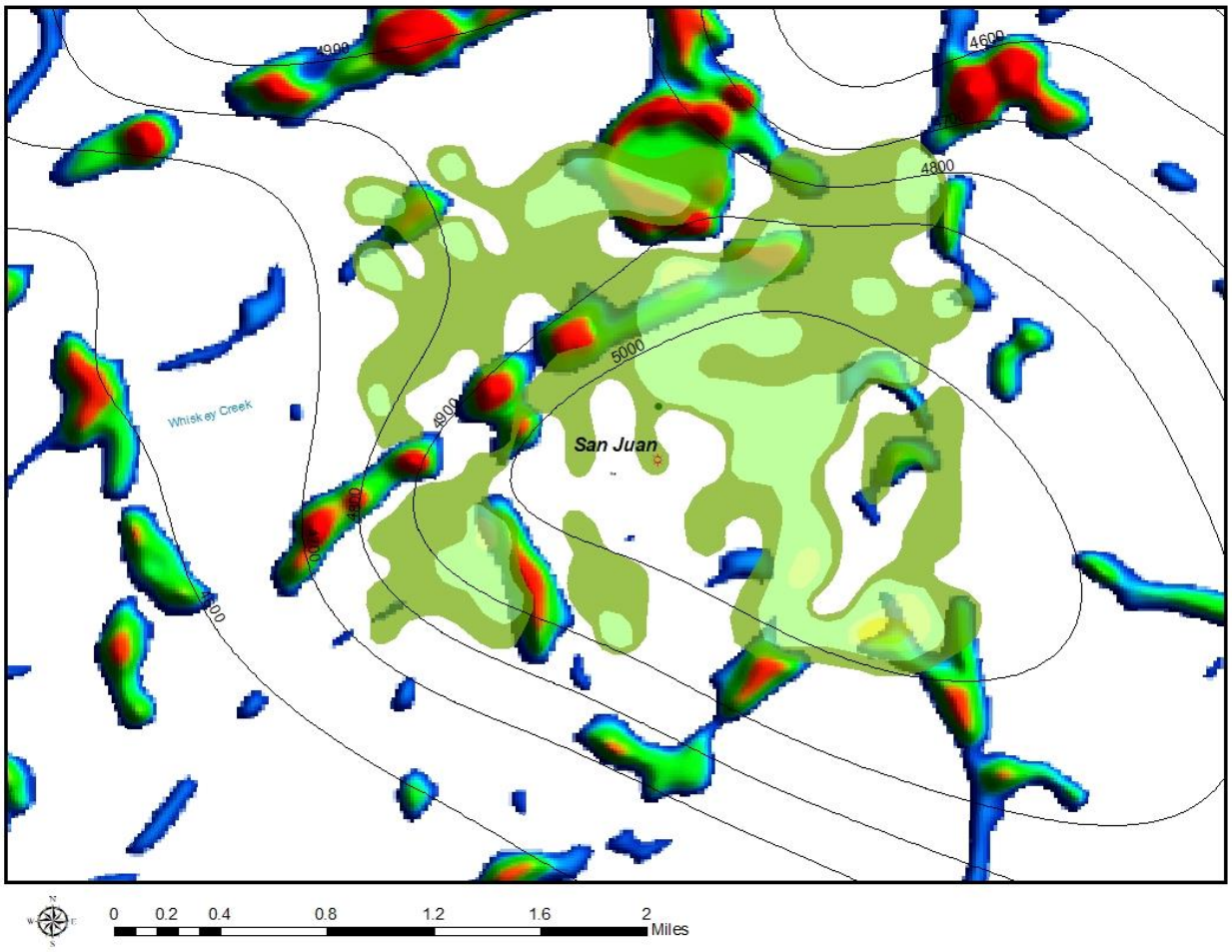


Figure 155. Integration of helium gas data from the Akah sample area with lineament density derived from the high-resolution aeromagnetic data. Precambrian structure derived from the high-resolution aeromagnetic data is also shown on the map. Anomalous helium soil gas readings correspond generally well with strong lineament density trends (red area) on the northwest flank of the Precambrian structural closure in the sample area. Other anomalous helium soil gas areas in the center of the Precambrian closure do not correspond to high lineament density trends.

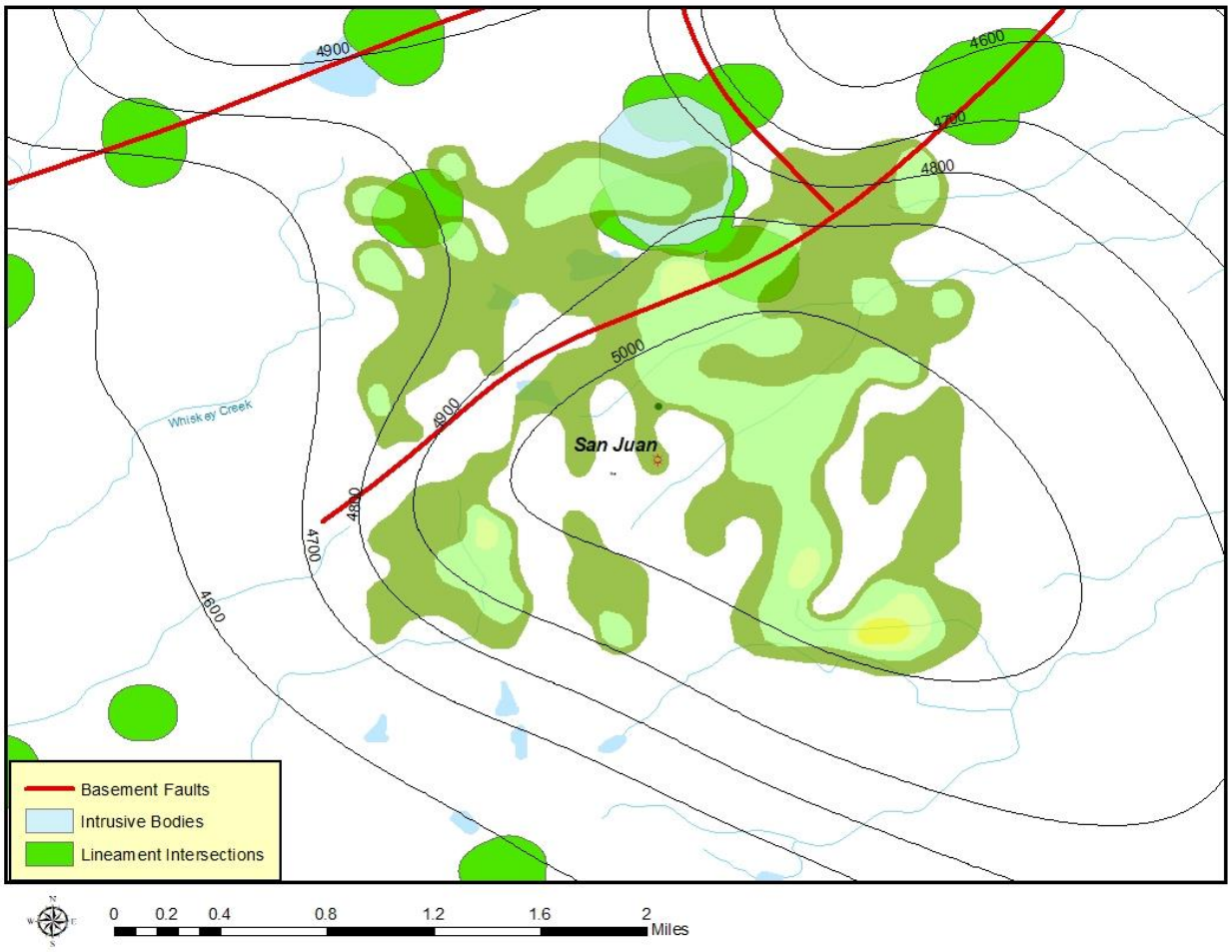


Figure 156. Comparison of helium gas data from the Akah sample area with the location of lineament intersections (green-colored areas) and intrusive bodies (light blue colored areas). Basement lineaments are shown as red lines. There is a generally good agreement between anomalous helium soil gas areas and the location of lineament intersections, intrusive bodies, and basement lineaments (red lines) on the northwest side of the Precambrian closure, while there appears to be no correspondence on the closure crest in the center of the sample area. The Precambrian structure is not strongly constrained by the high-resolution aeromagnetic data and could easily be located more to the northwest of the sample area.

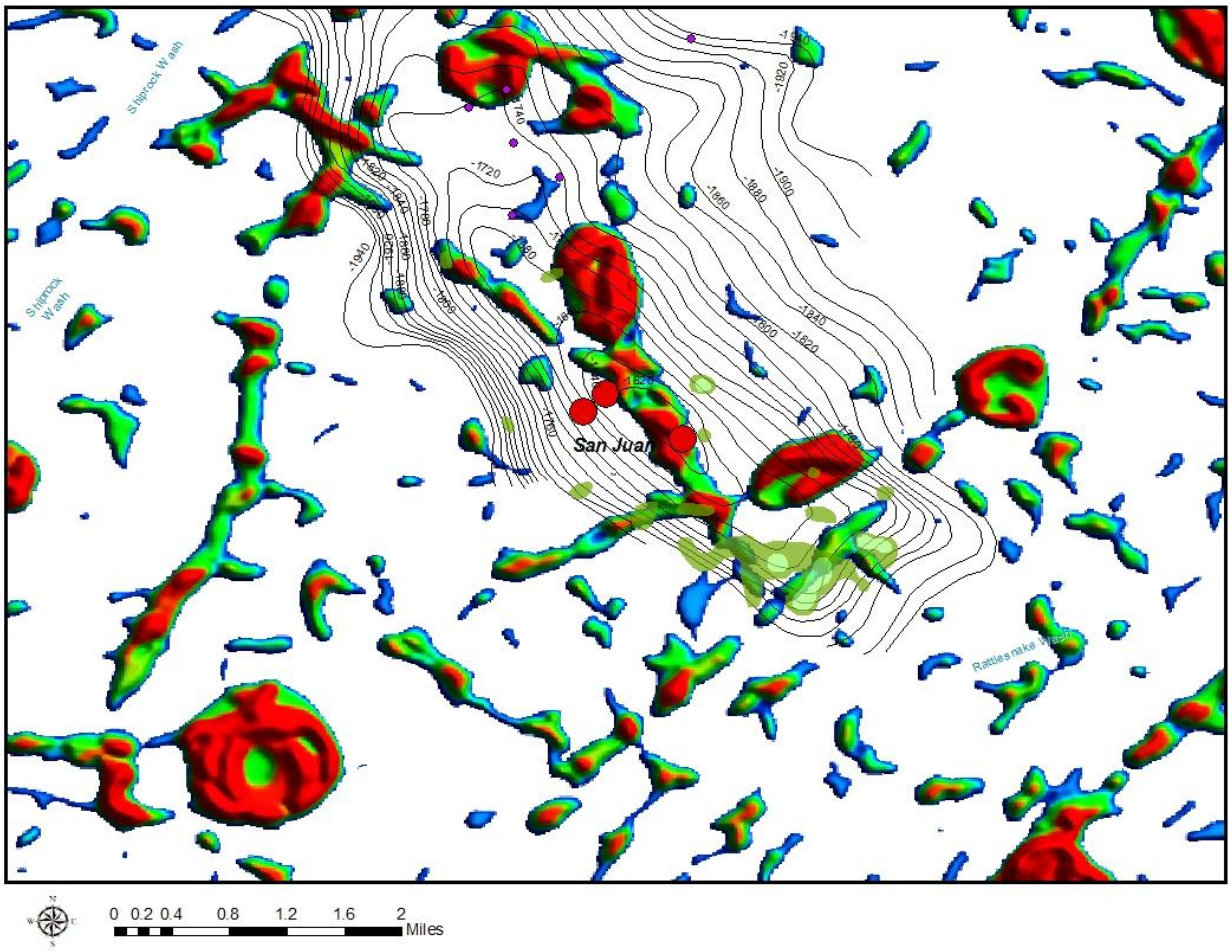


Figure 157. Integration of helium gas data from the Rattlesnake sample area with lineament density derived from the high-resolution aeromagnetic data. Mississippian Leadville structure is also shown on the map. Red dots represent wells that tested >4% helium in the Leadville helium reservoir and occur in areas of high lineament density (red areas) and highest fracture probably. The Rattlesnake helium field was produced and depleted in the 1940's and very weakly anomalous soil gas areas do not correspond to areas of high lineament density. Weak helium soil gas anomalous areas to the southwest portion of the structure may represent residual, undrained helium areas.

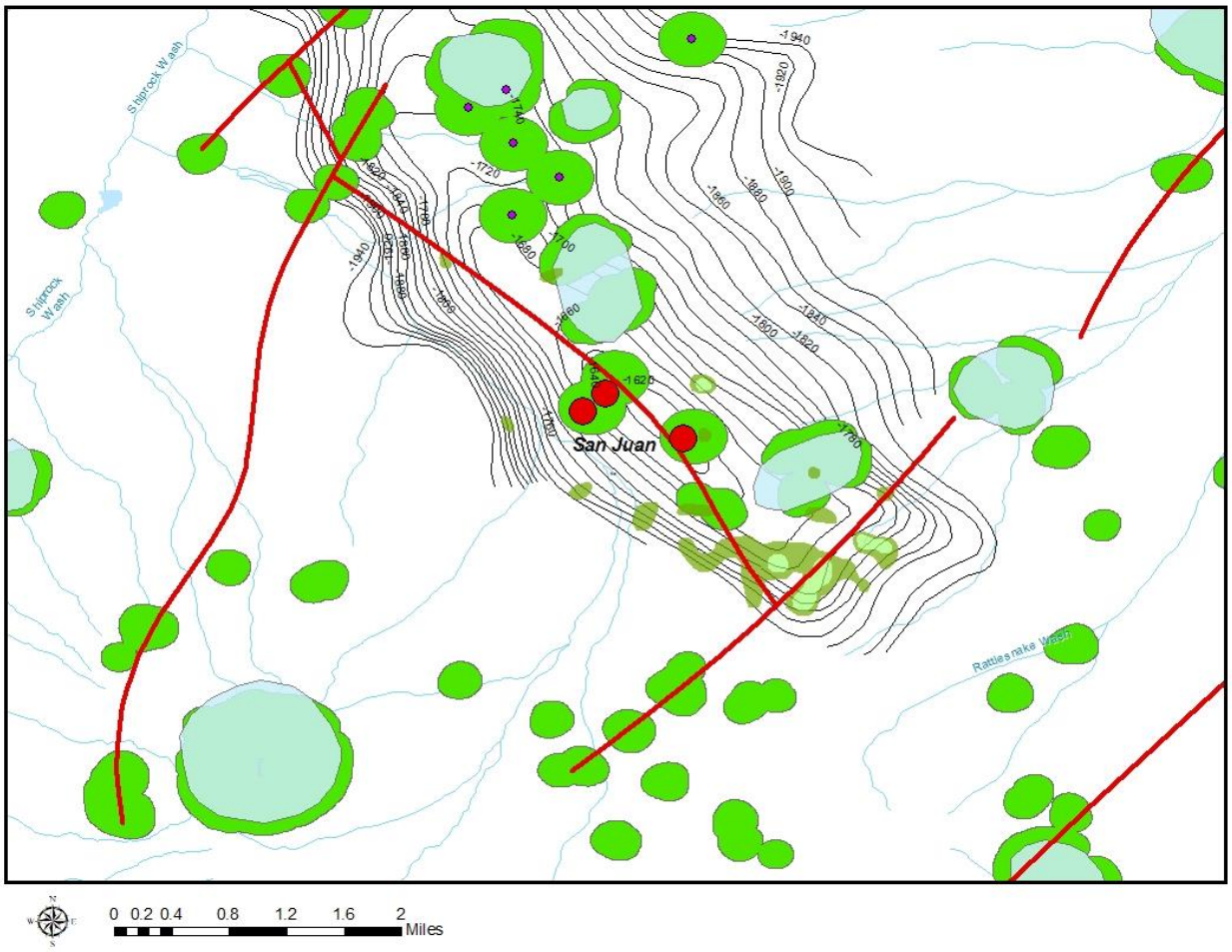


Figure 158. Comparison of helium gas data from the Rattlesnake sample area with the location of lineament intersections (green-colored areas) and intrusive bodies (light blue colored areas). Basement lineaments are shown as red lines. Wells that tested >4% helium from the Leadville reservoir (red dots) all occur on lineament intersections. Weak helium soil gas anomalous areas to the southwest portion of the structure may represent residual, undrained helium areas in the depleted Rattlesnake field.

## Conclusions

The results of the high-resolution aeromagnetic survey and helium soil gas sampling have shown that previously discovered and potential new helium accumulations can be identified using very low costs exploratory methods. Over 250 potential untested helium deposits were identified by this study within the high-resolution aeromagnetic survey area. Potential helium deposits are best identified by the correspondence of lineament intersections that lie on or adjacent to interpreted intrusive bodies using a high-resolution (0.25 X 1 mile grid) aeromagnetic survey. Helium soil gas surveys were found to be an effective means to further high-grade these prospective helium deposits that may occur in the subsurface. A proposed exploration workflow for identifying and high-grading helium prospects is shown in Figure 159.

Conducting additional high-resolution aeromagnetic surveys across the entire Defiance uplift area would give a view of the total helium resource potential within the Navajo Nation. The thermal susceptibility study and the determination of present-day heat flow proved useful in defining areas where helium deposits would have most likely been flushed or highly diluted by carbon dioxide. The heat flow mapping also defines areas that may be prospective for developing geothermal resources.

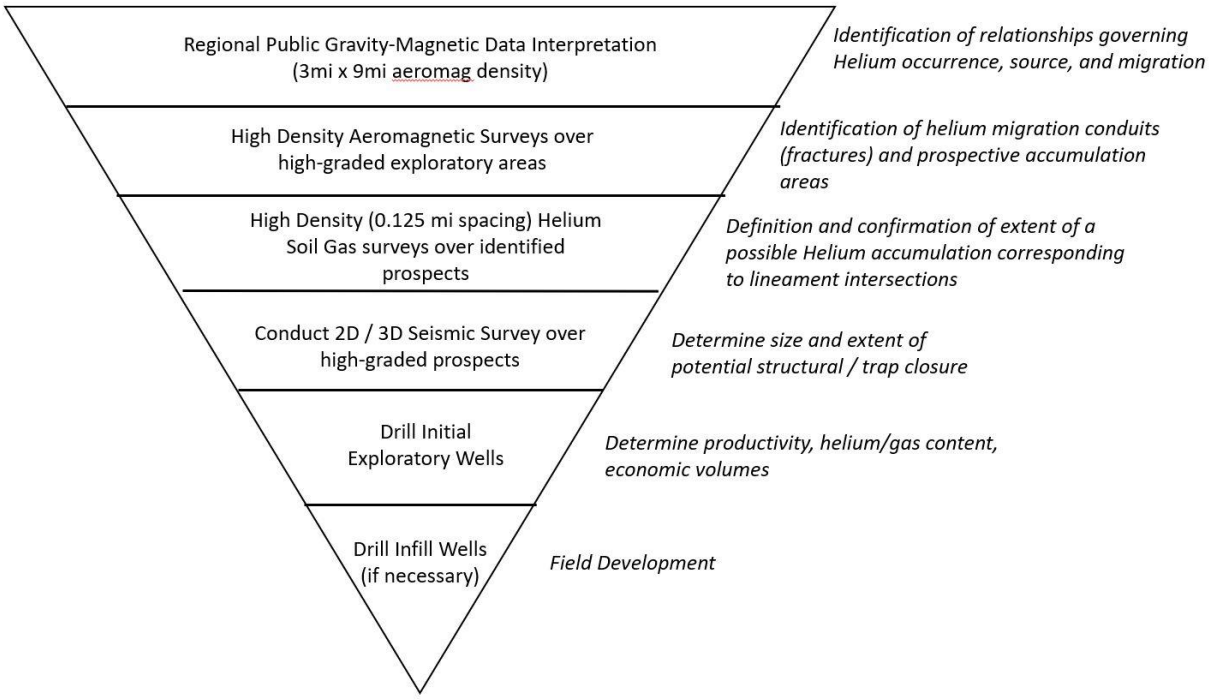


Figure 159. Proposed exploration workflow.

## Recommendations

Over 250 potential helium deposits were identified in this study based on the overlap of fracture intersections and intrusive body location using high-resolution aeromagnetic data. Additional high-resolution aeromagnetic surveys should be acquired to cover the entire Defiance uplift area and identify more potential helium leads. It is recommended that helium soil gas surveys be conducted over each of the leads identified in this study. 2D seismic data should be acquired over those leads that exhibit a strong helium soil gas response to confirm the presence of a structural trap in the sedimentary section. Ultimately, exploratory wells need to be drilled over those prospects with positive helium soil gas and structural trap results.

# References


Bahr, R., Lippolt, H.J. and Wernicke, R.S. 1994. Temperature-induced He4 degassing of specularite and botryoidal hematite: A He4 retentivity study. *Journal of Geophysical Research: Solid Earth*, **99**, 17 695- 17 707.

Ballentine, C.J. and Sherwood Lollar, B. 2002. Regional groundwater focusing of nitrogen and noble gases into the Hugoton-Panhandle giant gas field, USA. *Geochimica et Cosmochimica Acta*, **66**, 2483-2497.

Been, J.M., Hassemer, J.R. and Murrey, D.G. 1984. Methodology, geology and listing of analyses of helium samples in the Bisti, De-Na-Zin, and Ah-Shi-Sle-Pah Wilderness study areas, San Juan County, New Mexico. *USGS Open File Report 84-349*, 7p.

Boyce, J.W., Hodges, K.V., Olszewski, W.J. and Jercinovic, M.J. 2005. He diffusion in monazite: Implications for (U-Th)/He thermochronometry. *Geochemistry, Geophysics, Geosystems*, **6**, Q12004.

Broadhead, R.F. 2005. Helium in New Mexico – geologic distribution, resource demand and exploration possibilities. *New Mexico Geology*, **27**, 93-101.

Byrne, D.J., Barry, P., Lawson, M., Ballentine, C. 2017. Noble gases in conventional and unconventional petroleum systems. Geological Society, London, Special Publications.

Cherniak, D.J., Watson, E.B. and Thomas, J.B. 2009. Diffusion of helium in zircon and apatite. *Chemical Geology*, **268**, 155-166.

Danabalan, D. 2017. Helium: Exploration methodology for a strategic resource. PhD Thesis, Durham University, 295p.

Danabalan, D., Gluyas, J.G., Macpherson, C.G., Abraham-James, T.H., Bluett, J.J., Barry, P.H., and Ballentine, C.J. 2022. The principles of helium exploration. *Petroleum Geoscience*, **28**, 2021-2029.

Dodson, Martin H. 1973. Closure temperature in cooling geochronological and petrological systems. *Contributions to Mineralogy and Petrology*, **40**, 259-274.

Downey, M. 1984. Evaluating seals for hydrocarbon accumulations. *AAPG Bulletin*, **68**, 1752-1763.

Dunai, T.J. and Roselieb, K. 1996. Sorption and diffusion of helium in garnet: implications for volatile tracing and dating. *Earth and Planetary Science Letters*, **139**, 411-421.

Farley, K.A. 2000. Helium diffusion from apatite: General behavior as illustrated by Durango fluorapatite. *Journal of Geophysical Research: Solid Earth*, **105**, 2903-2914.

Farley, K.A. 2002. (U-Th)/He dating: Techniques, calibrations, and applications. *Reviews in Mineralogy and Geochemistry*, **47**, 819-844.

Friedman, I. and E.H. Denton, 1976, A Portable Helium Sniffer, Journal of Research U.S. Geological Survey, V. 4, No. 1, pp 35-36.

Gilifillan, S.M., Ballentine, C.J. et al. 2008. The noble gas geochemistry of natural CO2 gas reservoirs from the Colorado Plateau and Rocky Mountain provinces, USA. *Geochimica et Cosmochimica Acta*, **72**, 1174-1198.

Halford, D.T. 2018. Isotopic analyses of helium from wells located in the Four Corners area, southwestern US. Masters Thesis, Colorado School of Mines, 353 p.

Hinle, M.E. and Kilburn, J.E. 1980. Survey of helium in soil gases of Long Valley, California. *USGS Open File Report 80-612*, 19p.

Hinson, H.H. 1947. Reservoir characteristics of Rattlesnake oil and gas field, San Juan County, New Mexico. *AAPG Bulletin*, **31**, 731-771.

Holland, Philip W., 1984, An Analyzer for Determining Helium-4 in the Parts-Per-Billion Range, Report of Investigations 8853, U.S. Bureau of Mines, 14 pp.

Karlstrom, K.E. and Humphreys, E.D. 1998. Persistent influence of Proterozoic accretionary boundaries in the tectonic evolution of southwestern North America: Interaction of cratonic grain and mantle modification events. *Rocky Mountain Geology*, **33**, 161-179.

Koide, H. and Bhattacharji, S. 1975. Formation of fractures around magmatic intrusions and their role in ore localization. *Economic Geology*, 70, 781-799.

Lippolt, H.J., Leitz, M., Wernicke, R.S. and Hagedorn, B. 1994. (Uranium+thorium)/helium dating of apatite: experience with samples from different geochemical environments. *Chemical Geology*, **112**, 179-191.

Martel, D.J., O'Nions, R.K., Hilton, D.R. and Oxburgh, E.R. 1990. The role of element distribution in production and release of radiogenic helium: The Carnmenellis Granite, southwest England. *Chemical Geology*, **88**, 207-221.

Molenaar, C.M. and Halverson, D.V. 1969. Nomenclature chart of the Grand Canyon and adjacent areas. In *Geology and Natural History of the Grand Canyon region, Four Corners Geological Society Guidebook, Fifth Field Conference*, 68-77.

Pollack H. N., and Chapman, D. S., 1977, Mantle heat flow: Earth and Planetary Science Letters, v. 34, p. 174-184.

Rauzi, S.L. 2003. Review of helium production and potential in Arizona. *Arizona Geological Survey Open-File Report OFR 03-05*, 30p.

Reich, M., Ewing, R.C., Ehlers, T.A. and Becker, U. 2007. Low-temperature anisotropic diffusion of helium in zircon: implications for (U-Th)/He thermochronometry. *Geochimica et Cosmochimica Acta*, **71**, 3119-3130.

Reimer, G.M., 1976, Design and Assembly of a Portable Helium Detector for Evaluation as a Uranium Exploration Instrument, USGS Open-File Report 76-398, 18 pp.

Reimer, G.M. and Bowles, C.G. 1983. Helium concentrations in soil gas of the Ely and Delta 1deg x 2deg quadrangles, Basin and Range Province. *USGS Open File Report 83-589*, 25p.

Reiners, P.W. 2005. Zircon (U-Th)/He thermochronometry. *Reviews in Mineralogy and Geochemistry*, **58**, 151-179.

Reiners, P.W. and Farley, K.A. 1999. Helium diffusion and (U-Th)/He thermochronometry of titanite. *Geochimica et Cosmochimica Acta*, **63**, 3845-3859.

Rice, G., 2022. Vertical migration in theory and in practice. *Interpretation*, **10**, SB17-SB26.

Roberts, A.A. 1981. Helium emanometry in exploring for hydrocarbons, Part II. In *Unconventional Methods in Exploration for Petroleum and Natural Gas, Symposium II*, Southern Methodist University Press, Dallas, TX 136-149.

Semken, S. 2003. Black Rocks Protruding Up: The Navajo Volcanic Field. *New Mexico Geological Society Guidebook, 54$^{th}$ Field Conference, Geology of the Zuni Plateau*, 133-138.

Shuster, D.L., Flowers, R.M. and Farley, K.A. 2006. The influence of natural radiation damage on helium diffusion kinetics in apatite. *Earth and Planetary Science Letters*, **249**, 148-161.

Soreghan, G.S. and Soreghan, M.J. 2013. Tracing clastic delivery to the Permian Delaware basin, U.S.A.: Implications for paleogeography and circulation in westernmost equatorial Pangea. *Journal of Sedimentary Research*, **83(9)**, 786-802.

Sorenson, R. 2005. A dynamic model for the Permian Panhandle and Hugoton fields, western Anadarko basin. *AAPG Bulletin*, **89**, 921-938.

Stuart, F., Turner, G. and Taylor, R. 1994. He-Ar isotope systematics of fluid inclusions: resolving mantle and crustal contributions to hydrothermal fluids. In: Matsuda, J. (ed.) *Noble Gas Geochemistry and Cosmochemistry*. Terra Scientific Publishing, Tokyo, 261-277.

Valentine, G.A., Graettinger, A.H. and Sonder, I. 2014. Explosion depths for phreatomagmatic eruptions. *AGU Geophysical Letters*, 1-7.

Valentine, G.A., White, J.D.L., Ross, P., Graettinger, A.H. and Sonder, I. 2017. Updates to concepts on phreatomagmatic maar-diatremes and their pyroclastic deposits. *Frontiers in Earth Science*, **5**, 1-7.

Werner, S., 1953. Interpretation of magnetic anomalies at sheet-like bodies: Sveriges Geol. Undersok, Ser. C, Arsbok. 43(1949) no. 6.

Whitmeyer, S. J., and Karlstrom, K. E., 2007, Tectonic model for the Proterozoic growth of North America: Geosphere, v. 3, n. 4, p. 220-259.

Wollenweber, J., Alles, S., Kronimus, A., Busch, A., Stanjek, H. and Kross, B.M. 2009. Caprock and overburden processes in geological CO2 storage: An experimental study on sealing efficiency and mineral alterations. *Energy Procedia*, **1**, 3469-3476.

Wolf, R.A., Farley, K.A., and Silver, L.T. 1996. Helium diffusion and low-temperature thermochronometry of apatite. *Geochimica et Cosmochimica Acta*, **60**, 4231-4240.

## Thermal Study Refraction Station References

Herrmann, R. B., Dewey, J. W., and Park, S. K., 1966, The Dulce, New Mexico, earthquake of 23 January 1966: Bulletin of the Seismological Society of America, v. 70, n. 6, p. 2171-2183.

Hoffman, J. P., and Northrup, S. A., 1977, The Dulce, New Mexico earthquake Jan. 23, 1966: Earthquake Notes, v. 48, n. 4, p. 3-20.

Jaksha, L. H., and Evans, D. H., 1984, Reconnaissance seismic refraction reflection surveys in Northwestern New Mexico: Seismological Society of America Bulletin, v.74, n. 4, p.1263-1274.

Jaksha, L.H., 1982, Reconnaissance seismic refraction reflection surveys in southwestern New Mexico: Bulletin of the Geological Society of America, v.93, n. 10, p.1030-1037.

Lastowka, L. A., Sheehan, A. F., and Schneider, J. M., 2001, Seismic evidence for partial lithospheric delamination model of Colorado Plateau uplift: Geophysical Research Letters, v. 28, n. 7, p. 1319-1322.

Leidig, M. R., Bonner, J. L., and Reiter, D. L., 2005, Development of a velocity model for Black Mesa, Arizona, and the southern Colorado Plateau from multiple data sets: Bulletin of the Seismological Society of America, v 95, n. 6, p. 2136-2151.

Liu, K., Levander, A., Niu, F., and Miller, M. S., 2011, Imaging crustal and upper mantle structure beneath the Colorado Plateau using finite frequency Rayleigh wave tomography: Geochemistry, Geophysics, Geosystems, v. 12, n. 7, Q07001.

Lutter, W. J., Roberts, P. M., Thurber, C. H., Steck, L., Fehler, M. C., et al., 1995, Teleseismic P-wave image of crust and upper mantle structure beneath the Valles caldera, New Mexico: Initial results from the 1993 JTEX passive array: Geophysical Research Letters, v. 22, no. 4, pp. 505-508.

McCowan, D. W., 1978, High resolution group velocity analysis: Geoexploration, v. 16, n. 1-2, p.97-109.

Molenaar, C.M. and Halverson, D.V. 1969. Nomenclature chart of the Grand Canyon and adjacent areas. In Geology and Natural History of the Grand Canyon region: Four Corners Geological Society Guidebook, Fifth Field Conference, 68-77.

Prodehl, C., and Pakiser, L.C., 1980, Crustal structure of the southern Rocky Mountains from seismic measurements: Bulletin of the Geological Society of America, v.91, n.3, p. 147-155.

Roller, J. C., 1965, Crustal structure in the eastern Colorado Plateau Province from Seismic refraction measurements: Bulletin of the Seismological Society of America, v.55, n.1, p. 107-119.

Ryaboy, V., Baumgardt, D. R., Firbas, P., Dainty, A.M., 2001, Application of 3-d crustal and upper mantle velocity model of North America for location of regional seismic events: Pure and Applied Geophysics, v. 158, n1-2, p. 79-103.

Sheehan, A. F., Abers, G. A., Jones, C. H., and Lerner-Lam, A. L. 1995, Crustal thickness variations across the Colorado Rocky Mountains from teleseismic receiver functions. Journal of Geophysical Research, v. 100, m. B10, p. 20391-20404.

Shen, W., Ritzwoller, M. H., and Schulte-Pelkum, V., 2013, A 3-D model of the crust and uppermost mantle beneath the Central and Western US by joint inversion of receiver functions and surface wave dispersion: Journal of Geophysical Research, Solid Earth, v. 118, n. 1, p. 262-276.

Slack, P. D., Davis P. M., Baldridge, W. S., Olsen, K. H., Glahn, A., *et al*., 1996, The upper mantle structure of the central Rio Grande rift region from teleseismic P and S wave travel time delays and attenuation: Journal of Geophysical Research, 101, B7, 16003-16023.

Snelson, C. M., Henstock, T. J., Keller, G. R., Miller, K. C., and Levander, A., 1998, Crustal and uppermost mantle structure along the Deep Probe seismic profile: Rocky Mountain Geology, v. 33, n. 2, p. 181-198.

Stankova, J., Bilek, S. L., Rowe, C. A., and Aster, R. C., 2008, Characteristics of the October 2005 microearthquake swarms over Decadal time periods near Socorro, New Mexico: Bulletin of the Seismological Society of America, v. 98, n. 1, p. 93-105.

Steinhart, J. S., and Meyer, R. P. (editors), 1961, *Explosion Studies of Continental Structure, University of Wisconsin, 1956-1959*: Carnegie Institution of Washington, Publication 622, p. 226-383.

Toppozada, T. R., and Sanford, A. R., 1976, Crustal structure in Central New Mexico interpreted from the Gasbuggy Explosion: Bulletin of the Seismological Society of America, v. 66, n. 3, p. 877-886.

Warren, D.H. 1969. A seismic-refraction survey of crustal structure in central Arizona. Geological Society of America Bulletin, 80(2), 257-282.